

IRE Transactions



on ANTENNAS and PROPAGATION

Volume AP-8

MARCH, 1960

Number 2

Published Bimonthly

Theory of Coupled Folded Antennas

The Slot Antenna with Coupled Dipoles

Radiation Patterns of Finite-Size Corner-Reflector Antennas

The Flight Evaluation of Aircraft Antennas

Reciprocity and Scattering by Certain Rough Surfaces

Backscattering from a Finite Cone

Optimum Radar Integration Time

Temperature, Humidity and Refractive Index Spectra from Aircraft-Balloon Data

Aircraft Scintillation Spectra

Apparent Thermal Noise Temperatures in the Microwave Region

PUBLISHED BY THE
Professional Group on Antennas and Propagation

Administrative Committee

Arthur Dorne, *Chairman*

E. C. Jordan, *Vice-Chairman*

K. S. Kelleher, *Secretary*

S. A. Bowhill
R. N. Bracewell
J. W. Findlay
H. Fine

R. C. Hansen
S. M. King
R. K. Moore

W. H. Radford
E. K. Smith
K. M. Siegel
O. G. Villard, Jr.

Ex-Officio Members

J. I. Bohnert
H. G. Booker

R. L. Mattingly

D. C. Ports
P. H. Smith

Honorary Member

L. C. Van Atta

Chapter Chairmen

Albuquerque-Los Alamos

D. Thorn

Akron

J. R. Shoemaker

Boston

J. Ruze

Chicago

H. L. Woodbury

Columbus

H. B. Querido

Dayton

C. G. Conrad

Denver-Boulder

W. C. Coombs

Los Angeles

L. A. Kurtz

Orange Belt

W. S. Ward

Philadelphia

J. T. Beardwood

San Diego

H. Dickstein

San Francisco

E. Blasi

Syracuse

E. B. Mullen

Washington, D. C.

R. J. Adams

S. A. Bowhill, *Editor*

H. V. Cottony, *Associate Editor (Antennas)*

A. T. Waterman, Jr., *Associate Editor (Propagation)*

D. C. Ports, *Advertising Editor*

IRE TRANSACTIONS® PGAP IS A PUBLICATION DEVOTED TO
EXPERIMENTAL AND THEORETICAL PAPERS ON RADIO ANTENNAS,
ON GUIDED OR UNGUIDED PROPAGATION OF RADIO WAVES, AND
ON ALLIED FIELDS OF RADIO PHYSICS SUCH AS RADIO ASTRONOMY

MANUSCRIPTS should be submitted to Sidney A. Bowhill, Editor, 222 Electrical Engineering, Pennsylvania State University, University Park, Pa. Manuscripts should be original typewritten copy, double spaced, plus one carbon copy and two sets of copies of illustrations. Original illustrations will be called for if the paper is accepted. References should appear as footnotes and include author's name, title, journal, volume, initial and final page numbers, and date. Each paper must have a summary of not more than 200 words. News items concerning PGAP members and group activities should be sent to the News Editor, R. C. Hansen, Space Technology Laboratories, P.O. Box 95001, Los Angeles 45, Calif.

ORIGINAL ILLUSTRATIONS should be submitted as follows: All line drawings (graphs, charts, block diagrams, cutaways, etc.) should be inked uniformly and ready for reproduction. If commercially printed grids are used in graph drawings, author should be sure printer's ink is of a color that will reproduce. All halftone illustrations (photographs, wash, airbrush, or pencil renderings, etc.) should be clean and ready to reproduce. Photographs should be glossy prints. Call-outs or labels should be marked on a registered tissue overlay, not on the illustration itself. No illustration should be larger than 8 x 10 inches.

Copies can be purchased from THE INSTITUTE OF RADIO ENGINEERS, 1 East 79 St., New York 21, N.Y. PRICE PER COPY: members of the Professional Group on Antennas and Propagation, \$2.00; members of the IRE \$3.00; nonmembers, \$6.00. **ANNUAL SUBSCRIPTION PRICE:** PGAP members, included in PGAP fee of \$4.00; IRE members, \$8.50; Colleges and public libraries, \$10.00; nonmembers, \$17.00. **IRE TRANSACTIONS ON ANTENNAS AND PROPAGATION.** Copyright © 1960, by The Institute of Radio Engineers, Inc. Printed in U.S.A.

Second-class postage paid at Menasha, Wisconsin, under the act of August 24, 1912. Acceptance for mailing at a special rate of postage is provided for in the act of February 28, 1925, embodied in Paragraph 4, Section 412, P. L. & R., authorized October 26, 1927.

Bateman, R.
Bolljahn, J.T.
Brueckmann, H.
Bullington, K.
Carter, P.S.
Cohn, S.
Crawford, A.B.
Deschamps, G.A.
Duhamel, R.H.
Frederick, V.L.
Goodrich, R.
Hansen, R.C.
Hayden, E.C.
Hefley, G.
Hiatt, R.E.
Honey, R.C.
Johler, J.R.
Johnk, C.T.
Jones, E.M.T.
Jordan, E.C.
Kay, A.F.
Lawrence, R.S.
Little, C.G.
Lo, Y.T.
Marston, A.E.
Mattingly, R.L.
Morgan, S.P.
Morita, T.
Mortimore, T.N.
Norton, K.A.
Rogers, T.F.
Rumsey, V.H.
Ruze, J.
Schiffmacher, E.R.
Silberstein, R.
Sinclair, G.
Swenson, G.W.
Tanner, R.L.
Twersky, V.
Wait, J.R.
Woodyard, O.C.
Yen, J.L.

Allen, E.W.
Ament, W.S.
Austin, P.M.
Berkner, L.V.
Berning, W.S.
de Bettencourt, J.T.
Booker, H.G.
Brennan, D.G.
Brown, S.C.
Bullington, K.
Carroll, T.J.
Chisholm, J.H.
Findlay, J.W.
Gautier, T.N.
Gibbons, J.J.
Goldstein, L.
Haddock, F.T.
Helliwell, R.A.
Katzin, M.
Kline, M.
Kraus, J.D.
Lowenthal, M.
Manning, L.A.
Mentzer, J.R.
Norton, K.A.
Pfister, W.
Pierce, J.A.
Rice, S.O.
Rumsey, V.S.
Schmerling, E.R.
Seddon, J.C.
Siegel, K.M.
Slutz, R.J.
Smyth, J.B.
Straiton, A.W.
Wait, J.S.
Waynick, A.H.
Wheelon, A.D.

IRE Transactions

on

Antennas and Propagation

Volume AP-8

MARCH, 1960

Number 2

TABLE OF CONTENTS

Frontispiece.....	128
John B. Smyth, Retiring Editor.....	129
Editorial Comment.....	130

CONTRIBUTIONS

Theory of Coupled Folded Antennas.....	<i>C. W. Harrison, Jr. and Ronold King</i>	131
The Slot Antenna with Coupled Dipoles.....	<i>R. W. P. King and G. H. Owyang</i>	136
Radiation Patterns of Finite-Size Corner-Reflector Antennas.....	<i>A. C. Wilson and H. V. Cottony</i>	144
The Flight Evaluation of Aircraft Antennas.....	<i>George W. Leopard</i>	158
Reciprocity and Scattering by Certain Rough Surfaces.....	<i>W. S. Ament</i>	167
Backscattering from a Finite Cone.....	<i>Joseph B. Keller</i>	175
Optimum Radar Integration Time.....	<i>J. M. Flaherty and E. Kadak</i>	183
Power Spectra of Temperature, Humidity and Refractive Index from Aircraft and Tethered Balloon Measurements.....	<i>Earl E. Gossard</i>	186
Aircraft Scintillation Spectra.....	<i>Robert B. Muchmore</i>	201
Apparent Thermal Noise Temperatures in the Microwave Region.....	<i>Eric Weger</i>	213

COMMUNICATIONS

Patterns of a Radial Dipole on an Infinite Circular Cylinder: Numerical Values.....	<i>Curt A. Levis</i>	218
Linear Arrays with Arbitrarily Distributed Elements.....	<i>H. Unz</i>	222
Synthesis of Nonseparable Two-Dimensional Patterns by Means of Planar Arrays.....	<i>A. Ksienski</i>	224
A Method to Reduce Antenna Ground Reflections.....	<i>David Sabih</i>	225
Impulse Excitation of a Conducting Medium.....	<i>J. Galejs</i>	227
Electromagnetic Transients in Conducting Media.....	<i>S. H. Zisk</i>	229
Contributors.....		231



John B. Smyth (SM'52-F'56) was born in Pembroke, Ga., on June 8, 1914. He received the B.S. and M.S. degrees in 1934 and 1937, respectively, from the University of Georgia, Athens. From 1937 to 1938 he was on the technical staff of the Tennessee Eastman Corporation as a research physicist. He then continued his graduate studies at Brown University, Providence, R. I., receiving the Ph.D. degree in 1942. From 1942 to 1955 he was on the technical staff of the U. S. Navy Electronics Laboratory in San Diego, Calif., where he was engaged in wave propagation research. For ten years he directed the theoretical and experimental research program in tropospheric, ionospheric and radio meteorology studies at NEL. He was also involved in sonar propagation research. He organized the UCLA off-campus graduate program at NEL and acted as graduate advisor for UCLA. He holds appointments as Lecturer in Engineering at UCLA and Lecturer in Physics at San Diego State College.

In 1955 Dr. Smyth, with a number of his col-

leagues, formed Smyth Research Associates, where he holds the position of President and Technical Director of this organization. At SRA he has continued to expand his research interests in the general field of antennas and propagation. Under his vigorous leadership, the company has grown and broadened its activities in applied electronic research.

Dr. Smyth has authored numerous papers and reports dealing with wave propagation through nonhomogeneous media. He has been active in the affairs of URSI for many years, has been chairman of USA Commission II, and is currently International Vice President of Commission II. He has also served as a State Department appointee to the CCIR. He is a member of Phi Beta Kappa, Phi Kappa Phi, Pi Mu Epsilon, Xi Phi Xi, Sigma Xi, the American Acoustical Society, AAAS, and the American Physical Society. In 1945 he was awarded the IRE Seventh Region Electronic Region Award and has served on several IRE committees.

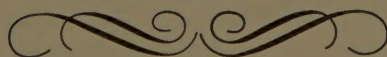


John B. Smyth, Retiring Editor

Our Professional Group takes this opportunity to acknowledge with deepest appreciation its indebtedness to John Smyth in his outstanding service as Editor of these TRANSACTIONS. John, in view of the press of other duties, has recently resigned as Editor and, as indicated elsewhere in the TRANSACTIONS, Dr. Sidney A. Bowhill is now taking over these duties.

The fact that we now have an internationally accepted journal prepared in suitable form to warrant acceptance by the scientific and engineering fraternity is due in very great part to John's ef-

forts. He has, as would be expected by those who know him, insisted on the highest caliber of TRANSACTIONS content. He has been the prime mover in assuring that the TRANSACTIONS format and editorial arrangements are a truly professional job. While he will be relieved of many of the onerous duties associated with the Editorship, the members of our Professional Group will continue to feel free to call upon him in the future in many ways with the expectation of obtaining, as usual, enthusiastic help and response.—A.H.W.



Editorial Comment

SINCE this is the first issue of the PGAP TRANSACTIONS which has appeared in bi-monthly form, it seems to be an appropriate time to review the functions and objectives of this journal.

First, it should be said that we view the TRANSACTIONS as essentially a scientifically oriented engineering journal. That is to say, it has a sufficiently wide circulation that any author publishing a paper in it can regard his work as thereby having become part of the accepted literature in the field. This does not mean that all contributions must be novel: there is a definite place for papers of a review nature, designed to expound the current status of a particular area or group of areas: such papers, indeed, have proved to be most useful when they have appeared in PROCEEDINGS OF THE IRE.

Papers presenting new material, to be published in the Contributions section of the TRANSACTIONS, are always welcome. Since these papers are carefully reviewed by experts in the specialized field, it is necessary for the author to submit two manuscripts complete with diagrams in addition to the original diagrams. Because of the nature of the publication and reviewing process, six months or more may elapse between submission of the paper and its publication, depending on the amount of revision of the paper which is thought necessary. The following may prove helpful in improving the quality of the paper and cutting down on the amount of revision:

- 1) The content of the paper should present new ideas, or shed new light on old ideas, in a way that will prove interesting to a number of readers of the periodical.

- 2) The material should be presented as concisely as possible. Standard derivations should not be reproduced, but reference should be made to

the appropriate source. Prior work relevant to the topic should always be referenced.

- 3) The information given in the paper should be as complete as possible (apart from trivial detail). All terms should be defined in such a way that a person not familiar with the notation can follow the argument. Reference should not be made to work in classified reports, or to any reports not generally available to the reading public.

With reference to subject matter, the TRANSACTIONS have, in the past, contained little material on Radio Astronomy or on Ionospheric Propagation. Both these fields come within the charter of the Professional Group on Antennas and Propagation, as defined, and papers in these fields will be given special consideration. The electromagnetic theory of scattering, treated by many papers in the recent PGAP Toronto Symposium Proceedings, is another field in which additional contributions will be welcomed.

Perhaps a word should be said on the place of "hardware" papers in the TRANSACTIONS. This is certainly not an exclusively theoretical journal. Many of the best papers have been experimental in nature. Provided that the principles embodied in it are new, any paper concerning "hardware" subjects will be given favorable consideration.

Last, the place of "Communications" in the PGAP TRANSACTIONS should be mentioned. In our view, these should be, essentially, letters to the Editor, which do not undergo the exhaustive review procedure that is undergone by Contributions. They should be brief, and should aim to bring out only one or two points, which merit rapid publication by virtue of their topical interest. Publication of such items can be expected in about three months from the date of receipt.

It is hoped that the quality of papers submitted to this Journal will enable it to maintain the high standard that has been set during past years.

contributions

Theory of Coupled Folded Antennas*

C. W. HARRISON, JR.[†] AND RONOLD KING[‡]

Summary—Formulas for the mutual and self-impedance of two identical nonstaggered parallel-folded dipoles are developed. A generalization of the theory permits determination of these impedances for any identical dual configuration of wires, no matter how complicated, provided the structures are symmetrical with respect to the driving points. If the impedance of any single-conductor solid-wire element in a symmetrical circular array of linear radiators is known, the impedance of each element in a similar array consisting of folded-wire structures is readily obtained. Two obvious practical uses of the theory are: 1) the determination of the performance of a two-element folded antenna array, when one antenna is a tuned parasite, functioning as a director or reflector; and 2) determination of the driving-point impedance of a folded antenna parallel to a highly-conducting plane.

INTRODUCTION

GENERALLY, the existing analyses of coupled linear radiators fall into two groups. In the first group, the distribution of current in each antenna is assumed to be sinusoidal in form. Using this assumption and the EMF method, Carter¹ in 1932, and Brown² in 1937, developed relations for mutual and self-impedance for coupled linear antennas. In the second group, the distribution of current in the coupled antennas and the associated mutual and self-impedances

are sought. The coupled antenna problem, using the integral equation formulation, was first solved by King and Harrison.³ This approach, which is called the retarded potential method, was later improved by Tai.⁴ The purpose of this investigation is to extend the theory of coupled antennas to include coupled folded-wire elements using the retarded potential technique.

In this paper, the simplest possible problem is solved; that of two identical parallel nonstaggered folded dipoles in proximity. The generalization of the method to more complicated folded-wire elements in arrays is then indicated.

THEORETICAL CONSIDERATIONS

Consider two identical parallel nonstaggered perfectly-conducting folded antennas spaced a distance c apart as shown in Fig. 1. Each structure consists of two wires of length $2h$, labeled 1 and 2, and of radius a , spaced a distance b apart. The conductors are shorted at their outer extremities. The driving points are centrally located in wires labeled 1. The assumption is made that the dimensions of each structure, and the spacing between them satisfies the following inequalities:

$$\left. \begin{aligned} a &\ll h, \\ \beta a &= 2\pi a/\lambda \ll 1 \\ \beta b &\ll 1, c \geq 5b \end{aligned} \right\}. \quad (1)$$

* Manuscript received by the PGAP, May 5, 1959; revised manuscript received, October 5, 1959. This paper originally appeared as Sandia Corp. Tech. Memo. 332-58(14), September 3, 1958. It was presented to the Albuquerque-Los Alamos Section of the PGAP, November 18, 1958.

[†] Sandia Lab., Sandia Base, Albuquerque, N. M.

[‡] Consultant to the Sandia Corp., and Professor of Applied Physics, Harvard University, Cambridge, Mass.

¹ P. S. Carter, "Circuit relations in radiating systems and applications to antenna problems," *PROC. IRE*, vol. 20, pp. 1004-1041; June, 1932.

² G. H. Brown, "Directional antennas," *PROC. IRE*, vol. 25, pp. 78-145; January, 1937.

³ R. King and C. W. Harrison, Jr., "Mutual and self-impedance for coupled antennas," *J. Appl. Phys.*, vol. 15, pp. 481-495; June, 1944.

⁴ C. T. Tai, "Coupled antennas," *PROC. IRE*, vol. 36, pp. 487-500; April, 1948.

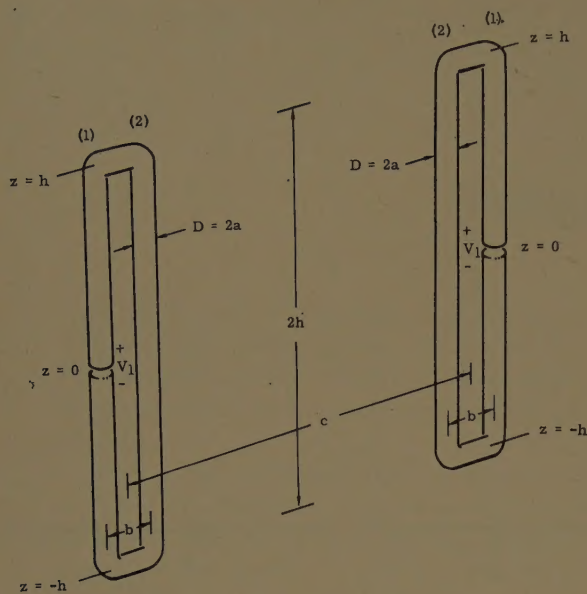


Fig. 1—Symmetrically-driven coupled folded dipoles.

Here, λ is the wavelength. If $c \approx b$, the standard method of analyzing the resulting composite circuit should be employed.⁵ Ordinarily, no advantage accrues by defining mutual and self-impedances for such circuits.

Assume that the antennas illustrated by Fig. 1 are symmetrically driven by identical impedanceless delta function generators of voltage V_1 . The two simultaneous integral equations applicable to the complete circuit follow.

For Wire 1

$$\begin{aligned} \int_{-h}^h I_1(z') K_a(z, z') dz' + \int_{-h}^h I_2(z') K_b(z, z') dz' \\ + \int_{-h}^h I_T(z') K_c(z, z') dz' \\ = -j \frac{4\pi}{\zeta} \left\{ C_1 \cos \beta z + \frac{V_1}{2} \sin \beta |z| \right\}. \quad (2) \end{aligned}$$

For Wire 2

$$\begin{aligned} \int_{-h}^h I_1(z') K_b(z, z') dz' + \int_{-h}^h I_2(z') K_a(z, z') dz' \\ + \int_{-h}^h I_T(z') K_c(z, z') dz' = -j \frac{4\pi}{\zeta} C_2 \cos \beta z. \quad (3) \end{aligned}$$

Here $I_1(z)$ and $I_2(z)$ are the currents along wires 1 and 2, respectively, in either folded antenna.

$$I_T(z) = I_1(z) + I_2(z) \quad (4)$$

$$K_a(z, z') = \exp(-j\beta \sqrt{(z - z')^2 + a^2}) / \sqrt{(z - z')^2 + a^2} \quad (5)$$

$K_b(z, z')$ and $K_c(z, z')$ are obtained from (5) by writing b for a and c for a , in the order mentioned.

$$\zeta = 120\pi \text{ ohms} \quad (6)$$

C_1 and C_2 are constants of integration.

Eqs. (2) and (3) have the boundary condition built in that the tangential component of electric field along the surface of each wire parallel to the z -axis is zero.

The first step in the solution of (2) and (3) is to express the first integral in (2) in the form

$$\begin{aligned} \int_{-h}^h I_1(z') K_a(z, z') dz' = \int_{-h}^h I_1(z') K_d(z, z') dz' \\ + \int_{-h}^h I_1(z') \{ K_a(z, z') - K_d(z, z') \} dz' \quad (7) \end{aligned}$$

where $K_d(z, z')$ is obtained from (5) by writing d for a throughout. In (7), d is an as yet arbitrary small effective radius that satisfies the condition $\beta d \ll 1$. Now consider the second integral on the right in (7). Since βd and βa are both small, this integral has a value significantly different from zero only when $z \approx z'$. In a small range near $z' = z$, the amplitude of the current varies slowly with z' ; hence $I_1(z') \approx I_1(z)$ and may be removed from under the sign of integration. When this has been done, the limits of integration $-h \leq z' \leq h$ may be replaced by $-\infty \leq z' \leq \infty$. Thus,

$$\begin{aligned} \int_{-h}^h I_1(z') \{ K_a(z, z') - K_d(z, z') \} dz' \\ \approx I_1(z) \int_{-\infty}^{\infty} \{ K_a(z, z') - K_d(z, z') \} dz' \approx I_1(z) \lambda_a \quad (8) \end{aligned}$$

where

$$\lambda_a = 2 \ln \frac{d}{a}. \quad (9)$$

Eq. (7) now becomes

$$\begin{aligned} \int_{-h}^h I_1(z') K_a(z, z') dz' \\ = \int_{-h}^h I_1(z') K_d(z, z') dz' + I_1(z) \lambda_a. \quad (10) \end{aligned}$$

The second integral in (2) is treated in the same manner. The result is

$$\begin{aligned} \int_{-h}^h I_2(z') K_b(z, z') dz' \\ = \int_{-h}^h I_2(z') K_d(z, z') dz' + I_2(z) \lambda_b \quad (11) \end{aligned}$$

where

$$\lambda_b = 2 \ln \frac{d}{b}. \quad (12)$$

⁵ Charles W. Harrison, Jr., "Folded Antennas," Ph.D. Dissertation, Harvard Univ., Cambridge, Mass.; 1954. Some of this material appeared under the same title as Tech. Rept. No. 193, Cruft Lab., Harvard Univ., March 1, 1954.

The two simultaneous integral equations now take the form

$$J_d(z) + I_1(z)\lambda_a + I_2(z)\lambda_b + \int_{-h}^h I_T(z')K_c(z, z')dz' = -j\frac{4\pi}{\zeta}\left\{C_1 \cos \beta z + \frac{V_1}{2} \sin \beta/z/\right\} \quad (13)$$

$$J_d(z) + I_1(z)\lambda_b + I_2(z)\lambda_a + \int_{-h}^h I_T(z')K_c(z, z')dz' = -j\frac{4\pi}{\zeta}C_2 \cos \beta z. \quad (14)$$

The notation

$$J_d(z) = \int_{-h}^h I_T(z')K_d(z, z')dz' \quad (15)$$

is used for convenience.

Adding (13) and (14), and setting $\lambda_a = -\lambda_b$, so that

$$d = \sqrt{ab} < b \quad (16)$$

results in the antenna equation

$$J_d(z) + \int_{-h}^h I_T(z')K_c(z, z')dz' = -j\frac{4\pi}{\zeta}\left\{\frac{(C_1 - C_2)}{2} \cos \beta z + \frac{V_1}{4} \sin \beta|z|\right\}. \quad (17)$$

Eq. (17) is essentially the same one King and Harrison³ (and later Tai⁴) solved subject to the boundary condition.

$$I_T(\pm h) = 0 \quad (18)$$

for two symmetrically-driven coupled single-conductor antennas. The solution is

$$Z^s = \frac{V_1}{2I_T(0)}. \quad (19)$$

Here Z^s is the driving-point impedance, looking into either antenna, of a symmetrically-driven array consisting of two single conductors of radius $d = \sqrt{ab}$, and of length $2h$ spaced a distance c apart. Numerical values of Z^s are available in the literature.⁶

On subtracting (14) from (13), the transmission line equation

$$I_1(z) - I_2(z) = -j\frac{4\pi}{\zeta\lambda_{ab}}\left\{(C_1 - C_2) \cos \beta z + \frac{V_1}{2} \sin \beta/z/\right\} \quad (20)$$

is obtained, where

$$\lambda_{ab} = \lambda_a - \lambda_b = 2 \ln \left(\frac{b}{a} \right). \quad (21)$$

Since the charge density is continuous around the bends in the antennas because wires of the same radius are employed, the boundary condition⁷

$$\left\{ \frac{\partial I_1(z)}{\partial z} - \frac{\partial I_2(z)}{\partial z} \right\} z = \pm h = 0 \quad (22)$$

applies.

The application of (22) to (20) permits the determination of $C_1 - C_2$. The value of this constant is

$$C_1 - C_2 = \frac{V_1}{2} \cot \beta h. \quad (23)$$

Also, from (20), for $z=0$,

$$I_1(0) = I_2(0) - j\frac{2\pi V_1 \cot \beta h}{\zeta\lambda_{ab}}. \quad (24)$$

Adding $I_1(0)$ to both sides of (24), and noting that $I_T(0) = I_1(0) + I_2(0)$, leads to

$$I_1(0) = \frac{I_T(0)}{2} - j\frac{\pi V_1 \cot \beta h}{\zeta\lambda_{ab}}. \quad (25)$$

Now $I_T(0)$ is given by (19), ζ by (6), and λ_{ab} by (21). Using these in (25) results in the expression (in mhos)

$$Y_0^s = \frac{I_1(0)}{V_1} = \frac{1}{4Z^s} - j\frac{\cot \beta h}{240 \ln \left(\frac{b}{a} \right)}. \quad (26)$$

By an entirely analogous argument, the driving-point admittance of two antisymmetrically-driven coupled folded antennas is obtained. The result in mhos is

$$Y_0^a = \frac{1}{4Z^a} - j\frac{\cot \beta h}{240 \ln \left(\frac{b}{a} \right)}. \quad (27)$$

In (27), Z^a is the driving-point impedance of either antenna in an antisymmetrically-driven two-element array consisting of single conductors of radius $d = \sqrt{ab}$ and of length $2h$ spaced a distance c apart. Numerical values of Z^a are available in the literature.⁶

Using standard circuit theory, it is easily shown that

$$\frac{1}{Y_0^s} = Z_{11} + Z_{12} \quad (28)$$

⁷ If wires of unequal diameter comprise a folded conductor antenna element, the boundary condition

$$\left\{ \frac{\partial A_1(z)}{\partial z} - \frac{\partial A_2(z)}{\partial z} \right\}_{z=\pm h} = 0$$

must be used. Actually (22) may be regarded as a specialized form of the vector potential condition delineated in this footnote.

⁶ R. King, "Theory of Linear Antennas," Harvard University Press, Cambridge, Mass., ch. III, Figs. 7.1 and 7.2 and Tables 7.1 and 7.2, pp. 279-280; 1956.

and

$$\frac{1}{Y_0^a} = Z_{11} - Z_{12} \quad (29)$$

where Z_{11} is the self-impedance of either folded dipole in the presence of the other, and Z_{12} is the mutual impedance. Thus

$$Z_{11} = \frac{Y_0^s + Y_0^a}{2Y_0^s Y_0^a} \quad (30)$$

$$Z_{12} = -\frac{Y_0^s - Y_0^a}{2Y_0^s Y_0^a} \quad (31)$$

Substituting (26) and (27) in these expressions gives

$$Z_{11} = D^{-1} \left[Z^s + Z^a - j \frac{Z^s Z^a \cot \beta h}{30 \ln b/a} \right] \quad (32)$$

and

$$Z_{12} = \frac{Z^s - Z^a}{D} \quad (33)$$

Here

$$D = 8Z^s Z^a \left\{ \frac{1}{4Z^s} - j \frac{\cot \beta h}{240 \ln \left(\frac{b}{a} \right)} \right\} \cdot \left\{ \frac{1}{4Z^a} - j \frac{\cot \beta h}{240 \ln \left(\frac{b}{a} \right)} \right\} \quad (34)$$

The well-known formula for the driving-point admittance of an isolated two-wire folded dipole is

$$Y_{in} = \frac{1}{4Z_d} - j \frac{\cot \beta h}{240 \ln \left(\frac{b}{a} \right)} \quad (35)$$

where Z_d is the self-impedance of an isolated symmetrical center-driven antenna of the same length as the folded dipole. The wire is of radius $d = \sqrt{ab}$, where a is the actual radius of the wire used in the folded antenna, and b is the conductor spacing. On comparing (35) with (26) and (27), it is evident that one need only substitute Z^s for Z_d to obtain a formula for Y_0^s and Z^a for Z_d to obtain a formula Y_0^a . The mutual and self-impedances of two coupled folded dipoles are then available from (30) and (31). This suggests that if a formula is available for the impedance of an isolated folded-wire configuration,⁸ it is a simple matter to obtain mutual and self-impedance information for the identical coupled structures. Likewise, if the impedance looking into any radiator of a circular array consisting of single-wire elements for any

permissible phase sequence is known,⁸ the impedance of the same array; with all elements replaced by folded-wire structures, is also known.

EXTENSION OF THE THEORY TO OTHER FOLDED-WIRE STRUCTURES

A symmetrically-folded antenna having two open-circuited ends is pictured in Fig. 2. The cross section of the structure is that of an equilateral triangle of leg length b . The conductors are of radius a and of length $2h$.

It is known that the driving-point admittance of this antenna, when isolated from its surroundings, is given by the expression.

$$Y_{in} = \frac{1}{9Z_d} - j \left\{ \frac{\sin 2\beta h}{1 - 2 \cos 2\beta h} \right\} \left\{ \frac{1}{90 \ln \left(\frac{b}{a} \right)} \right\} \quad (36)$$

Here Z_d is the impedance of an isolated solid-wire symmetrical center-driven antenna of radius $d = \sqrt[3]{ab^2}$ and half-length h .

Formulas for the mutual and self-impedance of a two-element array, when each element is identical to the structure pictured in Fig. 2, may now be developed, beginning with (36).

Y_0^s and Y_0^a are given by the relations

$$Y_0^s = \frac{1}{9Z^s} - j \left\{ \frac{\sin 2\beta h}{1 - 2 \cos 2\beta h} \right\} \left\{ \frac{1}{90 \ln \left(\frac{b}{a} \right)} \right\} \quad (37)$$

$$Y_0^a = \frac{1}{9Z^a} - j \left\{ \frac{\sin 2\beta h}{1 - 2 \cos 2\beta h} \right\} \left\{ \frac{1}{90 \ln \left(\frac{b}{a} \right)} \right\}, \quad (38)$$

respectively. Here, Z^s is the driving-point impedance of a symmetrically-driven two-element array. Each antenna consists of a single solid conductor of length $2h$ and effective radius $d = \sqrt[3]{ab^2}$. The spacing between conductors is c . Z^a is determined in precisely the same way, except that the antennas are antisymmetrically-driven. Eqs. (30) and (31) now permit calculation of Z_{11} and Z_{12} .

A four-wire re-entrant loop is portrayed by Fig. 3. The driving-point admittance of the isolated structure is

$$Y_{in} = \frac{1}{16Z_d} - j \frac{\cot \beta h}{480 \left\{ \left(\ln \frac{b}{a} \right)^2 - (\ln \sqrt{2})^2 \right\}} \cdot \left\{ 3 \ln \left(\frac{b}{a} \right) - \ln \sqrt{2} - 2 \ln \left(\frac{b}{a\sqrt{2}} \right) \sec 2\beta h \right\} \quad (39)$$

and the effective radius is

$$d = \sqrt[4]{ab^3 \sqrt{2}}. \quad (40)$$

⁸ R. King, "Linear Arrays: Currents, Impedances, and Fields, I," Cruft Lab., Harvard Univ., Cambridge, Mass., Scientific Rept. No. 1 (ser. 2); May 1, 1959.

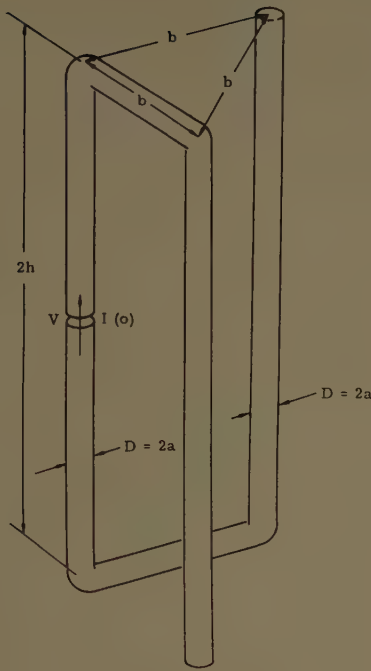


Fig. 2—Symmetrically-folded antenna with two open-circuited ends.

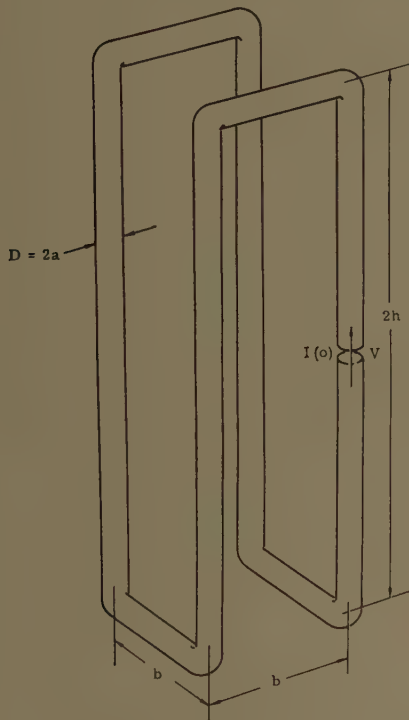


Fig. 3—Re-entrant loop.

Z_a is the impedance of the "equivalent" isolated symmetrical center-driven antenna. Y_0^s is obtained from (39) by substituting Z^s for Z_a ; Y_0^a by substituting Z^a for Z_a . As before, Z^s and Z^a are obtained from the theory of two solid-conductor coupled antennas of half-length h spaced a distance c apart. The effective radius is given by (40). Eqs. (30) and (31) are employed to determine Z_{11} and Z_{12} .

The driving-point admittance of an isolated folded antenna consisting of two wires of unequal diameter may be obtained from the formula

$$Y_{in} = \frac{1}{Z_D} \left\{ \frac{\ln\left(\frac{b}{a_2}\right)}{\ln\left(\frac{b^2}{a_1 a_2}\right)} \right\}^2 - j \frac{\cot \beta h}{120 \ln\left(\frac{b^2}{a_1 a_2}\right)}, \quad (41)$$

assuming that the terminals are located at the center of the wire of radius a_1 . Z_D is the driving-point impedance of a symmetrical center-driven antenna of half-length h and effective radius

$$D = \sqrt{b \sqrt{a_1 a_2} e^p} \quad (42)$$

where

$$p = \frac{\frac{1}{4} \left\{ \ln\left(\frac{a_1}{a_2}\right) \right\}^2}{\ln\left(\frac{b^2}{a_1 a_2}\right)}. \quad (43)$$

The input admittance of the structure when oriented parallel to a highly-conducting plane at a distance $c/2$ is obtained from (41) by replacing Z_D with Z^a . Z^a is the impedance of an antisymmetrically-driven array. The conductors in this array are of radius D , given by (42), half-length h , and spaced a distance c apart. Thus,

$$Y_0^a = \frac{1}{Z^a} \left\{ \frac{\ln\left(\frac{b}{a_2}\right)}{\ln\left(\frac{b^2}{a_1 a_2}\right)} \right\}^2 - j \frac{\cot \beta h}{120 \ln\left(\frac{b^2}{a_1 a_2}\right)}. \quad (44)$$

(It should be noted that the image antenna is in anti-phase with respect to the actual antenna and is spaced a distance $c/2$ below the ground plane.)

CONCLUSION

In this paper it has been shown, or at least inferred, that if a formula for the self-impedance of the isolated folded-wire structure can be found, one can immediately deduce mutual and self-impedance information for two identical structures in proximity to one another. This is possible because the impedances of symmetrically- and antisymmetrically-driven antenna arrays consisting of two parallel nonstaggered solid-conductor center-driven elements are known.

It is now possible to treat folded antenna coupled-circuit problems with the same facility as has been experienced in solving single-conductor antenna coupled-circuit problems in the past. In addition, circuitual relations may be developed for more elaborate folded antenna arrays. If it is possible to solve a problem involving single-conductor antenna arrays for transmission or reception, the same problem relating to folded-wire element arrays can also be solved.

The Slot Antenna with Coupled Dipoles*

R. W. P. KING† AND G. H. OWYANG‡

Summary—The problem of an array consisting of a slot antenna and two symmetrically-located cylindrical dipoles is formulated. The approximate distribution of the current along each antenna is obtained by a method of iteration. The radiation function, the coupling coefficients between the slot and the dipole, the relation between the magnetic current in the slot and the electric current in the dipole, and the input impedance of the slot in the presence of the dipoles have been obtained. An experimental setup for measuring the radiation patterns is described and measured and theoretical patterns are displayed.

I. INTRODUCTION

ARRAYS of cylindrical antennas are frequently used to obtain a desired field pattern. By complementarity, arrays of slots may also be employed to give a corresponding result. In a similar manner, the radiation pattern of a slot antenna may be altered by placing a passive dipole in front of the slot antenna.

The radiating system to be studied consists of a slot antenna and two metallic dipoles. The ideal slot antenna is cut in a perfectly conducting sheet of infinite size and vanishing thickness. The dipoles are made of thin, perfectly-conducting circular wires symmetrically located on each side of the slot. The rectangular coordinate system is chosen so that the slot antenna is along the x axis and its center coincides with the origin. The dipoles are at distances $\pm d$ on the z axis from the slot antenna and are parallel to the y axis, as shown in Fig. 1. The slot antenna is driven by a magnetic slice generator at the center of the slot. The dipoles are driven by electric slice generators which are equal in magnitude and phase. By the principle of complementarity, a slot cut in an infinitely thin metal sheet of infinite extent may be replaced by an infinitely thin strip of magnetic conductor which has the same geometry as the slot provided the electric field on one side of the metal sheet is reversed. In other words, the problem to be considered is the same as an array of a magnetic strip antenna located at the original position of the slot and two electric dipoles which are driven by sources of equal amplitude but opposite in phase.

Before treating the complete system, consisting of a slot and coupled dipoles, it is advantageous to consider the isolated electric dipole and the isolated slot separately. It is well known¹ that a slot antenna is equivalent to a magnetic strip antenna with the same geometric configuration carrying a magnetic current density which

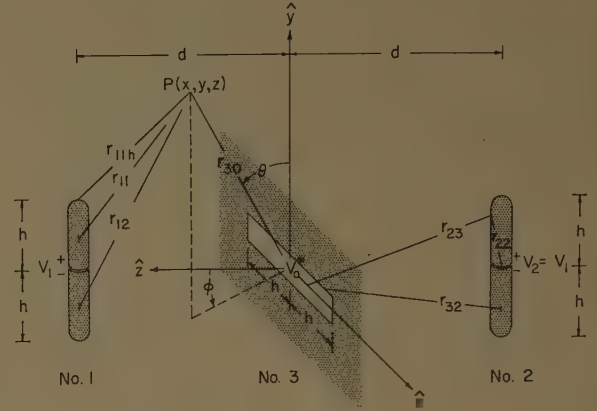


Fig. 1—Arrangement of slot antenna with coupled dipoles.

is equal to the transverse E field across the slot. Therefore, the problem to be analyzed may be considered to consist of two electric dipoles and a magnetic strip dipole; the latter is located at the slot (Fig. 1) with the ground screen removed. Since the electromagnetic field of the electric dipole is well known,² it is only necessary to define complementary quantities for the magnetic dipole. This will be done by arranging corresponding equations side by side. Asterisks are used to identify the quantities pertaining to the magnetic dipole. The Maxwell's equations are:

$$\text{curl } \mathbf{H}^* = -\mathbf{J}^* - j\omega\mu\mathbf{E}^*; \quad \text{curl } \mathbf{H} = \mathbf{J} + j\omega\epsilon\mathbf{E}, \quad (1a)$$

$$\text{curl } \mathbf{E}^* = j\omega\epsilon\mathbf{H}^*; \quad \text{curl } \mathbf{E} = -j\omega\mu\mathbf{H}, \quad (1b)$$

where the complex permittivity $\epsilon = \epsilon_0 + \sigma_0/j\omega$. The fields are related to the vector potentials as follows:

$$\mathbf{H}^* = \frac{-1}{\epsilon} \text{curl } \mathbf{A}^*; \quad \mathbf{H} = \frac{1}{\mu} \text{curl } \mathbf{A}. \quad (2a)$$

$$\mathbf{E}^* = \frac{-j\omega}{\beta_0^2} (\text{grad div } \mathbf{A}^* + \beta_0^2 \mathbf{A}^*);$$

$$\mathbf{E} = \frac{-j\omega}{\beta_0^2} (\text{grad div } \mathbf{A} + \beta_0^2 \mathbf{A}), \quad (2b)$$

where $\beta_0 = 2\pi/\lambda_0$. These vector potentials satisfy the general wave equation and can be expressed by the Helmholtz integrals:

$$\mathbf{A}^* = \frac{\epsilon}{4\pi} \int_v \mathbf{J}^* K_0 d\tau'; \quad \mathbf{A} = \frac{\mu}{4\pi} \int_v \mathbf{J} K_0 d\tau'. \quad (3a)$$

$$K_0 = \frac{1}{r_{ik}} e^{-j\beta_0 r_{ik}}; \quad r_{ik}^2 = (x_i - x_k)^2 + (y_i - y_k)^2 + (z_i - z_k)^2, \quad (3b)$$

* Manuscript received by the PGAP, June 9, 1959; revised manuscript received, October 12, 1959.

† Gordon McKay Lab., Harvard University, Cambridge, Mass.
‡ Radiation Lab., University of Michigan, Ann Arbor, Mich. Formerly at Gordon McKay Lab., Harvard University, Cambridge, Mass.

¹ More detailed discussion on this subject may be found in G. H. Owyang, "The Principle of Complementarity for Slot Lines and Antennas," Cruft Lab., Harvard Univ., Cambridge, Mass., Tech. Rept. No. 288; May 15, 1959.

² R. W. P. King, "The Theory of Linear Antennas," Harvard University Press, Cambridge, Mass., ch. 1; 1956.

where r_{ik} is the distance between the point of observation (subscript i) and the point of integration (subscript k). It is to be noted that \mathbf{H}^* is equivalent to an electric field \mathbf{E}' and \mathbf{E}^* is equivalent to a magnetic field \mathbf{H}' . For a dipole with a half-length h carrying a sinusoidally distributed total current I_m or I_m^* , the components of the electromagnetic field in cylindrical coordinates are as follows:³

$$\frac{H_\theta}{I_m} = \frac{-H_\theta^*}{I_m^*} = \frac{j}{4\pi r} [e^{-j\beta_0 r_{k1h}} + e^{-j\beta_0 r_{k2h}} - 2 \cos \beta_0 h e^{-j\beta_0 r_{k0}}], \quad (4a)$$

$$H_r = H_z = H_r^* = H_z^* = E_\theta = E_\theta^* = 0, \quad (4b)$$

$$\frac{E_r}{I_m \zeta_0} = \frac{E_r^*}{I_m^* \zeta_0} = \frac{1}{4\pi r} \left[\frac{z-h}{r_{k1h}} e^{-j\beta_0 r_{k1h}} + \frac{z+h}{r_{k2h}} e^{-j\beta_0 r_{k2h}} - \frac{2z}{r_{k0}} \cos \beta_0 h e^{-j\beta_0 r_{k0}} \right], \quad (4c)$$

$$\frac{E_z}{I_m \zeta_0} = \frac{E_z^*}{I_m^* \zeta_0} = \frac{-1}{4\pi} \left[\frac{1}{r_{k1h}} e^{-j\beta_0 r_{k1h}} + \frac{1}{r_{k2h}} e^{-j\beta_0 r_{k2h}} - \frac{2}{r_{k0}} \cos \beta_0 h e^{-j\beta_0 r_{k0}} \right], \quad (4d)$$

where

$$r_{k1h}^2 = (z-h)^2 + r^2; \quad r_{k2h}^2 = (z+h)^2 + r^2; \\ r_{k0}^2 = z^2 + r^2; \quad r_{ik}^2 = z^2 + r_{k0}^2, \quad (4e)$$

where the subscript k indicates the point of integration.

II. THE DISTRIBUTION OF CURRENT

By requiring continuity of the total electric fields at the surface of each antenna, the following relations are obtained:

$$\frac{\partial^2}{\partial y_1^2} A_{1y} + \beta_0^2 A_{1y} = \frac{\beta_0^2}{j\omega} E_{13y}' \equiv E', \quad (5a)$$

$$\frac{\partial^2}{\partial y_2^2} A_{2y} + \beta_0^2 A_{2y} = \frac{\beta_0^2}{j\omega} E_{23y}', \quad (5b)$$

$$\frac{\partial^2}{\partial x_3^2} A_{3x}^* + \beta_0^2 A_{3x}^* = \frac{\beta_0^2}{j\omega} (E_{32x}^* + E_{31x}^*) \equiv E^*. \quad (5c)$$

It has been assumed that the current (electric or magnetic) in each antenna is axial. A_{1y} and A_{2y} are the y components of the total electric vector potential on the surface of antennas No. 1 and No. 2, respectively, due to the electric currents in the antennas. A_{3x}^* is the x component of the magnetic vector potential on the magnetic strip due to the magnetic current.

Since the expression for the vector potentials and electric fields have the currents under the signs of integration, (5a)–(5c) are, in effect, simultaneous integro-differential equations relating the currents in the three

antennas. By symmetry of the physical arrangement, (5a) and (5b) are identical. However, it is still unknown how to handle two simultaneous integro-differential equations rigorously. If the right-hand term in (5) is a known function, then it can be solved by the method of iteration.

The electric field (E' or E^*) on the surface of one antenna due to the other may be approximated by the field of a similar isolated antenna. The distributions of this field at various distances d have been computed for an antenna with $h=0.25\lambda$; the relative amplitudes are shown in Fig. 2 and the relative phases are shown in Fig. 3. It is seen that this field may be approximated by a shifted cosinusoidal distribution $\cos qs$ when the separation d equals or exceeds two-tenths of a wavelength. The values of q are in Table I. For $d=0.1\lambda$, the distribution is nearly exponential. Since \mathbf{E} and \mathbf{E}' behave approximately like the respective vector potentials, the same distribution function may be used for both.

Let the cases of two different distribution functions be considered in parallel. Thus, (5) becomes

$$\frac{\partial^2}{\partial y_1^2} A_{1y} + \beta_0^2 A_{1y} = \begin{cases} E' \cos qy_1 \\ E' e^{-j\beta_0 |y_1|} \end{cases}, \quad (6a)$$

$$\frac{\partial^2}{\partial x_3^2} A_{3x}^* + \beta_0^2 A_{3x}^* = \begin{cases} E^* \cos qx_3 \\ E^* e^{-j\beta_0 |x_3|} \end{cases}. \quad (6b)$$

For an antenna symmetrically driven by a potential difference at its center, odd currents do not exist. Therefore, for antennas with even distributions of current, the solution of (6) is found to be

Cosinusoidal Distribution

$$A_y = \frac{-j}{v_0} [(C_1 - C_0) \cos \beta_0 y_1 + \frac{1}{2} V_0 \sin \beta_0 y_1 + C_0 \cos qy_1], \quad y_1 \geq 0, \quad (7a)$$

$$A_x^* = \frac{-j}{v_0} [(C_1^* - C_0^*) \cos \beta_0 x_3 + \frac{1}{2} V_0^* \sin \beta_0 x_3 + C_0^* \cos qx_3], \quad x_3 \geq 0, \quad (7b)$$

Exponential Distribution

$$A_y = \frac{-j}{v_0} [(D_1 - D_0) \cos \beta_0 y_1 + (\frac{1}{2} V_0 + D_0) \sin \beta_0 y_1 + D_0 e^{-\beta_0 y_1}], \quad y_1 \geq 0, \quad (7c)$$

$$A_x^* = \frac{-j}{v_0} [(D_1^* - D_0^*) \cos \beta_0 x_3 + (\frac{1}{2} V_0^* + D_0^*) \sin \beta_0 x_3 + D_0^* e^{-\beta_0 x_3}], \quad x_3 \geq 0, \quad (7d)$$

where

$$C_0 = \frac{jv_0 E'}{\beta_0^2 - q^2}, \quad C_0^* = \frac{jv_0 E^*}{\beta_0^2 - q^2}, \quad (7e)$$

$$D_0 = \frac{jv_0}{2\beta_0^2} E', \quad D_0^* = \frac{jv_0}{2\beta_0^2} E^*, \quad (7f)$$

³ *Ibid.*, p. 524.

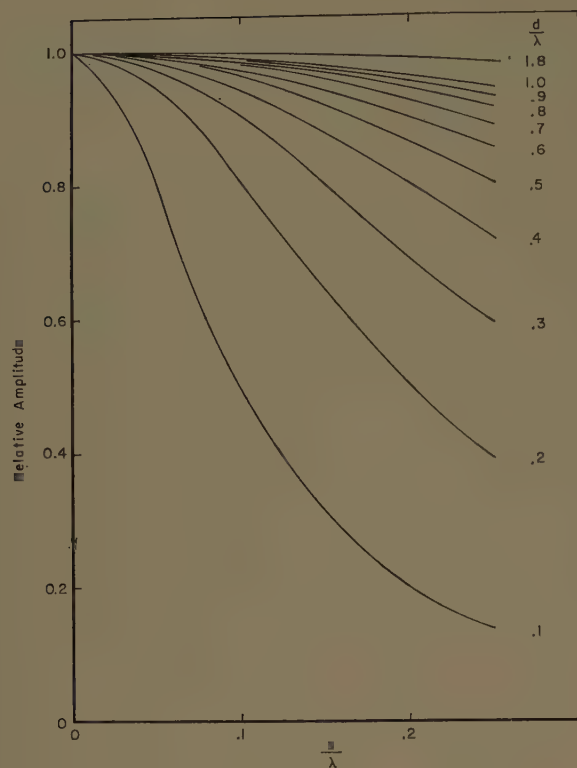


Fig. 2— E^* field along x axis due to an electric dipole—amplitude.

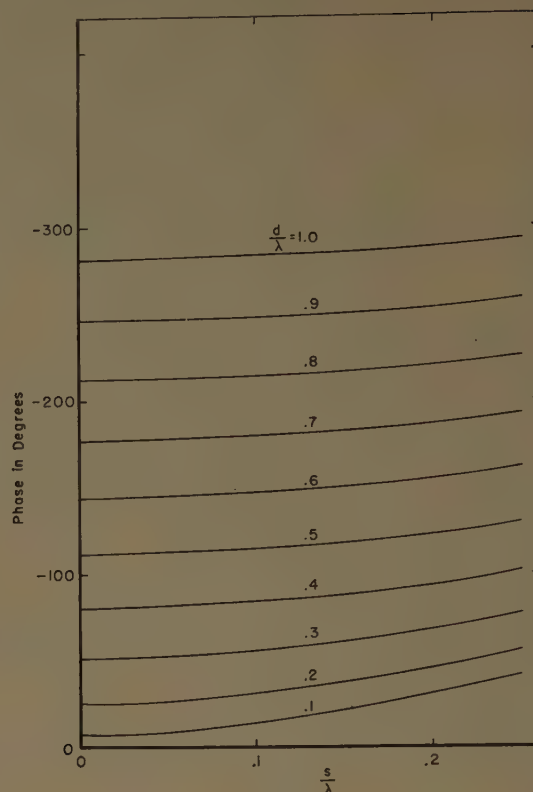


Fig. 3— E^* field along x axis due to an electric dipole—phase.

TABLE I

d/λ	q
0.2	5.24
0.3	4.03
0.4	3.22
0.5	2.66
0.6	2.26
0.7	1.96
0.8	1.72
0.9	1.54
1.0	1.39
1.8	0.78

and where V and V^* are the electric and magnetic potential differences at the driving point of the antennas; C_1 , C_1^* , D_1 and D_1^* are constants of integration.

With a technique similar to that described in the literature⁴ and with the following complex functions,

$$\psi_i(s) = \psi_i + \gamma_i(s), \quad (8a)$$

it follows that

$$I_i(s) = \frac{1}{\psi_i} \int_{-h}^h I_i(s') K_i(s, s') ds' - I_i(s) \gamma_i(s) - \int_{-h}^h [I_i(s') - I_i(s) g(s, s')] K_i(s, s') ds', \quad (8b)$$

where ψ_i is a constant and $\gamma_i(s)$ is a small correction term, when $g(s, s')$ is a properly selected approximate distribution function. Let the vector potentials as de-

fined in (3a) be inserted on the left in (7) and use be made of (8). Then let this expression be subtracted from (7) evaluated at the ends of antennas ($y_1 = h$, $x_3 = h$). By a process of iteration,⁴ the n th-order electric current on antenna No. 1 with a cosinusoidal distribution of E field is given by

$$[I_{1y}]_n = \frac{j^4 \pi}{\zeta_0 \psi} \sum_{m=0}^n \frac{F_m(h)}{\psi^m} \cdot \left\{ \left[\sum_{m=0}^n \frac{F_{y1m}}{\psi^m} \right] \sum_{m=0}^n \frac{1}{\psi^m} \left[\frac{1}{2} V_0 G_m(h) + C_0 H_m(h) \right] - \left[\sum_{m=0}^n \frac{F_m(h)}{\psi^m} \right] \sum_{m=0}^n \frac{1}{\psi^m} \left[\frac{1}{2} V_0 G_{y1m} + C_0 H_{y1m} \right] \right\}. \quad (9)$$

The magnetic current $[I_{3x}^*]_n$ on the magnetic strip antenna may be obtained from $[I_{1y}]_n$ by writing x for y and 3 for 1, adding an asterisk on ψ and V and putting

⁴ *Ibid.* p. 76.

ζ_0 in the numerator instead of in the denominator. The following relations are used in (9):

$$F_{si0} = F_0(s_i) - F_0(h), \quad F_0(s_i) = \cos \beta_0 s_i, \\ F_0(h) = \cos \beta_0 h, \quad (10a)$$

$$G_{si0} = G_0(s_i) - G_0(h), \quad G_0(s_i) = \sin \beta_0 s_i, \\ G_0(h) = \sin \beta_0 h, \quad (10b)$$

$$H_{si0} = H_0(s_i) - H_0(h), \quad H_0(s_i) = \cos q s_i, \\ H_0(h) = \cos q h, \quad (10c)$$

$$M_{sim} = M_m(s_i) - M_m(h), \quad (10d)$$

$$M_m(s_i) = -\gamma(s_i)M_{si(m-1)} - \int_{-h}^h [M_{si(m-1)}(s_i') \\ - M_{si(m-1)}(s_i)g(s_i, s_i')]K(s_i, s_i')ds_i', \quad (10e)$$

$$M_m(h) = -\int_{-h}^h M_{si(m-1)}(s_i')K(h, s_i')ds_i', \quad (10f)$$

where M stands for F , G or H . Since the distributions of the E' and E^* fields actually used are for antennas specifically a half-wavelength long, (9) is valid only when $h = 0.25\lambda$. Nevertheless, (9) is kept in the general form, because any distribution of E' and E^* fields can always be represented by Fourier series. The current in the antenna with an exponential distribution of the E field can be found in a similar manner. It can be shown that the zeroth-order current (electric and magnetic) distributions all have the following form:

$$[I_{js}]_0 = I_m \cos \beta_0 s_j. \quad (11)$$

III. THE ELECTROMAGNETIC FIELD

The field at any point $P(x, y, z)$ may be obtained by superposition of the separate fields due to the slot, the dipole and the image of the dipole.

The vector potentials A_1 and A_2 due to the electric current I_1 and I_2 in the wire dipole and its image, and the vector potential A_3^* due to the magnetic current I_3^* in the slot are

$$A_1 = \frac{\mu_0}{4\pi} \int_{-h}^h I_1 K_1 dy_1', \quad (12a)$$

$$A_2 = \frac{\mu_0}{4\pi} \int_{-h}^h I_2 K_2 dy_2', \quad (12b)$$

$$A_3^* = \frac{\epsilon_0}{4\pi} \int_{-h}^h I_3^* K_3 dx_3', \quad (12c)$$

$$K_i = \frac{e^{-j\beta_0 r_i}}{r_i},$$

$$r_i^2 = (x_i - x_i')^2 + (y_i - y_i')^2 + (z_i - z_i')^2, \quad (12d)$$

where r_i is the distance from the respective antennas to the point of observation. The length of each of the three antennas is $2h$.

A zeroth-order approximation of the electromagnetic field may be obtained by using the zeroth-order distributions of current as given by (11). The resulting vector potentials are:

$$A_i = |A_i| [C_{i1}(h, u) + C_{i2}(h, u)], \quad (13a)$$

$$C_{ik} = \int_0^h \cos \beta_0 s' K_{ik} ds'; \quad i = 1, 2, 3; \quad k = 1, 2, \quad (13b)$$

$$K_{ik} = \frac{e^{-j\beta_0 r_{ik}}}{r_{ik}}, \quad (13c)$$

where r_{i1} is the distance between the point of observation and the positive point of integration and r_{i2} is the corresponding distance to the negative point of integration (Fig. 1). The components of the electromagnetic field due to each element may be obtained from the appropriate vector potentials. The total field at any point is obtained by adding the respective components contributed from each element; thus,

$$E_x = \frac{j\zeta_0 x}{4\pi} \left[\frac{I_{1m}\tilde{k}_1}{x^2 + (z-d)^2} + \frac{I_{2m}\tilde{k}_2}{x^2 + (z+d)^2} \right] \quad (14a)$$

$$E_y = \frac{-j\zeta_0}{4\pi} [I_{1m}\tilde{l}_1 + I_{2m}\tilde{l}_2] + \frac{jI_{3m}^*}{4\pi} \frac{z}{y^2 + z^2} \tilde{h}_0, \quad (14b)$$

$$E_z = \frac{j\zeta_0}{4\pi} \left[\frac{z-d}{x^2 + (z-d)^2} I_{1m}\tilde{k}_1 + \frac{z+d}{x^2 + (z+d)^2} I_{2m}\tilde{k}_2 \right] \\ - \frac{jI_{3m}^*}{4\pi} \frac{y}{y^2 + z^2} \tilde{h}_0, \quad (14c)$$

$$H_x = \frac{j}{4\pi} \left[\frac{z-d}{x^2 + (z-d)^2} I_{1m}\tilde{h}_1 + \frac{z+d}{x^2 + (z+d)^2} I_{2m}\tilde{h}_2 \right] \\ - \frac{jI_{3m}^*}{4\pi\zeta_0} \tilde{l}_0, \quad (14d)$$

$$H_y = \frac{jI_{3m}^*}{4\pi\zeta_0} \frac{y}{y^2 + z^2} \tilde{m}, \quad (14e)$$

$$H_z = \frac{-jx}{4\pi} \left[\frac{I_{1m}\tilde{h}_1}{x^2 + (z-d)^2} + \frac{I_{2m}\tilde{h}_2}{x^2 + (z+d)^2} \right] \\ + \frac{jI_{3m}^*}{4\pi\zeta_0} \frac{z}{y^2 + z^2} \tilde{m}, \quad (14f)$$

where

$$\tilde{h}_i = e^{-j\beta_0 r_{i1h}} + e^{-j\beta_0 r_{i2h}}; \quad i = 1, 2, 3, \quad (14g)$$

$$\tilde{k}_i = (y-h)K_{i1h} + (y+h)K_{i2h}; \quad i = 1, 2, 3, \quad (14h)$$

$$\tilde{l}_i = K_{i1h} + K_{i2h}; \quad i = 1, 2, 3, \quad (14i)$$

$$\tilde{m} = (x-h)K_{31h} + (x+h)K_{32h}. \quad (14j)$$

Thus, expressions for the components of the approximate field due to a slot antenna with parasitic metallic dipoles in terms of the currents on these elements have been found.

IV. THE MUTUAL COUPLING BETWEEN THE SLOT AND THE METALLIC DIPOLES

The relation between the magnetic current in the slot and the electric current in the parasitic elements may be found approximately from the following circuit equations:

$$I_{1m}Z_{11} + I_{2m}Z_{12} + I_{3m}^*M_{13}^* = V_1, \quad (15a)$$

$$I_{1m}Z_{21} + I_{2m}Z_{22} + I_{3m}^*M_{23}^* = V_2 = -V_1, \quad (15b)$$

$$I_{1m}M_{31} + I_{2m}M_{32} + I_{3m}^*Z_{33}^* = V_3^*, \quad (15c)$$

where

I_{im} is the electric current in amperes,

I_{3m}^* is the magnetic current in volts,

V_i is the driving electric potential difference at the center of the cylindrical antenna in volts,

V^* is the driving magnetic potential difference at the center of the slot antenna in amperes,

Z_{ii} and Z_{ik} are the self- and mutual impedance at the driving point of the cylindrical antenna in ohms,

Z_s^* is the magnetic self-impedance at the driving point of the slot antenna in mhos,

M_{ik}^* is the dimensionless coupling coefficient relating the magnetic current to the voltage across the driving point of the electric dipole,

M_{ik} is the dimensionless coupling coefficient relating the electric current to the magnetic voltage across the driving point of the magnetic dipole.

The mutual terms in (15) may be replaced by the negative E field (E' or E^*) due to the respective elements and integrated over the entire length of the antenna concerned. By so doing, the mutual impedances and the coupling coefficients may be expressed as follows:

$$Z_{12} = \left[\frac{j\zeta_0}{4\pi} \int_{-h}^h \bar{l}_2 dy \right]_{x=0}^{x=d} = Z_{21}, \quad (16a)$$

$$M_{13}^* = \left[\frac{j}{4\pi} \int_{-h}^h \frac{z}{y^2 + z^2} \bar{h}_3 dy \right]_{z=0}^{z=d} \\ = -M_{23}^* = M_{32} = -M_{31}. \quad (16b)$$

The values of the coupling coefficient for various separations d are tabulated in Table II. Using (16) and $Z_{11}' = Z_{22}$, and for the case of parasitic dipoles, $V_1 = 0$, it can be shown that

$$\frac{I_{1m}}{I_{3m}^*} = \frac{-M_{13}^*}{Z_{11} - Z_{12}}. \quad (17)$$

The substitution of (16) in (14) yields the following relation:

$$\tilde{Z}^* = \frac{V_0^*}{I_{3m}^*} = Z^* + \frac{2(M_{13}^*)^2}{Z_{11} - Z_{12}}, \quad (18)$$

where \tilde{Z}^* is the magnetic input impedance in mhos of the slot in the presence of the metallic dipoles.

TABLE II
COUPLING COEFFICIENT BETWEEN SLOT ANTENNA
AND WIRE DIPOLE

$$h_{\text{slot}} = h_{\text{dipole}} = 0.25 \lambda$$

$$-M_{13}^* = m_1^* + jm_2^* = |M_{13}^*| e^{i\psi_M}$$

d/λ	m_1^*	m_2^*	$ M_{13}^* $	ψ_M^0
0.05	-0.4307	0.0458	0.433	173.9
0.10	-0.3643	0.0884	0.375	166.4
0.15	-0.2988	0.1258	0.325	157.2
0.20	-0.2363	0.1567	0.284	146.5
0.25	-0.1737	0.1763	0.247	134.5
0.30	-0.1148	0.1869	0.219	121.6
0.35	-0.0542	0.1690	0.177	107.8
0.40	-0.0099	0.1764	0.176	90.0
0.45	0.3299	0.1571	0.160	78.2
0.50	0.0675	0.1304	0.147	62.64
0.55	0.0758	0.0806	0.111	46.75
0.60	0.1078	0.0637	0.125	30.6
0.65	0.07818	0.0198	0.0806	14.2
0.70	0.1088	-0.0045	0.1088	0
0.75	0.0966	-0.0335	0.1022	-19.12
0.80	0.0694	-0.0566	0.0895	-39.2
0.85	0.0546	-0.0726	0.0908	-53.05
0.90	0.0299	-0.0806	0.0872	-69.65
0.95	0.0038	-0.0817	0.0817	-90.0
1.00	0.0197	-0.0753	0.078	-75.4

V. THE RADIATION FIELD

One of the most important properties of an antenna or array of antennas is the radiation pattern. Subject to the condition $r^2 \gg h^2$, the general expression (14) may be reduced to a simpler form. The rectangular components of the field given in Section III are readily transformed into spherical components (Fig. 1). For practical purposes, the field patterns in two planes are of most interest: the horizontal pattern, which is the field distribution as a function of azimuth angle ϕ with $\theta = \pi/2$, and the vertical pattern, which is a function of the meridional angle θ while $\phi = 0$. With $\theta = \pi/2$ and $\beta_0 h = \pi/2$, the radiation field of the array has the following significant components:

$$H_\phi^r = \frac{-jI_{3m}^*}{\pi \zeta_0} \frac{e^{-j\beta_0 R}}{R} F(\phi), \quad (19a)$$

$$E_\theta^r = \frac{-jI_{3m}^*}{\pi} \frac{e^{-j\beta_0 R}}{R} F(\phi), \quad (19b)$$

$$F(\phi) = \frac{\cos\left(\frac{\pi}{2} \sin \phi\right)}{2 \cos \phi} \\ + j \frac{M_{13}^*}{Z_{11} - Z_{12}} \zeta_0 \sin(\beta_0 d \cos \phi). \quad (19c)$$

For $\phi=0$ and $\beta_0 h = \pi/2$ and $(d/R)^2 \ll \sin^2 \theta$, the radiation field has the following components:

$$H_{\phi}^r = \frac{-jI_{3m}^*}{\pi \zeta_0} \frac{e^{-j\beta_0 R}}{R} F(\theta), \quad (20a)$$

$$E_{\theta}^r = \frac{-jI_{3m}^*}{\pi} \frac{e^{-j\beta_0 R}}{R} F(\theta), \quad (20b)$$

$$F(\theta) = \frac{1}{2} + j \frac{M_1^*}{Z_{11} - Z_{12}} \zeta_0 \frac{\cos\left(\frac{\pi}{2} \cos \theta\right)}{\sin \theta} \cdot \sin(\beta_0 d \sin \theta). \quad (20c)$$

The values of M_1^* may be evaluated from (16b) by numerical integration. The values of self- and mutual impedance of parallel identical cylindrical antennas are tabulated by King.⁵ The squares of the radiation functions have been computed using the second-order impedances for the separation $d < 0.5 \lambda$ and the zeroth-order values for the greater separations. These theoretical radiated power patterns, that is, $|F(\phi)|^2$ and $|F(\theta)|^2$ are shown in Figs. 4 to 9.

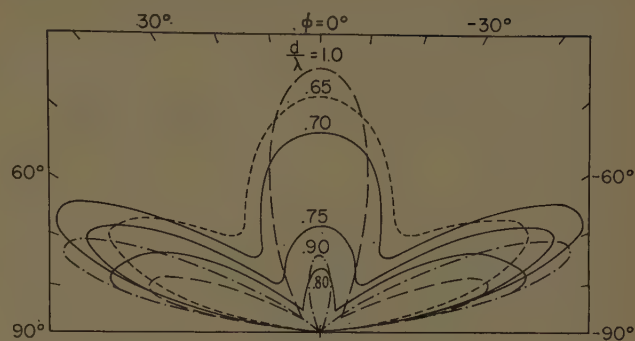


Fig. 6—Theoretical horizontal radiated power patterns with constant input current and infinite ground plane.

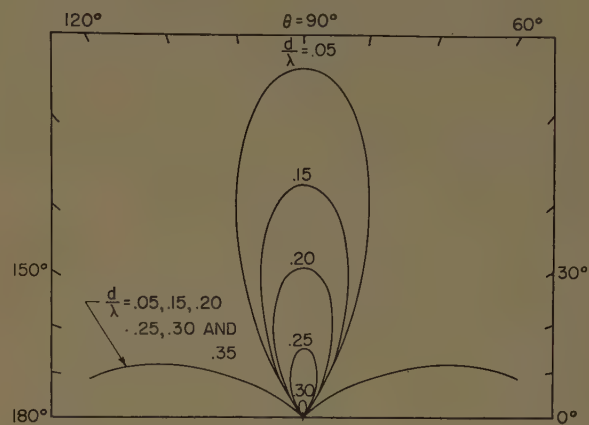


Fig. 7—Theoretical vertical radiated power patterns with constant input current and infinite ground plane.

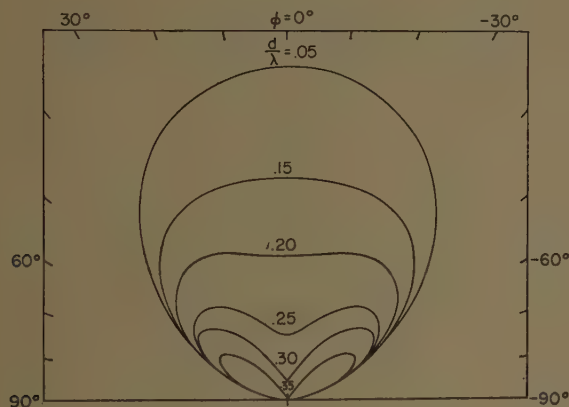


Fig. 4—Theoretical horizontal radiated power patterns with constant input current and infinite ground plane.

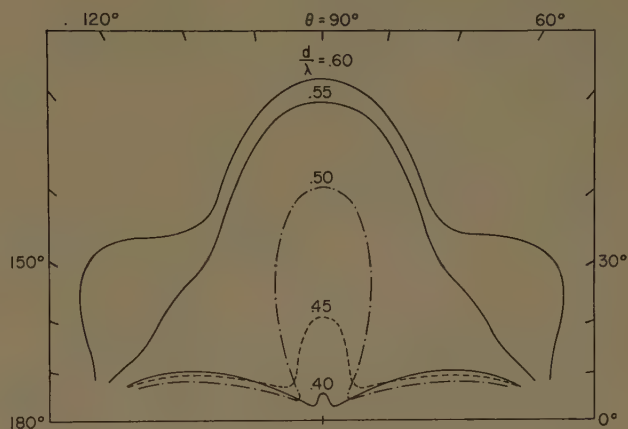


Fig. 8—Theoretical vertical radiated power patterns with constant input current and infinite ground plane.

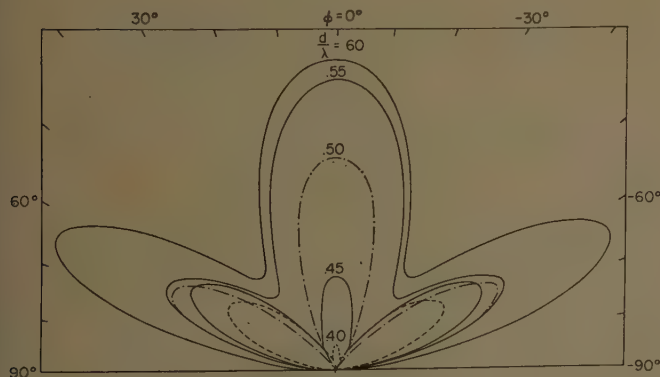


Fig. 5—Theoretical horizontal radiated power patterns with constant input current and infinite ground plane.

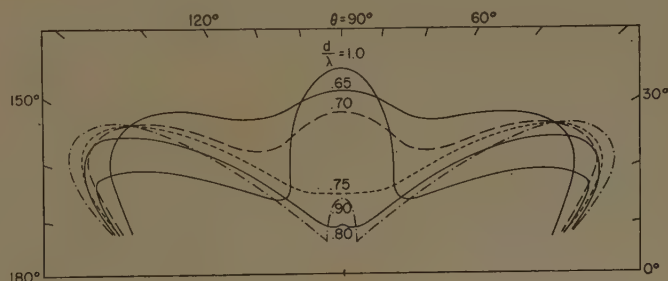


Fig. 9—Theoretical vertical radiated power patterns with constant input current and infinite ground plane.

⁵ *Ibid.*, p. 305.

VI. MEASUREMENTS

The radiation patterns have been measured with a pattern-measuring setup which operates at a frequency of 3000 mc. The antenna under test was used as a receiving antenna and was rotated to obtain its directional property. The received signal was detected by a crystal diode and then amplified and finally plotted on a polar recorder. The output of the transmitter was continuously registered on another recorder. The measurements were made using a slot with a single parasitic dipole in front of the slot instead of with a dipole symmetrically placed on each side, the case analyzed theoretically. Note that because of the presence of the slot, the image of the dipole in the conducting plane is not perfect.

The metallic screen, in which the slot antenna was located, was made of $\frac{1}{32}$ -inch thick aluminum sheet and measures approximately 1 meter in diameter. A square hole (12 inches \times 12 inches) was provided at the center of the aluminum screen to accept the plate in which the slot antenna was cut. In this arrangement, different slot antennas could easily be mounted on the circular screen. The slot antenna was cut in a small metallic sheet which was made to fit into the hole provided at the center of the circular ground plane. The width of the slot was 0.034 inch.

Two types of driving or loading devices were used in this measurement. 1) The microstrip drive consists of a thin conductor along the metal surface, but separated from it by a thin sheet of dielectric and connected to the center of the slot. The dielectric used was 0.005-inch acetate sheet. This was glued on the metal sheet. The inner conductor of a Microdot coaxial cable was glued on the acetate sheet to serve as the second conductor. The other end of the microstrip was connected to the inner conductor of a type *N* coaxial connector through a transition section. The outer conductor of the coaxial cable was connected to the ground plane. 2) The slot-line drive consists of two parallel slots. The slot antenna driven by a two-slot line is the complement of a strip antenna driven by a two-strip line.

The parasitic element was made of brass wire with a diameter of 0.034 inch and was supported in front of the slot by a piece of polyfoam block.

Both the vertical and horizontal patterns have been measured with various separations between the slot and its parasite. The measurement shows that the method of driving the slot antenna has little effect on the radiation pattern and the effectiveness of the two different drives are about the same.

The measured radiation patterns (power) for two separations d between the slot antenna and the coupled parasitic dipole are shown in Figs. 10 and 11. The general shapes of the corresponding theoretical and measured patterns agree well with one another except that the measured patterns have more minor minima and are less symmetrical than those predicted by the theory.

It has been assumed in the theoretical analysis that the ground screen is infinitely large so that there are no edge effects. In the experimental setup, the size of the ground plane is very small compared with the distance between the transmitter and the receiver, so that reflections from the edges produce standing waves on the ground plane that may contribute minor lobes to the radiation pattern. The reflections from the edges are more pronounced when the field has a large component along the surface of the ground plane. This effect is well indicated in the radiation patterns of a single slot antenna (Fig. 12). The radiation patterns may also be asymmetrical because of reflections from supporting structures and other objects behind the ground plane which are not exactly symmetrically located.

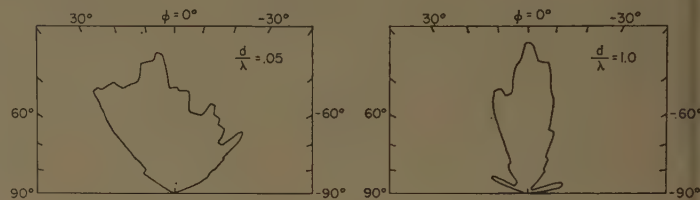


Fig. 10—Measured horizontal radiated power patterns with finite ground plane.

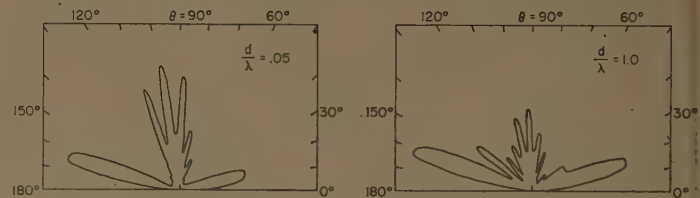


Fig. 11—Measured vertical radiated power patterns with finite ground plane.

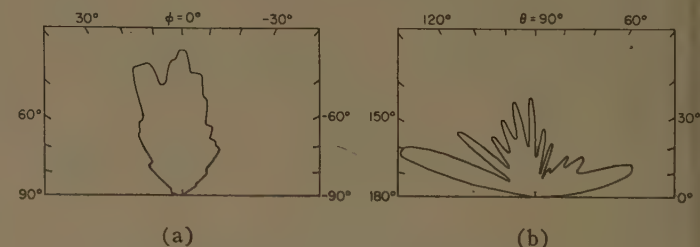


Fig. 12—Radiated power patterns of single slot antenna with finite ground plane. (a) Horizontal. (b) Vertical.

The distribution of the current along the coupled parasitic element whose half-length $h_2 = 0.25 \lambda = 10$ cm at a distance 1 cm above the ground plane was measured on the model designed for 40-cm wavelength. The parasitic dipole was made of a $\frac{1}{4}$ -inch-in-diameter brass rod supported above the slot antenna by a polyfoam block. The distribution of current was measured by moving a loop-probe along the surface of the coupled dipole. The measured distribution curve (Fig. 13) is found to be approximately sinusoidal as predicted by the theory.

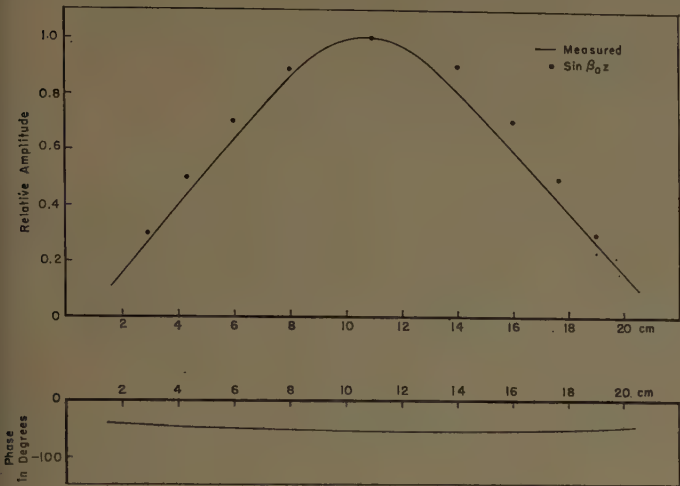


Fig. 13—Distribution of H field along parasitic dipole—
 $h_1=h_2=0.25 \lambda=10$ cm, $d=1$ cm.

Since the measured patterns were made with a parasitic dipole on one side of the slot only, it is desirable to investigate the effect caused by the absence of the parasitic dipole on the other side of the slot. This was accomplished by measuring the current at an arbitrary point in one dipole in the presence and in the absence of the other dipole. It was found that this current has a larger amplitude in the absence of the other dipole when the separation d between the dipole and the slot is small.

The measured results are as follows:

d/λ	0.025	0.05	0.10	0.15
I (without 2nd Dipole)				
I (with 2nd Dipole)	1.64	1.30	1.03	1.0

They may serve as an explanation for some of the differences between the theoretical and measured radiation patterns at small separation. They also indicate that when the separation d between the slot antenna and the coupled dipole is large, the coupling between the two parasitic antennas on opposite sides of the ground plane is negligible.

For qualitative purposes, it is convenient to visualize a slot antenna as equivalent to two short dipoles symmetrically located at each end of the slot and driven in phase with the ground screen removed. They are oriented parallel to the narrow edges of the slot. Thus the system of a slot and two parasitic dipoles is approximately equivalent to an array of four dipoles of which two are driven and separated by the length of the slot and two are the parasitic elements. These four dipoles are symmetrically placed on two perpendicular axes and their field patterns may be obtained from the theory of linear antennas. It is obvious in this arrangement that the presence of the second parasitic element tends to reduce the current in the first parasitic element when they are close together.

Radiation Patterns of Finite-Size Corner-Reflector Antennas*

A. C. WILSON† AND H. V. COTTONY†

Summary—Radiation patterns were measured for corner-reflector antennas having various combinations of widths and lengths of the reflecting surfaces. The widths of these ranged from 1 to 10 wavelengths, the lengths from 0.5 to 5 wavelengths. The aperture angle was, in general, set at a value required to maximize the gain. Radiation patterns are arranged according to the size of the reflecting surfaces. The effect of the widths and lengths of the surfaces on the widths of the main lobe and on the level of the radiation to the rear is summarized in a series of curves. A corner-reflector antenna with a collinear array of dipoles was designed, constructed, and tested to have sidelobe radiation below -40 -db level.

INTRODUCTION

CORNER-reflector antennas have certain characteristics which make them attractive for some applications. However, one of the drawbacks of the corner-reflector antenna has been a scarcity of quantitative experimental data on the effects of the various parameters such as lengths and widths of the reflecting surfaces and the magnitude of the angle of aperture on the performance of the corner-reflector antenna. Theoretical computations of the gain and the radiation pattern of this antenna almost always assume reflecting surfaces infinite in extent and aperture angles equal to 180° divided by an integer, e.g., 45° , 60° , or 90° . Wait¹ showed a method of obtaining pattern function G for an arbitrary aperture angle. However, the method still assumed reflecting surfaces infinite in extent. Therefore, while the radiation pattern in the forward direction might be predicted with reasonable accuracy, the method does not give any indication regarding the intensity of radiation diffracted to the rear of the corner structure. The performance of corner-reflector antennas became of interest to the National Bureau of Standards because they appeared to be well suited to communication via ionospheric scatter. From time to time, beginning in 1952, tests have been made on various aspects of performance of these antennas. A brief note of this work was made in a paper by Cottony.² A more detailed report on the gains of finite-size corner-reflector antennas was made in a more recent paper by the authors.³

Recent operating experience with the high-power, long-range, VHF ionospheric scatter circuits indicates a requirement for antennas which have very low secondary-lobe levels. Material on radiation patterns of corner-reflector antennas is included in a paper by Harris,⁴ but it does not cover the range of corner-reflector sizes of interest to this application. Therefore, in the fall of 1957, in connection with the design of an antenna for a specific application, the radiation patterns of a number of corner-reflector antennas were measured. The widths and lengths of the reflecting surfaces were made to cover the range reported by the authors.³ The aperture angles and the driven element positions were, in general, adjusted to values found in that paper to give the maximum gain. The material in this paper should be considered to be complementary to that previously given by the authors.³

The terminology employed here conforms to the American usage. Fig. 1(a) illustrates this terminology. The width of the reflecting surface, W , is the dimension parallel to the apex line. The aperture angle, θ , is that formed by the two reflecting surfaces. The dipole position, S , is the distance of the driven element from the apex.

MEASUREMENT TECHNIQUES

All of the measurements described here were carried out in the fall of 1957 at the NBS Table Mesa Field Station, near Boulder, Colo. The site for antenna range was selected on the basis of smoothness. All stones and other objects likely to cause interfering reflections were cleared away. The measurements were carried out at 2000 mc. The antenna being tested was used as a receiving antenna. The target transmitter antenna, also a corner reflector, was located approximately 200 feet (400 wavelengths) away. The radiation pattern was measured by rotating the antenna being tested around a vertical axis in the principal E - and H -planes. Suitable precautions against antenna tilt and other sources of error, as described in NBS Circular 598⁵ were observed. The reflecting surfaces were continuous sheets of aluminum or brass. The driven element was a half-wave dipole. The equipment included a commercially available automatic pattern recorder. The normal recording range of this equipment is 40 db. This was extended to 60 db by the use of a 20-db precision attenuator which was inserted ahead of the receiver for measurements in the forward direction. This attenuator was removed

* Manuscript received by the PGAP, August 14, 1959; revised manuscript received, October 12, 1959. The work reported herein was carried out on behalf of the U. S. Air Force under support extended by Detachment 1, Ground Electronics Engrg. and Installation Agency, STRATOCOM, AMC, Andrews Air Force Base, Washington, D. C.

† National Bureau of Standards, Boulder, Colo.

¹ J. R. Wait, "On the theory of an antenna with an infinite corner reflector," *Can. J. Phys.*, vol. 32, pp. 365-371; May, 1954.

² H. V. Cottony, "High-gain antennas for VHF scatter propagation," *IRE TRANS. ON COMMUNICATIONS SYSTEMS*, vol. CS-4, pp. 56-63; March, 1956.

³ H. V. Cottony and A. C. Wilson, "Gains of finite-size corner-reflector antennas," *IRE TRANS. ON ANTENNAS AND PROPAGATION*, vol. AP-6, pp. 366-369; October, 1958.

⁴ E. F. Harris, "An experimental investigation of the corner-reflector antenna," *Proc. IRE*, vol. 41, pp. 645-651; May, 1953.

⁵ H. V. Cottony, "Techniques for Accurate Measurement of Antenna Gain," NBS Circular, 598; December, 1958.

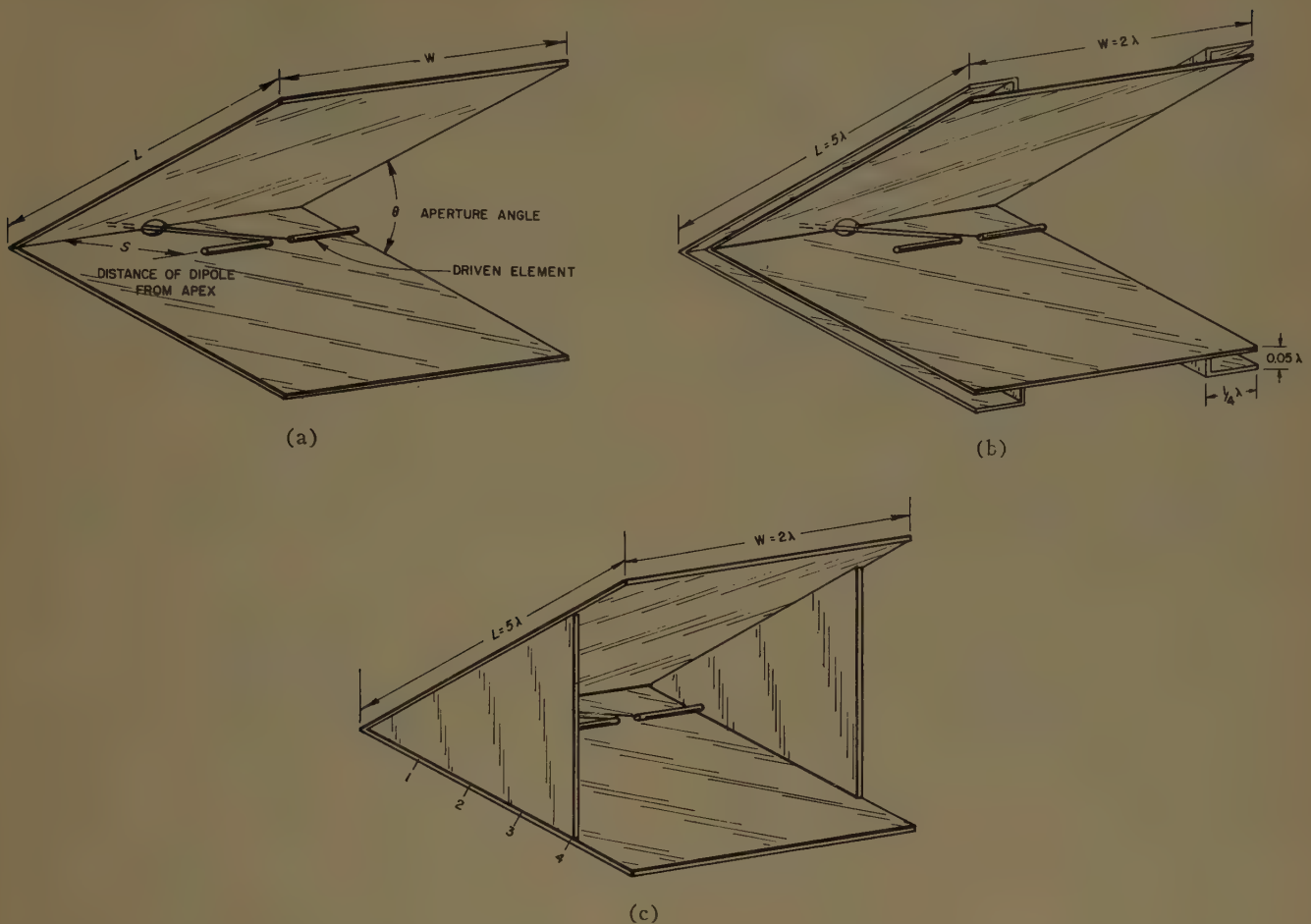


Fig. 1—Diagrams of the corner-reflector antenna showing the nomenclature and the symbols used in the text. (a) Corner-reflector antenna with no attachments. (b) Corner-reflector antenna with surface chokes. (c) Corner-reflector antenna with side plates measuring 4λ along the slant sides.

when the response went below the -20 -db level. The radiation patterns in this paper are tracings of the original records.

RESULTS

Results of this series of measurements are the radiation patterns presented in Figs. 2–47 and Figs. 51–54. For purposes of presentation, it has been found convenient to arrange them in a particular order. Figs. 2–7 are intended to show the effect of variation of one dimension, width or length, on the radiation pattern. The other dimension, length or width, is held constant at a maximum practical value. Figs. 8–47 may be termed a catalog of patterns, and present E - and H -plane patterns of antennas having various combinations of width and length of reflecting surfaces. These patterns are arranged first by the widths and then by the lengths of the reflecting surfaces. In these measurements, the angle of aperture and the position of the driven dipole were adjusted to values which were found to maximize the gain as reported previously.³ For reflector widths greater than 5 wavelengths, the aperture angle and the position of the dipole were made the same as for a width of 5 wavelengths.

Figs. 48 and 49 present the half-power beamwidths, in the E - and H -planes, respectively, for various combinations of reflector lengths and widths. Fig. 50 presents the average prevailing back radiation within the region of 120° – 180° – 120° for various combinations of reflector lengths and widths.

To study the effect of the variations in the angle of aperture on the radiation pattern, tests were carried out with a corner reflector having a width and length of 4 wavelengths. The prescribed angle of aperture for this combination of width and length is 45° . Radiation patterns were measured with the angle adjusted to 5 different values. The position of the dipole corresponded to that prescribed for first position for the angle used. Results of these tests are presented in Figs. 51 and 52.

Suggestions are sometimes advanced for suppression of radiation diffracted around the edges of the reflecting surfaces by the use of surface chokes, edging with radiation-absorbing material, dissipative coating of the edges, etc. In this investigation, tests were carried out on the use of surface chokes, with and without a filler of absorbing material. Fig. 1(b) illustrates the construction and the location of the surface chokes. No significant reduction in the back radiation was observed.

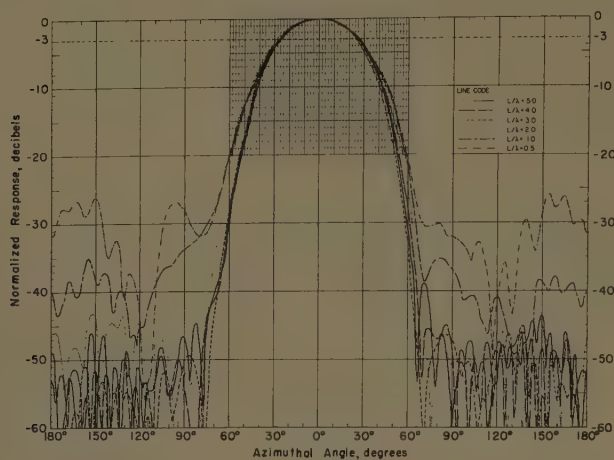


Fig. 2—The effect of lengths of reflecting surfaces on radiation pattern of corner-reflector antenna in *E*-plane. The width of corner-reflector antenna is 10 wavelengths in all cases. The aperture angle and the dipole position were adjusted to obtain maximum gain for the size of the reflecting surfaces used.

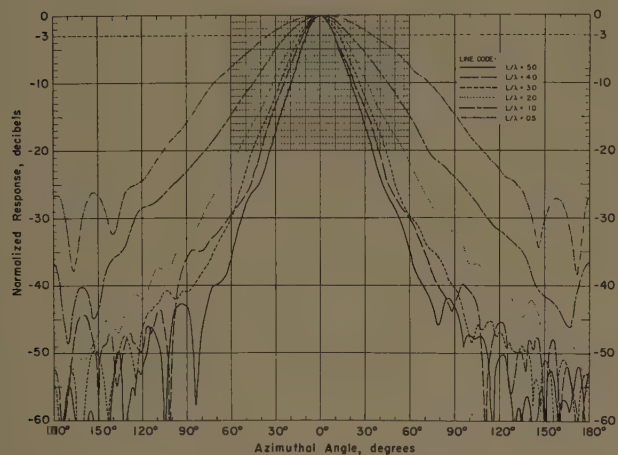


Fig. 3—The effect of lengths of reflecting surfaces on radiation pattern of corner-reflector antenna in *H*-plane. The width of corner-reflector antenna is 10 wavelengths in all cases. The aperture angle and the dipole position were adjusted to obtain maximum gain for the size of the reflecting surfaces used.

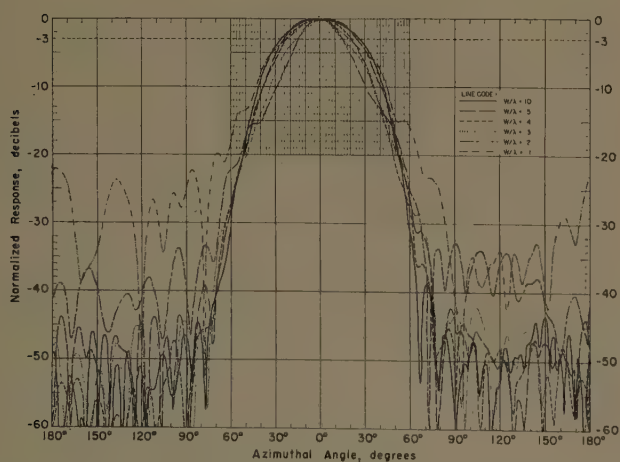


Fig. 4—The effect of widths of reflecting surfaces on radiation pattern of corner-reflector antenna in *E*-plane. The lengths of surfaces are 5 wavelengths in all cases. The aperture angle and dipole position were adjusted to obtain maximum gain for the size of the reflecting surfaces used.

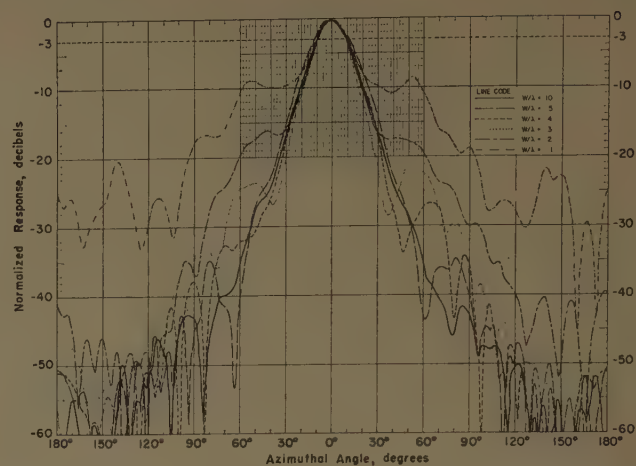


Fig. 5—The effect of widths of reflecting surfaces on radiation pattern of corner-reflector antenna in *H*-plane. The lengths of surfaces are 5 wavelengths in all cases. The aperture angle and dipole position were adjusted to obtain maximum gain for the size of the reflecting surfaces used.

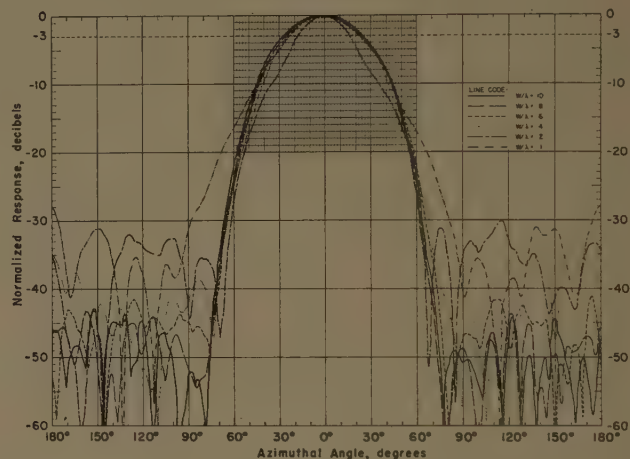


Fig. 6—The effect of widths of reflecting surfaces on radiation pattern of corner-reflector antenna in *E*-plane. The lengths of surfaces are 2 wavelengths in all cases. The aperture angle and dipole position were adjusted to obtain maximum gain for the size of the reflecting surfaces used.

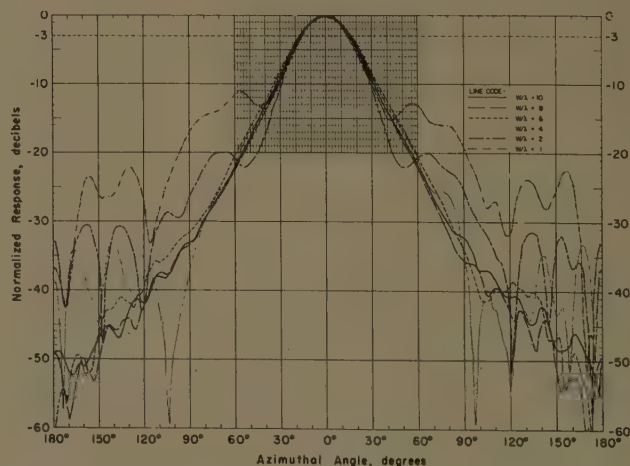


Fig. 7—The effect of widths of reflecting surfaces on radiation pattern of corner-reflector antenna in *H*-plane. The lengths of surfaces are 2 wavelengths in all cases. The aperture angle and dipole position were adjusted to obtain maximum gain for the size of the reflecting surfaces used.

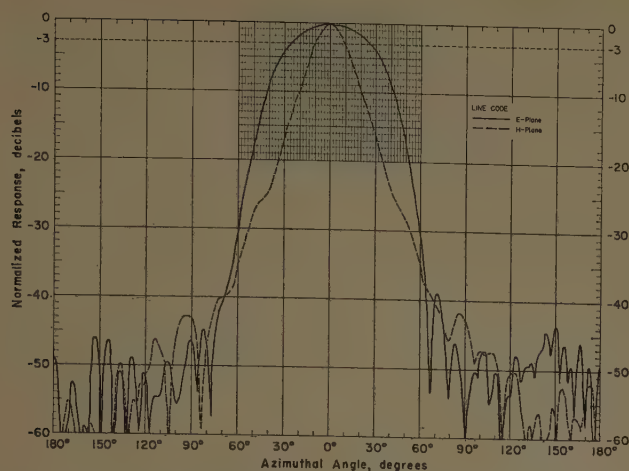


Fig. 8—Radiation patterns in the *E*- and *H*-planes for a corner-reflector antenna having a width of 10 wavelengths and a length of 5 wavelengths. Aperture angle = 45° ; dipole position, distance from apex 0.70λ .

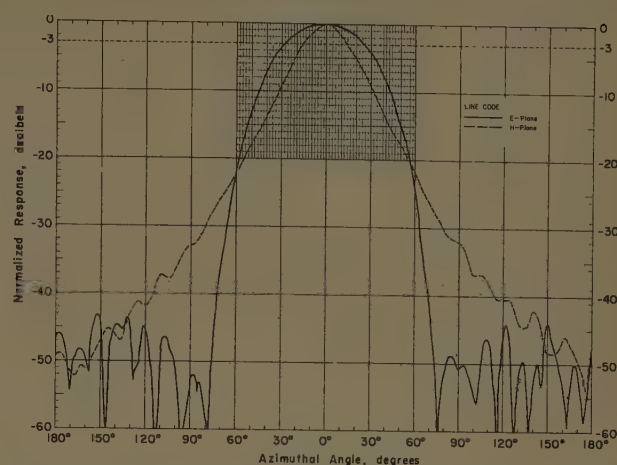


Fig. 11—Radiation patterns in the *E*- and *H*-planes for a corner-reflector antenna having a width of 10 wavelengths and a length of 2 wavelengths. Aperture angle = 71° ; dipole position, distance from apex 0.45λ .

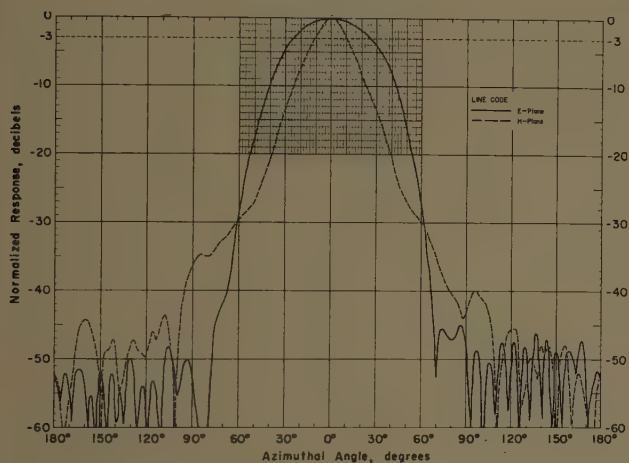


Fig. 9—Radiation patterns in the *E*- and *H*-planes for a corner-reflector antenna having a width of 10 wavelengths and a length of 4 wavelengths. Aperture angle = 50° ; dipole position, distance from apex 0.60λ .

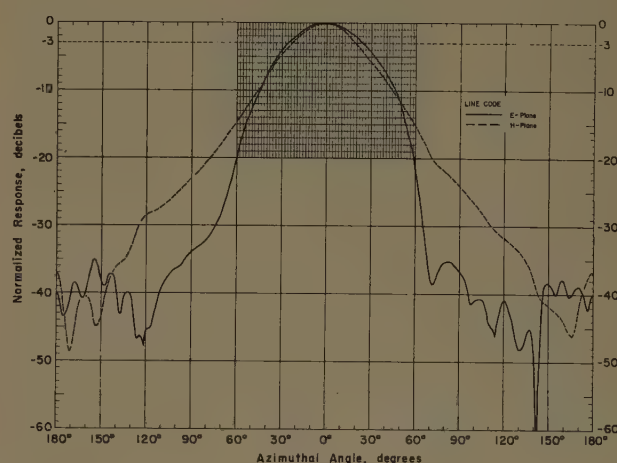


Fig. 12—Radiation patterns in the *E*- and *H*-planes for a corner-reflector antenna having a width of 10 wavelengths and a length of 1 wavelength. Aperture angle = 98° ; dipole position, distance from apex 0.30λ .

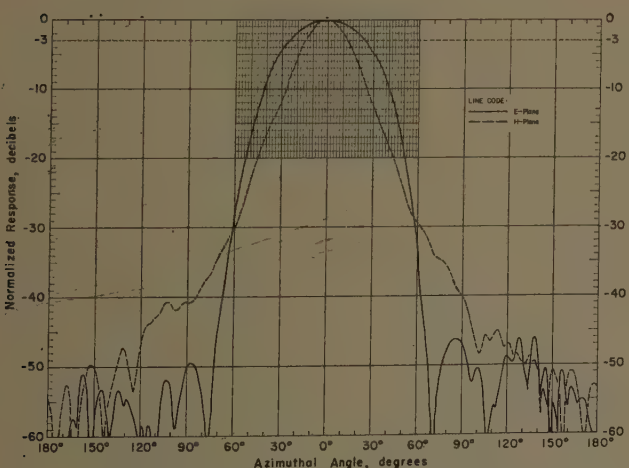


Fig. 10—Radiation patterns in the *E*- and *H*-planes for a corner-reflector antenna having a width of 10 wavelengths and a length of 3 wavelengths. Aperture angle = 57° ; dipole position, distance from apex 0.52λ .

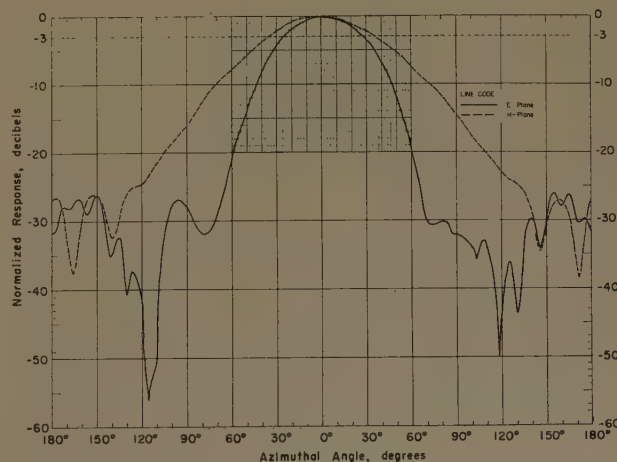


Fig. 13—Radiation patterns in the *E*- and *H*-planes for a corner-reflector antenna having a width of 10 wavelengths and a length of 0.5 wavelength. Aperture angle = 115° ; dipole position, distance from apex 0.25λ .

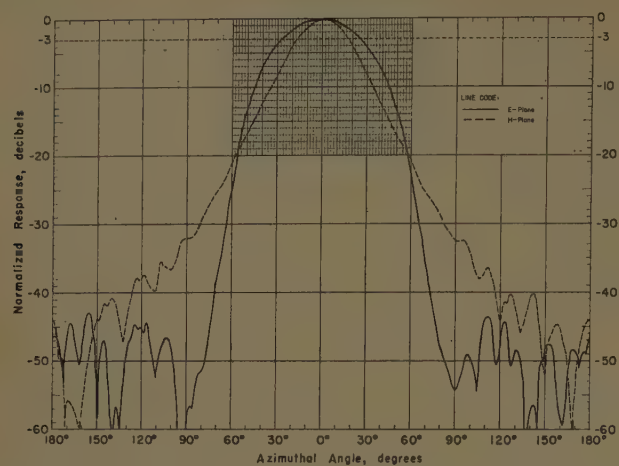


Fig. 14—Radiation patterns in the *E*- and *H*-planes for a corner-reflector antenna having a width of 9 wavelengths and a length of 2 wavelengths. Aperture angle = 71° ; dipole position, distance from apex 0.45λ .

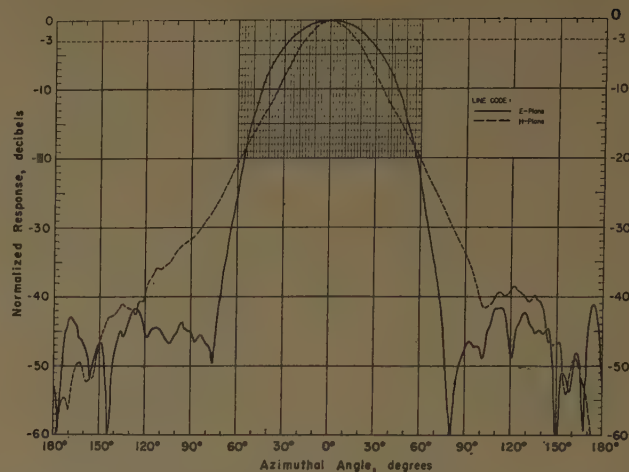


Fig. 17—Radiation patterns in the *E*- and *H*-planes for a corner-reflector antenna having a width of 6 wavelengths and a length of 2 wavelengths. Aperture angle = 71° ; dipole position, distance from apex 0.45λ .

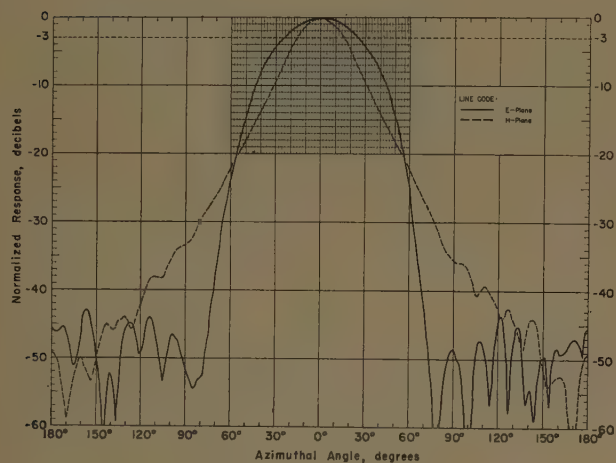


Fig. 15—Radiation patterns in the *E*- and *H*-planes for a corner-reflector antenna having a width of 8 wavelengths and a length of 2 wavelengths. Aperture angle = 71° ; dipole position, distance from apex 0.45λ .

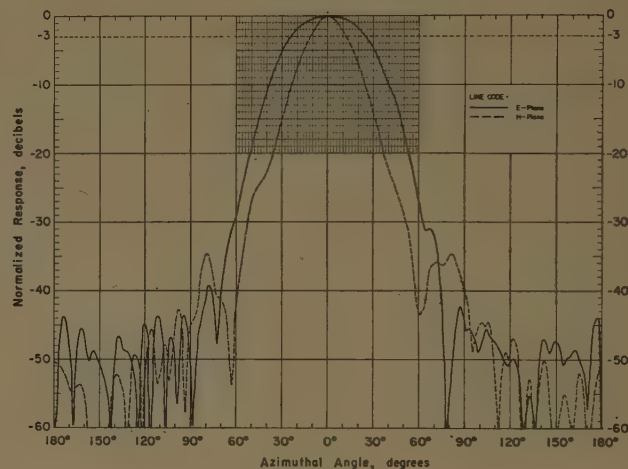


Fig. 18—Radiation patterns in the *E*- and *H*-planes for a corner-reflector antenna having a width of 5 wavelengths and a length of 5 wavelengths. Aperture angle = 45° ; dipole position, distance from apex 0.70λ .

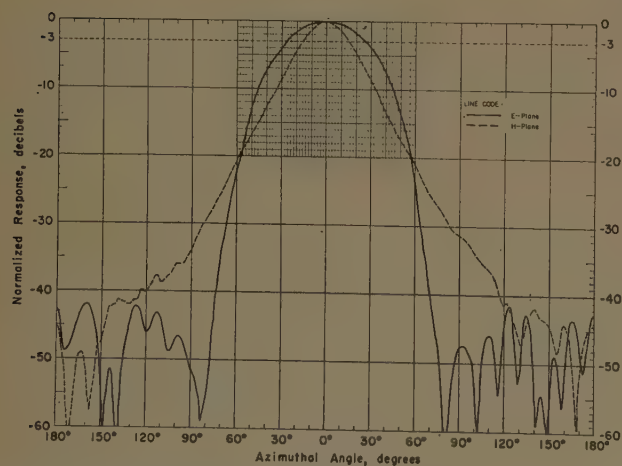


Fig. 16—Radiation patterns in the *E*- and *H*-planes for a corner-reflector antenna having a width of 7 wavelengths and a length of 2 wavelengths. Aperture angle = 71° ; dipole position, distance from apex 0.45λ .

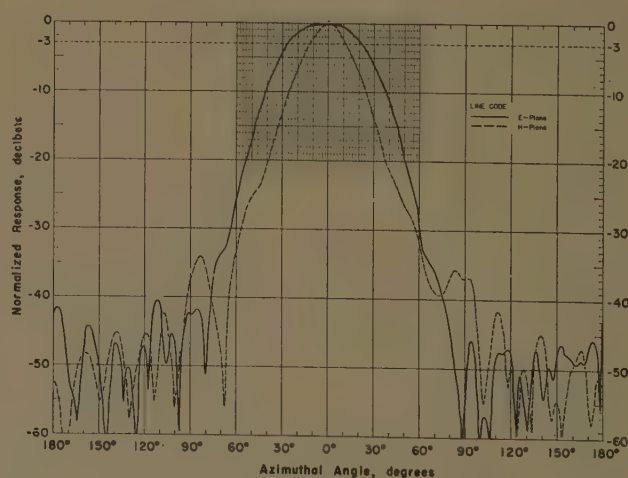


Fig. 19—Radiation patterns in the *E*- and *H*-planes for a corner-reflector antenna having a width of 5 wavelengths and a length of 4 wavelengths. Aperture angle = 50° ; dipole position, distance from apex 0.60λ .

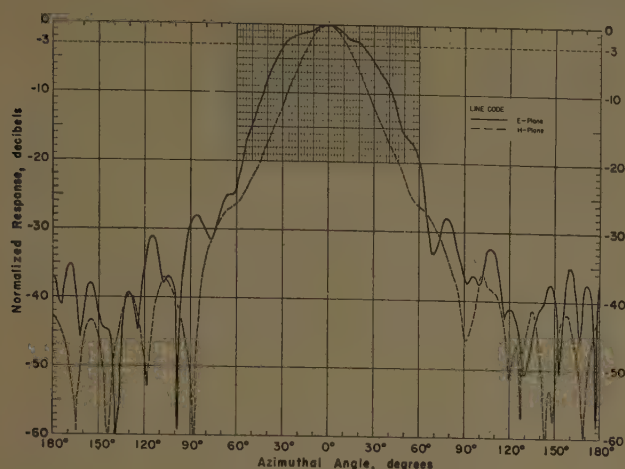


Fig. 20—Radiation patterns in the E - and H -planes for a corner-reflector antenna having a width of 5 wavelengths and a length of 3 wavelengths. Aperture angle = 57° ; dipole position, distance from apex 0.52λ .

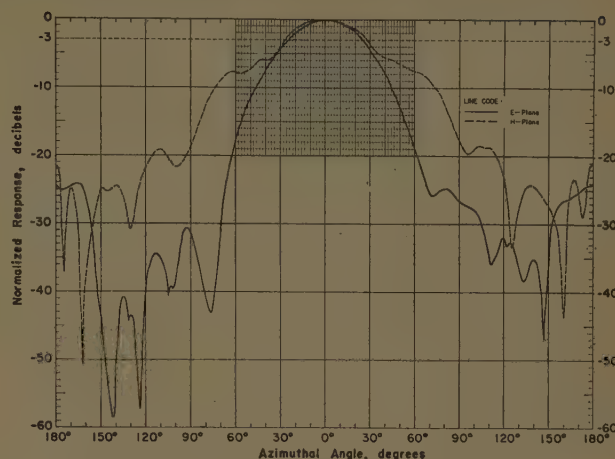


Fig. 23—Radiation patterns in the E - and H -planes for a corner-reflector antenna having a width of 5 wavelengths and a length of 0.5 wavelength. Aperture angle = 115° ; dipole position, distance from apex 0.25λ .

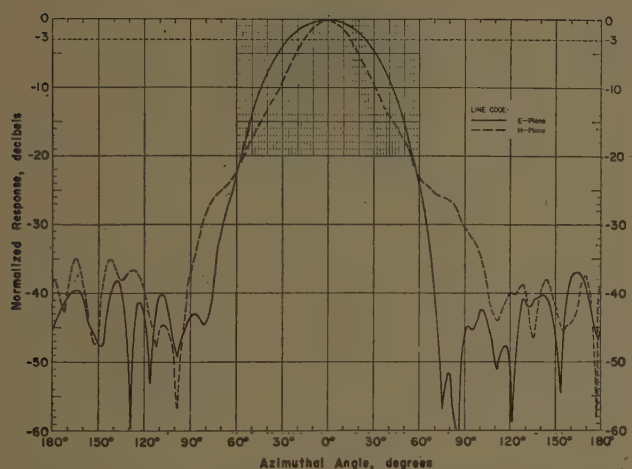


Fig. 21—Radiation patterns in the E - and H -planes for a corner-reflector antenna having a width of 5 wavelengths and a length of 2 wavelengths. Aperture angle = 71° ; dipole position, distance from apex 0.45λ .

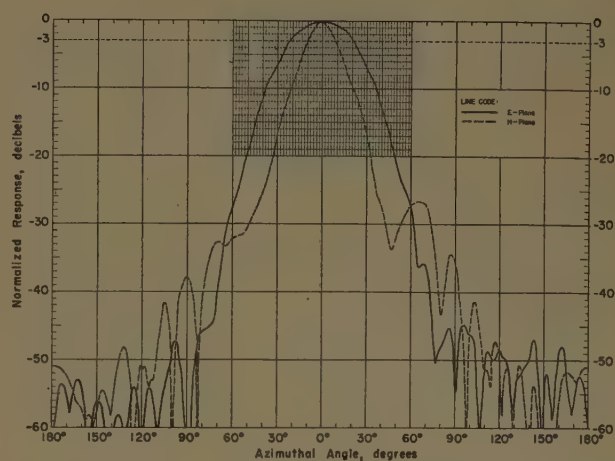


Fig. 24—Radiation patterns in the E - and H -planes for a corner-reflector antenna having a width of 5 wavelengths and a length of 5 wavelengths. Aperture angle = 45° ; dipole position, distance from apex 0.70λ .

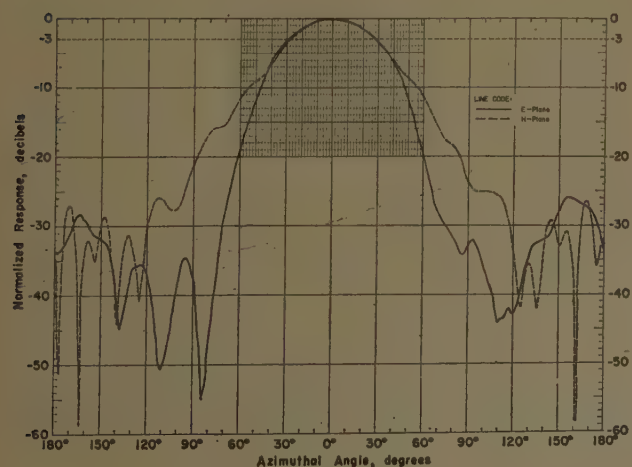


Fig. 22—Radiation patterns in the E - and H -planes for a corner-reflector antenna having a width of 5 wavelengths and a length of 1 wavelength. Aperture angle = 98° ; dipole position, distance from apex 0.30λ .

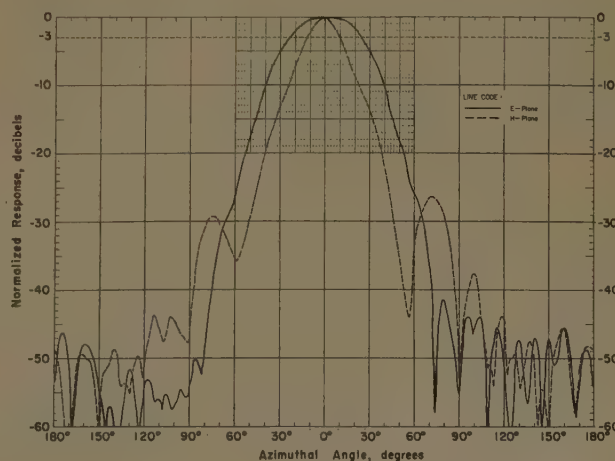


Fig. 25—Radiation patterns in the E - and H -planes for a corner-reflector antenna having a width of 4 wavelengths and a length of 4 wavelengths. Aperture angle = 45° ; dipole position, distance from apex 0.70λ .

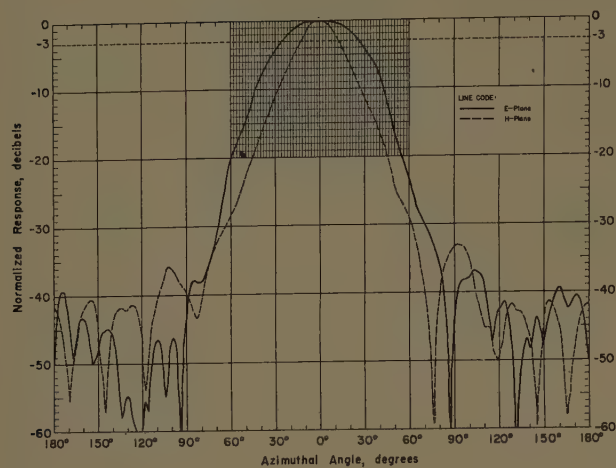


Fig. 26—Radiation patterns in the *E*- and *H*-planes for a corner-reflector antenna having a width of 4 wavelengths and a length of 3 wavelengths. Aperture angle = 54° ; dipole position, distance from apex 0.55λ .

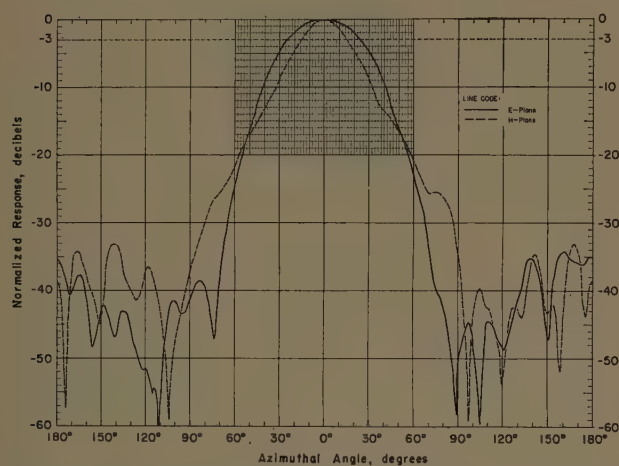


Fig. 27—Radiation patterns in the *E*- and *H*-planes for a corner-reflector antenna having a width of 4 wavelengths and a length of 2 wavelengths. Aperture angle = 66° ; dipole position, distance from apex 0.45λ .

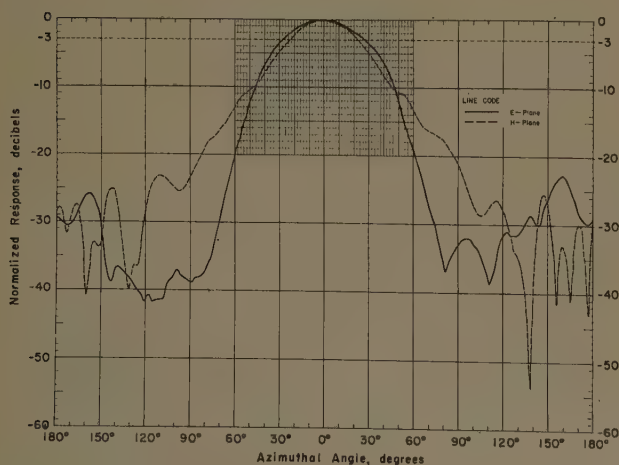


Fig. 28—Radiation patterns in the *E*- and *H*-planes for a corner-reflector antenna having a width of 4 wavelengths and a length of 1 wavelength. Aperture angle = 95° ; dipole position, distance from apex 0.30λ .

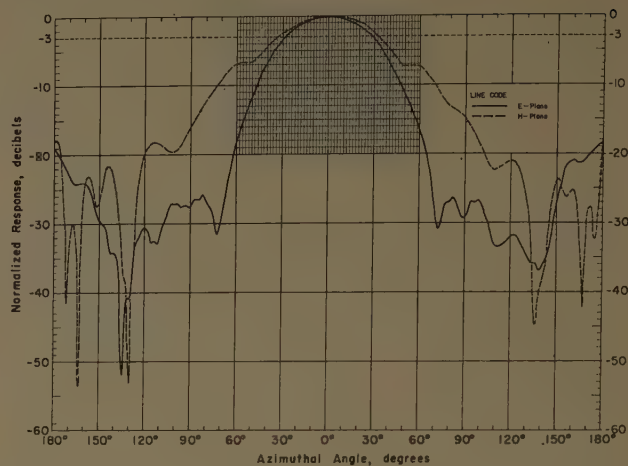


Fig. 29—Radiation patterns in the *E*- and *H*-planes for a corner-reflector antenna having a width of 4 wavelengths and a length of 0.5 wavelengths. Aperture angle = 125° ; dipole position, distance from apex 0.20λ .

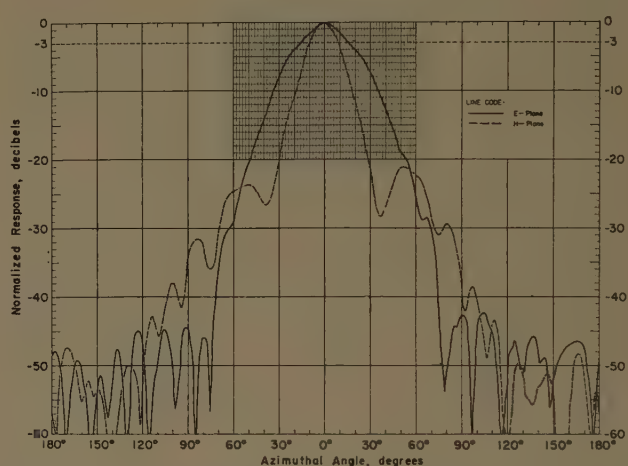


Fig. 30—Radiation patterns in the *E*- and *H*-planes for a corner-reflector antenna having a width of 3 wavelengths and a length of 5 wavelengths. Aperture angle = 45° ; dipole position, distance from apex 0.70λ .

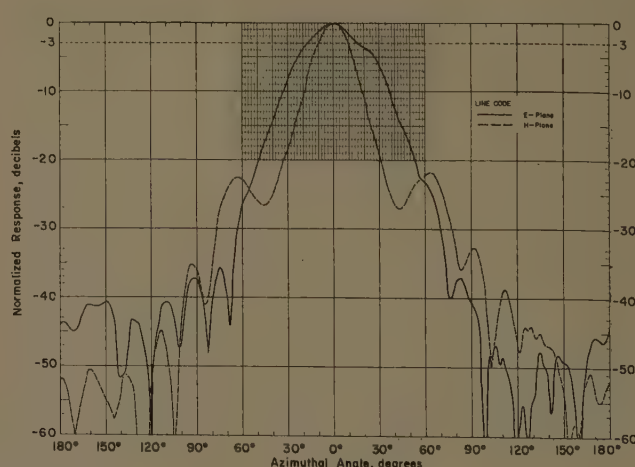


Fig. 31—Radiation patterns in the *E*- and *H*-planes for a corner-reflector antenna having a width of 2 wavelengths and a length of 4 wavelengths. Aperture angle = 45° ; dipole position, distance from apex 0.65λ .

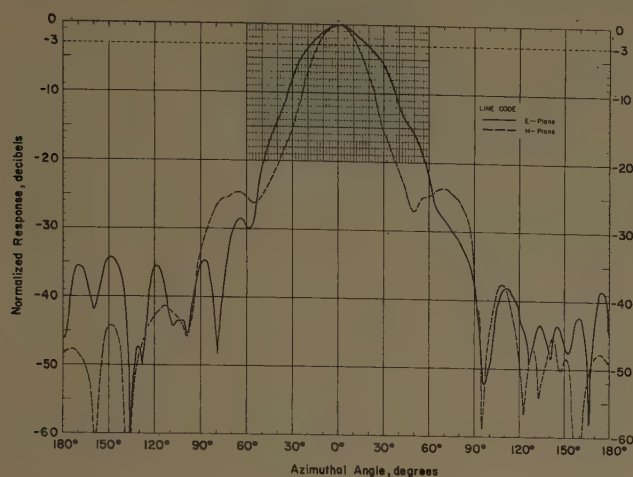


Fig. 32—Radiation patterns in the *E*- and *H*-planes for a corner-reflector antenna having a width of 3 wavelengths and a length of 3 wavelengths. Aperture angle = 48° ; dipole position, distance from apex 0.60λ .

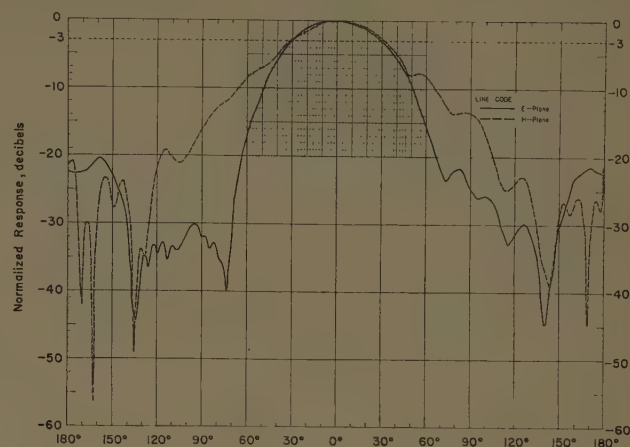


Fig. 35—Radiation patterns in the *E*- and *H*-planes for a corner-reflector antenna having a width of 3 wavelengths and a length of 0.5 wavelength. Aperture angle = 130° ; dipole position, distance from apex 0.20λ .

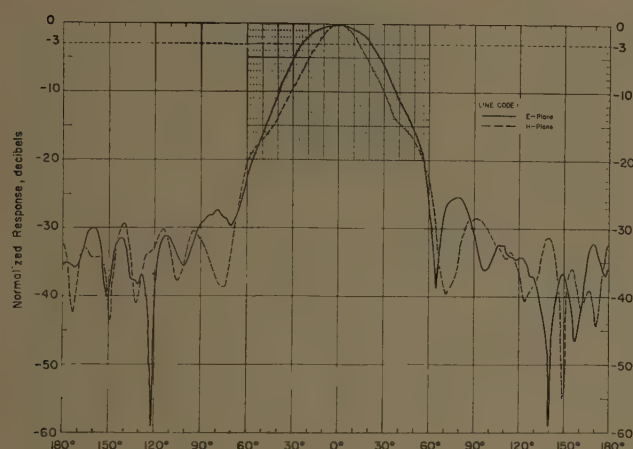


Fig. 33—Radiation patterns in the *E*- and *H*-planes for a corner-reflector antenna having a width of 3 wavelengths and a length of 2 wavelengths. Aperture angle = 61° ; dipole position, distance from apex 0.50λ .

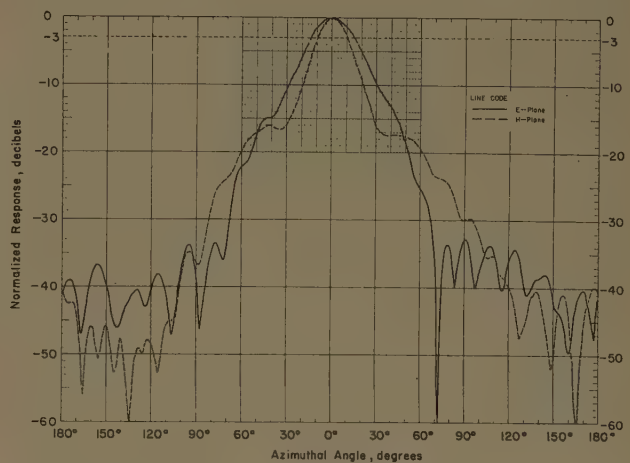


Fig. 36—Radiation patterns in the *E*- and *H*-planes for a corner-reflector antenna having a width of 2 wavelengths and a length of 5 wavelengths. Aperture angle = 50° ; dipole position, distance from apex 0.60λ .

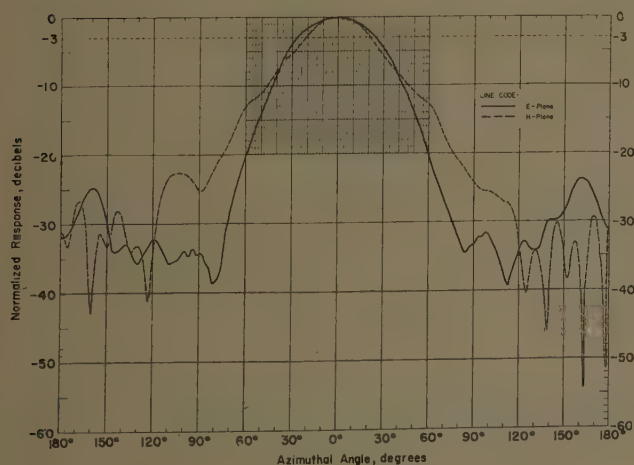


Fig. 34—Radiation patterns in the *E*- and *H*-planes for a corner-reflector antenna having a width of 3 wavelengths and a length of 1 wavelength. Aperture angle = 90° ; dipole position, distance from apex 0.30λ .

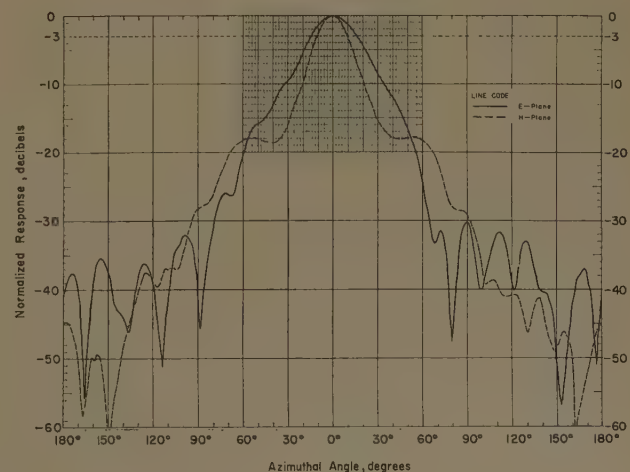


Fig. 37—Radiation patterns in the *E*- and *H*-planes for a corner-reflector antenna having a width of 2 wavelengths and a length of 4 wavelengths. Aperture angle = 52° ; dipole position, distance from apex 0.60λ .

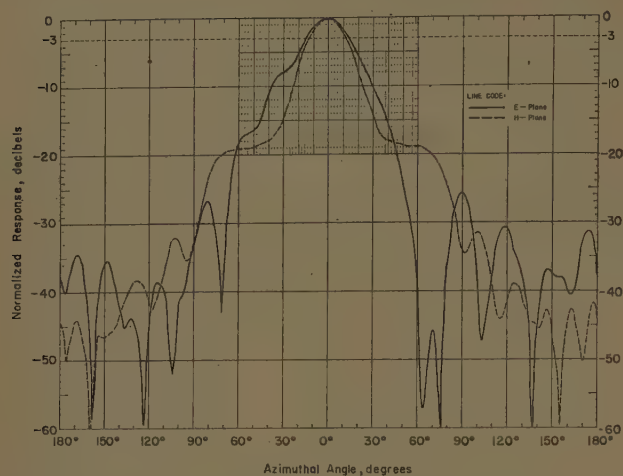


Fig. 38—Radiation patterns in the *E*- and *H*-planes for a corner-reflector antenna having a width of 2 wavelengths and a length of 3 wavelengths. Aperture angle = 55° ; dipole position, distance from apex 0.55λ .

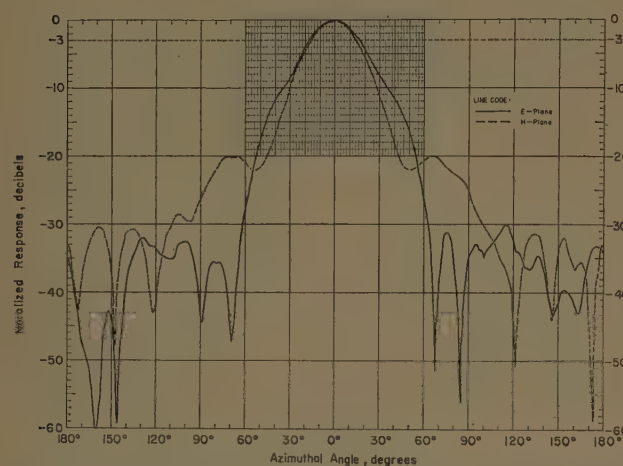


Fig. 39—Radiation patterns in the *E*- and *H*-planes for a corner-reflector antenna having a width of 2 wavelengths and a length of 2 wavelengths. Aperture angle = 60° ; dipole position, distance from apex 0.50λ .

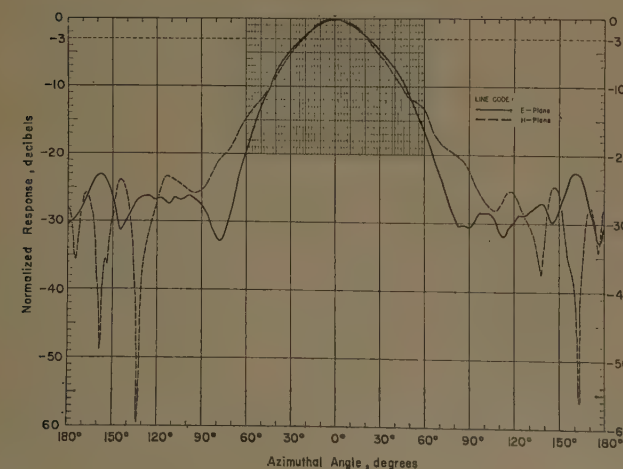


Fig. 40—Radiation patterns in the *E*- and *H*-planes for a corner-reflector antenna having a width of 2 wavelengths and a length of 1 wavelength. Aperture angle = 94° ; dipole position, distance from apex 0.30λ .

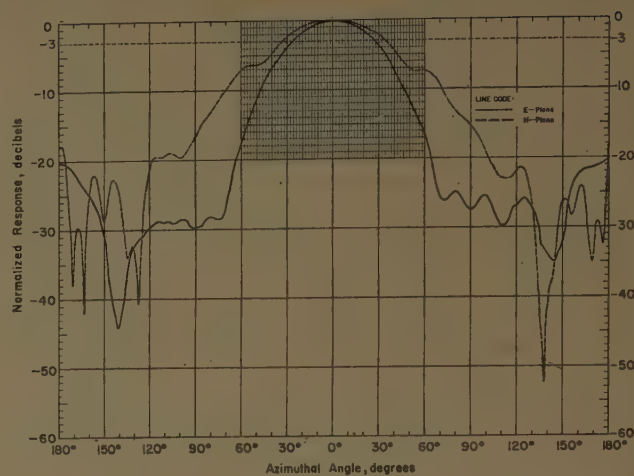


Fig. 41—Radiation patterns in the *E*- and *H*-planes for a corner-reflector antenna having a width of 2 wavelengths and a length of 0.5 wavelengths. Aperture angle = 125° ; dipole position, distance from apex 0.20λ .

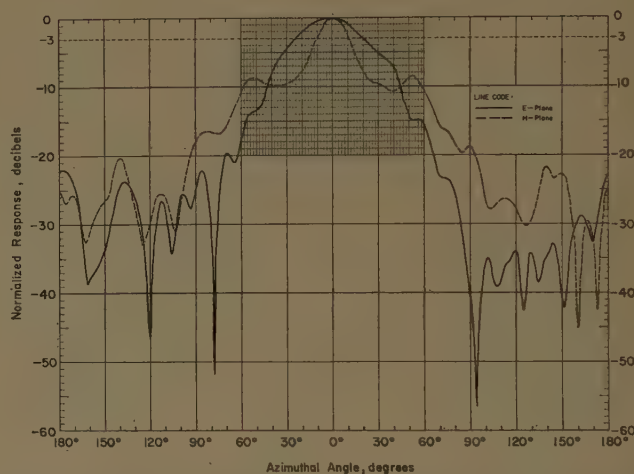


Fig. 42—Radiation patterns in the *E*- and *H*-planes for a corner-reflector antenna having a width of 1 wavelength and a length of 5 wavelengths. Aperture angle = 55° ; dipole position, distance from apex 0.55λ .

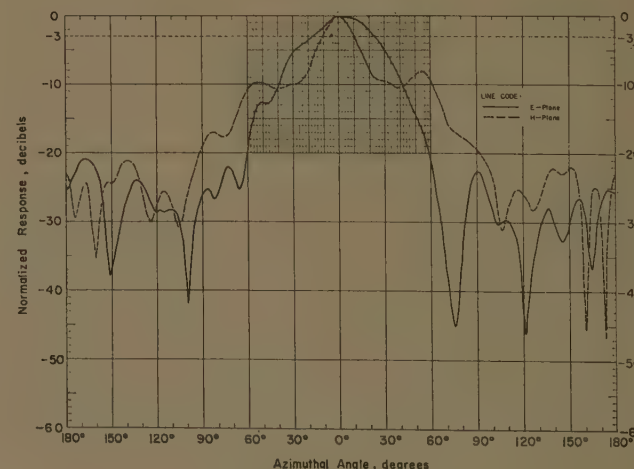


Fig. 43—Radiation patterns in the *E*- and *H*-planes for a corner-reflector antenna having a width of 1 wavelength and a length of 4 wavelengths. Aperture angle = 55° ; dipole position, distance from apex 0.55λ .

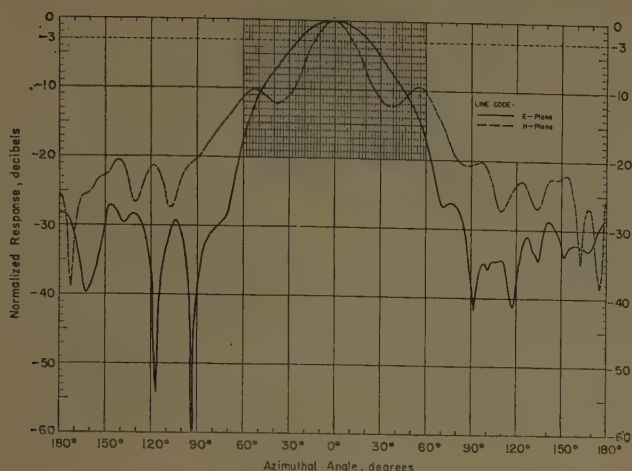


Fig. 44—Radiation patterns in the E - and H -planes for a corner-reflector antenna having a width of 1 wavelength and a length of 3 wavelengths. Aperture angle = 64° ; dipole position, distance from apex 0.45λ .

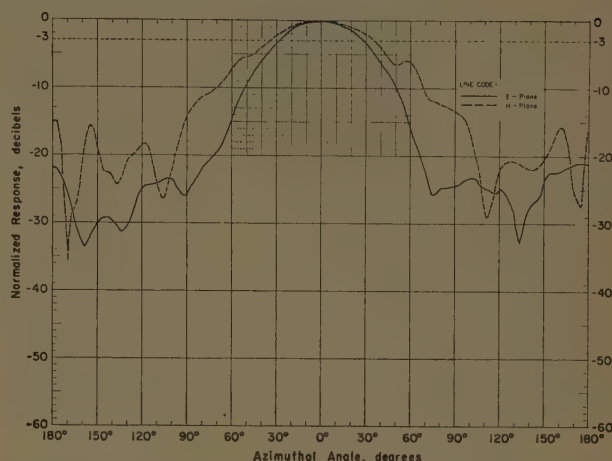


Fig. 47—Radiation patterns in the E - and H -planes for a corner-reflector antenna having a width of 1 wavelength and a length of 0.5 wavelengths. Aperture angle = 130° ; dipole position, distance from apex 0.20λ .

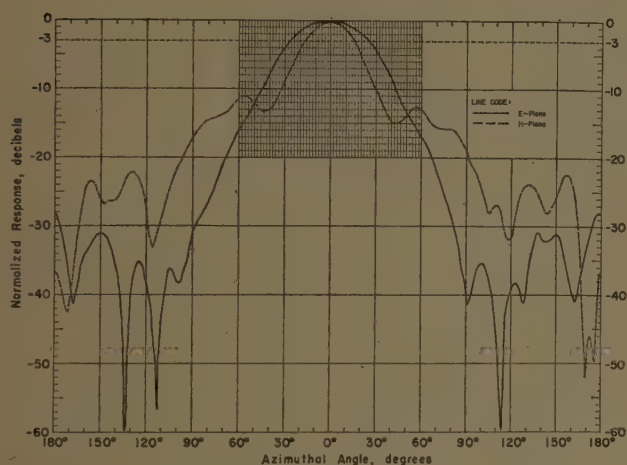


Fig. 45—Radiation patterns in the E - and H -planes for a corner-reflector antenna having a width of 1 wavelength and a length of 2 wavelengths. Aperture angle = 83° ; dipole position, distance from apex 0.35λ .

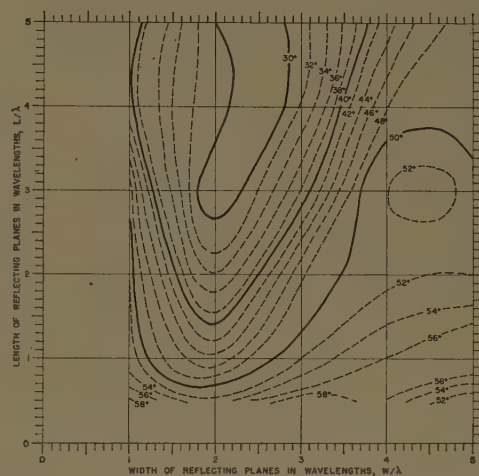


Fig. 48—Contours of half-power beamwidth in the E -plane for the corner-reflector antennas with various combinations of reflector sizes. The aperture angles were adjusted to obtain maximum gain for the size of the reflecting surfaces employed.

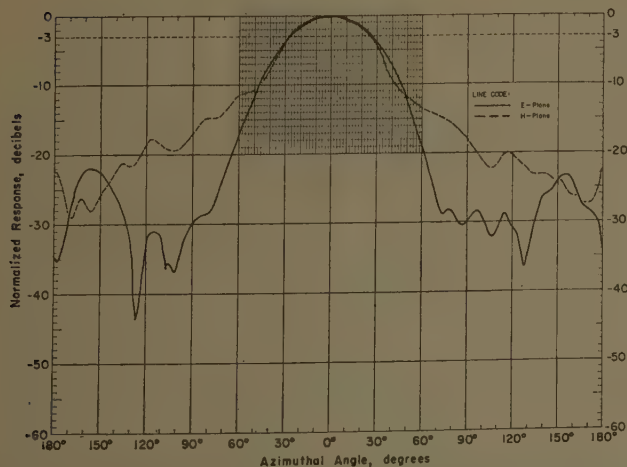


Fig. 46—Radiation patterns in the E - and H -planes for a corner-reflector antenna having a width of 1 wavelength and a length of 1 wavelength. Aperture angle = 110° ; dipole position, distance from apex 0.25λ .

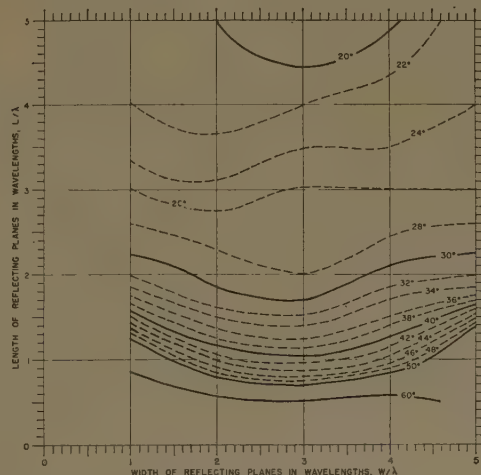


Fig. 49—Contours of half-power beamwidth in the H -plane for the corner-reflector antennas with various combinations of reflector sizes. The aperture angles were adjusted to obtain maximum gain for the size of the reflecting surfaces employed.

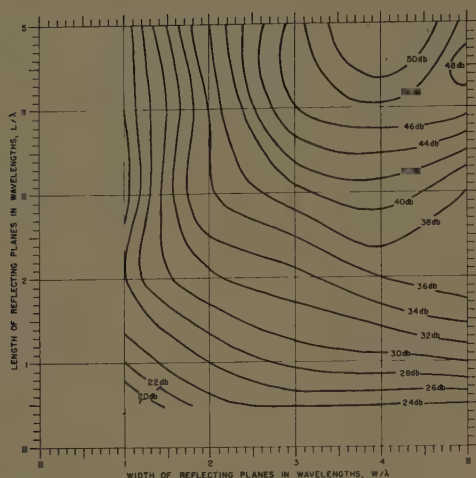


Fig. 50—Contours of prevailing back radiation for the corner-reflector antennas with various combinations of reflector sizes. The back radiation is the average of lobe maxima within the region 120° – 180° – 120° . The aperture angles were adjusted to obtain maximum gain for the size of the reflecting surfaces employed.

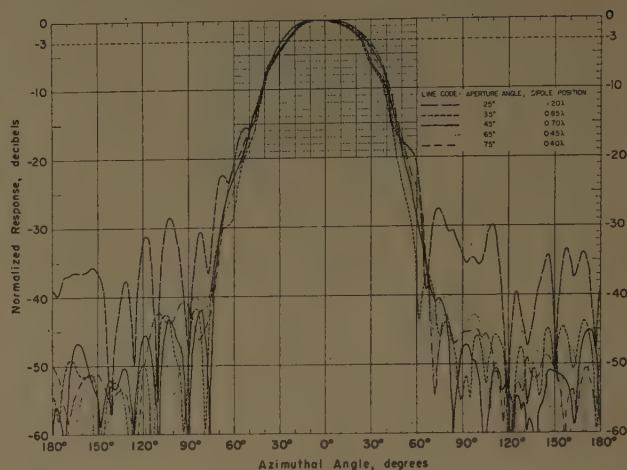


Fig. 51—Radiation patterns in the *E*-plane for a corner-reflector antenna having a width and a length equal to 4 wavelengths and aperture angle varying from 25° to 75° . Aperture angle of 45° and dipole position, $s/\lambda = 0.70$, are required to obtain maximum gain for the size of reflecting surfaces used.

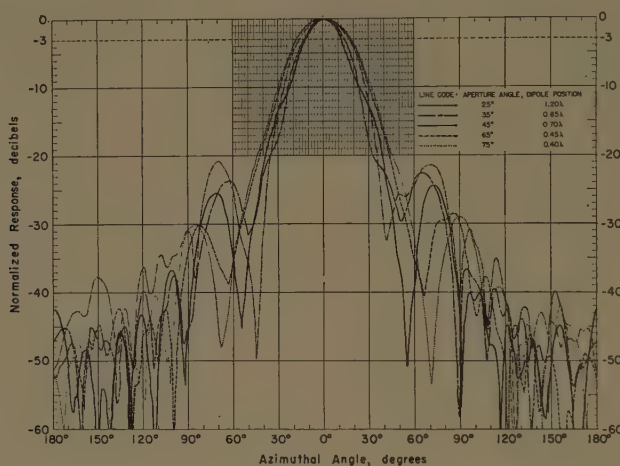


Fig. 52—Radiation patterns in the *H*-plane for a corner-reflector antenna having a width and length equal to 4 wavelengths and aperture angle varying from 25° to 75° . Aperture angle of 45° and dipole position, $s/\lambda = 0.70$, are required to obtain maximum gain for the size of reflecting surfaces used.

Suggestions have also been made to close the ends of the corner-reflector structure, thus making it appear like a horn. Fig. 1(c) illustrates the positions of the side plates within the corner-reflector structure. The intent of these suggestions is, likewise, to reduce the level of radiation diffracted to the rear. It has been found in the past that no additional gain is realized in this manner. In these tests, experiments were carried out with a corner reflector 2 wavelengths wide and 5 wavelengths long. Radiation patterns were made with no side plates and with side plates measuring 1, 2, 3, 4, and 5 wavelengths along the slant sides. Figs. 53 and 54 present the results of this comparison.

DISCUSSION OF RESULTS

It is convenient to consider that the radiated field to the rear of the corner-reflector antenna consists of two

components: the field diffracted around the edges of the reflecting surfaces and that which penetrates through the reflecting surfaces. The latter component may be very important if the reflecting surfaces consist of some kind of screening. In this investigation, the surfaces were of continuous sheet metal; therefore this component was not present. The diffracted radiation may in turn be considered to consist of two components, that diffracted by the forward edges of the surfaces and that diffracted by the side edges of the corner structure. The forward edges are parallel to the incident electric field whereas at the side edges the electric vector is largely normal to the diffracting edge. As is known, *e.g.*, Wait,⁶ the diffracted energy is much greater when the electric

⁶ J. R. Wait, "Radiation from a line source adjacent to a conducting half plane," *J. Appl. Phys.*, vol. 24, pp. 1528–1529; December, 1953.

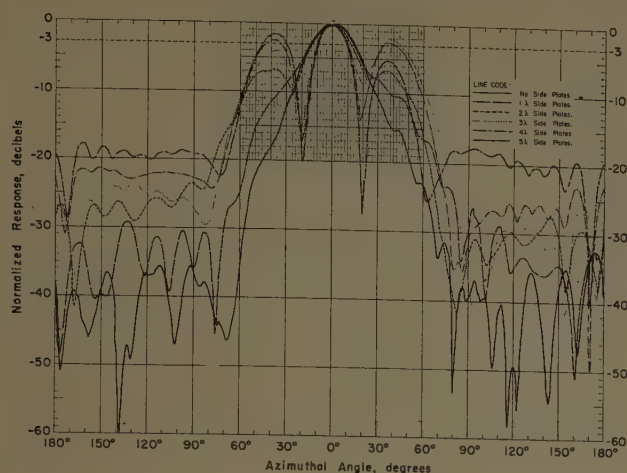


Fig. 53—Radiation patterns in the E -plane for a corner-reflector antenna having a width of 2 wavelengths and a length of 5 wavelengths with side plates measuring 1, 2, 3, 4 and 5 wavelengths along the slant sides. Aperture angle = 50° ; dipole position = 0.60λ .

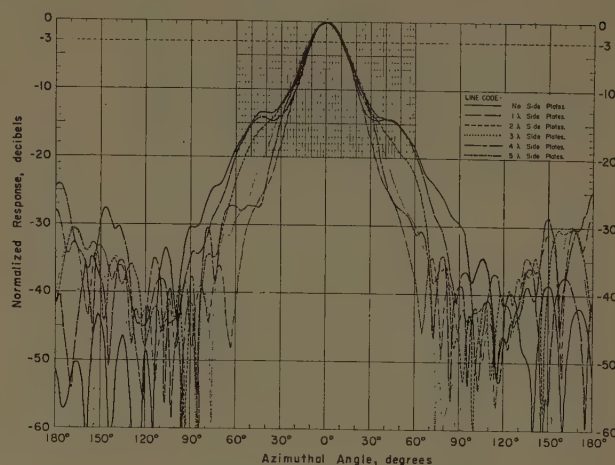


Fig. 54—Radiation patterns in the H -plane for a corner-reflector antenna having a width of 2 wavelengths and a length of 5 wavelengths with side plates measuring 1, 2, 3, 4 and 5 wavelengths along the slant sides. Aperture angle = 50° ; dipole position = 0.60λ .

vector is normal to a conducting edge than when it is parallel. Figs. 2–7 represent the results of the efforts to separate the two components. Fig. 2 presents the radiation patterns in the E -plane of a corner-reflector antenna having a width of 10 wavelengths and length of surfaces equal to 5, 4, 3, 2, 1, and 0.5 wavelengths. Fig. 3 presents the corresponding patterns in the H -plane. The physical aspects of the problem would lead one to expect that the variations in the lengths would be more noticeable in the H -plane patterns than in the E -plane. This is found to be substantially correct.

With lengths equal to 5, 4, and 3 wavelengths, the radiation patterns in the E -plane show the general level of the radiation to the rear to be at approximately -50 -db level. Reduction of the lengths below the 3-wavelength value begins to affect the back radiation level. The shape of the main lobe in the E -plane is not affected by the lengths of the surfaces. The radiation pattern in the H -plane is, however, quite sensitive to changes in the length of the surfaces. This applies to the width of the main lobe as well as the secondary radiation level. It should be noted at this point that, as the lengths are trimmed down, the angle of aperture is increased and the position of the dipole is brought closer to the apex of the corner reflector to maintain the optimized parameters of the antenna. The side edges of the reflectors then receive less illumination because they are closer to the null of the dipole pattern. This is believed to be the reason why the level of the back radiation in the E -plane is lower with reflector lengths of 4 wavelengths than it is with lengths of 5. Similarly, the back radiation level with lengths of 3 wavelengths appears to be slightly lower than with lengths of 4 or 5 wavelengths.

Fig. 4 and 5 compare the radiation patterns in the E - and H -planes, respectively, of a corner-reflector an-

tenna having reflecting surface lengths equal to 5 wavelengths, and widths varying from 10 to 1 wavelength. For widths equal to 3 wavelengths, or greater, the back radiation appears to be of the order of -45 to -50 db. For shorter widths, the back radiation rapidly increases. The width and the shape of the main lobe in the H -plane do not appear to be significantly affected by the width of the corner structure. The width of the main lobe in the E -plane is affected in a rather unexpected manner. As the widths of the reflecting surfaces are reduced from 5 wavelengths to 4, to 3, and to 2 wavelengths, the width of the main lobe becomes narrower. For reflector widths smaller than 2 wavelengths, the main lobe rapidly widens. This is consistent with the observation made during the measurement of gain reported previously.³ There, with the dipole in the first position, maximum gain was measured for corner-reflector widths between 1.8 and 2.2 wavelengths. A plausible physical explanation is that the energy contributed by the reflection at the outlying portions of the reflector structure is sufficiently out of phase with the total radiation as to reduce the gain in the forward direction and to broaden the main lobe. Figs. 6 and 7 are similar to Figs. 4 and 5 respectively, except that the lengths of the reflecting surfaces were fixed at 2 wavelengths. The results are substantially the same.

Figs. 8–47 constitute a catalog of radiation patterns in both principal planes obtained for various combinations of widths and lengths of reflecting surfaces. To restrict the figures to a reasonable number, the angles of aperture and the positions of the dipole were limited to those prescribed for maximum gain by the authors.³ To check the effect of varying the aperture angle for a corner-reflector antenna of fixed dimensions, radiation patterns were measured for one having a width and length equal to 4 wavelengths. The optimized value of

the aperture angle for these dimensions is 45° . The patterns were measured with the aperture angle adjusted to 5 values ranging from 25° to 75° . The position of the dipole corresponded to the optimum value for a given aperture angle. The radiation patterns in the E -plane appear to be affected relatively little by moderate variations in the angle. For the smaller values of the angle, the back radiation increased sensibly. In the H -plane, the principal effect of aperture angle variations appears to be on the width of the main lobe. This width is minimum for the prescribed angle. For angles either smaller or larger than the prescribed, the beamwidth increases. As was the case in the E -plane, the back radiation in the H -plane was increased noticeably when the aperture angle was made considerably smaller. It did not appear to be affected by increasing the angle.

Figs. 53 and 54 compare the radiation patterns, in E - and H -planes respectively, of corner-reflector antennas each having a width of 2 wavelengths and a length of 5 wavelengths, but having the ends of the corner-reflector structure closed in to various degrees. The radiation patterns in the E -plane show most clearly the effect of such closure. They show that, far from reducing the back radiation, they greatly increase it. If one defines the beamwidth of the main lobe as being measured between the -3 -db points, then the main beam is made more narrow by the addition of the end closures. However, additional lobes are introduced approximately 38° to each side of the main lobe which, for closures of 3 wavelengths and greater, come to within 3 or 4 db of the main lobe. While without end closures, the back radiation level was approximately -35 db; with the closures of 3 to 5 wavelengths the level increased to a -20 -db value. In the H -plane, the effect of the closures is to narrow the main beam slightly, but increase the back radiation level considerably. Past experience with measurements of gain of corner-reflector antennas with and without the end closures indicates the effect on the over-all gain is negligible.

APPLICATION TO LOW SECONDARY-LOBE LEVEL ANTENNAS

A conventional corner-reflector antenna with a single half-wave dipole as the driven element possesses only a moderate degree of gain and directivity. Additional directivity in the E -plane may be obtained readily by increasing the width of the corner reflector and substituting a collinear array of dipoles in lieu of the half-wave dipole as the driven element. A low secondary-lobe level may be retained by grading the current distribution in the array in accordance with Dolph-Tchebychev or equivalent principles.

In an operational antenna, it is not generally practical on the basis of cost, wind resistance, etc., to have continuous metal sheets as reflecting surfaces. It is, therefore, necessary to substitute a grating of wires for

the metal sheets. An investigation of the shielding properties of a wire grating was beyond the scope of this investigation. However, there is available in the published literature the results of an experimental investigation on the subject.⁷ Fig. 55 reproduces these data. Since the original data were limited to front-to-back ratio of 35 db, these data were extrapolated to a 50-db level.

The results of this investigation have been applied to a recent specific application involving a proposed high-power transmitting antenna for VHF ionospheric scatter communication. For reasons of noninterference with local services, it was necessary to restrict the width of the main beam to approximately 10° in the E -plane. It was further necessary to restrict the general level of the secondary radiation to a level not to exceed -40 db. The requirement for the narrow width of the main lobe in combination with that for -40 -db secondary-lobe level pointed to the use of collinear array of dipoles with a Dolph-Tchebychev⁸ current distribution. This array finally was set at 10 half-wave dipoles, 0.80 wavelength apart center-to-center. The dimensions of the corner-reflector structure were selected to have a width of 10 wavelengths and a length of reflecting surfaces equal to 2 wavelengths. The wire grating was selected to have a wire diameter of 0.00034 wavelength and a spacing of 0.0042 wavelength. Fig. 55 predicts this combination of diameter and spacing, indicated by a cross, to result in a front-to-back ratio of approximately 43 db.

A scaled experimental model of this antenna was constructed for operation at 400 mc (a scaling factor of approximately 10). Fig. 56 is a photograph showing a view of this antenna. Fig. 57 shows the radiation patterns of this antenna in the E - and H -planes. The width of the main lobe in the E -plane is seen to be within the 10° limits. The secondary radiation level is below the -40 -db limit everywhere except in the immediate neighborhood of the main lobe; there, the level is up to approximately -39 db. Check of pattern stability with time and changes in temperature and weather conditions showed it to be quite stable. Measurements of radiation pattern at frequencies departing from the design frequency showed the operating bandwidth (determined by the preservation of the pattern) to be adequate for the applications likely to be considered for such antennas. By grading the phase of the currents in the collinear array, it was found possible to shift the direction of the main beam up to and somewhat beyond

⁷ "Reliable High-Frequency Communications," Developmental Engr. Corp., Washington, D. C., Rept. No. 3-P-7, 7th Prog. Rept. on Signal Corps Contract DA-36-039 SC-64486; January 1-April 30, 1957.

⁸ C. L. Dolph, "A current distribution for broadside arrays which optimize the relationship between beam width and side-lobe level," *PROC. IRE*, vol. 34, pp. 335-348; June, 1946. See also discussion by H. J. Riblet, vol. 35, pp. 489-492; May, 1947.

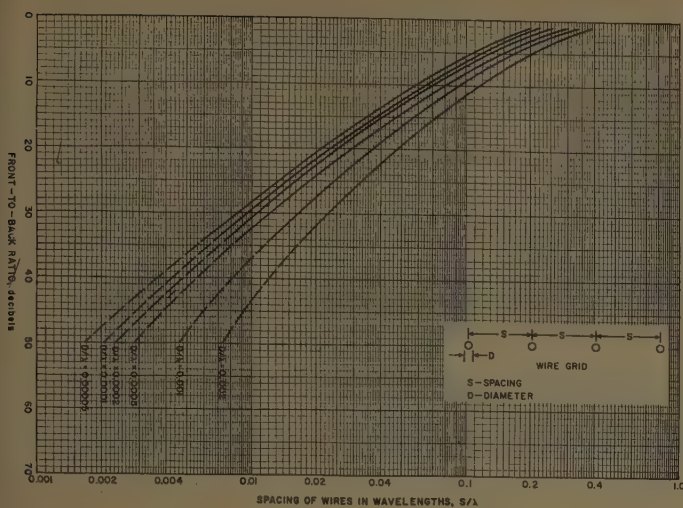


Fig. 55—Screening property of wire grating as function of wire diameter and spacing. Dashed portions of curves represent extrapolations of original data. D/λ is diameter of wires in wavelengths; wave at normal incidence; electric vector parallel to grid wires.

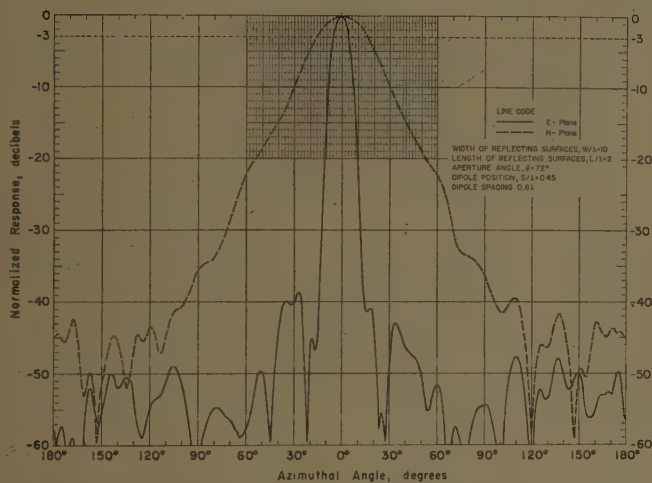


Fig. 57—Radiation patterns in *E*- and *H*-planes of a corner-reflector antenna using a collinear array of 10 half-wavelength dipoles as the driven element with a Dolph-Tchebychev current distribution to limit the side lobes.

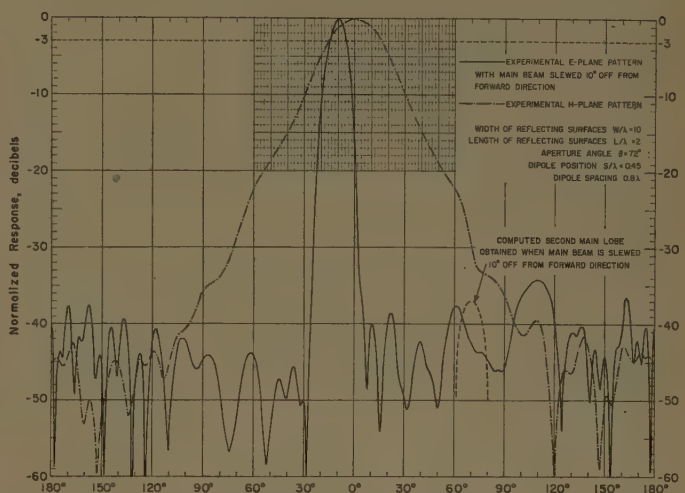


Fig. 58—Radiation patterns in *E*- and *H*-planes of the corner-reflector antenna with main beam in *E*-plane slewed 10° off from forward direction.



Fig. 56—A view of the experimental corner-reflector antenna.

10° without impairing the pattern significantly. Fig. 58 illustrates the radiation patterns obtained using such phase displacement.

CONCLUSION

The results of measurements described here show that quite low levels of secondary radiation may be obtained by the use of corner-reflector antennas of moderate dimensions. Thus, -40 -db levels may be obtained by using reflector structures 3 wavelengths wide and 2 wavelengths long. To realize -50 -db levels, the widths should be increased to about 4 and the lengths to approximately 3 wavelengths. To obtain greater gain and higher directivity in the *E*-plane, the width of the corner-reflector structure may be extended and a collinear array substituted for the dipole as the driven

element. To realize greater directivity in the *H*-plane, several corner-reflector antennas may be stacked one above the other.

No satisfactory means of reducing energy diffracted by the edges of the reflecting surfaces have been found other than by reducing the illumination of the edges. The closing-in of the ends of the corner-reflector structure by use of the "side flaps" deteriorated the radiation pattern.

The available literature on the screening efficiency of wire grating appears to be satisfactory for use in the design of the reflecting surfaces.

ACKNOWLEDGMENT

The measurements were carried out with the assistance of W. L. Martin.

The Flight Evaluation of Aircraft Antennas*

GEORGE W. LEOPARD†

Summary—Flight evaluation of communication-navigation-identification antennas installed on new types of aircraft is required to confirm model measurements. The paper reviews the parameters involved in such an evaluation under both standard and nonstandard propagation conditions. The predicted signal level across the receiver terminals connected to an isotropic antenna is employed as the standard of comparison with the scale-model antenna patterns. The procedures employed and the results obtained are briefly discussed.

THE flight evaluation of communication, navigation, and identification aircraft antenna installations is planned with the aim of confirming the accuracy and reliability of previously-determined model patterns. Design approval of the antenna systems on a new type of aircraft is normally given on the basis of scale model patterns and other laboratory tests prior to the completion of the first airplane, with the understanding that the flight test results must essentially confirm the model patterns. Experience has shown that, due to the various compromises required in the manufacture of small-scale antenna and aircraft models, the numerous pitfalls awaiting inexperienced personnel, and the lack of clearly-defined standards,¹ such flight radiation measurements are required as a final check on the validity of the model patterns on each new type of aircraft. It is similarly necessary to stress the fact that only by knowing or controlling many of the flight test conditions, which are too frequently neglected, can good correlation between model patterns and flight test data be obtained.

THE GEOMETRY OF THE PROBLEM

The following discussion^{2,3} is applicable for frequencies above 50 mc. The geometry of the conditions of the flight test is given in Fig. 1. Propagation takes place along two paths between the ground antenna and the aircraft antenna. At the receiving antenna, interference will occur between the direct and the indirect rays because the indirect-ray path is longer. The electrically longer path is due to the longer physical path plus the angle of lag which occurs at the point of reflection. The

amount of the interference is proportional to the magnitude of the indirect ray, which in turn is proportional to the absolute value of the reflection coefficient.

PROBLEM UNDER "STANDARD" CONDITIONS

The ratio of the resultant field to the free-space field, E_d/E_0 or $g(\theta)$, for a smooth $4/3$ radius earth under "standard" atmospheric conditions, and using isotropic transmitting and receiving antennas, may be expressed⁴ as:

$$\frac{E_d}{E_0} = g(\theta) = [1 + \overline{DR}^2 + 2DR \cos(\theta - \phi)]^{1/2} \quad (1)$$

where

D = divergence factor

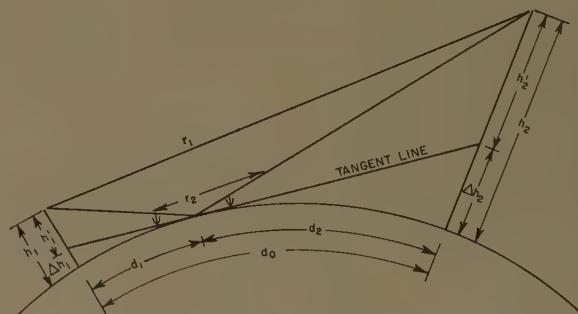
R = absolute magnitude of the reflection coefficient

θ = physical path-length difference expressed in electrical degrees.

ϕ = phase angle of the reflection coefficient.

The divergence factor is defined as the ratio of the field strength obtained after reflection from a spherical surface to that obtained after reflection from a plane surface, the radiated power, total axial distance, and type of surface being the same in both cases, and the solid angle being a small elemental angle approaching

⁴ *Ibid.*, p. 130.



- d_0 = distance along surface of earth between antennas
- d_1 = distance along surface of earth between ground antenna and point of reflection
- d_2 = distance along surface of earth between point of reflection and aircraft antenna
- h_1 = ground antenna height
- h_1' = effective ground antenna height above tangent line
- Δh_1 = altitude of tangent line at ground station
- h_2 = aircraft antenna height
- h_2' = effective aircraft antenna height above tangent line
- Δh_2 = altitude of tangent line at distance d_0 from ground station
- r_1 = direct-ray path between antennas
- ψ = grazing angle
- r_2 = indirect-ray path between antennas

Fig. 1—Geometry of two-path propagation.

* Manuscript received by the PGAP, March 23, 1959; revised manuscript received, September 10, 1959.

† Communication and Navigation Branch, Electronics Test Div., Naval Air Test Center, Patuxent River, Md.

¹ A. Dorne, "Proposed Program for Standardizing Model Aircraft Antenna Radiation Pattern Measurements," Dorne and Margolin, Inc., Westbury, N. Y., Rept.; April 10, 1953.

² J. W. Plummer, *et al.*, "UHF Propagation Over Land and Water," NATC, Patuxent River, Md., Final Rept. Project PTR EL 929; April 10, 1951.

³ H. R. Reed and C. M. Russell, "UHF Propagation," John Wiley and Sons, Inc., New York, N. Y., pp. 127-148; 1953.

zero in magnitude. The divergence factor can be shown to be:⁵

$$D \doteq \left[1 + \frac{2d_1d_2}{rd \tan \chi} \right]^{-1/2} \quad (2)$$

where r is the earth's radius corrected for normal refraction (5280 miles), and the other factors are defined in Fig. 1. The variation of the divergence factor with change in grazing angle is illustrated in Fig. 2 for two values of ground antenna heights and for a distance of 50 miles. A grazing angle of one degree or more is normally employed in the antenna evaluation. The use of unity as the value of the divergence factor will not introduce a significant error under most conditions encountered in practice.

If the discussion is confined to vertical polarization, which is of major interest, the Fresnel reflection coef-

ficient may be expressed by:⁶

$$R_v e^{j\phi_v} = \frac{n^2 \sin \psi - \sqrt{n^2 - \cos^2 \psi}}{n^2 \sin \psi + \sqrt{n^2 - \cos^2 \psi}} \quad (3)$$

where

$$n^2 = \epsilon_r - j60\sigma\lambda$$

ϵ_r = dielectric constant of reflecting surface

σ = conductivity of reflective surface

λ = wavelength of propagated wave in meters.

It is seen that the value of the reflection coefficient is determined by the character of the surface at the zone of reflection and by the grazing angle. Figs. 3 and 4 are graphs of the angle of lag and magnitude respectively, of the reflection coefficient for a vertically-polarized wave.

Another variable in the equation for $g(\theta)$ is the phase shift due to increase in path length, which can be shown to be:⁷

$$\theta = \frac{2\pi}{\lambda} \left(2 \frac{h_1 h_2}{d} \right) \text{radians} \quad (4)$$

with λ , h and d expressed in similar units. This path-length difference is combined with the phase shift ϕ (due

⁵ *Ibid.*, p. 102-109.

⁶ *Ibid.*, p. 90.

⁷ *Ibid.*, p. 100.

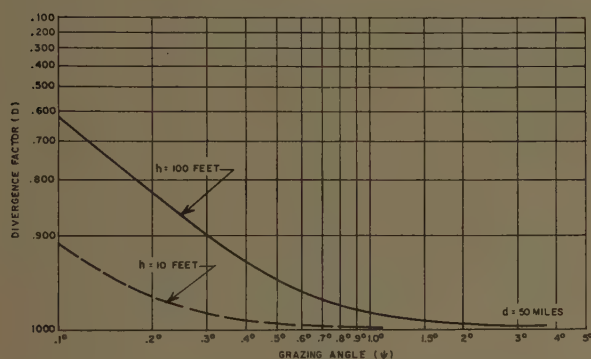


Fig. 2—Variation of divergence factor with change in grazing angle.

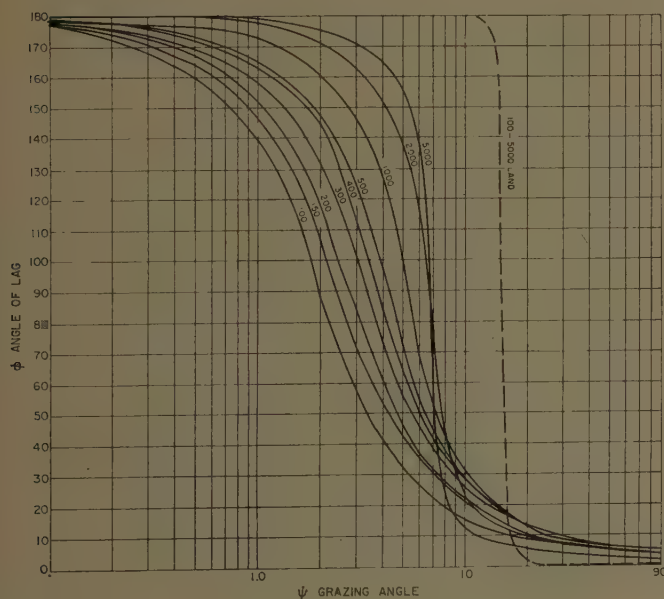


Fig. 3—Angle of lag of reflection coefficient (vertical polarization). Dashed curves for land of average conductivity; solid curves for sea water; numbers refer to frequency in megacycles.

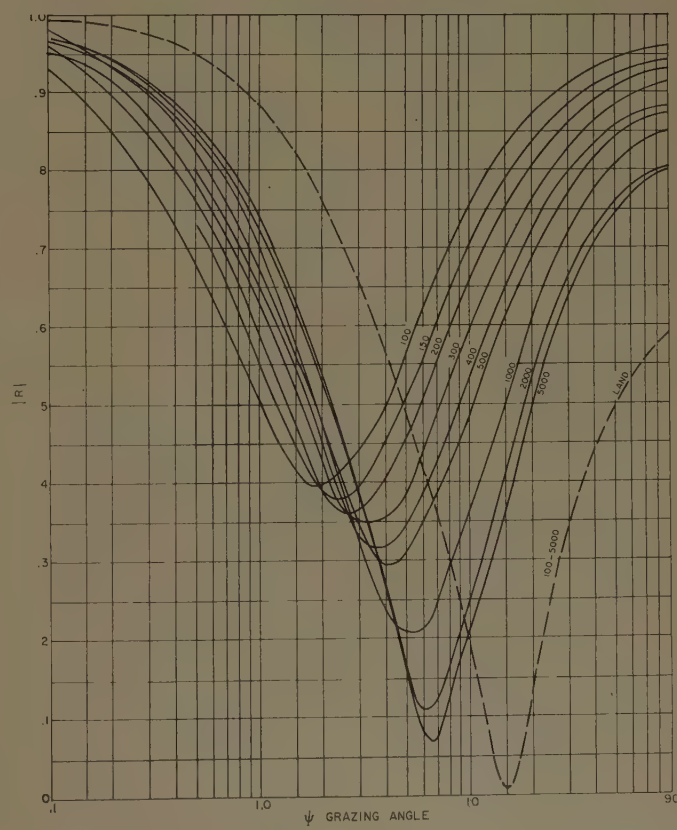


Fig. 4—Magnitude of reflection coefficient (vertical polarization). Dashed curves for land of average conductivity; solid curves for sea water; numbers refer to frequency in megacycles.

to reflection) to give the total phase lag of the reflected ray.

Fig. 5 is a plot of the resultant field at a frequency of 1186 mc under a specific set of conditions and furnishes an example of the basic interference pattern. Due to the steep field intensity gradients present in the interference pattern, it is essential that the aircraft altitude and range be properly chosen when conducting radiation tests. Measurements are usually made near the center of an interference lobe maximum where a greater volume of space of a relatively constant signal level may be expected. If all measurements are made when the airplane is flying at an altitude and distance such that the combined phase shift is an even multiple of 2π ,

$\cos(\theta - \phi)$ becomes unity in the equation for $g(\theta)$. If the value of the divergence factor is also assumed to be unity, then

$$g(\theta)_{\max} = [1 + R^2 + 2R]^{1/2} = 1 + R.$$

(5)

The proper conditions for flight measurements are chosen by reference to Fig. 6.

EFFECT OF REFLECTING SURFACE ROUGHNESS

In general, propagation conditions are not "standard." The assumption of a smooth earth reflecting surface and the variation in the index of refraction of the atmosphere are the greatest additional sources of error. The effects of the changes in these two parameters must be avoided if accurate and repeatable results are to be achieved.

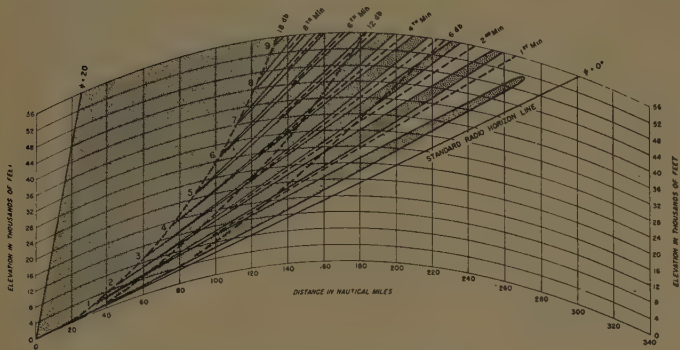


Fig. 5—Theoretical radiation pattern for ground-to-air propagation over smooth salt water; 4/3 earth radius used to correct for standard atmosphere refraction.

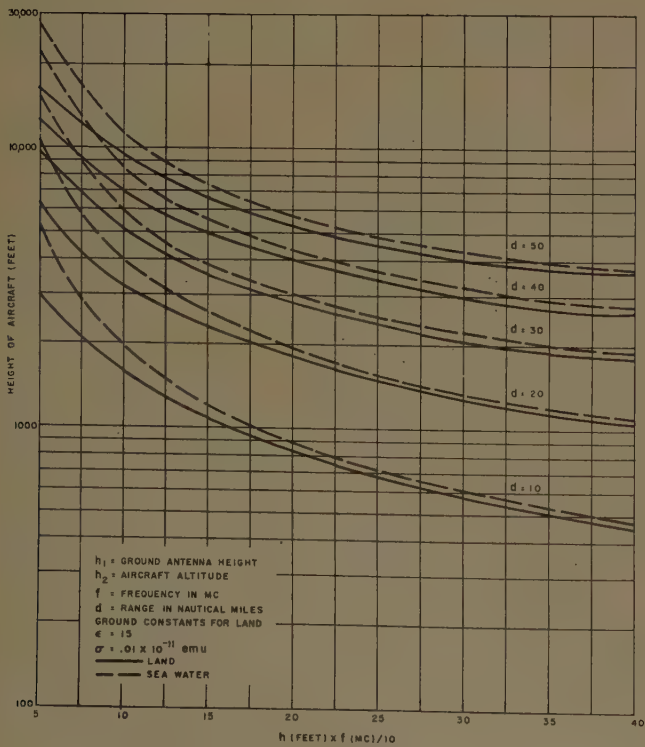


Fig. 6—Location in space of first ground reflection interference maximum.

Frequency: 1186 mc
Polarization: vertical°
Ground antenna height: 70.5 feet
Ground antenna: 7-element array dished up 5° electrically, 6 db gain over a dipole
Airplane antenna: half-wave dipole
Transmitter power: 5 kw
Receiver sensitivity: -85 dbm
System loss: 18 db

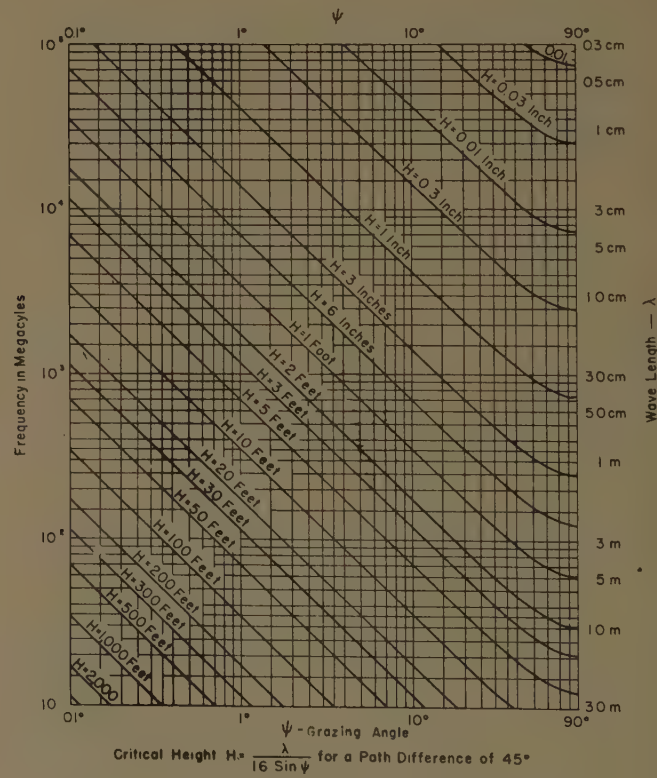


Fig. 7—Criterion for roughness of a reflecting surface.

It is essential that the reflecting zone be clear of obstacles of a size that will cause excessive scattering. Rayleigh's criterion for surface roughness may be stated⁸ as:

$$H = \lambda / (16 \sin \psi) \quad (6)$$

where H is the critical height of surface irregularities and λ the wavelength, both expressed in the same units of length, and ψ the grazing angle of the incident ray. A graph of the critical angle vs frequency for various values of H is presented in Fig. 7. It should be remembered that the transition from specular to diffuse reflection is not sharply defined. The change in character of the reflection takes place gradually as the grazing angle is increased. Thus, a moderate amount of scatter can be expected at the critical obstruction height. It is im-

⁸ *Ibid.*, p. 237.

portant to insure that obstacles in the reflecting zone are well below the value given by the chart for a particular choice of frequency and grazing angle. For instance, for specular reflection at low grazing angles (such as 1°) at 1000 mc, there should not be a great number of obstacles which exceed two feet in height. If at all possible, a water reflecting zone is employed. This requirement is vividly shown by reference to the comparisons of reflection coefficient magnitudes measured in flight with theory in Fig. 8. The correlation between the theoretical curve and the measured points at low grazing angles is fairly good over water at L-band. The overland data in Fig. 8 show diffuse reflection at all grazing angles over land. The reflecting zones employed in making these measurements were the Chesapeake Bay and the Naval Air Station, Patuxent River, runway area. The latter area is mostly flat with some small buildings, and occasional surface irregularities.

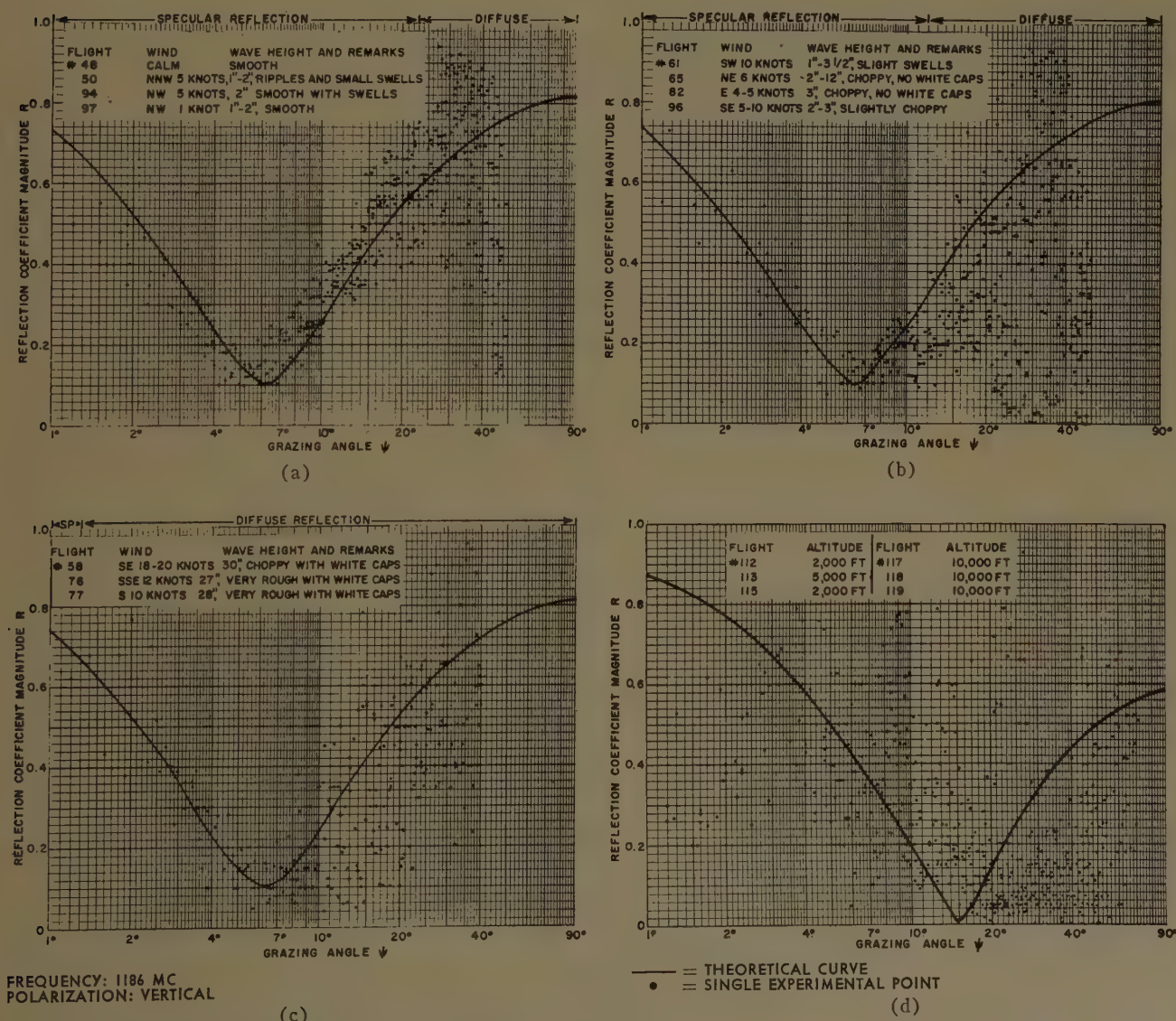


Fig. 8—Comparison of measured reflection coefficient magnitudes with theory at L-band. (a) Propagation over smooth bay water. (b) Propagation over slightly rough bay water. (c) Propagation over rough bay water. (d) Propagation over land.

CHANGE IN REFRACTIVE INDEX

The most unpredictable parameter to be encountered in antenna radiation flight tests is the refractive index of the atmosphere. The rate of bending of the propagated wave is a function of the gradient of the atmospheric index of refraction. Fig. 9 shows a theoretical curve of the received signal strength at a frequency of 1186 mc for ground-to-air propagation in a standard atmosphere, with the airplane flying at a constant altitude of 10,000 feet under the conditions shown on the graph. The inset curve is that of the refractive index of a theoretical standard atmosphere. It is noted that the maxima and the minima of the received signal curve, known as the interference pattern, are numbered for convenience beginning with the outermost maximum. The theoretical radio horizon in this case is 133 nautical miles, with the first minimum at about 100 miles.

Fig. 10 shows a typical experimentally-measured interference pattern obtained under a set of conditions similar to those stated in the theoretical curve of Fig. 9. Refractometer data plotted in the inset of Fig. 10 show the measured state of the atmosphere to be quite uni-

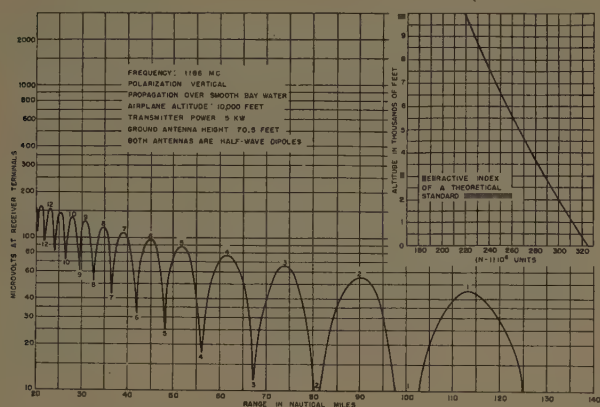


Fig. 9—Theoretical received signal strength for ground-to-air propagation in a typical "smooth" atmosphere.

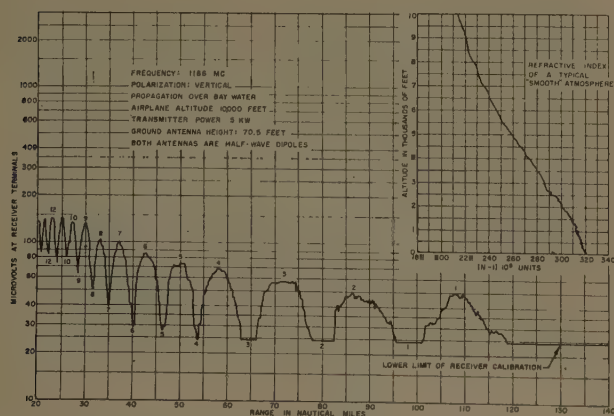


Fig. 10—Measured received signal strength for ground-to-air propagation in a typical "smooth" atmosphere.

form and similar to the theoretical standard atmosphere, and for that reason this has been called a "smooth" atmosphere. A high degree of similarity is shown between the measured and the theoretical interference patterns. The general level of the curves and the location of interference maxima and minima are in close agreement.

Fig. 11 shows another typical measured interference pattern, obtained under the same geometrical conditions as Fig. 10, but on another day, when the refractometer data showed large irregular fluctuations in the refractive index as the altitude increased. The fluctuations produced abnormal values of dn/dh (change in refractive index with change in altitude). This has been called a "rough" atmosphere for that reason. A comparison of many such measured interference patterns, obtained under both "smooth" and "rough" atmospheric conditions, reveals several marked differences which are shown in the typical interference patterns of Figs. 10 and 11. While the patterns are generally quite similar at ranges less than 50 miles, the differences are often pronounced at ranges in excess of about 50 miles. The ranges at which the two-path interference maxima and minima occur agree quite closely with theory when the atmosphere is "smooth" and no ducting is present. When the atmosphere is "rough," the measured values of these ranges may vary by more than 10 per cent from those indicated by theory, especially at the longer ranges. Unexpected signal fluctuations often occur at random places on the interference patterns when the atmosphere is "rough." The data indicate that "rough" atmospheres were encountered approximately 25 per cent of the time during the above propagation data flight tests. The data, together with Figs. 8-11, were prepared by Browne.⁹

⁹ W. M. Browne, "Propagation in the 960 to 1215 mc Range," NATC, Patuxent River, Md., Combined Final Rept. Projects PTR EL 44012.3 and 44012.4, ser. ET312-412; October 27, 1954.

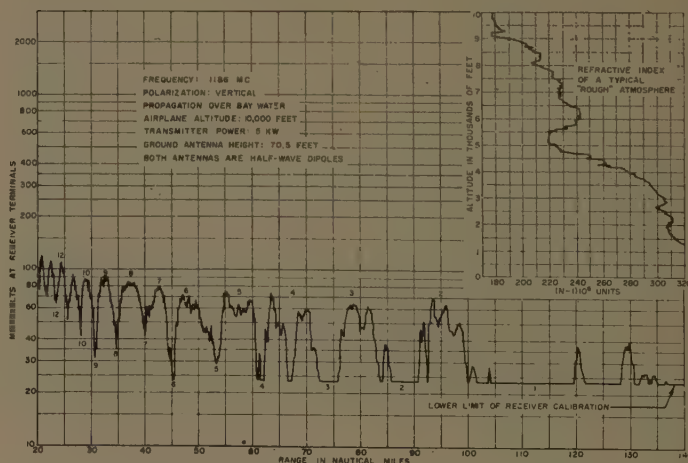


Fig. 11—Measured received signal strength for ground-to-air propagation in a typical "rough" atmosphere.

DUCTS

Even greater deviations from the "standard" atmosphere than those shown in Fig. 11 may be expected under certain conditions. Whenever a horizontal layer of air has its normal properties altered so that the refractive index decreases rapidly with increase in height, strong downward bending of any nearly horizontal rays traversing the layer will occur, the curvature often exceeding that of the earth.

In general, ducts are divided into two categories, ground based and elevated. The underside of a ground-based duct is in contact with the earth's surface, while the base or underside of an elevated duct overlies a layer of normal air. Ground-based ducts are caused, for example, by the nocturnal cooling of the surface of the earth, or when dry air flows from land out over cooler water. Elevated ducts are generally caused by a meteorological process called subsidence, slow downward and outward settling of a large mass of air, which becomes drier than the normal air below and in addition produces a temperature inversion.

Elevated ducts occur widely, but are most frequently found in the United States along the coast of Southern California at elevations of 1000 to 5000 feet and vary in depth from a few feet to 1000 feet. It is most important that the engineer be alert for abnormal results which would indicate the presence of a duct.

STANDARD FOR COMPARISON TO MODEL PATTERNS

Scale-model antenna patterns are normally referred to a theoretical isotropic antenna signal level. In order to compare the flight evaluation results to the scale model patterns, the theoretical signal level to be expected from an isotropic antenna located at the same point in space and under the conditions of the flight test is required. The theoretical signal level is based on the numerical evaluation of various factors herein referred to as gains or losses when considered as a part of the over-all transmission path. The net difference between the gains and losses, when equated to a suitable expression for the power density at the receiving antenna P , will give the expected signal level incident on the receiver terminals. The losses may be classified as those due to 1) space transmission attenuation, and 2) system losses in the ground and air installations.

Free-space transmission loss is based on the signal loss between isotropic antennas separated by a distance d . This distance may be considered as the radius of a sphere of radiation whose center is the transmitting antenna and on whose surface may be found the receiving antenna. The power density at the receiving antenna is equal to the transmitted power divided by the area of the surface of the sphere, A . Thus,

$$P = \frac{P_T}{A} = \frac{P_T}{4\pi(1609)^2 d^2} \text{ (watts/square meter)} \quad (7)$$

P_T = transmitted power

d = distance in statute miles (1 mile = 1609 meters).

The received power (P_R) is equal to the product of the power density and the effective area (a_{eff}) of an isotropic antenna,¹⁰ which is $0.08 \lambda^2$.

$$P_R = A_{eff} \times P = \frac{0.08 \lambda^2 P_T}{4\pi(1609)^2 d^2} = \frac{0.08(300)^2 P_T}{4\pi(1609)^2 f^2 d^2} \quad (8)$$

where

f = frequency in megacycles

and

$$\lambda = 300/f$$

The free-space transmission loss in db

$$P_L = 10 \log \frac{P_T}{P_R} = 10 \log \frac{4\pi(1609)^2 f^2 d^2}{0.08(300)^2} \quad (9)$$

$$= 36.5 + 20 \log fd.$$

Another major factor to be considered is the gain or loss due to the amplitude and phase of the signal traveling via the reflected ray path when it arrives at the receiving antenna. This requires the evaluation of the expression for $g(\theta)$, given in (1), which has already been discussed. Examples of detailed calculations to determine $g(\theta)$ and interference pattern microvolt contours using this method (such as Fig. 5) are given by Reed and Russell.¹¹

In-flight field intensity measurements for the purpose of checking aircraft antenna patterns on a given frequency are usually performed by flying over a fixed reference point on 24 different evenly-spaced compass headings. The altitude, range and ground antenna heights are chosen from Fig. 6 so that the airplane is in the center of a lobe maximum.

In practice, the theoretical isotropic signal level is determined by calculating the gains and losses (in db) as follows.

- 1) Gain due to transmitted power (db above 1 watt).
- 2) Ground antenna gain relative to an isotropic antenna.
- 3) Gain (or loss) due to the ground reflection, $g(\theta)$.
- 4) Transmission space attenuation loss,

$$P_L = 36.5 + 20 \log fd. \quad (10)$$

- 5) Measured system losses in both ground and aircraft installations.

¹⁰ J. D. Kraus, "Antennas," McGraw-Hill Book Co., Inc., New York, N. Y., p. 42; 1950.

¹¹ Reed and Russell, *op. cit.*, ch. 5.

The difference between the gains and the losses determines the effective power P_{eff} dissipated in the receiver input impedance, which creates a signal voltage E (expressed in microvolts), across the 50-ohm receiver terminals. Thus

$$P_{eff} = 10 \log \frac{(E \times 10^{-6})^2}{50} = - \text{dbw (net loss)}. \quad (11)$$

The negative sign is employed to indicate that the value is below the reference level of 1 watt. Solving for the signal level results in:

$$E = \sqrt{50 \text{ antilog} \frac{120 - \text{dbw (net loss)}}{10}}. \quad (12)$$

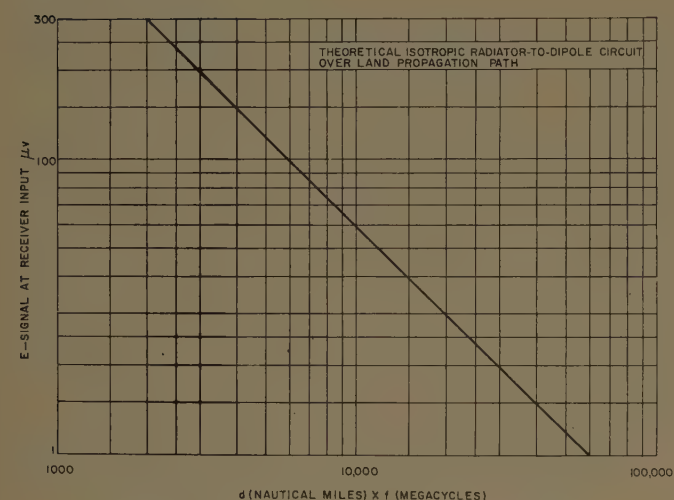


Fig. 12—Expected signal at receiver input as a function of frequency and range (overland propagation path).

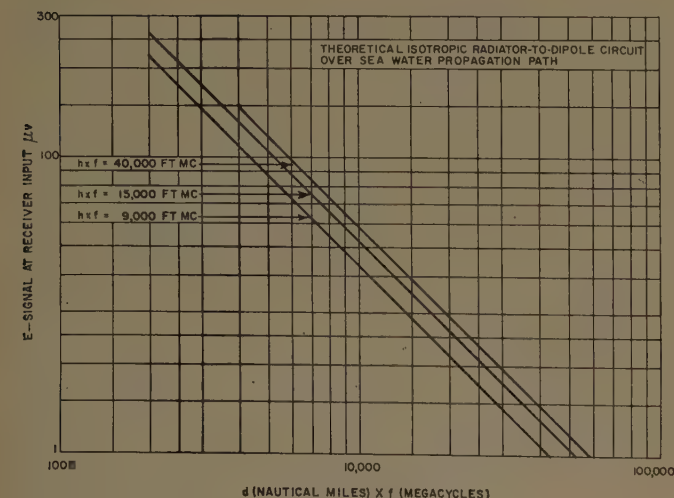


Fig. 13—Expected signal at receiver input as a function of frequency, range and ground antenna height (over salt water propagation path).

Figs. 12 and 13 are charts of isotropic levels employed in practice and require only a correction for ground antenna gain over a dipole, system loss, and transmitter power output (reference level, 9 watts).

INSTRUMENTATION

Comparison of the lobe structures shown in Figs. 5 and 14 clearly shows the advantage of installing the ground station antenna as low as practicable, especially for frequencies in the L-band and higher, in order to be assured of a wide first lobe and hence a large volume of space in which the field intensity is fairly constant. At the same time, the reflecting area should be smooth, preferably water. Fig. 15 is a plot of the distance to the

$\epsilon = 15$
 $\sigma = 0.01 \times 10^{-11} \text{ emu}$
 System loss: 0 db
 Transmitter power output: 9 watts
 f = frequency in megacycles
 d = distance in nautical miles
 Elevated antenna (aircraft)
 Located at first ground
 Reflection maximum (by fig. 6)
 E = signal at receiver input in μv

$\epsilon = 81$
 $\sigma = 4.6 \times 10^{-11} \text{ emu}$
 System loss: 0 db
 Transmitter power output: 9 watts
 f = Frequency in megacycles
 d = Distance in nautical miles
 Elevated antenna (aircraft)
 Located at first ground
 Reflection maximum (by fig. 6)
 E = signal at receiver input in μv
 h = height of ground antenna in feet

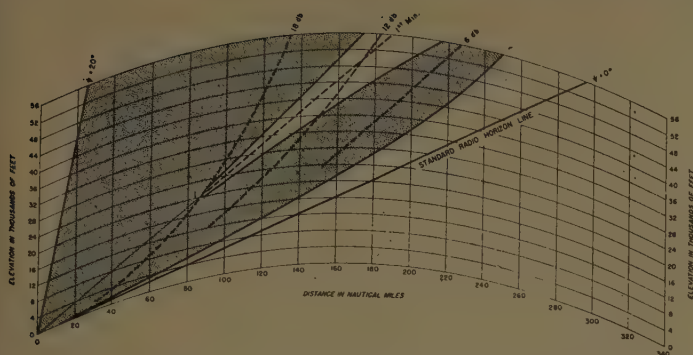


Fig. 14—Theoretical radiation pattern for ground-to-air propagation over smooth salt water; $4/3$ earth radius used to correct for standard atmosphere refraction.

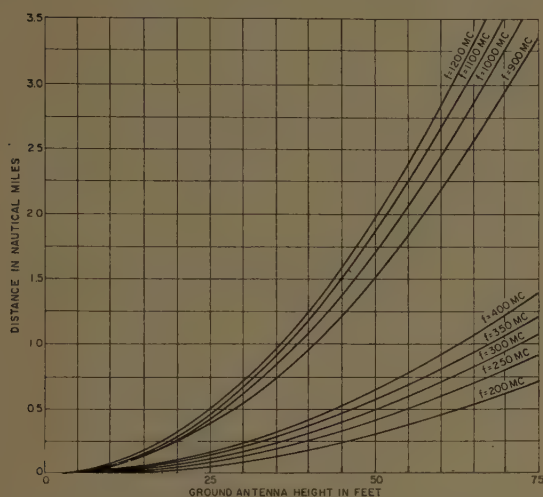


Fig. 15—Distance to reflecting point for first interference maximum.

reflecting point for the first interference maximum for various ground antenna heights.

The simple instrumentation employed for L -band measurements is shown in Fig. 16. Transmission is from the aircraft. The aircraft's own TACAN transmitter is employed after a temporary modification to prevent double pulsing and to increase the pulse repetition frequency. A power-monitoring device completes the airborne instrumentation. The receiving antennas presently employed at the ground station are pyramidal horns with 20 db gain over an isotropic radiator. They are installed 12 feet above mean sea level with a reflecting zone in the Chesapeake Bay. The receiver is calibrated under the same conditions of pulse width and pulse repetition frequency as employed in the test.

PROCEDURE

An initial radial run at the altitude indicated by Fig. 6, from over the ground station to slightly beyond the reference point, will readily confirm that the maximum is at the point, predicted by the figure, closer in or further out. A discrepancy may be corrected by instructing the

Frequency: 1186 mc
Polarization: vertical
Ground antenna height: 15 feet
Ground antenna: 7-element array dished up 5° electrically, 6 db gain over a dipole
Airplane antenna: half-wave dipole
Transmitter power: 5 kw
Receiver sensitivity: -85 dbm
System loss: 18 db

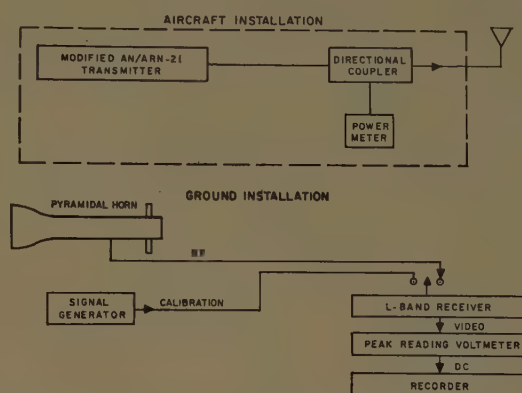


Fig. 16—Block diagram, aircraft and ground instrumentation.

pilot to increase or decrease his altitude. A 24-heading cloverleaf flight pattern is employed for the actual test, radiating for a few seconds as the reference point is passed with the airplane in "normal cruise" attitude. The resulting 24 data points may then be referred to the isotropic antenna level determined from Fig. 12 or 13 and plotted directly on the horizontal azimuth model pattern. The above procedures are covered in greater detail in an NATC report.¹²

RESULTS

Fig. 17 is the record of a flight test shown superimposed on the corresponding model pattern in the azimuth plane. The ordinate indicates the cumulative percentage of measurements exceeding the levels shown on the abscissa. The average correlation between model and flight data has been acceptable. Fig. 18 shows the average of model measurements and flight measurements of six recent aircraft types referred to an isotropic antenna and plotted on the same graph.

¹² G. W. Leopard and W. S. Bartels, "Naval Air Test Center Methods for Flight Evaluation of Aircraft Antennas," NATC, Patuxent River, Md., Final Rept. Project PTR AV 44009; October, 1958.

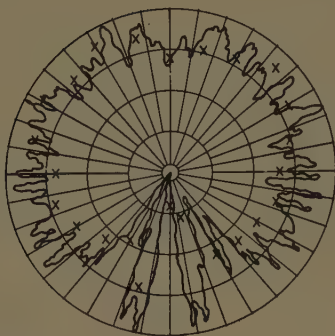


Fig. 17—Comparison of flight test results and model pattern. Flight data: X; frequency: 1070 mc; isotropic level=3.2 scale divisions.

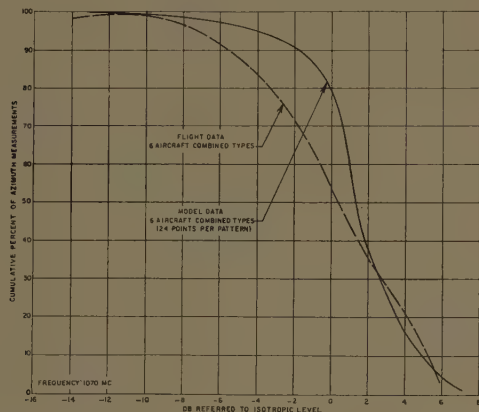


Fig. 18—Comparison of flight and model data at same points.

Though not directly related to the evaluation procedure, Figs. 19 and 20 are included to illustrate the effect of aircraft type on antenna efficiency, and the relative efficiencies of the three principal types of antennas. It should be remembered in studying the graphs that most of the annular slot and tailcap antennas are on jet aircraft. The stub antennas predominate on the less speedy propeller and helicopter types.

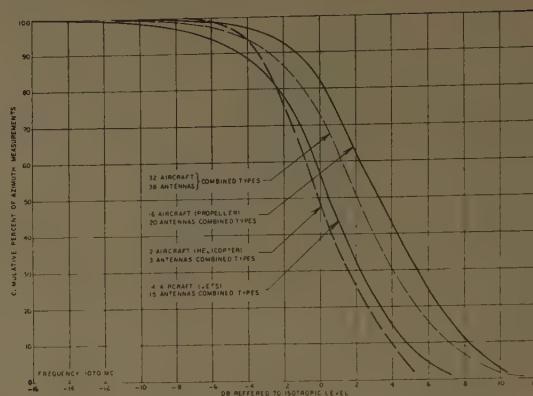


Fig. 19—Comparison of antenna flight test results on different aircraft types.

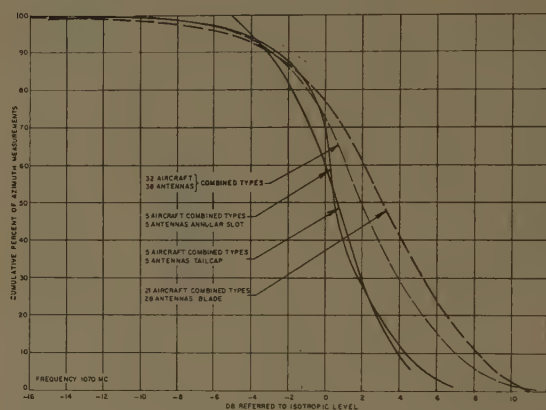


Fig. 20—Comparison of flight tests of various types of antennas installed on aircraft.

ACKNOWLEDGMENT

The paper is based on work performed by a number of engineers at Naval Air Test Center over a period of years. Special acknowledgment is due W. S. Bartels for his suggestions and criticism.

Reciprocity and Scattering by Certain Rough Surfaces*

W. S. AMENT†

Summary—Reciprocity theorems are developed for the average field specularly reflected, and the average power randomly scattered, to a point by a statistically described array of objects. A reciprocal quasivariational expression for the average power is developed for use when the self-consistent method applies to calculating currents in the individual objects. This formula is applied to calculate differential scattering cross sections for two idealized arrays bounded by plane "rough surfaces." General conclusions, relating to reciprocity, power conservation, grazing behavior, etc., for rough surface scattering, are made and applied heuristically to show that grazing reflection and backscatter from the rough ocean should be independent of polarization.

INTRODUCTION

THE rough surface scattering problem is one of determining statistical averages of fields and powers scattered by objects having various statistically defined configurations in an array bounded geometrically by the "rough surface." The problem is particularly difficult because, in general, no solution is at hand for any of the possible configurations. One therefore derives, by approximate methods, the fields to be averaged, and uses general physical principles both for aid in the derivations and for judging the merits of final results.

Electromagnetic reciprocity is one principle which can be applied usefully to the problem. Toward this end we first derive exact reciprocity theorems for averages of fields and for the mean-square fluctuation of fields scattered by statistically described arrays containing no nonreciprocal elements.

The conventional self-consistent method is described, in which one first calculates the average illuminating field, the resulting average radiating current for each object, and the specularly reflected field of the array as a whole.

We then derive a reciprocity theorem of the following import: A unit point source current J at p induces the self-consistently computed currents j in a fixed object O of the array. The currents j then act as a new source and radiate a self-consistently calculated partial field e to a point p' outside the object. A unit current J' at p' similarly causes self-consistently computed currents j' in O , which reradiate the self-consistently computed partial field e' at p . The reciprocity theorem is that $J \cdot e' = J' \cdot e$.

As it is generally difficult to calculate e from the j self-consistently, an equivalent calculation is given as an integral, over the surface of O , of the product of j and the average illuminating field due to J' . As j may be only an approximate solution of the basic self-consistent problem, the above reciprocity theorem may not be

satisfied by the e, e' thus computed. Reciprocity is retrieved by forming the analog of Schwinger's variational expression among the approximate currents in, and illuminating fields on, the fixed object O .

For O fixed and for source J fixed at p , the exact partial field e at p' would vary with varying configurations of the other objects of the array. The quasivariational expression gives an e in definite phase relation with J and therefore represents an approximation, especially when the e from each object is added powerwise to determine scattered power at p' . But this expression yields a properly reciprocal formula for randomly scattered power which takes some account of the fact that not only the fields illuminating O , but also the fields reradiated by O , have been affected by all other objects.

A standard "vacuum" calculation has been to compute j in O self-consistently, thus taking account of effects of other objects; then to compute the reradiation of j as if O were in a vacuum. Randomly scattered power, plus power in the specularly reflected wave, should equal incident power; this conservation of power is indicated to hold for a correct vacuum calculation but reciprocity is generally violated, as are considerations arising from the second law of thermodynamics in certain geometries.¹ The second law appears always satisfied for the "reciprocal" calculation developed in this paper. When the statistical array is bounded on the average by a horizontal plane "rough surface" such as the mean-sea-level plane, and when near grazing incident and scatter directions are considered, the reciprocal calculation should be particularly good, because in this case the reradiated fields are, by the geometry, most affected by other objects, and the power unaccounted for in the formal result is scattered mainly at steeper angles.

These general conclusions are brought out in discussions of the application of the reciprocal calculation to two model rough surfaces. The ideas are then applied heuristically to a wavy surface, such as the rough ocean, to deduce that specular reflection and backscatter should be independent of polarization at near grazing incidence.

STATISTICAL RECIPROCITY THEOREMS

We consider a set of objects O_i variously arranged in a domain D fixed in space. Let $J_1(p), J_2(p)$ be current sources of monochromatic electromagnetic waves propagating according to $\exp(-i\omega t)$ from the regions S_1, S_2

* Manuscript received by the PGAP, June 18, 1959. This paper was prepared at the Naval Research Laboratory.

† Office of Naval Research, 429 Oxford St., London W1, Eng.

¹ W. S. Ament, "Forward- and back-scattering from certain rough surfaces," IRE TRANSACTIONS ON ANTENNAS AND PROPAGATION, vol. AP-4, pp. 369-373; July, 1956.

outside D . If the electromagnetic properties of space and of each object are described by scalar permeabilities μ and dielectric constants ϵ effective at ω , the well-known reciprocity relation

$$\int_{S_1} J_1(\mathbf{p}) \cdot \mathbf{E}_{2,\text{tot}}(\mathbf{p}) d\mathbf{p} \equiv \int_{S_1} \mathbf{J} \cdot \mathbf{E}_{2,\text{tot}} \\ = \int_{S_2} J_2 \cdot \mathbf{E}_{1,\text{tot}} \quad (1)$$

holds, where $\mathbf{E}_{1,\text{tot}}(\mathbf{p})$ is the total electric field caused at \mathbf{p} by the radiations from the currents J_1 in S_1 , etc. Now $\mathbf{E}_{\text{tot}} = \mathbf{E}_0 + \mathbf{E}$, where \mathbf{E}_0 is the field in the absence of all objects in D , and \mathbf{E} is the net field scattered by the objects in their particular arrangement in D . Clearly

$$\int_{S_1} J_1 \cdot \mathbf{E}_{2,0} = \int_{S_2} J_2 \cdot \mathbf{E}_{1,0} \quad (2)$$

so that

$$\int_{S_1} J_1 \cdot \mathbf{E}_2 = \int_{S_2} J_2 \cdot \mathbf{E}_1. \quad (3)$$

Let $\langle Q \rangle_D$ denote the average, over-all arrangements of the objects in D , of the general quantity Q . Since (3) holds for each arrangement, we have

$$\left\langle \int_{S_1} J_1 \cdot \mathbf{E}_2 \right\rangle_D = \int_{S_1} J_1 \cdot \langle \mathbf{E}_2 \rangle_D = \int_{S_2} J_2 \cdot \langle \mathbf{E}_1 \rangle_D; \quad (4)$$

the average coherent scattering by the scattering body D satisfies the reciprocity principle.

Furthermore, if, for a particular arrangement, $\mathbf{E} = \langle \mathbf{E} \rangle_D + \mathbf{E}'$, then $\langle \mathbf{E}' \rangle_D = 0$. Eqs. (3) and (4) lead to

$$\int_{S_1} J_1 \cdot \mathbf{E}_2' = \int_{S_2} J_2 \cdot \mathbf{E}_1',$$

whence

$$\left\langle \left| \int_{S_1} J_1 \cdot \mathbf{E}_2' \right|^2 \right\rangle_D = \left\langle \left| \int_{S_2} J_2 \cdot \mathbf{E}_1' \right|^2 \right\rangle_D. \quad (5)$$

For unit dipole sources, we let

$$J_1(\mathbf{p}) = \hat{V}_1 \delta(\mathbf{p}_1, \mathbf{p}), \quad J_2(\mathbf{p}) = \hat{V}_2 \delta(\mathbf{p}_2, \mathbf{p}),$$

and (5) becomes

$$\langle |\hat{V}_1 \cdot \mathbf{E}_2'|^2 \rangle_D = \langle |\hat{V}_2 \cdot \mathbf{E}_1'|^2 \rangle, \quad (6)$$

whereas (4) becomes $\hat{V}_1 \cdot \langle \mathbf{E}_2 \rangle_D = \hat{V}_2 \cdot \langle \mathbf{E}_1 \rangle_D$.

Eq. (6) is a reciprocity relation for the average of the square of one component of the incoherent portion \mathbf{E}' of the scattered field. Under suitable restrictions (5) and (6) may be converted into reciprocity theorems for the incoherent scattered power flux.

For each arrangement of the O_i in D , the field \mathbf{E}_{tot} is a solution of Maxwell's equations appropriate to the given source current $\mathbf{J}(\mathbf{p})$. Solutions for particular arrangements are practically unobtainable, and generally of lesser importance than "average" solutions such as $\langle \mathbf{E} \rangle_D$, $\langle |\mathbf{E}'|^2 \rangle_D$. We are thus led to formulate the scat-

tering problem in terms of average quantities, making the following "self-consistent" assumptions: Temporarily fixing the position and orientation of a typical object O in D , we determine a subdomain d of D such that O is interior to d and the remaining objects are interior to $D-d$. We then remove O and (assuming the original source currents J_1 in S_1) calculate, in principle, the resulting average field $\mathbf{e}_1(\mathbf{q}) \equiv \langle \mathbf{E}_{1,\text{tot}}(\mathbf{q}) \rangle_{D-d}$ at a general point \mathbf{q} in d . We then replace O in d , and assume that $\mathbf{e}_1(\mathbf{q})$ forms the total field incident at \mathbf{q} in O . (We know that the fields scattered by O form part of the excitations of objects in $D-d$ and that these objects consequently rescatter fields adding up to say $\mathbf{e}_1''(\mathbf{q})$. Strongly expressed, our assumption is that

$$\langle |\mathbf{e}_1''|^2 \rangle_{D-d}^{1/2} \geq \langle \mathbf{e}_1'' \rangle_{D-d}$$

is negligible compared with $|\mathbf{e}_1(\mathbf{q})|$ throughout d . We shall also assume that $\Delta \mathbf{e}_1 = \mathbf{E}_{1,\text{tot}} - \mathbf{e}_1$ has negligible effect on averages to be computed, compared with the effect of $\langle \mathbf{e}_1 \rangle$.)

We now discuss the reciprocity aspects of fields and currents obtained as solutions of the self-consistently formulated scattering problem. For clarity, the objects will be considered perfectly conducting. Here the incident field \mathbf{e}_1 at a point \mathbf{q} in the surface O' of O induces an (average) surface current density $j_1(\mathbf{q})$ which satisfies the familiar integral equation

$$\mathbf{e}_{1t}(\mathbf{q}) + \int_{O'} j_1(\mathbf{q}') \cdot \mathbf{K}(\mathbf{q}', \mathbf{q}) d\mathbf{q}' = 0, \quad (7)$$

where $\mathbf{e}_{1t}(\mathbf{q})$ is the component of $\mathbf{e}_1(\mathbf{q})$ tangent to O' at \mathbf{q} , and $\mathbf{K}(\mathbf{q}, \mathbf{q}') = \mathbf{K}(\mathbf{q}', \mathbf{q})$ is the dyadic Green's function (for the empty space conditions assumed when $\mathbf{e}_1''(\mathbf{q})$ is neglected). Let the former source distribution J_2 be present in S_2 outside D , and cause, at O , the incident field $\mathbf{e}_2(\mathbf{q}) = \langle \mathbf{E}_{2,\text{tot}}(\mathbf{q}) \rangle_{D-d}$ and surface currents j_2 which satisfy, with \mathbf{e}_2 , the integral equation (7). We may then regard j_2 as the source of a field \mathbf{e}_2' with electric vector \mathbf{F}_2 . By (4) we now have

$$A_{1,2} \equiv \int_{S_2} J_2 \cdot \langle \mathbf{F}_1 \rangle_{D-d} = \int_{O'} j_1 \cdot \langle \mathbf{E}_{2,\text{tot}} \rangle_{D-d} = \int_{O'} j_1 \cdot \mathbf{e}_{2t},$$

the last equality following from the perfect conductivity of O . Forming the analogous relation among J_1 , j_2 , and using (7), we get

$$A_{2,1} \equiv \int_{S_1} J_1 \cdot \langle \mathbf{F}_2 \rangle_{D-d} = \int_{O'} j_2 \cdot \mathbf{e}_{1t} \\ = - \int_{O'} \int_{O'} j_1(\mathbf{q}') \cdot \mathbf{K}(\mathbf{q}', \mathbf{q}) \cdot j_2(\mathbf{q}) \\ = \int_{O'} j_1 \cdot \mathbf{e}_{2t} = A_{1,2} \equiv A. \quad (8)$$

This is then a reciprocity relation among the self-consistently calculated coherent fields scattered by a particular object O in D . It is not easy, however, to arrive at a useful analog of (5) for the incoherent part of the fields scattered by O because both the currents in

O as well as the field scattered by the average current in O should vary under rearrangements of the objects in $D-d$.

Now let us assume that \mathbf{e}_1 and \mathbf{e}_2 are known, but that for the corresponding solutions j_1, j_2 of (7), we have available only the approximations j_1^*, j_2^* . It may then occur that

$$A_{2,1}^* \equiv \int_{O'} j_2^* \cdot \mathbf{e}_1 \neq \int_{O'} j_1^* \cdot \mathbf{e}_2 \equiv A_{1,2}^*, \quad (9)$$

so that the two approximations to A are not the same. Reciprocity is retrieved by

$$A^* = -A_{1,2}^* A_{2,1}^* \div \left\{ \int_{O'} \int_{O'} j_1^*(\mathbf{q}) \cdot \mathbf{K}(\mathbf{q}, \mathbf{q}') j_2^*(\mathbf{q}') \right\}. \quad (10)$$

Furthermore the results are stationary for small variations of j_1^*, j_2^* about the self-consistently correct j_1, j_2 . Practically, A^* may not be closer to A than $A_{1,2}^*$ or $A_{2,1}^*$, for currents in the objects in $D-d$ are likely to be in error with consequent error in the $\mathbf{e}_{1i}, \mathbf{e}_{2i}$ available for a practical calculation. Note that, with O fixed, the A 's have a definite phase relation with the original sources; hence, A represents a coherent contribution to the scatter from the objects O_i in D . For fixed O , moving O_j in $D-d$, the scatter from J_1 via O into S_2 has a fluctuating component not accounted for here.

For each particular arrangement of the objects in $D-d$, one can in principle form the symmetric dyadic Green's function $\mathbf{K}(\mathbf{r}, \mathbf{r}')$ for points \mathbf{r}, \mathbf{r}' not in or on the objects of $D-d$, with \mathbf{K} satisfying the boundary conditions at the surface of each of those objects. Then, for the particular partial fields $\mathbf{e}_1, \mathbf{e}_2$ scattered by O , we can use the particular $\mathbf{K}(\mathbf{r}, \mathbf{r}')$ in Schwinger's variational expression to show the reciprocal relation $J_1 \cdot \mathbf{e}_2 = J_2 \cdot \mathbf{e}_1$. Averaging over the arrangement of objects in $D-d$ we then arrive at $\langle J_1 \cdot \mathbf{e}_2 \rangle = \langle \mathbf{e}_1 \cdot J_2 \rangle$ as an exact result, independent of the self-consistent approach. For a practical computation one has neither the particular fields illuminating O nor the particular $\mathbf{K}(\mathbf{r}, \mathbf{r}')$; we have used the self-consistently computed average illuminating fields and the free-space Green's function in (10).

ROUGH SURFACE REFLECTION AND BACKSCATTER

We let the domain D be the $y > 0$ half-space, and let the source region S_1 be removed to a great distance r along the line $x = r \cos \theta, y = -r \sin \theta$, where $0 < \theta < \pi$. (θ is called the grazing angle.) Then, in the neighborhood of $(0, 0, 0)$ the incident wave E_{01} is approximately plane, and propagates according to $\exp(ikx \sin \theta + iky \cos \theta) = \exp(i\alpha x + i\rho y)$, where, with $\text{Im}(k) > 0, \rho \equiv \sqrt{k^2 - \alpha^2}$ satisfies $\text{Im}(\rho) \geq 0$. Then, near $(0, 0, 0)$, the average coherent wave $\langle E_1 \rangle_D$, scattered by the objects in D , is an approximately plane wave propagating according to $R \exp(i\alpha x - i\rho y)$. Here $R \equiv \{ \langle E_1 \rangle_D / E_{01} \} |_{(0,0,0)}$ will generally depend on θ and the polarization \hat{P} of E_{01} ,

R is called the reflection coefficient of the rough plane surface D' which bounds D . (Here D' and $y=0$ are identical.)

With the second source region S_2 inserted in $y < 0$ at great distance r' along a direction specified by θ', ϕ' (i.e., along $x = -r' \cos \theta' \cos \phi', y = -r' \sin \theta', z = -r' \cos \theta' \sin \phi'$), we calculate the average coherent scattered field A of (8) for an object O_i in D near $(0, 0, y_i)$. Here A will depend on the polarizations of E_{01}, E_{02} , the direction angles θ, θ', ϕ' , and on r, r', y_i, J_1, J_2 . By means of suitable limiting and averaging processes we may eliminate these latter parameters to obtain a dimensionless differential scattering cross section σ of a unit area of the surface:

$$\sigma \frac{dxdz}{4\pi} = \frac{[\text{Average power sum of fields with polarization parallel to } J_2, \text{ scattered in the direction } \theta', \phi' \text{ by all objects in the semi-infinite column of cross section } dxdz \text{ centered on } (0, 0, y)]}{[\text{Power flux, } P_0, \text{ of the polarized wave } E_{01} \text{ at } (0, 0, 0)]}. \quad (11)$$

[Here the calculation may be performed in terms of the coherent A of (8), giving scattered powers too small by the previously mentioned fluctuating term.]

For strictly two-dimensional problems, we may similarly define a (dimensionless) differential scattering coefficient σ_L for a unit length of the one-dimensional surface $y=0$ by replacing the left-hand side of (11) with $\sigma_L dx / (2\pi)$ and eliminating dz and ϕ' in the right-hand side. The denominator 4π in (11) is chosen so that if the element $dxdz$ scatters the power $P_0 dxdz$ isotropically, and the whole resultant flux at S_2 is polarized parallel to J_2 , then $\sigma = 1$; the choice of 2π in the definition of σ_L is made for analogous reasons.

Example I

For examples of the application of the general methods of obtaining R and σ or σ_L given above, we consider two rather artificial rough surfaces. In the first surface, the objects O_i are perfectly conducting half planes (plates) parallel to $x = u \sin \beta, y = u \cos \beta$, with edges in $y=0$. Averages, such as $\langle \rangle_D$, will be taken over arrangements of edges in the x axis; the edges are arranged randomly except that the average number of edges per unit length is N .

For horizontally polarized incident waves ($E \parallel$ all edges) we have a scalar diffraction problem. We let a unit line current $J_1(x, y) = J_1(\mathbf{p})$ be related to the resultant field $E_{01}(x', y') = E_{01}(\mathbf{p}')$ through

$$\begin{aligned} E_{01}(\mathbf{p}') &= J_1(\mathbf{p}') G(\mathbf{p}', \mathbf{p}) \equiv J_1(\mathbf{p}') G(\mathbf{p}, \mathbf{p}') \\ &= J_1(\mathbf{p}) \frac{i}{4} H_0^{(1)}(kr) \\ &\sim J_1(\mathbf{p}) (-i8\pi k r)^{-1/2} e^{ikr}, \quad |kr| \gg 1, \end{aligned} \quad (12)$$

where

$$r = |\mathbf{p} - \mathbf{p}'| = [(x - x')^2 + (y - y')^2]^{1/2}.$$

Thus when J_1 is now removed to a sufficient distance in the θ direction it produces the approximate plane wave $E_0 \exp(i\alpha x + i\mu y)$ incident on all edges near $x=0$. We assume that the resulting average current j_1 in the plate with edge at x' near $x=0$ varies with u , the distance along the plate from the edge, according to $j_1(u) = j_1 \exp[i(\alpha s + \mu c)u]$, where $c = \cos \beta$, $s = \sin \beta$, and where j_1 and μ are to be determined. The domain d , in which lies the typical plate O_0 with edge at $x=0$, is bounded by $y=0$ and by parallel planes at small distance ϵ from O_0 .

The field $e_1(u)$, incident at \mathbf{p} on O_0 at distance u from the edge is given by

$$e_1(u) = E_0 e^{i(\alpha s + \mu c)u} + \left\langle j_1 \sum_i \left[\int_0^\infty e^{i(\alpha s + \mu c)u_i} G(\mathbf{p}_i, \mathbf{p}) du_i e^{i\alpha x_i} \right] \right\rangle_{D-d}.$$

Replacing

$$\left\langle \sum_i [\] \right\rangle_{D-d} \quad \text{with} \quad \left\{ \int_{-\infty}^{-\epsilon} + \int_{\epsilon}^{\infty} N[\] dx_i \right\},$$

we find that, when $\epsilon \rightarrow 0$,

$$e_1(u) = E_0 e^{i(\alpha s + \mu c)u} - \frac{j_1 N e^{i(\alpha s + \mu c)u}}{c(k^2 - \alpha^2 - \mu^2)} + \frac{j_1 N e^{i(\alpha s + \mu c)u}}{2c\rho(\rho - \mu)}. \quad (13)$$

Toward determining j_1 and μ , we demand that the portion of e_1 with an $e^{i\mu y}$ dependence vanish; the absence of any vestige of the incident field at great depths in $y > 0$ is physically required by the shadowing effects of the plates. Hence $Nj_1/c = -2\rho(\rho - \mu)E_0$. We further require, on physical grounds, that at great u , the relation between the current $j_1(u)$ assumed in O_0 and the incident field $e_1(u)$ be the same as that for an infinite perfectly conducting plane. That is, (7) implies

$$e_1(u) = - \int_0^\infty \{ j_1 e^{i(\alpha s + \mu c)u'} G(u', u) \} du';$$

for $|ku| \gg 1$, this becomes

$$e_1(u) \simeq \frac{-j_1 i e^{i(\alpha s + \mu c)u}}{2\{k^2 - (\alpha s + \mu c)^2\}^{1/2}}. \quad (14)$$

Thus, from (13),

$$e_1 = \frac{-ij_1}{2\{k^2 - (\alpha s + \mu c)^2\}} = \frac{-Nj_1/c}{k^2 - \alpha^2 - \mu^2} = \frac{2\rho(\rho - \mu)E_0}{k^2 - \alpha^2 - \mu^2} = \frac{2\rho E_0}{\rho + \mu}. \quad (15)$$

It follows that μ is a properly selected root of

$$k^2 - \mu^2 - \alpha^2 + (2Ni/c)\{k^2 - (\alpha s + \mu c)^2\}^{1/2} = 0. \quad (16)$$

When $\alpha=0$, $s=0$, $c=1$, we have

$$\sqrt{k^2 - \mu^2} [\sqrt{k^2 - \mu^2} + 2Ni] = 0; \quad (17)$$

from the *last* factor we get $\mu = +\sqrt{k^2 + 4N^2}$ as the correct root in this limiting case.

To get R , we calculate, for \mathbf{p}' in $y < 0$, the average wave

$$\langle E_1(\mathbf{p}') \rangle_D = j_1 \left\langle \sum_i \int_0^\infty e^{i(\alpha s + \mu c)u_i} G(\mathbf{p}', \mathbf{p}_i) du_i e^{i\alpha x_i} \right\rangle$$

as an integral. Hence

$$\langle E_1 \rangle = RE_0 e^{i(\alpha x - \rho y)} = \frac{-Nj_1 e^{i(\alpha x - \rho y)}}{2c\rho(\rho + \mu)};$$

and from (15),

$$R = \frac{\rho - \mu}{\rho + \mu} \equiv R_{11}.$$

We see that if D is regarded as a homogeneous medium, and $e_1(u) = TE_0$ is the average field in the medium, $1+R=T$ and $\rho(1-R)=\mu T$. Thus D is a medium with the propagation constant $k' = [\alpha^2 + \mu^2]^{1/2}$, and the boundary conditions at the $y=0$ interface are continuity of field and its normal derivative.

Calculating the coherent scatter of O_0 to the distant line source J_2 in the r' direction we have

$$\begin{aligned} A_{1,2}^* &= J_2 \cdot e_{12} = \int_0^\infty j_1(u) \cdot e_2(u) du \\ &= \frac{-1}{(\) + (\ ')} \frac{2\rho'}{\rho' + \mu'} E_0' 2\{k^2 - (\)^2\} E_0 \frac{2}{\rho + \mu} \\ &= \frac{-8\rho\rho'}{(\rho' + \mu')(\rho + \mu)} \frac{E_0 E_0'}{(\) + (\ ')} \cdot \{k^2 - (\)^2\}^{1/2} \\ &\equiv B_{12}^* E_0 E_0'. \end{aligned} \quad (18)$$

[Here

$$(\) \equiv (\alpha s + \mu c), \quad (\ ') \equiv (\alpha' s + \mu' c).]$$

This is unsymmetric only in the last factor; setting $\alpha \rightarrow \alpha'$ and $\mu \rightarrow \mu'$ yields B_{21}^* . We form the symmetric estimate

$$\begin{aligned} A^* &= -A_{1,2}^* A_{2,1}^* \\ &\div j_1 j_2 \int_0^\infty \int_0^\infty e^{i(\)u} e^{i(\ ')u'} G(u, u') du du', \end{aligned}$$

obtaining

$$\begin{aligned} A^* &= \frac{-8\rho\rho'\{k^2 - (\)^2\}^{1/2}\{k^2 - (\ ')^2\}^{1/2} E_0 E_0'}{[\{k^2 - (\)^2\}^{1/2} + \{k^2 - (\ ')^2\}^{1/2}](\rho + \mu)(\rho' + \mu')[(\) + (\ ')]} \\ &\equiv B^* E_0 E_0'. \end{aligned} \quad (19)$$

Since $A^* \simeq J_1 \cdot e_{21} \simeq (-i8\pi k r)^{1/2} E_0 e_{21}$ we have, assuming random scattering from each plate,

$$\sigma_L(\theta', \theta) = 2\pi r N \left| \frac{e_{21}}{E_0} \right|^2 = \frac{N |B^*|^2}{4k}. \quad (20)$$

For vertical polarization, we assume a line source K of the magnetic field H_0 , which is polarized parallel to the edges. The problem is again scalar with the difference that the normal derivative of h (the magnetic field parallel to the edges) vanishes on each plate. We have

$$H_{01}(p') = K_1(p) G(p, p')$$

$$h_1(u) = H_0 e^{i(\alpha s + \rho c)u}$$

$$+ \left\langle \sum_i k_1 \int_0^\infty e^{i(\alpha s + \mu c)u_i} \frac{\partial G(p_i, p)}{\partial n_{pi}} du_i e^{i\alpha x_i} \right\rangle_{D-d},$$

$$\frac{\partial h_1(u)}{\partial n_u} = iH_0(\alpha c - \rho s) e^{i(\alpha s + \rho c)u} - \frac{N e^{i(\cdot)u} k_1 [k^2 - (\cdot)^2]}{c(k^2 - \alpha^2 - \mu^2)} + \frac{N k_1 (\alpha c - \rho s)^2 e^{i(\alpha s + \rho c)u}}{2c\rho(\rho - \mu)}.$$

Again assuming that the coefficient of $\exp [i(\alpha s + \rho c)u]$ vanishes, we have

$$H_0 = \frac{iN}{2c} k_1 \frac{(\alpha c - \rho s)}{\rho(\rho - \mu)}.$$

When k_1 is such that $\partial(h_1 + h_i)/\partial n_u$ vanishes at large u on the i th plate, we have

$$- \frac{1}{2} i k_1 [k^2 - (\cdot)^2]^{1/2} = \frac{-N k_1 [k^2 - (\cdot)^2]}{c(k^2 - \alpha^2 - \mu^2)},$$

whence

$$k^2 - \mu^2 - \alpha^2 + (2iN/c) \{k^2 - (\cdot)^2\}^{1/2} = 0,$$

which is identical with (16) as an equation for determining μ , and leads to

$$k_1 = \frac{-4\rho \{k^2 - (\cdot)^2\}^{1/2}}{(\rho + \mu)(\alpha c - \rho s)} H_0.$$

[For $\alpha=0, s=0, c=1, \mu \simeq k$ here as specified by the first factor of (17).] In $y < 0$ we have

$$\langle H_1 \rangle = R H_0 e^{i(\alpha x - \rho y)} = \frac{iN k_1 \{k^2 - (\alpha s - \rho c)^2\}^{1/2} e^{i(\alpha x - \rho y)}}{2c\rho(\rho + \mu)},$$

or

$$R = \frac{\rho - \mu \cos(\theta - \beta)}{\rho + \mu \cos(\theta + \beta)} \equiv R_\perp. \quad (21)$$

For single plate scattering, the present version of (9) is

$$K_1 h_{21} = \int_0^\infty du \frac{\partial h_1}{\partial n_u} k_2(u) - \int_0^\infty \int_0^\infty du du' k_1(u) \frac{\partial^2 G(u, u')}{\partial n_u \partial n_{u'}} k_2(u') = \int_0^\infty du \frac{\partial h_2}{\partial n_u} k_1(u) = K_2 h_{12}.$$

Now

$$A_{21}^* = \int_0^\infty du \frac{\partial h_1}{\partial n_u} k_2(u) = \frac{\frac{1}{2} k_1 k_2 \{k^2 - (\cdot)^2\}^{1/2}}{(\cdot) + (\cdot)'},$$

or

$$A_{21}^* = \frac{8\rho\rho'}{(\rho + \mu)(\rho' + \mu')} \cdot \frac{\{[k^2 - (\cdot)^2][k^2 - (\cdot)']^2\}}{(\alpha c - \rho s)(\alpha' c - \rho' s)} \cdot \frac{H_0 H_0'}{(\cdot) + (\cdot)'} \cdot \{k^2 - (\cdot)^2\}^{1/2}.$$

$A_{12}^* \neq A_{12}^*$ is obtained by putting primes in the last factor. In forming A^* we must evaluate

$$\int_0^\infty \int_0^\infty k_1(u) k_2(u') \frac{\partial^2 G}{\partial n_u \partial n_{u'}} du du' = \frac{-\frac{1}{2} k_1 k_2 [\{k_1^2 - (\cdot)^2\}^{1/2} + \{k^2 - (\cdot)'\}^{1/2}]}{(\cdot) + (\cdot)'} = \frac{-8\rho\rho' \{[k^2 - (\cdot)^2][k' - (\cdot)']^2\}^{1/2}}{(\rho + \mu)(\rho' + \mu')(\alpha c - \rho s)(\alpha' c - \rho' s)} \cdot \frac{\{k^2 - (\cdot)^2\}^{1/2} + \{k^2 - (\cdot)'\}^{1/2}}{(\cdot) + (\cdot)'} \cdot H_0 H_0'.$$

Dividing this into $-A_{12}^* A_{12}^*$ we get

$$A^* = \frac{+8\rho\rho'}{(\rho + \mu)(\rho' + \mu')} \cdot \frac{[k^2 - (\cdot)^2][k^2 - (\cdot)']^2}{(\alpha c - \rho s)(\alpha' c - \rho' s)} \cdot \frac{H_0 H_0'}{[(\cdot) + (\cdot)'] [\{k^2 - (\cdot)^2\}^{1/2} + \{k^2 - (\cdot)'\}^{1/2}]} \equiv B_{12}^* H_0 H_0'. \quad (22)$$

By the argument leading to (20) we have

$$\sigma_L = N |B_{12}^*| / (4k).$$

One notes that the sign of (22) is opposite to that of (19). But A^* in (22) is a "scattering coefficient" for the magnetic vector which becomes one for the electric vector on change of sign.

Now we will let $Q = N/k$ be small, the plates be normal to $y=0$, and we will consider grazing incident and scattering angles θ, θ' . Thus $c=1, s=0, \rho \simeq k\theta, \rho' \simeq k\theta'$, and $\mu = k\sqrt{\theta^2 + 2iQ}$ for both polarizations. The result, for both cases, is (with $Z \equiv \theta/\sqrt{Q} \ll 1$)

$$\sigma_L = \sigma_L(\theta, \theta') = \frac{Z^2 Z'^2}{8}. \quad (23)$$

For backscatter, $\theta' = \theta$ and

$$\sigma_L = \sigma_L(\theta, \theta) = Z^4/8, \quad (24)$$

which is to be compared with a previously derived² $\sigma_L = Z^2$. In that derivation, no account of reciprocity was taken.

For somewhat less grazing conditions, we obtain³

$$\sigma = 4 \left| \frac{Z}{Z + \sqrt{Z^2 + 2i}} \right|^2 \left| \frac{Z'}{Z' + \sqrt{Z'^2 + 2i}} \right|^2 \left| \frac{1}{\sqrt{Z^2 + 2i} + \sqrt{Z'^2 + 2i}} \right|^2. \quad (25)$$

We also have

$$R = - \left\{ \frac{\sqrt{Z^2 + 2i} - Z}{\sqrt{Z^2 + 2i} + Z} \right\}$$

as before.² For

$$Z \rightarrow 0, \quad |R^2| = 1 - 4Z, \quad \text{but for } Z \gg 1, \quad |R^2| \sim Z^{-4}/4, \\ \sigma \sim \frac{1}{4} [Z^{1/2} + Z'^{1/2}]^{-2}.$$

It will be noted that for $\beta \neq 0$, $|R_\perp| \neq |R_\parallel|$; in fact, the replacement of the plate medium by a "homogeneous medium" breaks down for the case \perp . Furthermore, in both cases $R(\theta) \neq R(\pi - \theta)$ for $\beta \neq 0$, in violation of reciprocity. On the other hand R_\perp vanishes properly when either incident or reflected direction is parallel to the plates, *i.e.*, when $\cos(\theta + \beta)$ or $\cos(\theta - \beta) = 0$, respectively. $R_\perp = 0$ in the latter case is clear from (21); in the former we find that $\mu = \rho + 0(\cos^2(\beta + \theta))$ is the requisite solution of (16) for $(\beta + \theta) \simeq \pi/2$.

While one can force the equality of $R(\theta)$ with $R(\pi - \theta)$ in a number of ways, *e.g.*, by using for both $\frac{1}{2}[R(\theta) + R(\pi - \theta)]$ no natural method of a variational type seems at hand; we regard $R(\theta) \neq R(\pi - \theta)$ as a result of the approximate currents used here for convenience. (In particular, edge currents are neglected.) Previous analysis⁴ suggests that

$$|R|^2 = \sigma_L(\theta, \pi - \theta)N/(k \sin^2 \theta).$$

This is symmetric in $(\theta, \pi - \theta)$ when symmetric, single scatter estimates are used for σ_L . On the other hand, this $|R|^2$ is generally smaller than the previous forms, leaving even more power unaccounted for. In particular for $\beta = 0$, $\sigma_L(\theta, \pi - \theta) = \sigma_L(\theta, \theta) = k^2\theta^4/(8N^2)$ at grazing θ so that $|R^2|$ would be $k^2\theta^4/8N$ instead of ~ 1 as intuitively required.

Note that R_{11} and R_1 go to -1 for $\theta \rightarrow 0$, so that the major field components go to zero at $y = 0$. When $\beta = \pm \pi/2$ and $y = 0$ is perfectly conducting, $|\mu| = \infty$ and $R_{11} = -1$, $R_1 = +1$ for all θ as physically required.

In summary, for near grazing angles and for an average spacing of many wavelengths between plates, the

reflection coefficient and differential scattering cross section σ are independent of polarization. At extreme grazing, $\sigma(\theta, \theta')$ is of the symmetric form $f(\theta)f(\theta')$ and reflection is nearly perfect; at higher angles reflection is poor and the factorization $f(\theta)f(\theta')$ no longer applies. The differential cross section for backscatter varies as θ^4 in the grazing limit. This "surface" is never smooth by the Rayleigh criterion.

Example II

We suppose that space is described by a lossless propagation constant k , and that an average unit volume in $z < 0$ contains N point scatterers, each described by the scattering coefficient A . Thus a scalar wave ϕ satisfies

$$(\nabla^2 + k^2)\phi = 0 \quad (26)$$

at every particle-free and source-free point. If ϕ_0 is an incident wave, with prescribed source at \mathbf{r}_0 in $z > 0$, satisfying (26) and the usual radiation conditions elsewhere, the total field at a particle-free point $\mathbf{r} \neq \mathbf{r}_0$, or incident on a point occupied by a particle, is given by

$$\phi(\mathbf{r}) = \phi_0(\mathbf{r}) + A \sum_n \phi(\mathbf{r}_n)G(|\mathbf{r}_n - \mathbf{r}|), \quad (27)$$

where $G(\mathbf{r}) = e^{ikr}/(4\pi r)$, \mathbf{r}_n is the position vector of the n th particle in $z < 0$, and the summation runs over all particles. The configurational average $\langle \phi \rangle$ is that obtained when each particle independently traverses all points in $z < 0$. Invoking the self-consistent assumption, we then have

$$\langle \phi(\mathbf{r}) \rangle = \phi_0(\mathbf{r}) + NA \int_{-\infty}^0 \int_{-\infty}^{\infty} \int_{-\infty}^{\infty} \langle \phi(\mathbf{r}') \rangle \cdot G(|\mathbf{r}' - \mathbf{r}|) dx' dy' dz'. \quad (28)$$

By assuming $\langle \phi \rangle$ to be a down-going plane wave in $z < 0$, the integrals are readily calculated and ϕ determined everywhere. It is more instructive, however, to apply $(\nabla^2 + k^2)$ to both sides of (28), which yields $(\nabla^2 + k'^2)\langle \phi \rangle = 0$ in $z < 0$, where $k'^2 = k^2 + NA$. The appropriate boundary conditions at the "boundary" $z = 0$ are that $\langle \phi \rangle$ and $\partial \langle \phi \rangle / \partial z$ be continuous. For the plane incident wave $\phi_0 = \exp(ikx \cos \alpha_1 - ikz \sin \alpha_1)$, we then have, with $\sqrt{(1)} \equiv [k'^2 - k^2 \cos^2 \alpha_1]^{1/2}$

$$\langle \phi \rangle = \begin{cases} e^{ikx \cos \alpha_1} (e^{-ikz \sin \alpha_1} + R e^{ikz \sin \alpha_1}), & z > 0 \\ \{ \quad \quad \quad \} T \exp(-iz\sqrt{(1)}), & z < 0 \end{cases} \quad (29)$$

where

$$R = \frac{k \sin \alpha_1 - \sqrt{(1)}}{[\sqrt{(1)} + k \sin \alpha_1]}; \quad T \equiv T(\alpha_1) = \frac{2k \sin \alpha_1}{[\quad]}.$$

The wave (29) is the self-consistently calculated excitation of a particle at depth z , which we wish to use to estimate the differential scattering cross section $\sigma(\theta_1, \theta_2)$ per unit area of $z = 0$. [See (11).] For excitation of unit amplitude and power P_0 , a particle scatters the power $|A|^2 P_0 / (4\pi)^2$ per unit solid angle, isotropically.

² *Ibid.*, see (5) on p. 370.

³ *Ibid.*, see (12) on p. 373.

⁴ *Ibid.*, see (4) on p. 370, in which for $f(0, 0)$ read $f(\theta, \theta)$ and for $\sin \theta$ read $\sin^2 \theta$.

Thus, the power per steradian scattered by a particle at depth z in any direction is $|TA|^2 P_0 / (4\pi)^2$. If this power emerges into $z > 0$, we find (on the assumption that the scattered fields in an θ_2 direction are incoherent) that the total flux per unit area of the surface, scattered in the θ_2 direction, is

$$P_0 \sigma(\theta_1, \theta_2) = \{NP_0 |TA|^2 / (4\pi)^2\} \int_0^\infty \exp[-2z \operatorname{Im} \sqrt{(1)}] dz, \\ \text{or } \sigma(\theta_1, \theta_2) = N |AT(\theta_1)|^2 / [32\pi^2 \operatorname{Im} \sqrt{(1)}] \equiv \bar{\sigma}_1. \quad (30)$$

The result, being independent of θ_2 , clearly does not satisfy the (readily-proved) scalar version of the statistical reciprocity theorem (6). Furthermore, it predicts finite power scattered tangentially to the surface, in violation of the second law of thermodynamics.⁵ Qualitatively, these faults are rooted in the implicit assumption that the waves scattered by the particle in $z < 0$ travel rectilinearly, not being scattered by the other particles and uninfluenced by the fact that $z < 0$ acts in part as a homogeneous medium described by k' .

As an improvement, we apply the reciprocity theorem (8) in an obvious way: the particle would produce a field of amplitude

$$T(\theta_1)T(\theta_2)A \exp[-z \operatorname{Im} \{\sqrt{(1)} + \sqrt{(2)}\}]$$

at the source of a plane wave arriving from the θ_2 direction and having complex amplitude 1 at the origin. Again assuming the particles to scatter incoherently, we obtain

$$\sigma(\theta_1, \theta_2) = \frac{N |T(\theta_1)T(\theta_2)A|^2}{32\pi^2 \operatorname{Im} \{\sqrt{(1)} + \sqrt{(2)}\}}. \quad (31)$$

Here the reciprocity is obvious, and one readily finds that $T \rightarrow 0$ sufficiently rapidly in the grazing limit to meet the requirements of the second law.

We now examine the results (30), (31) from the point of view of energy conservation, making the simplifying assumption that nowhere is wave energy converted into heat. Here examination of the power incident on and scattered by a single lossless particle leads to the result

$$\operatorname{Im}(A) = k |A|^2 / (4\pi). \quad (32)$$

We have $\operatorname{Im}(k') = \operatorname{Im}[(k^2 + NA)^{1/2}]$; in the case of small NAk^{-2} this becomes

$$\operatorname{Im}(k') \simeq N |A|^2 / (8\pi),$$

whence

$$4\pi \bar{\sigma}_1 \simeq |T(\theta_1)|^2 \sin \alpha_1. \quad (33)$$

In this dilute limit, the power flux diminution per unit distance of travel of the coherent wave propagating according to k' is equal to the power incoherently scat-

tered by all the particles in an average unit volume, under the wave's excitation. For our obliquely incident wave, we have from (29), (33):

$$\sin \alpha_1 (1 - |R^2|) \simeq 4\pi \bar{\sigma}_1. \quad (34)$$

Thus the scattering cross section (30) accounts for all the power penetrating the surface if we include the power scattered in all directions and not merely that into $z > 0$.

In the limit $NA \rightarrow 0$, $T \rightarrow 1$ and $R \rightarrow 0$; the reciprocal form (31) now yields

$$\sigma(\theta_1, \theta_2) = \frac{\sin \alpha_1 \sin \alpha_2}{\sin \alpha_1 + \sin \alpha_2}. \quad (35)$$

This agrees with Chandrasekhar's⁶ "scattering function" S for the "once-scattered" contribution to the flux re-entering $z > 0$. Chandrasekhar's general solution⁷ (accounting for all orders of scattering) for the lossless case is

$$\sigma_{\text{total}}(\theta_1, \theta_2) = \frac{\sin \alpha_1 \sin \alpha_2}{\sin \alpha_1 + \sin \alpha_2} H(\sin \alpha_1) H(\sin \alpha_2), \quad (36)$$

where $H(x)$ increases monotonically from $H(0) = 1$ to $H(1) \simeq 3$. Because of the H functions, σ_{total} exceeds our σ significantly except for $\alpha_1 \ll 1$, $\alpha_2 \ll 1$, when $H \simeq 1$ and the results become identical. Physically, the inference is that most of the power, scattered out of the obliquely traveling wave near to $z = 0$, escapes at high angles leaving not much to escape, after multiple scattering, in the near grazing θ_1 direction. (Similarly, the "once-scattered" approximation is good at all angles in the case of lossy particles ($\operatorname{Im} A \simeq |A|$), because the energy absorbed at each scatter is so large; $H(\sin \alpha) \simeq 1$ in this case.)

HEURISTIC EXTENSIONS TO GRAZING CONDITIONS

The factor $1/(\sin \theta_1 + \sin \theta_2)$ of (35) and (36) (*Example II*) also appears in Chandrasekhar's σ 's for atmospheres of nonisotropic scatterers. This factor is believed to be caused by the lack of specular reflection in (35), (36) and Chandrasekhar's atmospheres. With reflection coefficients R approaching -1 at grazing, the analogous factors in (31) and in the previous large-scale parallel plate surface (*Example I*) approach constant values in the grazing limit, and the expressions for σ factor into $f(\theta_1)f(\theta_2)$. This factorization is believed to pertain to any large-scale rough surface producing a complete shadow, for the following heuristic reasons: The surface is specified partially by a scale height H and correlation length L , so that most of the surface lies within distance H of some horizontal mean plane, and the local structure is unaffected statistically by the particular surface struc-

⁶ S. Chandrasekhar, "Radiative Transfer," p. 146; for reciprocity considerations see p. 172 and elsewhere.

⁷ *Ibid.*, see also (120), p. 85.

⁵ *Ibid.*, see Appendix A on p. 372.

ture at horizontal distances greater than L . Then, subject to the material of the surface (taken as lossless here), specular reflection becomes good at grazing angles θ satisfying Rayleigh's criterion $|kH \sin \theta| \ll 1$. Further when $kL(1 - \cos \theta) \ll 1$, we may expect that the total illumination of a particular "patch" of surface, consisting of the direct wave and a wave traveling horizontally from surface elements on the source side of the patch, is reasonably constant except for a variation in amplitude proportional to θ . Then the currents J in the patch vary as θ . This is furthermore required for the reradiations from all J to cancel the incident wave below the surface. This cancellation is due to radiation from what may be thought of as a horizontal array of end-fire antennas confined in boxes of dimensions approximating $H \times L \times L$, with main beam parallel to the incident propagation vector. The direction of specular reflection lies at angle 2θ off the axis of this beam and therefore within the beam for small enough θ . Hence, the reflection coefficient approaches the coefficient for reradiation through the surface in the incident direction, or $R \rightarrow -1$, regardless of polarization. The currents J in a unit (horizontal) surface area then radiate a total power $P(\theta) \propto \theta^2$, with the shape of the power pattern being independent of θ since the current distribution varies in amplitude only. For energy conservation, we therefore have $P(\theta) = (1 - |R|^2) \sin \theta$ whence $R \simeq -1 + a\theta$, $\text{Re}(a) > 0$. (This last does not appear automatically in a calculation of R alone, and may possibly be of use in prescribing J .) In some direction θ' , the scattered energy density is $\theta'^2 F(\theta')$, in which azimuth and polarization are

implied. If θ' is also a near-grazing angle, scattering in the θ direction due to illumination from the θ' direction is similarly $\theta'^2 F(\theta)$, which, by reciprocity, must equal $\theta^2 F(\theta')$. It follows that $F(x) \sim Kx^2$ for small x and the differential scattering cross section, for grazing incident and scattering angles, goes as $K\theta^2\theta'^2$, where K incorporates polarization and azimuthal variables. In particular, the backscattering cross section goes as $K\theta^4$.

Now we argue plausibly that K is independent of polarization for fairly general surfaces not made sensitive to polarization by Faraday screen construction. It is easy to visualize the current distributions J as being independent of polarization except for the obvious amplitude factor required to make the polarized reradiation add up to $R = -1$ in the grazing limit. Thus, the current density is higher for vertically than for horizontally-polarized sources. The currents generally flow in surface elements tilted appreciably with respect to the specular direction, which is close to horizontal. Similarly, the significant currents are in surfaces of the same tilt with respect to the backscatter direction, which is almost directly opposite the specular direction. Thus individual current elements radiate the same fields in the specular and the backscatter direction and, on the previous visualization that the phase variation of the current along the surface is independent of polarization, the backscatter is likewise independent. The conclusion has the same degree of plausibility as the visualization. Experimental evidence over rough sea water indicates that for grazing incidence, backscatter and $R \rightarrow -1$ are independent of polarization.

Backscattering from a Finite Cone*

JOSEPH B. KELLER†

Summary—Backscattering is calculated for an acoustic wave incident on a hard or soft finite cone, and for an electromagnetic wave incident on a perfectly-conducting finite cone. Two shapes of cone are treated, one with a flat base and the other with a rounded base. The calculation is based on the geometrical theory of diffraction. It is probably valid for wavelengths as large as the cone dimensions or smaller. Graphs of the backscattering cross section vs cone angle and vs wavelength are given for axial incidence on the flat-based cone. Suggestions for shaping an object to minimize its backscattering are also included.

I. INTRODUCTION

THE backscattering from a finite cone is calculated in this report by means of the geometrical theory of diffraction.^{1,2} Three different physical problems are considered. One is that of an acoustic wave incident upon a rigid cone. The second is that of an acoustic wave incident upon a perfectly soft (pressure-release) cone. The third, and perhaps most important, is that of an electromagnetic wave incident upon a perfectly-conducting cone. In all cases, two different types of cones are treated. One is a truncated right circular cone with a flat base. The other has a rounded base which is a portion of a sphere. The sphere and cone join smoothly, with no sharp edge. For simplicity, the incident wave is assumed to be plane and only the backscattered field is found, although both of these limitations could easily be removed.

The theory employed here represents the backscattered field as a superposition of fields on various rays. Some of these are the ordinary optical rays which are reflected from the cone and the others are diffracted rays. In the next section, the various rays are described and a qualitative description of the backscattering process is given. In Sections III–V, the quantitative results are derived and examined. Graphs of the backscattering cross section are also presented. In the conclusion,

* Manuscript received by the PGAP, April 7, 1959; revised manuscript received, December 1, 1959. Some of the results reported here were contained in a report entitled, "Radar Return from Metallic Objects," written in January, 1958 when the author was a consultant to the General Electric Co., Missiles and Ord. Systems Dept., Aerodynamics Lab., Commun. Section. Most of the other results were contained in a paper with the present title read at the Washington, D. C. meeting of URSI in May, 1958. They were all contained in Inst. of Math. Sciences, New York University, New York, N. Y., Res. Rept. No. EM-127; February, 1959. This research was sponsored by the AF Cambridge Res. Center, Air Res. and Dev. Command under Contract No. AF 19(604)1717.

† Inst. of Math. Sciences, New York University, New York, N. Y.
¹ J. B. Keller, "A geometrical theory of diffraction," *Proc. Symp. Appl. Math.*, McGraw-Hill Book Co., Inc., New York, N. Y., vol. 8, pp. 27–52; 1958. (See section on Calculus of Variations and Its Applications.)

² J. B. Keller, "Diffraction by an aperture," *J. Appl. Phys.*, vol. 28, pp. 426–444; April, 1957.

Section VI, suggestions are made about shaping an object to minimize its backscattering cross section.

Most of the previous theoretical results on backscattering from cones have concerned semi-infinite cones. For such cones, the acoustic diffraction problem was solved exactly and explicitly by Carslaw³ and the electromagnetic problem by Hansen and Schiff.⁴ Their solutions were given as infinite series which were difficult to evaluate. For the case of axial incidence, the backscattered fields were evaluated for small angle and large angle cones by Schensted,⁵ Siegel, Crispin, and Schensted⁶ and Felsen.^{7,8} For off-axial incidence on small-angle cones, they were evaluated by Felsen.⁹ For axial incidence, Felsen¹⁰ has also evaluated the backscattered fields approximately for cones of any angle. Another approximate result for the backscattered field was found by Spencer¹¹ using the Kirchhoff method. All of these results pertain to the field diffracted from the tip and yield what we call the tip-diffraction coefficient. As we shall see, this field is not important for the flat-based cone, but it is important for the round-based cone.

The Kirchhoff method has been applied to the finite cone by Siegel, *et al.*¹² Siegel¹³ has also treated the case of axial incidence on the flat-based finite cone by a variant of our method. However, his result is incorrect because of an error in his formula for the field scattered from a wedge. This error was later corrected.¹⁴

³ H. S. Carslaw, *Math. Ann.*, vol. 75, pp. 133–147; 1914.

⁴ W. W. Hansen and L. I. Schiff, Microwave Lab., Stanford University, Stanford, Calif., Quart. Repts. 1, 2, 3, 4, Contract W28-099-333; November, 1947–September, 1948.

⁵ C. E. Schensted, "Application of Summation Techniques to the Radar Cross-Section of a Cone," presented at Symp. on Microwave Optics, McGill Univ., Montreal, Can.; June, 1953.

⁶ K. M. Siegel, J. W. Crispin, and C. E. Schensted, "Electromagnetic and Acoustical Scattering from a Semi-Infinite Cone," *Rad. Lab., Univ. of Michigan, Ann Arbor, Res. Rept. UMM-92*; February, 1953. Also, *J. Appl. Phys.*, vol. 26, pp. 309–313; March, 1955.

⁷ L. B. Felsen, "Back Scattering from Wide-Angle and Narrow-Angle Cones," presented at Symp. on Microwave Optics, McGill Univ., Montreal, Can.; June, 1953.

⁸ L. B. Felsen, "Backscattering from wide-angle and narrow-angle cones," *J. Appl. Phys.*, vol. 26, pp. 138–151; February, 1955.

⁹ L. B. Felsen, "Plane-wave scattering by small-angle cones," *IRE TRANS. ON ANTENNAS AND PROPAGATION*, vol. AP-5, pp. 121–129; January, 1957.

¹⁰ L. B. Felsen, "Back Scattering from a Semi-Infinite Cone," *Microwave Res. Inst., Polytechnic Inst. of Brooklyn, N. Y., Memo. 43*, R-675-58, PIB-603; July, 1958.

¹¹ R. C. Spencer, "Back Scattering from Conducting Surfaces," *Air Force Cambridge Res. Labs., Cambridge, Mass., Rept. CRL-E5070*; April, 1951.

¹² K. M. Siegel, H. A. Alperin, R. R. Bonkowski, J. W. Crispin, A. L. Moffett, C. E. Schensted, and I. V. Schensted, *J. Appl. Math.*, vol. 26, pp. 297–305; 1955.

¹³ K. M. Siegel, *Appl. Sci. Res.*, vol. 7, sect. B, p. 293; 1958.

¹⁴ K. M. Siegel, R. F. Goodrich, and V. H. Weston, *Appl. Sci. Res.*, vol. 8, sect. B; 1959.

II. QUALITATIVE DESCRIPTION

Let us consider a plane wave incident upon a finite cone with a flat base. We denote the half-angle of the cone by γ and the radius of the base by a . (See Fig. 1.) Let ϕ denote the angle between the incident rays and the axis of the cone, with the range of ϕ given by $0 \leq \phi \leq \pi$. The extreme values $\phi=0$ and $\phi=\pi$ denote incidence along the axis, upon the tip and base, respectively. When $\phi=\pi$, the incident rays hit the base normally and therefore produce specularly-reflected rays which return to the source. When $\phi=(\pi/2)-\gamma$, the incident rays are normal to the curved surface of the cone and also give rise to specularly reflected rays which return to the source. For all other values of ϕ , no specularly reflected rays are returned to the source. As a consequence, the backscattering is strongest at $\phi=\pi$ and $\phi=(\pi/2)-\gamma$.

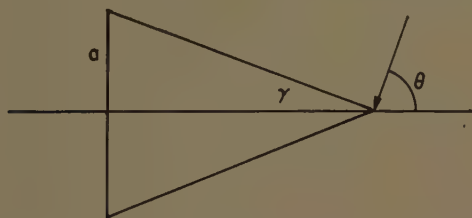


Fig. 1—Cross section of a finite cone of half-angle γ with a flat base of radius a . The tip of the cone is the origin of a polar coordinate system and the angle ϕ is measured from the axis.

When $\phi \neq \pi$, $(\pi/2)-\gamma$ the only backscattered rays are diffracted ones. The field on a ray diffracted from the tip is proportional to k^{-1} , that on a ray diffracted from the edge is proportional to $k^{-1/2}$, and that on a surface-diffracted ray decreases exponentially with k . Therefore for large k , or more precisely for large ka , the edge-diffracted rays are most important, the tip-diffracted rays are next and the surface rays least. Rays doubly diffracted at edges also have fields proportional to k^{-1} so they are equal in importance to tip-diffracted rays. When $\phi=0$ or π , the edge-diffracted rays have a caustic on the axis, so their field there is multiplied by $k^{1/2}$. In this case the singly-diffracted edge rays contribute a field proportional to k^0 and the doubly-diffracted ones a field proportional to $k^{-1/2}$. Thus when $\phi=0$, the doubly-diffracted edge rays are more important than the singly-diffracted tip ray. In addition the amplitude of the singly-diffracted edge field is independent of k , just like the incident field.

When ϕ lies in the interval $0 < \phi < \gamma$ or the interval $\pi/2 < \phi < \pi$, two rays singly diffracted at the edge are returned to the source. Therefore, in these ranges, the backscattered field will be an oscillatory function of ka , due to interference between these two rays. When ϕ lies in the interval $\gamma < \phi < \pi/2$ only one ray singly diffracted at the edge returns to the source. Therefore the field will not oscillate as ka varies, except for a small

oscillation due to interference with a doubly-diffracted ray. In all these cases, the amplitude of the field will be proportional to $(ka)^{-1/2}$.

Let us now consider the same problem for the finite cone of Fig. 2. This cone has a spherical rear surface which joins the cone smoothly. Now a will denote the radius of the rear surface. In this case, specularly reflected rays are returned to the source for all values of ϕ in the range $(\pi/2)-\gamma \leq \phi \leq \pi$. In the range $0 \leq \phi < (\pi/2)-\gamma$ only tip- and surface-diffracted rays return to the source. When $\phi=0$ the surface-diffracted rays have a caustic on the axis so their field there is multiplied by $k^{1/2}$. The relative importance of these two kinds of rays depends upon the value of ka . For very large values of ka , the tip ray is more important, while for smaller values of ka the surface rays are dominant. When the tip ray is dominant, interference does not occur, so the field does not oscillate as ka varies.

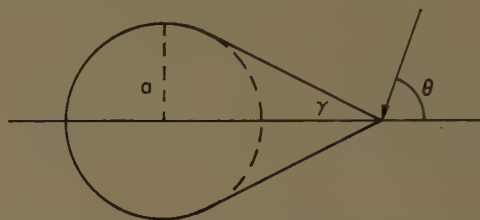


Fig. 2—Cross section of a finite cone of half-angle γ with a spherical base of radius a . The cone is tangential to the sphere where they join.

III. FLAT-BASED CONE—SINGLE DIFFRACTION

We shall first determine the backscattered field for the flat-based cone when $\phi \neq 0, (\pi/2)-\gamma, \pi$. The field on rays singly diffracted from the edge will be called u_{e1} . According to a previous work,² it is given by

$$u_{e1}(P) = [r_1(1 + \rho_1^{-1}r_1)]^{-1/2} e^{ikr_1} D_1 u_i(P_1) + [r_2(1 + \rho_2^{-1}r_2)]^{-1/2} e^{ikr_2} D_2 u_i(P_2). \quad (1)$$

In (1), P denotes the point at which the field is being determined while P_1 and P_2 denote the two points on the edge from which rays are diffracted to P . The point on the edge nearest to P is P_1 and its distance from P is r_1 . D_1 is the diffraction coefficient which depends upon the directions of the incident and diffracted rays at P_1 . The nonvanishing radius of curvature of the diffracted wavefront at P_1 is ρ_1 , and the incident field is u_i . The corresponding quantities with the subscript "2" are evaluated at P_2 , the point on the edge farthest from P . When ϕ lies in the range $\gamma < \phi < \pi/2$ only the P_1 term is present in (1) since then the point P_2 is hidden by the cone.

To evaluate the right side of (1), let us introduce the polar coordinates r, θ . In terms of them, the incident field is assumed to be given by

$$u_i(r, \theta) = A \exp[-ikr \cos(\theta - \phi)]. \quad (2)$$

In (2), A is a constant, which is a vector in the electromagnetic case. The coordinates of P_1 are a csc γ and $\pi - \gamma$ so $u_i(P_1) = A \exp [ika \csc \gamma \cos (\gamma + \phi)]$. Similarly, $u_i(P_2) = A \exp [ika \csc \gamma \cos (\gamma - \phi)]$. The radius ρ_1 is just the signed distance along the diffracted ray from P_1 to the axis, which is a caustic of the diffracted rays. A simple geometrical calculation yields

$$(1 + \rho_1^{-1}r_1) = \frac{r \sin \theta}{a} \quad (3)$$

$$(1 + \rho_2^{-1}r_2) = \frac{-r \sin \theta}{a}. \quad (4)$$

To calculate D_1 for an acoustic wave, we utilize (A10) of the previous paper.¹⁵ In that equation we must set β

Here $n = 3/2 + \gamma/\pi$. The upper sign in (5) applies to the cone on which the field vanishes (the soft cone) while the lower sign applies to one on which the normal derivative vanishes (the hard cone). To obtain D_2 , we need merely change the sign of ϕ in (5). In the electromagnetic case, these same diffraction coefficients can be used, the upper sign applying to the electric field component parallel to the edge and the lower sign to the component normal to the edge.

For large r , it is convenient to express r_1 and r_2 in the phase factors in terms of r and θ by $r_1 \approx r + a \csc \gamma \cos (\gamma + \phi)$ and $r_2 \approx r + a \csc \gamma \cos (\gamma - \phi)$. In the amplitudes, it is sufficient to use $r_1 \approx r_2 \approx r$. Upon combining all these results, and setting $\theta = \phi$, we obtain from (1) in the scalar case

$$u_{e1}(r, \phi) = \frac{\sqrt{a} \sin (\pi/n) A \exp \left[ikr + 2ka \csc \gamma \cos (\gamma + \phi) + i\frac{\pi}{4} \right]}{nr\sqrt{2\pi k} \sin \phi} \cdot \left[\left(\cos \frac{\pi}{n} - 1 \right)^{-1} \mp \left(\cos \frac{\pi}{n} - \cos \frac{3\pi - 2\phi}{n} \right)^{-1} \right]. \quad (6)$$

This result holds for $\gamma < \phi < \pi/2$ when only one edge-diffracted ray returns to the source. In the range $0 < \phi < \gamma$ and $\pi/2 < \phi < \pi$ when two such rays occur, u_{e1} is given by the right side of (6) plus the same expression with ϕ replaced by $-\phi$. Thus in this range,

$$u_{e1}(r, \phi) = \frac{\sqrt{a} \sin (\pi/n) A e^{ikr}}{nr\sqrt{2\pi k} \sin \phi} \left\{ \exp i \left[2ka \csc \gamma \cos (\gamma + \phi) + \frac{\pi}{4} \right] \left[\left(\cos \frac{\pi}{n} - 1 \right)^{-1} \mp \left(\cos \frac{\pi}{n} - \cos \frac{3\pi - 2\phi}{n} \right)^{-1} \right] \right. \\ \left. + \exp i \left[2ka \csc \gamma \cos (\gamma - \phi) - \frac{\pi}{4} \right] \left[\left(\cos \frac{\pi}{n} - 1 \right)^{-1} \mp \left(\cos \frac{\pi}{n} - \cos \frac{3\pi + 2\phi}{n} \right)^{-1} \right] \right\}. \quad (7)$$

$= \pi/2$ because the incident ray is normally incident on the edge. We also set $\theta = \alpha$ because we will consider only backscattering. We find at once that at P_1 , $\alpha = \pi - \phi$ while at P_2 , $\alpha = \pi + \phi$. Thus we obtain

$$D_1 = \frac{e^{i\pi/4} \sin (\pi/n)}{n\sqrt{2\pi k}} \left[\left(\cos \frac{\pi}{n} - 1 \right)^{-1} \mp \left(\cos \frac{\pi}{n} - \cos \frac{3\pi - 2\phi}{n} \right)^{-1} \right]. \quad (5)$$

¹⁵ Keller, *op. cit.*, footnote 2, (A10) is written incorrectly and should read

$$D = \frac{e^{i\pi/4} \sin (\pi/n)}{n \sin \beta \sqrt{2\pi k}} \left[\left(\cos \frac{\pi}{n} - \cos \frac{\theta - \alpha}{n} \right)^{-1} \mp \left(\cos \frac{\pi}{n} - \cos \frac{\theta + \alpha + \pi}{n} \right)^{-1} \right].$$

(In the last term, $3\pi + 2\phi$ must be replaced by $2\phi - \pi$ when $\pi/2 \leq \phi \leq \pi$.) In (6) and (7), the upper signs hold for the soft cone and the lower signs for the hard cone.

In the electromagnetic case, (6) and (7) also apply. The soft-cone result applies to the electric field component parallel to the edge at P_1 ; *i.e.*, perpendicular to the plane containing P and the axis. The hard-cone result applies to the electric field component normal to the edge at P_1 ; *i.e.*, lying in the plane containing P and the axis.

The result (6) is not valid at $\phi = (\pi/2) - \gamma$ where it becomes infinite. For this value of ϕ , the specularly-reflected ray must also be taken into account. The result (7) is not valid at $\phi = 0, \pi$ where it becomes infinite. For these values of ϕ , the diffracted rays form a caustic on the axis, and in addition at $\phi = \pi$, the specularly-reflected rays must be considered.

Let us first obtain a modified form of (7) valid at $\phi=0$. To this end, we define $\rho=r \sin \theta$, which is the distance of P from the axis. We also define $\delta=\cos^{-1}(a/r)$ and note that $\rho \cos \delta=a \sin \theta$. Now we must re-examine (7) before setting θ equal to ϕ , with $\phi=0$. Therefore we return to (1), set $u_i(P_1)=u_i(P_2)$ and $D_1=D_2$, use (3) and (4), and in the phase set $r_1=(r \cos \theta+a \cot \gamma) \sin \delta+(a-\rho) \cos \delta$. For r_2 , we use the same formula with $-\rho$ in place of ρ . Then (1) becomes, after some simplification, instead of (7)

$$u_{e1}(r, \theta) = \frac{a \sin (\pi/n) A \exp [2ika \cot \gamma]}{nr\sqrt{2\pi k\rho \cos \delta}} \left[\left(\cos \frac{\pi}{n} - 1 \right)^{-1} \mp \left(\cos \frac{\pi}{n} - \cos \frac{3\pi}{n} \right)^{-1} \right] \cdot \left[\exp ik(r \cos \theta \sin \delta - \rho \cos \delta) + i \frac{\pi}{4} + \exp ik(r \cos \theta \sin \delta + \rho \cos \delta) - i \frac{\pi}{4} \right]. \quad (8)$$

This is of the form given in (A15) of the above-mentioned work.² Therefore we may apply the axial caustic correction given there. Upon doing so and eliminating δ , we obtain for θ small

$$u_{e1}(r, \theta) = \frac{a \sin (\pi/n) A \exp [ik(r + 2a \cot \gamma)]}{nr} J_0(ka \sin \theta) \left[\left(\cos \frac{\pi}{n} - 1 \right)^{-1} \mp \left(\cos \frac{\pi}{n} - \cos \frac{3\pi}{n} \right)^{-1} \right]. \quad (9)$$

At $\theta=0$, the Bessel function J_0 is equal to one. Thus at $\theta=0$, (9) becomes the following, which is the backscattered field at $\phi=0$

$$u_{e1}(r, 0) = \frac{a \sin (\pi/n) A \exp [ik(r + 2a \cot \gamma)]}{nr} \left[\left(\cos \frac{\pi}{n} - 1 \right)^{-1} \mp \left(\cos \frac{\pi}{n} - \cos \frac{3\pi}{n} \right)^{-1} \right]. \quad (10)$$

Now we consider $\phi=\pi$. Again we must return to (1) and keep $\theta \neq \pi$. Proceeding as above, we obtain from (1)

$$u_{e1}(r, \theta) = \frac{a \sin (\pi/n) A \exp [-2ika \cot \gamma]}{nr\sqrt{2\pi k\rho \cos \delta}} \left[\left(\cos \frac{\pi}{n} - 1 \right)^{-1} \mp \left(\cos \frac{\pi}{n} - \cos \left(\frac{\pi}{2n} + \frac{\delta}{n} \right) \right)^{-1} \right] \cdot \left[\exp ik(-r \cos \theta \sin \delta + [a - \rho] \cos \delta) + i \frac{\pi}{4} + \exp ik(-r \cos \theta \sin \delta + [a + \rho] \cos \delta) - i \frac{\pi}{4} \right]. \quad (11)$$

Upon applying the caustic correction to (11), we obtain

$$u_{e1}(r, \theta) = \frac{a \sin (\pi/n) A \exp [-ik(r \cos \theta \sin \delta + 2a \cot \gamma)]}{nr} J_0(ka \sin \theta) \cdot \left[\left(\cos \frac{\pi}{n} - 1 \right)^{-1} \mp \left(\cos \frac{\pi}{n} - \cos \left(\frac{\pi}{2n} + \frac{\delta}{n} \right) \right)^{-1} \right]. \quad (12)$$

Although (12) is finite at any finite distance r along the axis, it becomes infinite as r becomes infinite because then $\delta=\cos^{-1}(a/r)$ tends to $\pi/2$. Of course there is also a reflected field u_R on and near the axis, given by

$$u_R(r, \theta) = \mp A \exp [-ik(r \cos \theta + 2a \cot \gamma)],$$

$$|r \sin \theta| < a, \quad \theta > \frac{\pi}{2}. \quad (13)$$

The total field $u(r, \theta)$ is the sum of the reflected and diffracted fields. Its form on the axis for large r can be computed from (12) and (13) by first setting $\theta = \pi$ and $\delta = (\pi/2) - (a/r)$. Then for large r ,

$$u = u_k + u_{e1} = A \exp [ik(r - 2a \cot \gamma)] \left[\mp 1 \mp \frac{a \sin(\pi/n)}{nr} \left(1 - \frac{ika^2}{2r} \right) \left(\cos \frac{\pi}{n} - \cos \left(\frac{\pi}{n} - \frac{a}{nr} \right) \right)^{-1} \right] \\ = \mp \frac{ika^2 A}{2r} \exp [ik(r - 2a \cot \gamma)]. \quad (14)$$

Eqs. (6), (7), (10) and (14) give the backscattered field for all directions of incidence except $\phi = (\pi/2) - \gamma$. From these equations we can compute the backscattering cross section $\sigma(\phi) = 4\pi r^2 |u|^2 |A|^{-2}$. We obtain for the scalar cases (upper sign for soft cone, lower sign for hard cone)

$$\frac{\sigma(0)}{\pi a^2} = \frac{4}{n^2} \sin^2 \frac{\pi}{n} \left[\left(\cos \frac{\pi}{n} - 1 \right)^{-1} \mp \left(\cos \frac{\pi}{n} - \cos \frac{3\pi}{n} \right)^{-1} \right]^2 \quad (15)$$

$$\frac{\sigma(\pi)}{\pi a^2} = (ka)^2 \quad (16)$$

$$\frac{\sigma(\phi)}{\pi a^2} = \frac{2 \sin^2(\pi/n)}{n^2 \pi k a \sin \phi} \left[\left(\cos \frac{\pi}{n} - 1 \right)^{-1} \mp \left(\cos \frac{\pi}{n} - \cos \frac{3\pi - 2\phi}{n} \right)^{-1} \right]^2 \quad \gamma < \phi < \frac{\pi}{2} \quad (17)$$

$$\frac{\sigma(\phi)}{\pi a^2} = \frac{2 \sin^2(\pi/n)}{n^2 \pi k a \sin \phi} \left| \exp [-i(2ka \sin \phi - \pi/4)] \left[\left(\cos \frac{\pi}{n} - 1 \right)^{-1} \mp \left(\cos \frac{\pi}{n} - \cos \frac{3\pi - 2\phi}{n} \right)^{-1} \right] \right. \\ \left. + \exp [i(2ka \sin \phi - \pi/4)] \left[\left(\cos \frac{\pi}{n} - 1 \right)^{-1} \mp \left(\cos \frac{\pi}{n} - \cos \frac{3\pi + 2\phi}{n} \right)^{-1} \right] \right|^2, \quad 0 < \phi < \gamma \quad (18)$$

$$\frac{\sigma(\phi)}{\pi a^2} = \frac{2 \sin^2(\pi/n)}{n^2 \pi k a \sin \phi} \left| \exp [-i(2ka \sin \phi - \pi/4)] \left[\left(\cos \frac{\pi}{n} - 1 \right)^{-1} \mp \left(\cos \frac{\pi}{n} - \cos \frac{3\pi - 2\phi}{n} \right)^{-1} \right] \right. \\ \left. + \exp [i(2ka \sin \phi - \pi/4)] \left[\left(\cos \frac{\pi}{n} - 1 \right)^{-1} \mp \left(\cos \frac{\pi}{n} - \cos \frac{2\phi - \pi}{n} \right)^{-1} \right] \right|^2, \quad \frac{\pi}{2} < \phi < \pi. \quad (19)$$

Eqs. (10) and (15) are not valid when $\gamma = \pi/2$, in which case the cone becomes a circular disk. In that case, the right side of (10) must be replaced by that of (14) and that of (15) by the right side of (16).

In the electromagnetic case when $\phi \neq 0, \pi$ we may define the plane Γ containing the axis of the cone and the source (or an incident ray). Let us suppose that the incident wave is linearly polarized and that the incident electric field makes the angle Ψ with the normal to this plane. Then the component of the incident field normal to the edge at the points of diffraction is proportional to $\sin \Psi$ and that parallel to the edge is proportional to $\cos \Psi$. Thus the backscattered field component normal to the plane Γ is given by $u_{e1}^S(r, \phi) \cos \Psi$ and that parallel to the plane Γ is $u_{e1}^H(r, \phi) \sin \Psi$. Here u_{e1}^S and u_{e1}^H are the backscattered scalar fields. The superscript S refers to the soft cone and H to the hard cone. From these results we find that the backscattering

cross section σ_{EM} for the electromagnetic case is given by

$$\sigma_{EM}(\phi) = \sigma_S(\phi) \cos^2 \psi + \sigma_H(\phi) \sin^2 \psi \quad \phi \neq 0, \pi. \quad (20)$$

For axial incidence $\phi = 0, \pi$ the backscattered field \mathbf{E} is given by

$$\mathbf{E} = \frac{1}{2}(u^S - u^H) \mathbf{E}_i. \quad (21)$$

Here \mathbf{E}_i is the incident field at the body while u^S and u^H denote the scalar backscattered fields, which may be reflected, diffracted from edges, or diffracted around curved surfaces. The relation (21) holds for backscattering along the axis of any body of revolution. It can be proved by considering the fields on the various rays.¹⁶

¹⁶ B. R. Levy and J. B. Keller, "Diffraction by a Spheroid," EM Res. Div., Inst. Math. Sci., New York University, N. Y. Rept. No. EM-130; April, 1959. Also in *Can. J. Phys.*, vol. 38, pp. 128-144; January, 1960.

Upon combining (21) with (10), we obtain

$$\frac{\sigma_{EM}(0)}{\pi a^2} = \frac{4 \sin^2(\pi/n)}{n^2} \left(\cos \frac{\pi}{n} - \cos \frac{3\pi}{n} \right)^{-2}. \quad (22)$$

Graphs of $\sigma(0)$ vs γ , based on (22) and (15), are shown in Fig. 3. From (21) and (14) we find

$$\frac{\sigma_{EM}(\pi)}{\pi a^2} = (ka)^2 \quad (23)$$

As in the scalar case, when $\gamma = \pi/2$ and the cone is a disk, the right side of (22) must be replaced by that of (23).

IV. FLAT-BASED CONE—DOUBLE DIFFRACTION

Some of the singly-diffracted rays produced by the incident ray traverse the base of the cone, hit the opposite edge and produce doubly-diffracted rays. Some of these rays return to the source, contributing to the backscattering. We shall now analyze this effect in the case of axial incidence upon the tip of the cone since, in this case, the effect of double diffraction is greater than that of tip diffraction.

The field on a ray singly diffracted at P_1 is given by the first term on the right side of (1). For a ray traversing the base of the cone, $\rho_1 = -a$ and the diffraction coefficient D_1 is given by

$$D = \frac{e^{i\pi/4} \sin(\pi/n)}{n(2\pi k)^{1/2}} \left[\left(\cos \frac{\pi}{n} - \cos \frac{3\pi}{2n} \right)^{-1} \mp \left(\cos \frac{\pi}{n} - \cos \frac{3\pi}{2n} \right)^{-1} \right]. \quad (24)$$

For the soft cone, (24) shows that $D=0$. This ray reaches the point P_2 on the opposite edge when $r_1 = 2a$. The field on this ray at P_2 is

$$u_{e1}(P_2) = D(2a)^{-1/2} \exp[2ika - i\pi/2] u_i(P_1). \quad (25)$$

Similarly, the field $u_{e1}(P_1)$ on a ray produced at P_2 is given by the right side of (25) with $u_i(P_1)$ replaced by $u_i(P_2)$, but with the same diffraction coefficient.

The field (25) may be considered to be the incident field which gives rise to a doubly diffracted ray. The doubly-diffracted field $u_{e2}(P)$ at a point P which is near, but not on the axis, will consist of two terms like those in (1), since two doubly-diffracted rays pass through P . One of these comes from P_1 and another comes from P_2 . Thus we have

$$u_{e2}(P) = [r_1(1 + \rho_1^{-1}r_1)]^{-1/2} e^{ikr_1} D_3 u_{e1}(P_1) + [r_2(1 + \rho_1^{-1}r_2)]^{-1/2} e^{ikr_2} D_4 u_{e1}(P_2). \quad (26)$$

If the point P is far from the cone and near the axis, D_3 and D_4 are both equal to D which is given by (24).

We now proceed to simplify (26) exactly as we did in obtaining (10) from (1). In fact, by comparing (1) and

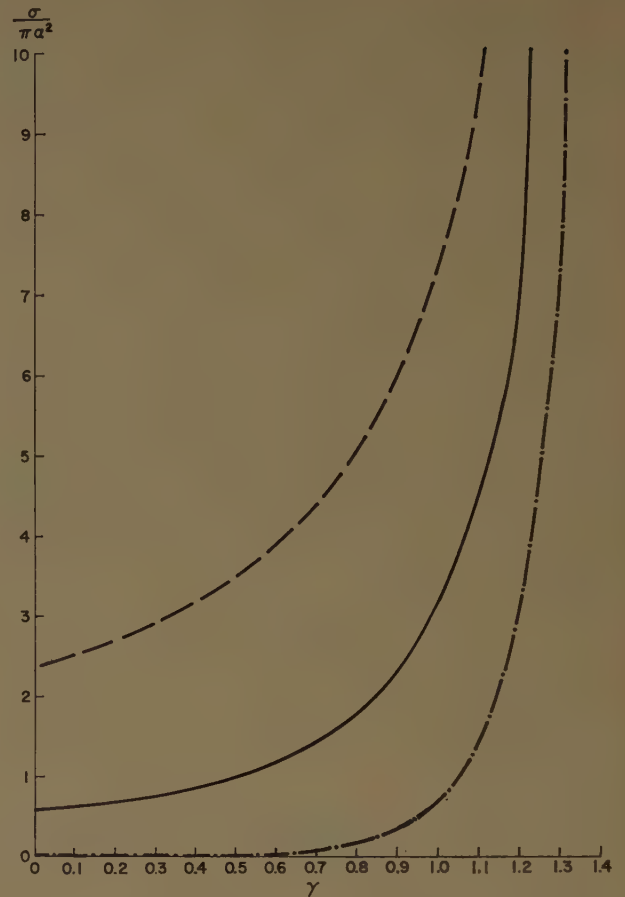


Fig. 3—Graphs of the backscattering cross section for axial incidence on the flat-based cone of Fig. 1. The ordinate is $\sigma(0)/\pi a^2$ and the abscissa is γ , the half-angle of the cone. The solid curve, based on (22), applies to the electromagnetic case. The dashed and broken curves, based on (15), apply to the acoustic cases of hard and soft cones, respectively. These equations include only the singly-diffracted field and are independent of ka . At $\gamma = \pi/2$, $\sigma(0)/\pi a^2$ has the finite value $(ka)^2$ in all three cases

(26) we see that they differ only by the factor $D_3 u_{e1}(P_1)/D_1 u_i(P_1)$. This is so because for $\phi=0$, $u_{e1}(P_1) = u_{e2}(P_2)$. Furthermore, for P far from the cone and near the axis, D_1 and D_2 are equal just as D_3 and D_4 are. As a consequence, we can obtain the simplified form of (26) by multiplying (10) by the factor given above. Since $u_{e1}(P_1)$ as given by (25) contains $u_i(P_1)$, the factor becomes $D^2(2a)^{-1/2} \exp[2ika - i\pi/2] (D_1)^{-1}$. In this way we obtain for the hard cone

$$u_{e2}^H(r, 0) = \frac{2 \sin^2(\pi/n) a^{1/2} A e^{ikr} \exp[2ika(\cot \gamma + 1) - i\pi/4]}{n^2(\pi k)^{1/2} r} \cdot \left(\cos \frac{\pi}{n} - \cos \frac{3\pi}{2n} \right)^{-2}. \quad (27)$$

For the soft cone, $D=0$ and therefore

$$u_{e2}^S(r, 0) = 0. \quad (28)$$

Let us now combine the singly- and doubly-diffracted backscattered fields. For the hard cone, (10) and (27) yield

$$u_{e1}^H(r, 0) + u_{e2}^H(r, 0) = \frac{aA \sin(\pi/n) \exp[ik(r + 2a \cot \gamma)]}{nr} \cdot \left[\left(\cos \frac{\pi}{n} - 1 \right)^{-1} + \left(\cos \frac{\pi}{n} - \cos \frac{3\pi}{2n} \right)^{-1} + \frac{2 \sin(\pi/n) \exp[2ika - i\pi/4]}{n(\pi ka)^{1/2}} \cdot \left(\cos \frac{\pi}{n} - \cos \frac{3\pi}{2n} \right)^{-2} \right]. \quad (29)$$

The backscattering cross section $\sigma_H(0)$ is now $4\pi r^2 A^{-2}$ multiplied by the square of the absolute value of the right-hand side in (29). For the soft cone, (10) and (15) still apply since $u_{e2}^S(r, 0) = 0$.

For the electromagnetic case, we insert (10) for u^S and (29) for u^H into (21). Then if A denotes the vector amplitude of the incident field at the cone, we obtain

$$E_{e1}(r, 0) + E_{e2}(r, 0) = - \frac{aA \sin(\pi/n) \exp[ik(r + 2a \cot \gamma)]}{nr} \cdot \left[\left(\cos \frac{\pi}{n} - \cos \frac{3\pi}{n} \right)^{-1} + \frac{\sin(\pi/n) \exp[2ika - i\pi/4]}{n(\pi ka)^{1/2}} \cdot \left(\cos \frac{\pi}{n} - \cos \frac{3\pi}{2n} \right)^{-2} \right]. \quad (30)$$

The backscattering cross section $\sigma_{EM}(0)$ is $4\pi r^2 |A|^{-2}$ multiplied by the square of the absolute value of the right-hand side in (30). Graphs of $\sigma(0)$ vs ka , based on (29) and (30), are shown in Fig. 4.

V. CONE WITH A SPHERICAL BASE

Let us now consider backscattering from the cone of Fig. 2. When the direction of incidence lies in the range $\pi/2 - \gamma < \phi \leq \pi$, some incident ray hits the cone normally and is reflected back to the source. The backscattering cross section for such directions is then given by the well-known geometrical optical formula

$$\sigma_S = \sigma_H = \sigma_{EM} = \pi a^2 \quad \pi/2 - \gamma < \phi \leq \pi. \quad (31)$$

When the direction of incidence lies in the range $0 \leq \phi < \pi/2 - \gamma$, only a tip-diffracted ray and one or more surface-diffracted rays return to the source. In the range $0 \leq \phi \leq \gamma$, infinitely many surface-diffracted rays return to the source, and they form an axial caustic extending in the direction of the source. The field on this caustic is the same as the diffracted part of the backscattered field from a sphere, if rays which make complete revolutions around the sphere are excluded. The

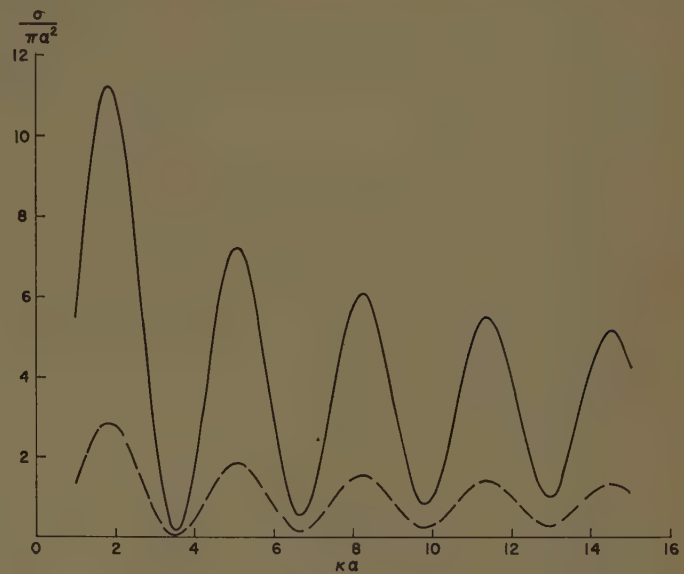


Fig. 4—Graphs of the backscattering cross section for axial incidence on the flat-based cone of Fig. 1. Single and double diffraction are both included. The ordinate is $\sigma(0)/\pi a^2$ and the abscissa is ka . The cone angle $\gamma = 0.2$ radians $= 11.5^\circ$. The solid curve, based on (30), applies to the electromagnetic case. The dashed curve, based on (29), applies to the acoustic case of a hard cone.

latter field is given in (95) and (96) of Levy and Keller.¹⁷ If we add this field to that on the tip-diffracted ray, we obtain in the scalar case

$$u(r, \phi) = \frac{aAe^{ikr}}{2r} [2C(\phi)(ka)^{-1} + G(ka)^{1/3}e^{-\tau(ka)^{1/3}} \cdot \exp[ika(\pi + 2 \csc \gamma \cos \phi)]], \quad 0 \leq \phi \leq \gamma. \quad (32)$$

In (32), $C(\phi)$ is the tip-diffraction coefficient for backscattering which depends upon ϕ and upon whether the cone is soft or hard. The constants G and τ are also different in the two cases and are given by

$$G_S = -4\pi^2 6^{-4/3} [A'(q_S)]^{-2} e^{i\pi/3}, \quad \tau_S = e^{-i\pi/6} 6^{-1/3} q_S \pi, \quad A(q_S) = 0 \text{ (soft cone)} \quad (33)$$

$$G_H = -2\pi^2 6^{-1/3} q_H^{-1} [A(q_H)]^{-2} e^{i\pi/3}, \quad \tau_H = e^{-i\pi/6} 6^{-1/3} q_H \pi, \quad A'(q_H) = 0 \text{ (hard cone)}. \quad (34)$$

In these equations, the subscripts S and H refer to the soft and hard cones. The function $A(q)$ is the Airy function. The roots q_S and q_H are given by Levy and Keller.¹⁷ The tip-diffraction coefficient has been determined by Felsen and the others referred to previously.

In the electromagnetic case, we may use (21) to obtain the contribution to E from surface-diffracted rays in the range $0 \leq \phi \leq \gamma$. This is so because for these rays in this range, the rear hemisphere accounts for the backscattering, and it is axially symmetric about any axis in this range. The field backscattered from the

¹⁷ B. R. Levy and J. B. Keller, "Diffraction by a smooth object," *Commun. Pure and Appl. Math.*, vol. 12, pp. 159–209; February, 1959.

tip must be computed with the aid of the tip-diffraction coefficient matrix which we will also denote by $C(\phi)$. Thus we have

$$\begin{aligned} \mathbf{E}(r, \phi) = & \frac{a}{2r} e^{ikr} \left[2(ka)^{-1} C(\phi) + \frac{(ka)^{1/3}}{2} \right. \\ & \cdot \exp [i\pi(\pi + 2 \csc \gamma \cos \phi)] \\ & \times [G_S e^{-\tau_S(ka)^{1/3}} - G_H e^{-\tau_H(ka)^{1/3}}] \left. \right] \mathbf{E}_i, \quad 0 \leq \phi \leq \gamma \quad (35) \end{aligned}$$

This result can be simplified by omitting the term $G_S \exp [-\tau_S(ka)^{1/3}]$ since it is much smaller than the term $G_H \exp [-\tau_H(ka)^{1/3}]$.

VI. CONCLUSION

On the basis of the preceding considerations, it is possible to draw some conclusions about shaping an object to minimize its backscattering cross section σ . These conclusions follow.

1) The object should not have any flat, cylindrical or conical surfaces which might be hit normally by an incident wave. Such surfaces can only be hit normally from a narrow range of directions. Although they yield very strong reflections within this range, they yield correspondingly small return in all other directions. For example, an object with an ogival nose instead of a conical one yields a smaller reflection when it is hit normally, but it can be hit normally from a greater range of directions. The decision about whether to include flat, cylindrical or conical surfaces and thus permit big reflections in a small range of directions and very little in other directions, or to exclude them and use only doubly-curved surfaces which yield a somewhat smaller reflection over a larger range of directions, must be based on operational considerations.

If only a limited range of directions of incidence need be considered, then the following conclusions apply.

2) The object should have no surface which can be

hit normally from the range of incidence directions under consideration. This is the case for a finite cone when the incidence directions are confined to the neighborhood of the axis.

3) If the object does have a surface which can be hit normally, that surface should be as curved as possible. Thus if the object is a cone with a rounded tip and if the incidence directions are nearly axial, the tip should have as small a radius as possible.

4) The object should have no edge which can be hit normally by an incident ray. Thus if the object is a finite cone with a flat or curved rear surface, the conical and rear surfaces should join smoothly and not meet at a sharp edge. Whether a sharply-curved surface behaves as an edge or not depends upon the relative sizes of its radius of curvature and the wavelength. The larger the radius compared to the wavelength, the less the surface behaves like an edge. Of course, rounding off such an edge diminishes the backscattering from axial and nearly axial directions, but it increases backscattering in certain directions near the rear from which reflection from the round edge now becomes possible.

Suppose the object is a finite cone with incidence directions which are nearly axial; then these conclusions apply.

5) It should have a rounded rather than a flat rear surface. This diminishes the contribution of the surface rays which traverse the rear surface.

6) The rear surface should not be axially symmetric. This will eliminate the caustic of the diffracted rays on the axis, in the case of axial incidence. Thus it will significantly cut down the cross section for such incidence.

7) The rear surface should probably have some sharp edges or conical tips. This will help to interrupt the surface rays on the rear surface and cause them to radiate most of their energy away from the surface.

Suggestions similar to some of these have been made by S. Silver and by K. M. Siegel.

Optimum Radar Integration Time*

J. M. FLAHERTY† AND E. KADAK‡

Summary—The practice of integrating periodic low-level signals with time in order to improve the SNR of a coherent signal in an ambient of incoherent noise is extremely useful and generally understood. In cases where the signal continues as long as the observer desires to integrate, the SNR can of course be improved by lengthening the integration period without limit. However, in the case of a radar system trying to detect a very rapidly-approaching target, it is obvious that one does not have an unlimited length of time to perform the signal integration and arrive at a decision. The authors have derived an expression which reveals what the optimum integration period is when the radius of the region to be protected, and the velocity of the approaching target, are known.

SINCE it is necessary that any device which is to serve as a detector of some form of energy must collect or accumulate a finite amount of it before its presence can be detected, the fundamental importance of the integration process necessary for signal detection is readily appreciated. Our particular purpose in this paper is to examine one of the important aspects of signal integration in the field of target detection by radar means. The speed and great destructive power of existing and potential enemy attackers such as jet bombers and guided missiles makes it imperative that they be detected at a great distance. In order to defend a given region, it is therefore important to know the optimum integrating time for the particular circumstances under which the radar equipment is operating. We have derived an equation for the optimum integration time based on a tactical situation in which the target to be detected enters the radar antenna beam at such a great distance that initially no significant signals are received from it. It is further assumed that the target never leaves the radar antenna beam. Although this is not at present a common tactical situation, it is likely to become one for the following reasons.

Fig. 1 shows the essential features of the tactical situation involved in defending a particular area, such as a city or communications center, from enemy attack by ICBM's. The incoming missile should produce much less signal modulation than other types of aircraft because of its probable structural and flight characteristics. As a result, it may be desirable to integrate for very great lengths of time compared to the integration times employed in most present radars. Since no great amount of maneuvering is to be expected on the part of the missile, it follows a relatively straight-line course towards its target. This means that fixed antenna arrays with overlapping beams will probably prove to be much more effective than a rotating antenna system. It is

also unlikely that the missile could approach the city from more than a limited range of azimuths because of the relative geographical locations, on the earth, of the possible launching sites and the site that the missile is to destroy. Because of these conditions, it is likely that radar receiver sensitivity will be further increased by developments which will increase the time interval over which one can integrate the signal. Greater receiver sensitivity and transmitter power will be required for the radar detection of missiles than for the detection of aircraft primarily for two reasons. First, the highly-streamlined missiles, designed to travel at speeds greater than Mach 1, have a very low radar cross-sectional area when viewed from the head-on aspect. Second, these missiles must be detected at greater ranges than conventional aircraft, since the missile's extremely high speed of approach does not allow much time for proper counter-measures. This is possible since the missiles are above the horizon at such great ranges.

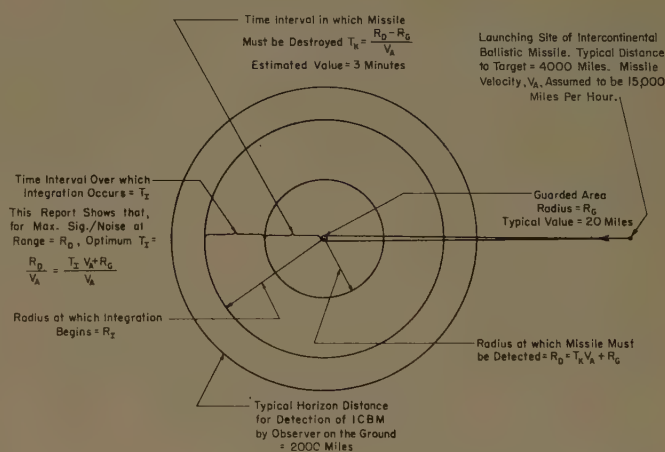


Fig. 1—Tactical situation for radar detection of ICBM. Radar is assumed to be located in center of guarded area.

With this situation in mind, it becomes immediately obvious that one must decide what the optimum integration time would be under these circumstances. The major feature of the analysis which follows is the explicit determination of the effect which the approach velocity of the missile has upon the optimum integrating time. It is considered self-evident that if one merely wanted to detect a stationary target, he would integrate as long as necessary to obtain the desired SNR. However, when the target is approaching the radar set at constant velocity, the maximum SNR would be provided by an integration time extending from the time at which the signal first was large enough to be useful to the time at which a final decision must be made. This

* Manuscript received by the PGAP, March 12, 1959; revised manuscript received, September 28, 1959.

† Westinghouse Air Arm Div., Baltimore, Md. Formerly Westinghouse Research Labs., Pittsburgh, Pa.

‡ Westinghouse Research Labs., Pittsburgh, Pa.

optimum integration time is now calculated on the basis of the following assumption. One knows at least approximately the maximum speed of the missiles that he must detect and destroy, the radius of the region which must be protected, and the time required to meet the attack once the attacking missile has been detected. These three quantities in turn determine the range at which the SNR must be made a maximum in order to provide the greatest protection for the guarded area. These relationships are shown as follows:

$$R_D = T_K V_A + R_G, \quad (1)$$

where

R_D = distance from guarded area center at which missiles must be detected in order to have sufficient time to destroy them,

T_K = maximum time required to destroy missiles after they have been detected,

V_A = approach velocity of enemy missile, and

R_G = radius of guarded area which is to be protected from enemy attack.

Now that R_D has been calculated, it is possible to calculate the integration time which will produce the greatest SNR at that range under the given circumstances. In making such a calculation it is helpful to keep in mind the qualitative relationships between signal, noise and range shown in Fig. 2. For the case of a specific constant-velocity missile the abscissa can be considered to represent time. Such time, T , is measured prior to T_0 , which is the time at which the missile would arrive at the radar, set at the center of the guarded area.

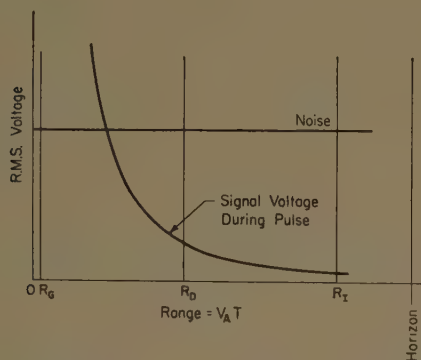


Fig. 2—Signal and noise voltage vs range. (Typical relative levels) T_0 = time at which missile would arrive at radar; T = time prior to T_0 ; V_A = velocity of constant-speed missile.

In the following calculation of optimum integrating time, it is assumed that the pulse repetition rate employed is such that a large number of pulses are received within the integration period, and that during this period all of the pulses received by the antenna are RF integrated in that the signal voltages are added in phase. No amplification is considered, since it would affect signal and noise identically and thus not affect their ratio.

Let

P_{PT} = peak power of transmitted pulse,

σ_T = scattering cross section of target,

G = power gain of transmitting antenna,

T_I = time during which pulses are added,

f_R = repetition frequency of pulses,

A = effective area of receiving antenna,

v_{SPRMS} = RMS voltage of integrated received signal during pulses,

r = resistance at output of integrator, and

P_{SP} = peak power of received pulse after integration.

Then, if

$$K_S = f_R \sqrt{P_{PT} \left(\frac{\sigma_T G A}{16\pi^2} \right) r}, \quad (2)$$

$$v_{SPRMS} = K_S \int_{(R_D/V_A)}^{(R_D/V_A + T_I)} \frac{dT}{V_A^2 T^2} = \frac{K_S}{V_A} \left[\frac{1}{R_D} - \frac{1}{R_D + T_I V_A} \right]. \quad (3)$$

Now to calculate the peak power P_{SP} contained in the above signal, the expression is squared and divided by the resistance at the integrator output.

$$P_{SP} = \frac{K_S^2}{V_A^2 r} \left[\frac{1}{R_D} - \frac{1}{R_D + T_I V_A} \right]^2. \quad (4)$$

Next we can write the following expression for noise power, P_N .

P_N = sum of power of all noise samples received during integrated signal pulse.

Then, if $K_N = f_R k \theta \Delta_f$ where

k = Boltzmann's constant,

Δ_f = noise bandwidth, and

θ = absolute temperature,

$$P_N = K_N \int_{R_D/V_A}^{(R_D + T_I V_A)/V_A} dt = K_N T_I. \quad (5)$$

Therefore, the SNR in power is

$$\frac{P_{SP}}{P_N} = \frac{K_S^2 \left[\frac{1}{R_D} - \frac{1}{R_D + T_I V_A} \right]^2}{K_N T_I}. \quad (6)$$

In voltage, the SNR is

$$\frac{v_{SPRMS}}{v_{NRMS}} = \frac{K_S}{\sqrt{r V_A} \sqrt{K_N}} \left[\frac{1}{\sqrt{T_I R_D}} - \frac{1}{\sqrt{T_I (R_D + T_I V_A)}} \right], \quad (7)$$

v_{NRMS} = noise RMS voltage after integration.

Now differentiating the voltage SNR expression with respect to T_I , setting the resulting expression equal to zero and solving for T_I as shown below:

$$\frac{d \frac{v_{SPRMS}}{v_{NRMS}}}{dT_I} = \frac{1}{\sqrt{r} V_A} \frac{K_S}{\sqrt{K_N}} \left\{ (R_D^{-1})(-1/2)(T_I^{-3/2}) + (R_D + T_I V_A)^{-1}(-1/2)(T_I^{-3/2}) - (T_I^{-1/2})(-1)(R_D + T_I V_A)^{-2} V_A \right\} = 0 \quad (8)$$

$$T_I V_A = R_D \quad (9)$$

$$T_I = \frac{R_D}{V_A} = \frac{T_K V_A + R_G}{V_A} \quad (10)$$

Thus it has been shown that the optimum integrating time for the situation described above is equal to the distance (from the center of the guarded area) at which the missile must be detected in time to destroy it, divided by the approach velocity of the missile.

The consequence of these relationships were next investigated by substituting typical values into the above expression for T_I . The approach velocity of an ICBM would be in the order of 15,000 mph. At present, it is not possible to destroy a missile after detection by means of an antimissile in less than 1/20 of an hour. Therefore, Let T_K equal 0.05 hour. The radius of most large city areas likely to be considered worthwhile for atomic destruction is less than 20 miles. Therefore, let R_G equal 20 miles. When these quantities are substituted into the expression for the optimum integrating time, the following observations can be made:

$$T_I = \frac{T_K V_A + R_G}{V_A} = \frac{\left(\frac{1}{20} \text{ hour} \times 15,000 \text{ mph} \right) + 20 \text{ miles}}{15,000 \text{ mph}} = 3.04 \text{ minutes or } 182.5 \text{ seconds or } 0.05065 \text{ hour.} \quad (11)$$

The radius of the guarded area is negligible compared with the additional radial distance at which the missiles

must be detected to be destroyed before reaching the guarded area, so it is approximately true that in terms of the tactical situation, the integration time should roughly equal the time required to destroy the missile after it has been detected. Now, according to an approximate calculation, the missile should rise above the terrestrial horizon approximately 400 seconds (or 6.7 minutes) before it would arrive at the target, so this analysis is applicable as far as horizon considerations are concerned. However, in cases where the horizon is closer in time to the radius at which the missile must be detected, R_D , than the optimum integration time calculated by the above method, that value is of course incorrect. In such cases, the correct optimum integration time is equal to the time from the horizon to R_D .

At present, the longest integrating times found in most radar systems do not exceed 0.01 to 0.1 of a second. Good long-time integrators, particularly of the RF variety, which are the most effective type, are not easy to build, and since transmitter spurious-frequency spread and target modulation are both factors which seriously limit the value of long integration, the advantages of such integration have not yet been fully realized. Even if the transmitter frequency spread were reduced to below 1/180 cps, the target modulation, which should be much less in the case of a missile than in the case of an airplane target, would limit the length of the comb-filter integrating time, which would be of value, to less than three minutes. However, it appears that some portion of future efforts to improve radar detection systems for defense against ICBM's should be dedicated to the improvement of transmitters in regard to stability and development of simpler long-time RF integration devices.

BIBLIOGRAPHY

- [1] A. Hertzberg, "The Wings of Icarus," Res. Trends Cornell Aeronautical Lab., Inc., Buffalo, N. Y., vol. 111, no. 2, pp. 3-6; Summer, 1955.
- [2] L. J. Carter, Ed. "Technical review," *J. Brit. Interplanetary Soc.*, vol. 1, pp. 28-36; January/February, 1956.

Power Spectra of Temperature, Humidity and Refractive Index from Aircraft and Tethered Balloon Measurements*

EARL E. GOSSARD†

Summary—Fifty-seven spectra of temperature, vapor pressure and refractive index were computed from captive balloon data taken at elevations up to 3000 feet MSL. Eight spectra of refractive index were obtained using an aircraft equipped with a microwave refractometer. It was found that atmospheric stability apparently has a pronounced effect on the variation of turbulent intensity with height. Although the spectra of all three parameters generally approach a $-5/3$ power law at high wave numbers, stability seems to have a controlling influence on spectral form at the low-frequency end of the wave number range studied. It is therefore concluded that methods of computing microwave scattered fields from the mean square dielectric perturbations and scale size obtained from the auto covariance are unreliable. The forms of the experimental auto covariances appear to be best represented by an exponential function or perhaps by a Modified Bessel Function of the second kind and $1/3$ order. The temperature-humidity cospectrum may influence the shape of the refractive index spectrum, especially under unstable conditions. The equivalence of Eulerian space and time spectra is verified for refractive index by a series of aircraft-balloon fly-bys.

INTRODUCTION

IN the last decade scattered electromagnetic fields have been explored extensively for communications and radar. Their importance lies in the fact that they are quite measurable far beyond the horizon.

There have been several theories proposed to explain beyond-the-horizon fields. The most widely accepted is the Booker-Gordon theory[1], which assumes that the field is produced by scattering from turbulent dielectric inhomogeneities in the portion of the atmosphere illuminated by the antennas. In some respects the Booker-Gordon theory has agreed well with experimental data and in some respects it has not, depending on what is assumed about the turbulent structure of the atmosphere. According to theory, a simple relation exists between the scattered field and the spectrum of atmospheric refractive-index fluctuations. Recently, there has been much discussion concerning the atmospheric spectra of dynamically passive¹ parameters and their relation to the refractive index spectrum.

If the universal equilibrium theory of turbulence is assumed to be correct, and if we are interested in wave numbers which fall in the so-called inertial subrange, the turbulent energy spectrum is found to be proportional to k^{-q} , where $q=5/3$ and k is wave number. By definition of the inertial subrange, mean-square fluctuations of velocity are conserved² in the inertial transfer

of energy between wave numbers. The corresponding assumption about a dynamically passive parameter (such as specific humidity for example) is controversial. Bolgiano [2], Silverman [3], Batchelor [4], Corrsin [5], and Obukhov [6] believe mean-square fluctuations of such things as temperature and refractive index are conserved through the spectrum and thus arrive at a $-5/3$ power for the wave number dependence as in the case of the energy spectrum. Corrsin gave strong theoretical support for the $-5/3$ law for the case of decaying isotropic turbulence in an enclosed, insulated volume, while Bolgiano treated a more realistic case for the atmosphere by assuming statistical steady state and a constant spatial gradient of the diffusing quantity.

On the other hand Eichi Inoue [7] makes an assumption which in essence means that heat rather than temperature squared is conserved in its transfer through the spectrum. He arrives at a temperature spectrum proportional to $k^{-7/3}$. Villars and Weisskopf [8] find a similar spectrum using the assumption that temperature fluctuations arise from adiabatic effects due to compressibility. Alternatively, they used another assumption analogous to that used in the mixing-length theory of turbulence and found a spectrum proportional to $k^{-9/3}$. This spectrum is supported by some experimental evidence in radio propagation.

One of the principal objectives of the present measurement program was to establish the actual spectral law for refractive index and its component parameters—pressure, temperature, and humidity. Another goal of the meteorological program was to learn more about the effect of stability (buoyancy effects) on atmospheric spectra and on the scale size and intensity of atmospheric turbulence. Possible height dependence was also investigated and the relationship of the spectra of temperature and humidity to that of refractive index was examined. In order to evaluate some of the results it was necessary to examine the relationship between Eulerian space and time spectra at higher wave numbers than have been previously investigated.

THEORY

Scattering Theory

Pekeris [9] and Booker and Gordon [1] have shown that the problem of scattering of plane waves by a randomly inhomogeneous medium can be expressed in simple mathematical form if certain restrictive assumptions are made. The perturbations of refractive index must be small enough so that single scattering can be assumed, and they are also assumed to be discrete, though random, throughout the various ranks of turbu-

* Manuscript received by the PGAP, September 5, 1959.

† Radio Meteorology Section, U. S. Navy Electronics Laboratory, San Diego, Calif.

¹ By a dynamically passive parameter we mean one which does not affect the dynamics of turbulence, such as absolute humidity in the absence of condensation.

² Conserved is used here in the sense that insertion of energy at the low wave number end of the inertial subrange proceeds at the same rate as removal of energy at the high wave numbers.

lons.³ The transmitter and receiver must be sufficiently far from the scattering volume, V , so that the scattering angle is independent of the position of the scattering elements within the volume. However, the volume can usually be subdivided in order to satisfy this restriction, and the various volume subdivisions treated separately.

With these assumptions, the scattered field (the envelope of the radio frequency oscillations) at the receiver becomes

$$\frac{E_s}{E_0} = \frac{2\pi}{\lambda^2 R} \sin X \int_V \Delta n \exp(-i\mathbf{k} \cdot \mathbf{r}) d\mathbf{r}$$

where X is the angle between the incident radiation, E_0 , and the direction from the scattering volume to the receiver, λ is the wavelength, n is the refractive index, R is the distance from the scatterer to the receiver, and \mathbf{r} is the position vector of the scatterer. \mathbf{k} is the vector difference between the wave number of the incident radiation and that toward the receiver.

Writing $A(\mathbf{k})$ as the transform of $\Delta n(\mathbf{x})$ and using (*) to indicate complex conjugate, the equation for the scattered power at the receiver is

$$\frac{P_s}{P_0} = \frac{4\pi^2}{\lambda^4 R^2} \sin^2 X \{A(\mathbf{k}) A(\mathbf{k})^*\}$$

if

$$|\mathbf{k}| \gg V^{-1/3}$$

$$|A(\mathbf{k})|^2 = V \int_r \overline{\Delta n(\mathbf{x}) \Delta n(\mathbf{x} + \mathbf{r})} d\mathbf{r}$$

and

$$\overline{\Delta n(\mathbf{x}) \Delta n(\mathbf{x} + \mathbf{r})} = \int_{\mathbf{k}} F(\mathbf{k}) \exp(i\mathbf{k} \cdot \mathbf{r}) d\mathbf{k}$$

where

$$F(\mathbf{k}) = \frac{|A(\mathbf{k})|^2}{8\pi^3 V}$$

If the turbulence is isotropic, $F(\mathbf{k})$ will be independent of direction and can be expressed in terms of scalar k , $k = |\mathbf{k}|$, the spectrum of which is

$$E(k) = 4\pi k^2 F(k).$$

Finally, the equation for the scattered power [2] is

$$\frac{P_s}{P_0} = \frac{8\pi^4}{\lambda^4 R^2} V \sin^2 X \frac{E(k)}{k^2}$$

where $k = (4\pi/\lambda) \sin(\theta/2)$ and θ is the scattering angle.

The problem of atmospheric turbulence has been too difficult to permit any very general solution to indicate the form of $E(k)$, the power spectrum of refractive index. However, for limited ranges of k some deductions

³ Inoue introduced the term "turbulon" to describe the turbulent entity to which less descriptive terms such as "blob" or "bubble" have often been applied.

can be made about the spectral form of dynamically passive parameters such as specific humidity under restrictive conditions.

Turbulence Theory

Consider the diffusion equation for a parameter, Ψ , in a decaying, isotropic turbulence. Assume the medium to be incompressible with no mean gradients of U or Ψ . The equation at point P is

$$\frac{\partial \Psi}{\partial t} + U_i \frac{\partial \Psi}{\partial x_i} = \nu_\Psi \frac{\partial^2 \Psi}{\partial x_j \partial x_j} \quad (1)$$

At P'

$$\frac{\partial \Psi'}{\partial t} + U_j \frac{\partial \Psi'}{\partial x_j'} = \nu_\Psi \frac{\partial^2 \Psi'}{\partial x_k' \partial x_k'} \quad (2)$$

U is wind speed, and ν_Ψ is the diffusivity coefficient of Ψ . Let $\Psi = \bar{\Psi} + \psi$ and $U = \bar{U} + u$. The equation for the spatial correlation function is obtained as follows. Multiply (1) by ψ' and (2) by ψ . Averaging over-all terms and adding, with $\xi_i = x_i' - x_i$, we get

$$\frac{\partial \overline{\psi \psi'}}{\partial t} - \frac{\partial \overline{u_i \psi \psi'}}{\partial \xi_i} + \frac{\partial \overline{u_j' \psi \psi'}}{\partial \xi_j} = 2\nu_\Psi \frac{\partial^2 \overline{\psi \psi'}}{\partial \xi_k \partial \xi_k} \quad (3)$$

Noting that $-\overline{u_i' \psi \psi'} = \overline{u_i \psi \psi'} = p(r) \xi_i / r$ where $p(r) = |\overline{u_i \psi \psi'}|$ and $|\xi_i| = r$, (3) becomes

$$\begin{aligned} \frac{\partial R(r)}{\partial t} - 2 \left\{ 2 \frac{p(r)}{r} + \frac{\partial p(r)}{\partial r} \right\} \\ = 2\nu_\Psi \left\{ \frac{2}{r} \frac{\partial R(r)}{\partial r} + \frac{\partial^2 R(r)}{\partial r^2} \right\} \end{aligned} \quad (4)$$

where $R(r) = \overline{\psi \psi'}$ is the spatial covariance of ψ .

The equation for the "energy" spectrum of ψ may be obtained by multiplying (4) by $(2/\pi) \cos k_1 r$ and integrating over r from 0 to ∞ . If the transforms of $R(r)$ and $p(r)$ are defined as

$$\begin{aligned} R(r) &= \int_0^\infty E_1(k_1) \cos k_1 r dk_1 \\ p(r) &= \int_0^\infty k_1 Z_1(k_1) \sin k_1 r dk_1 \end{aligned} \quad (5)$$

a differential equation for the one dimensional "energy" spectrum, $E_1(k_1)$, results upon substitution. Kovasznay, Uberoi and Corrsin [10] and Bolgiano [2] have shown that the three-dimensional energy spectrum of the fluctuations of ψ is related to the one-dimensional spectrum as follows:

$$E(k_1) = -2k_1 \frac{\partial E_1(k_1)}{\partial k_1} \quad \text{and} \quad Z(k_1) = -2k_1 \frac{\partial Z_1(k_1)}{\partial k_1} \quad (6)$$

Upon substitution, we obtain the equation for the three-dimensional spectrum:

$$\frac{\partial E}{\partial t} = 2k^2 Z - 2\nu_\Psi k^2 E. \quad (7)$$

This result was first obtained by Corrsin [5]. It may be interpreted as follows. The last term represents a diffusive smearing of the initial patchiness of ψ and leads to a corresponding decrease in the "energy" (first term) in the spectrum with time. The diffusion occurs almost entirely at the very high wave numbers and the "energy" from the lower wave numbers is transferred to the higher wave numbers by the inertial transfer term (middle term) where

$$\int_0^\infty k^2 Z(k) dk = 0.$$

It appears that ψ^2 is conserved as it migrates through the spectrum. This is by no means intuitively obvious. For example, if ψ is temperature it might seem reasonable that heat flux rather than rate of ψ^2 be constant in the turbulent exchange between wave numbers.

An analysis of the energy spectrum (u^2 rather than ψ^2) leads to an equation analogous to (7) [11]. Here, it seems quite reasonable that u^2 should be conserved as it is transferred through the spectrum. If viscous dissipation is confined to the very high wave numbers, there will probably be a range in which viscous dissipation can be neglected. The energy spectrum $E_u(k)$ should then depend only on the (constant) rate of transfer of energy, ϵ , through the spectrum. Dimensional analysis then leads to

$$E_u(k) \propto \epsilon^{2/3} k^{-5/3}. \quad (8)$$

If ψ^2 is conserved through the spectrum, a similar range of wave numbers should exist through which its rate of transfer is constant, ϵ_ψ , for example. If the spectrum of ψ depends only on ϵ_ψ and ϵ , dimensional analysis leads to

$$E(k) \propto \epsilon_\psi \epsilon^{-1/3} k^{-5/3} \quad (9)$$

as shown by Batchelor [4] and Bolgiano [2]. This range of wave numbers is called the "inertial subrange." The wave number dependence given by (9) depends directly on the conservation implied in (7). If rate of transfer of $\sqrt{\psi^2}$ had been assumed constant instead of ψ^2 , dimensional analysis would have led to a wave number dependence of $-7/3$ instead of $-5/3$. Such a dependence was found by Villars and Weisskopf [8] for the refractive index spectrum when they assumed that perturbations in refractive index came from adiabatic fluctuations in density. Such a dependence was also found by Eiichi Inoue [7] when he assumed that rate of heat transfer per unit time and mass was conserved through the spectrum.

The assumptions made by Corrsin are not very realistic for the atmosphere under normal conditions. Bolgiano [2] has analyzed the problem assuming statistical steady state and a constant mean gradient of ψ . He finds in this case, as in that considered by Corrsin, that ψ^2 is conserved in its transfer through the spectrum. It appears, therefore, that the $-5/3$ law has a fairly firm theoretical basis if a wave number range exists in

the atmosphere which is large compared with the input wave number of u and ψ and which is small compared with the wave numbers at which viscous dissipation and smearing occur.

Expanding about $k=0$, Corrsin was able to show that $E(k)$ was parabolic for small k . Using this behavior for small k and the $-5/3$ power law in the inertial subrange, Ogura [12] has suggested the interpolation formula:

$$E(k) = A \left(\frac{k}{k_0} \right)^2 \left\{ 1 + \left(\frac{k}{k_0} \right)^2 \right\}^{-11/6} \quad (10)$$

k_0 is an arbitrary wave number, and A is an arbitrary constant. The corresponding autocorrelation function is

$$\rho(r) = \frac{R(r)}{R(0)} = \frac{2^{2/3}}{\Gamma(1/3)} (k_0 r)^{1/3} K_{1/3}(k_0 r) \quad (11)$$

which for small r becomes

$$\rho(r) \cong 1 - \frac{2^{2/3}}{\Gamma(4/3)} \frac{\Gamma(2/3)}{(k_0 r)^{2/3}} \quad (12)$$

One of the objects of the present study was to compare the experimental data with the various theoretical spectra and correlation functions.

DATA COLLECTION

Area of Operations

The area of operations is shown in Fig. 1. An SNB-5 aircraft flew a saw-tooth pattern from San Diego to San Clemente Island and then to Palos Verdes Estates, where it made a spiral descent in the neighborhood of a captive balloon. It then flew a saw-tooth pattern back to San Diego. The dashed lines in the figure show three scattered-field microwave links in operation while the meteorological measurements were being taken. Distances are indicated in statute miles.

Captive Balloon Data

One type of data was taken with a captive balloon which was flown from terrain which was 900 feet above sea level. The balloon was flown at altitudes up to 3000 feet MSL. The balloon site was at Palos Verdes Estates, which is located on a point projecting out from the Southern California coast near Los Angeles. The seaward exposure of the balloon-borne elements was completely unobstructed by coastal terrain. The captive balloon instrumentation has been described by A. L. Crozier [13]. A 600-cubic-foot Sefang balloon with a free lift of 18 pounds was used to raise the sensing elements (Fig. 2). The sensing elements were Western Electric thermistor beads (D-170575) with a time constant of about 0.5 second. The beads were used in matched pairs, one of which was wrapped with a fine cotton wick and measured wet bulb temperature. Fluctuations of temperature and wet bulb temperature were measured and vapor pressure and refractive index fluctuations were computed by digital computer.



Fig. 1—Area of operations. Microwave links are dashed lines with distances in statute miles.



Fig. 2—Palos Verdes captive balloon installation.

Wind Data

Wind profiles were obtained from a series of pilot balloon observations taken continuously during the tests.

Aircraft Measurements

An SNB-5 aircraft, equipped with a microwave refractometer, EERL Type IV, collected data on refractive index profiles near the test site. The profiles were recorded on an Esterline-Angus recorder with a time constant of about one second. During two of the final tests the refractometer was equipped with an Offner 542 Dynograph Recorder with a frequency response which was good to about 120 cps, and refractive-index spatial spectra were measured by aircraft for comparison with the balloon spectra.

Pressure Fluctuation Measurements

One spectrum of atmospheric turbulent pressure fluctuations was obtained from a tower using a modified T-21 microphone with a capacitance bridge pickup which was amplified and recorded on a 1-milliamper Esterline-Angus recorder. This barovariograph system

has been described by Johnson and Chiles [14]. The frequency response of the pressure system was limited only by the recorder response.

DATA ANALYSIS

Power Spectrum Computation

Digital sampling techniques were used for all data reduction, and computations were performed by digital computer. Covariances were first computed. The power-spectrum estimates were then obtained by taking the Fourier transforms of the auto and cross-covariances. Methods described by Press and Tukey [15] were used to determine the sample size and ordinate density required to obtain the necessary reliability in the power spectrum estimates. For details of this, see the Appendix.

Turbulent Scale Size and Intensity

The turbulent intensities, $R(0)$, are shown in Tables I and II for temperature, vapor pressure, and refractive index. They are the mean square fluctuation of the data.

The scale size listed in Table I is the average value for temperature and humidity from each data sample. It is defined as

$$L = \frac{1}{R(0)} \int_0^m R(r) dr.$$

R is the covariance, and m is the maximum r . r is the lag distance in the spatial covariance analysis. For the balloon data, $r = U\tau$ (see the section on "Comparison of Eulerian Space and Time Spectra") where U is average wind speed and τ is lag time in the time covariance analysis. For the frequency band analyzed, the covariance function was often truncated before it fell to zero, and T could not be accurately computed by this method. The scale size was then computed by assuming that the covariance was exponential in form. The covariance function was plotted on semilog paper and if the resulting plot was nearly linear (as it generally was), its slope was taken as a measure of the scale size of the turbulence.

Similarity and Stability Criteria

The following similarity and stability criteria were computed:

$$\text{Reynold's Number: } Re = \frac{dU}{dz} \frac{L^2}{\nu}$$

$$\text{Richardson's Number: } Ri = B^2 / \left(\frac{dU}{dz} \right)^2$$

$$\text{Vaisala frequency: } B = \left(\frac{g}{\theta} \frac{d\theta}{dz} \right)^{1/2}.$$

θ is potential temperature, z is height, U is wind speed, L is the scale size obtained as indicated above, ν is the kinematic viscosity. The potential temperature gradient, $d\theta/dz$, was obtained by averaging the gradients on

TABLE I
BALLOON DATA

Date	Time	Eleva- tion (ft MSL)	Degrees of Freedom	Samples per second	Wind Knots/Deg	Scale Size (ft)	Temp. (°C)		Vapor Pressure (mb)		Refractive Index (<i>N</i>)†	
							<i>q</i>	<i>R</i> (0)‡	<i>q</i>	<i>R</i> (0)	<i>q</i>	<i>R</i> (0)
3/10	1346	1000	67	8.0	*10.0/185	511	2.26	0.116	2.86	0.260	2.33	4.20
3/10	1350											
3/10	1400	1500	70	8.0	*10.0/185	208	1.73	0.034	2.40	0.238	2.40	5.31
3/10	1404											
3/10	1416	2000	56	8.0	*12.0/185	169	1.79	0.289	1.96	1.314	2.00	31.40
3/28	1418											
3/28	0923	1500	115	8.0	4.0/120	126	1.80	0.021	1.57	0.055	1.83	1.22
3/28	0931											
3/28	0935	1800	57	8.0	4.0/120	220	1.67	0.113	2.10	0.098	2.26	3.03
3/28	0938											
3/28	1007	1100	95	2.0	1.0/—	407	1.40	0.014	1.90	0.173	1.67	3.96
3/28	1029											
3/28	1134	1500	99	8.0	11.0/208	247	1.70	0.032	2.06	0.054	2.00	0.915
3/28	1143											
3/28	1255	3000	77	4.0	3.9/192	412	1.57	0.304	1.63	0.414	1.57	12.02
3/28	1307											
3/28	1316	2500	74	4.0	4.2/228	290	1.67	0.120	1.73	0.245	1.90	7.19
3/28	1325											
3/28	1340	1500	54	4.0	7.0/203	330	1.67	0.056	2.33	0.171	2.56	4.73
4/16	1346											
4/16	1414	1000	105	2.5	4.0/310	91	1.73	0.059	1.63	0.050	1.56	0.950
4/16	1435											
4/16	1440	1200	100	5.0	3.5/310	197	1.83	0.075	1.40	0.027	1.67	0.958
4/16	1444											
4/16	1445	1200	100	2.0	3.5/310	77	1.63	0.017	1.33	0.014	1.26	0.345
4/16	1449											
4/16	1549	1200	55	5.0	3.5/310	41	1.90	0.025	1.57	0.020	1.50	0.509
4/24	1551											
4/24	0826	1500	113	4.0	11.5/101	824	1.96	0.072	2.00	0.046	1.96	1.53
4/24	0842											
4/24	1021	1400	117	4.0	4.2/079	250	1.76	0.092	1.93	0.197	2.23	4.07
4/24	1026											
4/24	1100	1400	80	2.0	4.6/088	131	2.20	0.084	1.90	0.031	1.73	0.596
4/25	1104											
4/25	1008	1500	117	5.0	5.0/190	229	2.16	0.049	1.60	0.018	1.60	0.591
4/25	1019											
4/25	1052	2000	113	4.0	3.0/150	222	2.00	0.151	2.06	0.498	2.16	9.54
4/25	1057											
4/25	1100	2000	113	4.0	3.0/150	147	2.00	0.161	2.13	0.349	2.10	13.28
4/25	1105											

* Winds taken from 1600 PST Los Angeles pibal.

† $N = (n - 1) \times 10^6$, where n is refractive index. For the balloon data, N is computed by digital computer from

$$N = \frac{77.6}{T} \left(P + \frac{4810}{T} e \right)$$

where T is the temperature in °K, P is atmospheric pressure and e is vapor pressure.‡ The $R(0)$'s are obtained in the course of the correlation analysis from (16) of the Appendix.TABLE II
AIRPLANE DATA

Column 1	Column 2	Column 3	Column 4	Column 5	Column 6	Column 7	Column 8	Column 9
Date	Time	Elevation (ft. MSL)	Degrees of Freedom	Samples Per Second	Airplane Speed (Knots)	Scale Size (feet)	Refractive Index (<i>N</i>)	
							<i>q</i>	<i>R</i> (0)
4/24/58	1042	1400	82	100	130	246	2.33	3.29
4/24/58	1044	1400	108	100	130	84	2.17	5.95
4/24/58	1046	1400	58	100	130	136	2.23	1.21
4/24/58	1054	1500	100	100	130	142	2.13	3.01
4/25/58	1044	2000	94	100	130	147	2.83	4.17
4/25/58	1048	2000	113	100	130	78	2.60	2.32
4/25/58	1059	4000	113	200	130	28	2.17	0.017
4/25/58	1107	6000	117	100	130	24	1.60	0.010

the 0400 PST and 1600 PST Los Angeles radiosonde observations at the height of the captive balloon. The wind gradients were obtained from the pibals taken at the captive balloon site during the experiments.

The data taken from pibals and raobs are shown in Table III. In all cases the numbers shown in Table III apply to the local region of the lower atmosphere in which the spectral runs were made. Some of the parameters, especially wind shear, occasionally are not very representative of the sounding as a whole. Local values of Richardson's Number are sometimes deceptively large.

Reynold's Number is a well-known criterion of similarity and must have the same value for dynamically similar flows. The constitution of the number shows that it depends not only on the viscosity, but on appropriate linear dimensions and velocity. In selecting the appropriate form of Reynold's Number, we have assumed that the vertical wind shear in the atmosphere will have a considerable influence on the turbulent velocity in the medium and that vertical scale size will be closely related to the more readily measurable horizontal scale size.

Richardson's Number is often used as a criterion to determine whether turbulence will increase or decrease. The flow should remain turbulent if the work done by the Reynold's stresses [represented by $(dU/dz)^2$] is at least as great as the work necessary to maintain the turbulence against gravity (represented by the Vaisala frequency). A critical Richardson's Number would therefore be a criterion of "just no turbulence." Various estimates of critical values above which turbulence tends to die out range from $\frac{1}{4}$ to 1.0, although some experimental results with boundary layers in the atmosphere have led to much higher values.

The Vaisala, or Brunt, frequency is a measure of static stability of the medium. In studies of linear atmospheric processes (such as gravity waves) in contrast with processes in which nonlinear terms dominate the equations of motion (such as turbulence), the Vaisala frequency appears as a critical parameter in atmospheric perturbations. A detailed study of its effect on oscillations in a stable atmosphere has been given by Gossard and Munk [16].

RESULTS

The results of sixty-five spectrum and correlation analyses for five days representing different weather types are summarized in Tables I and II.

The morning raob on March 28, 1958 at San Diego showed a thoroughly mixed atmosphere to at least 10,000 feet. In the afternoon the 1600 PST raob indicated that a slight temperature inversion had descended to about 7000 feet MSL. The Los Angeles raobs indicate instability to at least 6000 feet all day. However, Table

TABLE III
RAOB AND PIBAL DATA

Column 10	Column 11	Column 12	Column 13	Column 14	Column 15
Date	Time	Elevation (ft MSL)	Re	Ri	B
3/10/58	1346	1000	—*	—*	0.0078
3/10/58	1350				
3/10/58	1400	1500	—	—	0.0078
3/10/58	1404				
3/10/58	1416	2000	—	—	0.0078
3/10/58	1418				
3/28/58	0923	1500	1,249	0.662	0.0096
3/28/58	0931				
3/28/58	0935	1800	3,807	0.662	0.0096
3/28/58	0938				
3/28/58	1007	1100	13,031	0.662	0.0096
3/28/58	1029				
3/28/58	1134	1500	4,760	0.662	0.0096
3/28/58	1143				
3/28/58	1255	3000	2,263	22.8	0.0096
3/28/58	1307				
3/28/58	1316	2500	1,336	16.0	0.0096
3/28/58	1325				
3/28/58	1340	1500	1,740	15.9	0.0096
3/28/58	1346				
4/16/58	1414	1000	331	3.6	0.0113
4/16/58	1435				
4/16/58	1440	1200	1,552	3.6	0.0113
4/16/58	1444				
4/16/58	1445	1200	231	3.6	0.0113
4/16/58	1449				
4/16/58	1549	1200	64	3.6	0.0113
4/16/58	1551				
4/24/58	0826	1500	16,295	5.4	0.0083
4/24/58	0842				
4/24/58	1021	1400	4,167	0.69	0.0083
4/24/58	1026				
4/24/58	1100	1400	1,239	0.59	0.0083
4/24/58	1104				
4/25/58	1008	1500	3,604	0.45	0.0070
4/25/58	1019				
4/25/58	1052	2000	3,417	1.93	0.0145
4/25/58	1057				
4/25/58	1100	2000	1,498	1.93	0.0145
4/25/58	1105				

* Santa Monica pibal not adequate for wind gradient.

III shows that the Richardson's Number became quite large in the afternoon of March 28 as a result of very small wind shear at the altitude at which the balloon was flown. The weather was characterized by swelling cumulus and gusty winds. On the other hand, April 16, 1958 was relatively stable. The morning Los Angeles raob shows a strong surface-based inversion. Although the inversion lifted during the day, the lapse rate beneath it remained fairly stable, as shown by the Vaisala frequency and Richardson's Number. The Los Angeles raobs taken on April 24, 1958, showed a small inversion forming at about 2000 feet MSL as the day progressed. However, the atmosphere was fairly unstable at the altitudes at which the balloon and aircraft were flown, as shown by Table III. On April 25, 1958, a refractometer sounding showed a prominent superrefractive layer with a base at 1700 feet and a top at 5000 feet MSL. Two balloon spectra and four aircraft spectra were obtained within the superrefractive (and stable) layer.

Scale Size and Intensity

Table I shows that neither intensity nor scale size measured by captive balloon seems to be significantly related to wind speed at the balloon. However, atmospheric stability seems to have a pronounced effect on the height variation of both scale size and intensity.

On March 28, 1958, seven balloon runs at several elevations were made. As shown by the three runs at 1500 feet, there is considerable variation in scale size and intensity even at the same elevation. However, a consistent increase in scale size and intensity with height seems evident, as shown by Fig. 3. It should be noted that the scale and intensity increased up to an elevation of at least half the probable depth of the convective layer. This pattern of variation with height is supported by that produced by the runs made on March 10, 1958, which was also unstable and is in sharp contrast to the variation with height observed on April 25, as shown by Fig. 4.

On April 25, the aircraft made four runs with the microwave refractometer. Two runs were made at 2000 feet, one at 4000 feet, and one at 6000 feet MSL. The refractometer sounding shown in Fig. 5 indicates that the runs were distributed through a superrefractive layer. They indicate a strong *decrease* in both scale size and intensity with elevation through the layer.

Power Spectra

The spectrum information appears in Tables I and II under column "q," which is the average slope of the spectra on log-log plots. The reliability of the spectral estimates is indicated by the degrees of freedom shown in Tables I and II for each run (see Appendix).

The runs on March 28 often show two distinct regions of different slopes (Figs. 6–8). For this reason the q values in the tables are somewhat misleading since they represent an average slope for the whole frequency range analyzed. Average balloon spectra for March 28, April 16, April 24, and April 25 are shown in Figs. 9–11. A tendency for a change in slope at about $k=0.14$ on March 28 appears even in the average curves. The spectra consist of a high-frequency region in which the slope approximates the $-5/3$ to be expected in the inertial subrange and a region of higher (negative) slope of about $-7/3$ at lower frequencies. The run at 1800 feet showed the most pronounced change in slope through the spectrum. It was therefore decided to examine the low frequencies in this run in more detail, at the sacrifice of the greater ordinate accuracy maintained for the higher frequencies. This was done by averaging groups of eight data bits from the original sample. The sample size was therefore reduced to one-eighth the original size and the spectrum was recomputed. The results are shown as the dashed curve in Fig. 12. It is seen that the spectrum appears to be approaching a peak at scales greater than 628 feet ($k<0.01$). This suggests a

scale of energy input for this day greater than 1000 feet. Transition to the inertial subrange occurred at a wave number of about 0.14 on March 28.

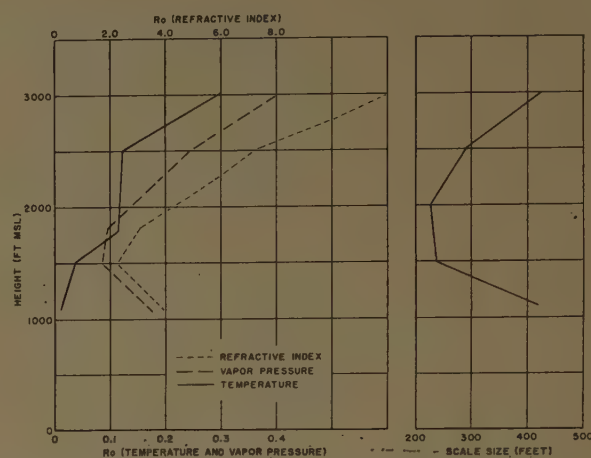


Fig. 3—Effect of height on scale size and intensity of fluctuations of temperature, vapor pressure, and refractive index on March 28, 1958; from tethered balloon data taken under thermally unstable conditions.

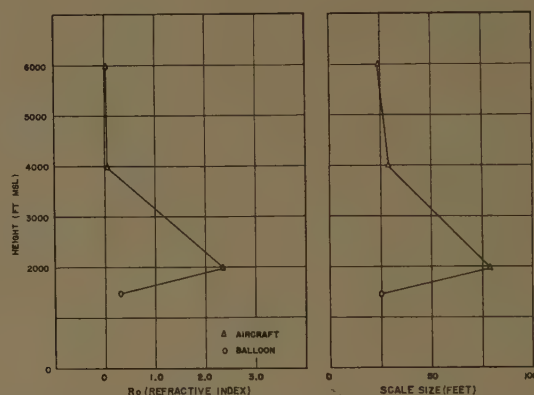


Fig. 4—Effect of height on intensity and scale size of refractive index fluctuations on April 25, 1958; from aircraft data taken within a stable layer.

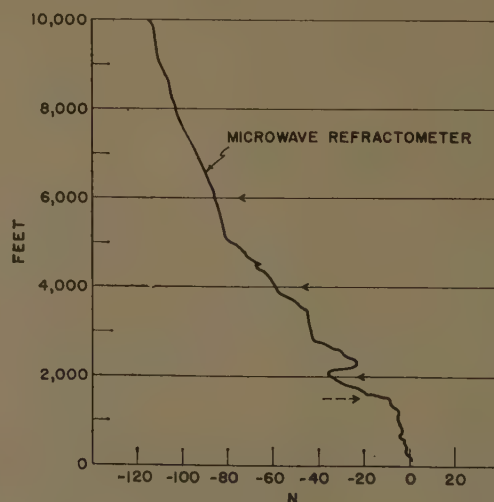


Fig. 5—Microwave refractometer soundings, April 25, 1958. Altitude vs modified refractive index.

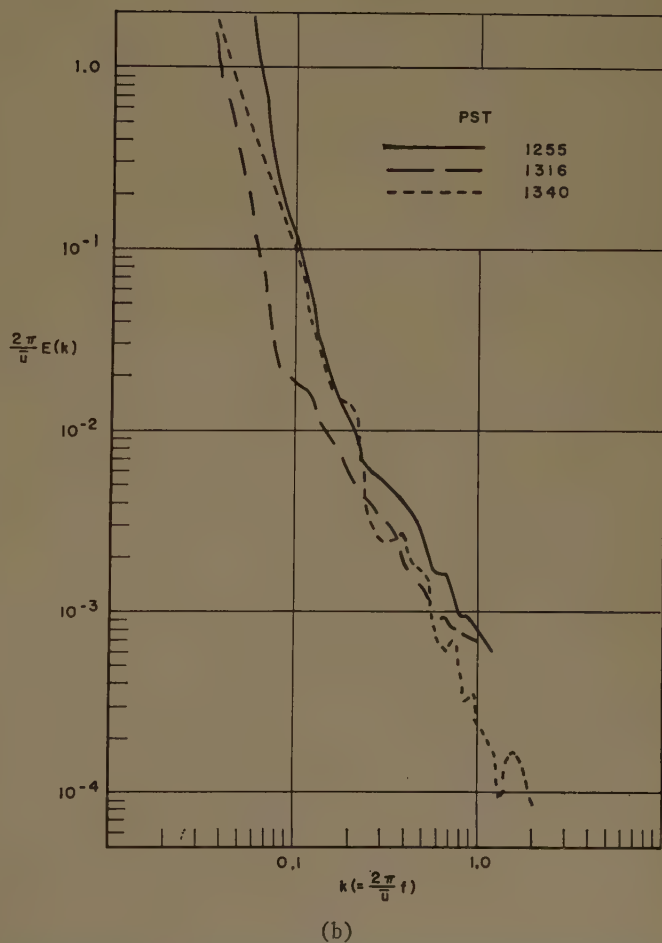
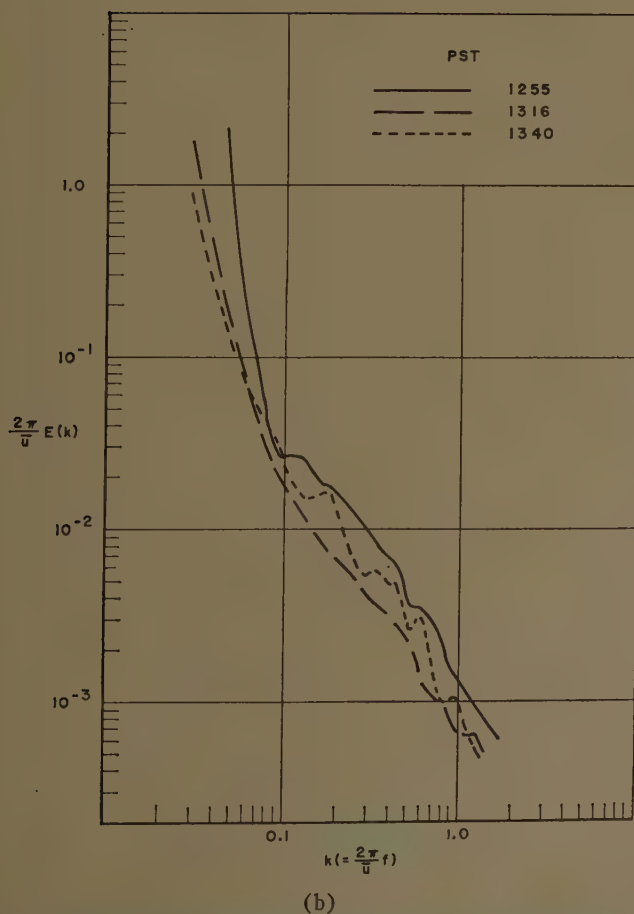
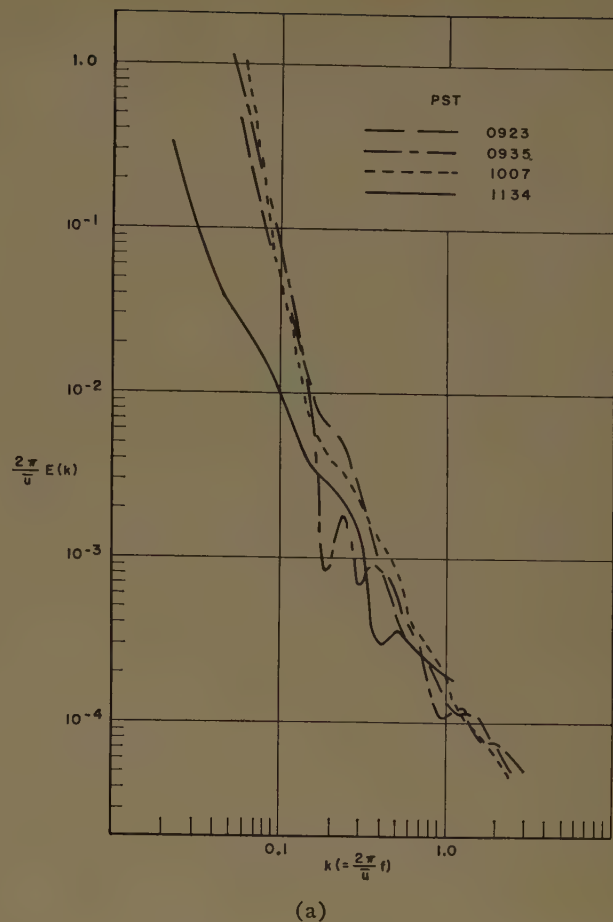
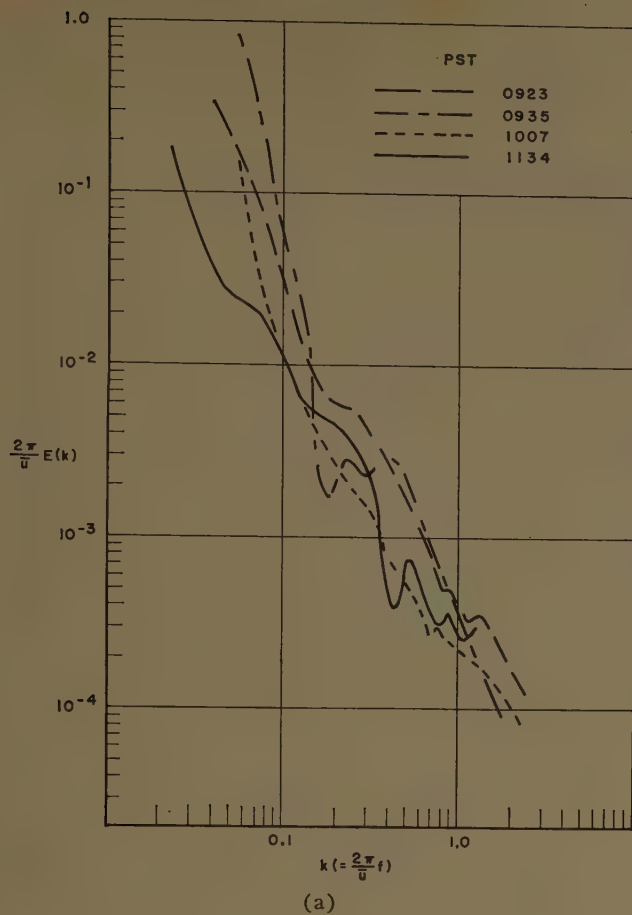


Fig. 6—Spectra of temperature on March 28, 1958, from data taken by tethered balloon. k is in ft^{-1} . (a) morning, (b) afternoon.

Fig. 7—Spectra of vapor pressure on March 28, 1958, from data taken by tethered balloon. k is in ft^{-1} . (a) morning, (b) afternoon.

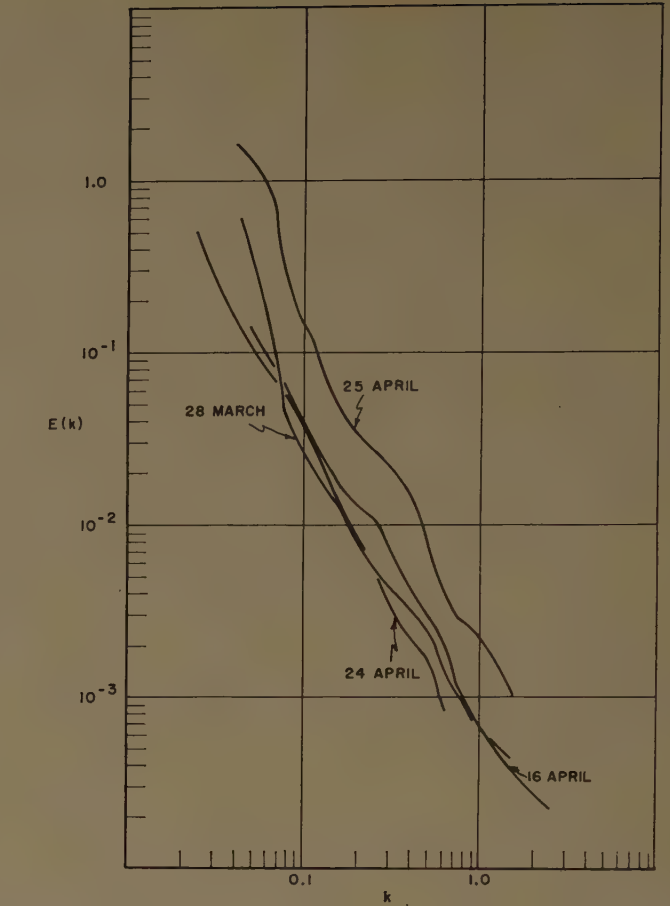
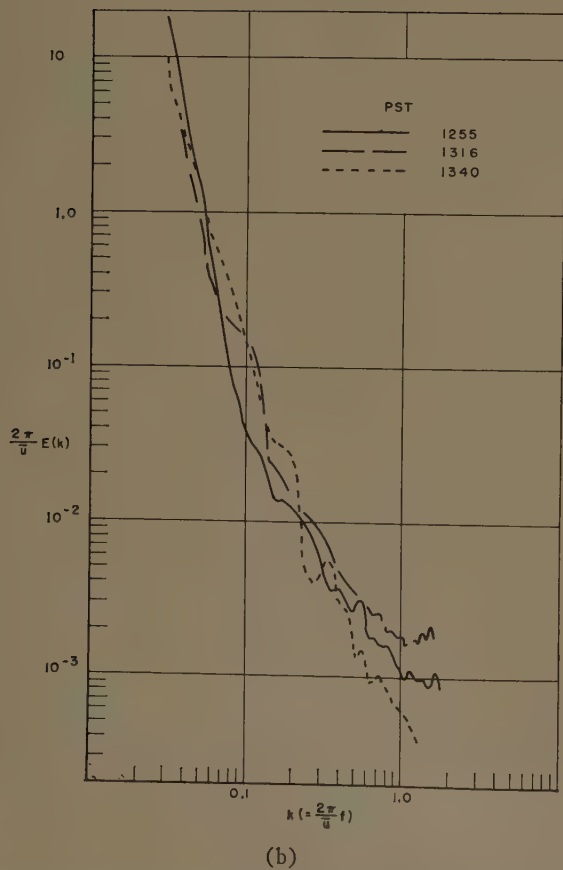
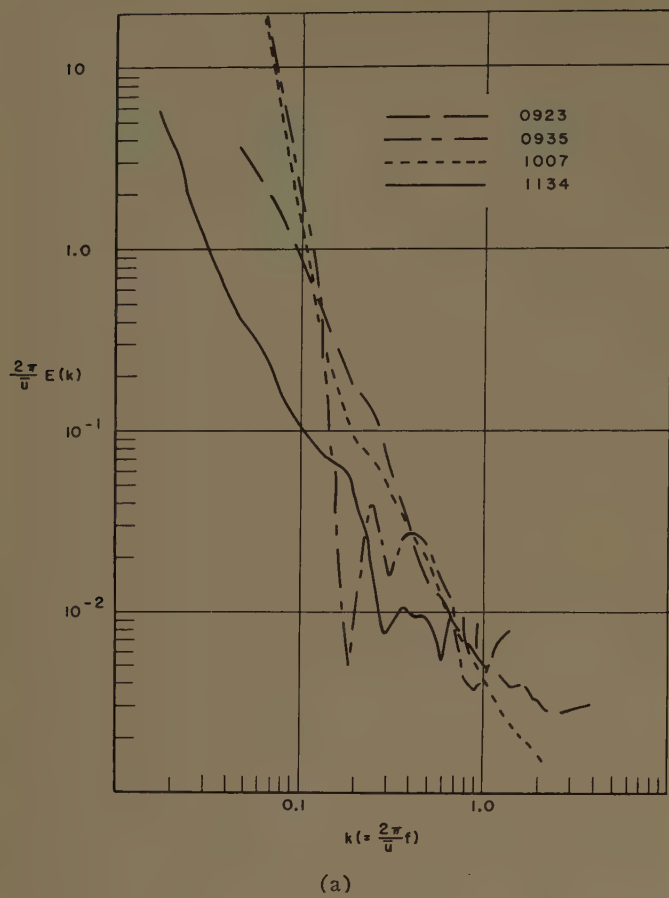


Fig. 9—Average temperature spectra for March 28, April 16, April 24, and April 25, 1958. From data taken by tethered balloon.

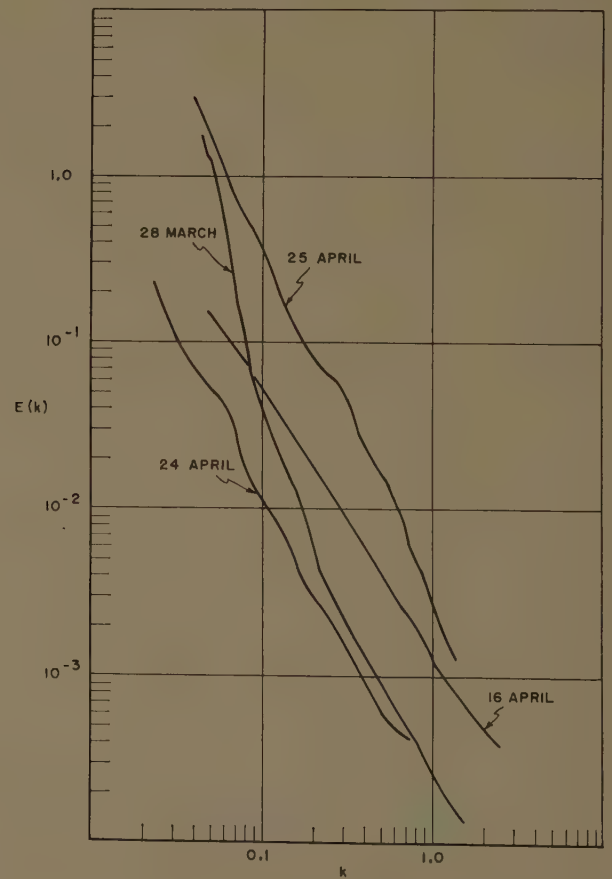


Fig. 10—Average vapor pressure spectra for March 28, April 16, April 24, and April 25, 1958. From data taken by tethered balloon.

Fig. 8—Spectra of refractive index on March 28, 1958, from data taken by tethered balloon. k is in ft^{-1} . (a) morning, (b) afternoon.

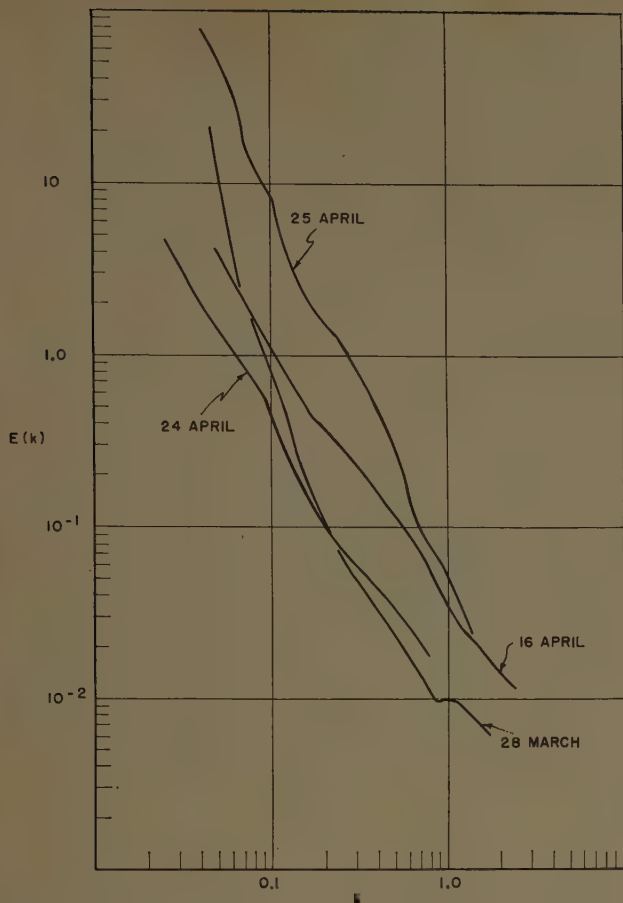


Fig. 11—Average refractive index spectra for March 28, April 16, April 24, and April 25, 1958. From data taken by tethered balloon.

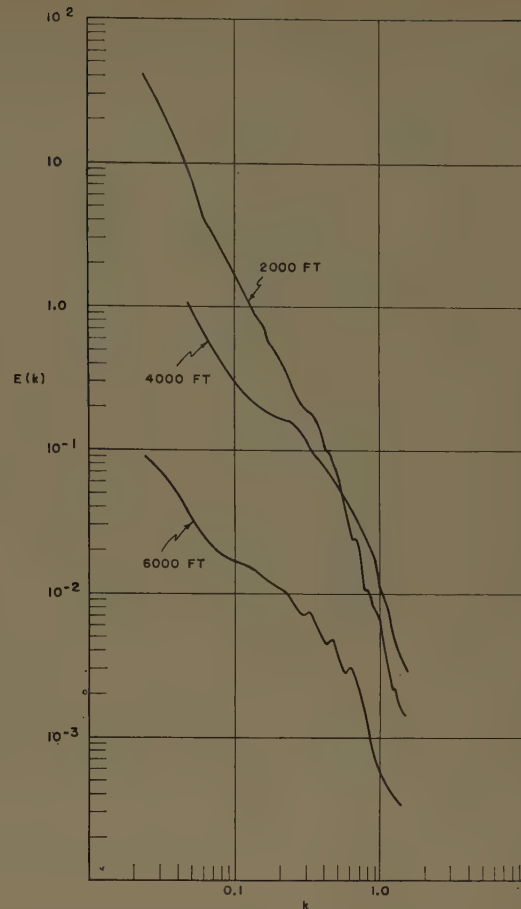


Fig. 13—Spectra taken by aircraft at various elevations through superrefractive layer, April 25, 1958. The run at 2000 feet MSL was made at 1048 PST and was similar to the 2000-foot run made at 1044 PST.

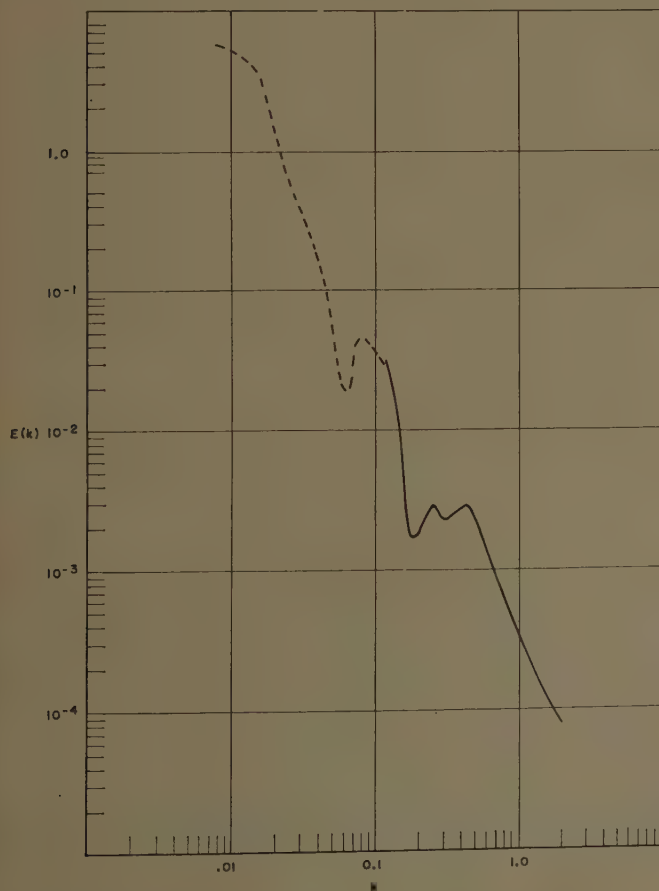


Fig. 12—Temperature spectrum at 1800 feet MSL, March 28, 1958. Dashed portion of curve has only about 10 degrees of freedom (see Appendix).

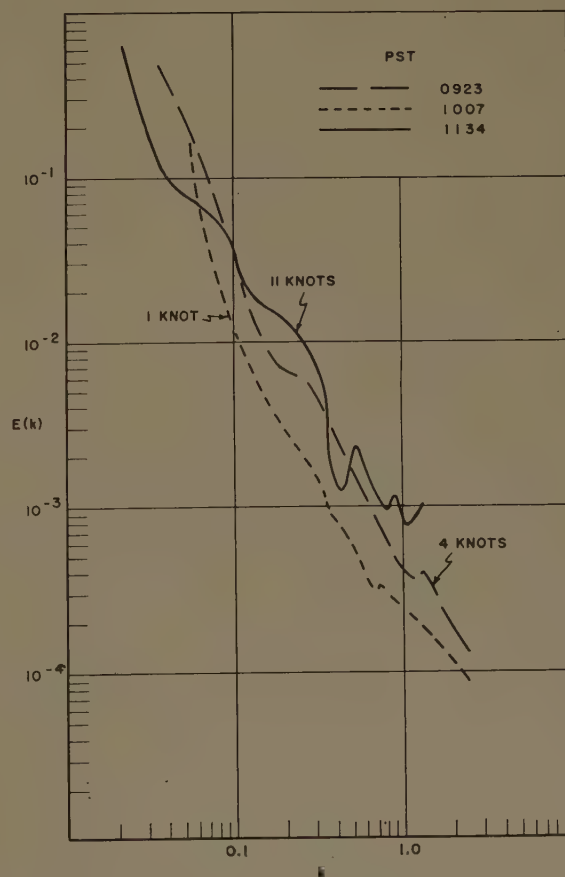


Fig. 14—Spectra for three different wind speeds, March 28, 1958.

The aircraft spectra taken on April 25 within the superrefractive layer show a tendency exactly opposite to those of March 28 (Fig. 13). Again the spectra appear to approach a $-5/3$ slope at high wave numbers and to depart radically from $-5/3$ at lower wave numbers at both the 4000- and 6000-foot levels. However, the departure is toward smaller (negative) slopes, and it increases with elevation. The spectra at 2000 feet MSL within the refractive layer are nearly linear, while those higher within the refractive layer show less and less energy in the lower wave numbers. It is interesting that the energy in the highest wave numbers appears to be fairly conservative. It seems that one, or possibly two, scales of energy insertion lie in or near the range of the spectrum considered in this report. The shape of the spectrum depends critically on where this range lies with respect to the input scales. Thermal stability is an important factor in determining the scales of energy input.

These data cast doubt on any methods of computing scattered fields at microwave frequencies which use intensity and scale size of refractive index perturbations obtained from measured auto covariance. The spectrum at high wave numbers often differs appreciably in form from that at lower wave numbers. It is the lower wave numbers that influence the measured intensity, but, according to the usual theoretical treatment, it is the higher wave numbers that are effective in scattering microwaves. Atmospheric stability appears to have a pronounced effect on the form of the spectrum and the magnitude of the power in the low frequencies, but relatively little effect on the power at high frequencies.

Wind speed has a greater effect on the frequency spectrum than any other single factor when measured at a point in space. However, this effect is mostly just the rate of advection of the inhomogeneities past the recording point and almost disappears when the spectra are plotted vs wave number, as shown by Fig. 14.

Correlation Functions

A great deal of interest has centered about the form of the correlation or covariance function of refractive index, although the power spectrum is of more direct importance to scattered field propagation. The principal correlation functions which have been considered in the literature on electromagnetic propagation and meteorology have been the following:

Exponential

$$\rho(r) = e^{-r/l}$$

Modified exponential

$$\rho(r) = \left(1 + \frac{r}{e}\right) e^{-r/l} \quad (13)$$

Gaussian

$$\rho(r) = e^{-r^2/l^2}$$

Modified Bessel function second kind (1st order)

$$\rho(r) = \frac{r}{l} K_1\left(\frac{r}{l}\right)$$

Modified Bessel function second kind (1/3 order)

$$\rho(r) = \frac{2^{2/3}}{\Gamma(1/3)} \left(\frac{r}{l}\right)^{1/3} K_{1/3}\left(\frac{r}{l}\right)$$

The exponential correlation function was first used by G. I. Taylor in his pioneering work in the statistical theory of turbulence. It was used by Booker and Gordon [1] in their theory of forward scattering of electromagnetic energy by turbulent inhomogeneities. The three functional forms following the exponential in (13) have been used mostly by workers in the field of electromagnetic propagation and have been chosen mainly because of an intuitive suspicion of the discontinuity in slope at the origin which characterizes the exponential function.

The last function shown in (13) has the soundest theoretical support. It is based on the theoretical behavior of the spectrum as outlined under "turbulence theory" above. For very small wave numbers, Corrsin [5] showed that the spectrum should be parabolic in form. Ogura [12] has proposed an interpolation formula for the spectrum which satisfies the parabolic requirement at low wave numbers and the $-5/3$ law in the inertial subrange. Since the function is analytic, the corresponding form of the correlation function can be obtained by using the transform relationship of power spectrum and correlation function. Thus Ogura obtains the modified Bessel function of $\frac{1}{3}$ order.

In the study reported here a simple test was applied to the experimentally obtained correlation functions in order to check their agreement with the various theoretical forms. If the curvature⁴ of the above functions is examined it is seen that the curvatures of the modified exponential, Gaussian and modified Bessel (1st order), are less than those of the exponential, while that of Ogura's function is greater than the exponential in the range of interest. All correlation functions were therefore plotted on semilog paper. Negative curvature of the semilog plots then indicates one of the former functions, while zero curvature or positive curvature on semi-log plots supports either the exponential or Ogura's function. The following results were obtained:

⁴ Curvature is used here as the second derivative of the function. Thus the modified exponential, Gaussian and modified Bessel, second kind, 1st order, has either a negative curvature, or a smaller positive curvature than the exponential.

Balloon Data (number of cases)

Curvature	+	0	-	Mixed
Temperature	10	8	2	0
Vapor pressure	6	10	3	1
Refractive index	13	5	1	1

Aircraft Data (number of cases)

Curvature	+	0	-	Mixed
Refractive index	3	3	1	1

The results seem to give strong support to either the exponential function or Ogura's function. This result is at variance with conclusions reached by Edmonds, Bos-tick and Cerhardt[17] which were based on the form of spectra of refractive index which they obtained by aircraft over Colorado at elevations up to 20,000 feet. They found that the modified exponential correlation function gave the best agreement with their spectra in the range of scale size from approximately 40 to 400 feet. However our data indicate that this is a scale size range in which considerable day-to-day variability is to be expected.

Pressure Spectrum

Fig. 15 shows spectra of pressure, temperature, vapor pressure, and refractive index recorded simultaneously on March 13, 1957. The data were recorded at San Diego on a tower 500 feet above sea level. The refractive index spectrum is the computed spectrum using the recorded temperature and vapor pressure. On theoretical grounds one would expect the pressure spectrum to have a greater (negative) slope than the $-5/3$ anticipated for the temperature and vapor pressure spectra. No such difference is evident from the data. However, no conclusions can safely be drawn from a single sample, especially since all the spectra show slopes greater than $-5/3$. More pressure spectra will be obtained in the near future. It should be noted at this point that the refractive index spectrum on March 13 is somewhat different in form from the other spectra. This will now be shown to be a result of significant cross covariance between temperature and vapor pressure.

Temperature-Humidity Cospectrum

One of the interesting results of the atmospheric spectrum analyses was the fact that the cospectrum of temperature and humidity is often not negligible. This implies that the spectrum of refractive index need not be identical in shape to that of temperature and humidity even if the latter have the same spectral form. To see this, we linearize the refractive index equation for small perturbations and, using average values of pressure, temperature, and humidity appropriate to the Palos

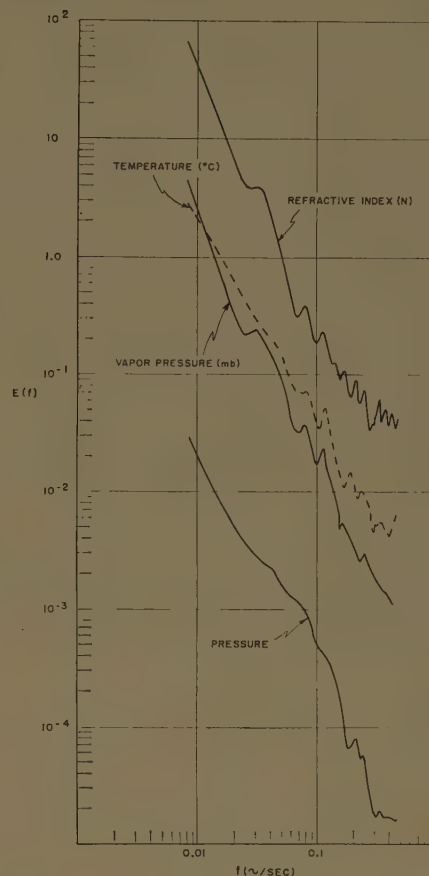


Fig. 15—Spectra of pressure, temperature, vapor pressure, and refractive index, taken simultaneously on March 13, 1957.

Verdes site, we find

$$N' = 0.25p' - 1.4T' + 4.6e'$$

where the prime indicates departure from the average and N , p , T , and e are respectively, modified refractive index, pressure in millibars, temperature in degrees Centigrade, and vapor pressure in millibars. The standard deviation of pressure was found to be so small (0.063 mb) that the first term on the right was completely negligible, so only spectra of temperature and humidity need be considered. Therefore:⁵

$$L_N = 2L_T + 21L_e - 13L_{Te}$$

where L is the ordinate of the power spectrum and the subscripts indicate the variable to which the spectrum applies. L_{Te} is the cospectrum (real part of the cross-spectrum) of temperature and humidity.

The assumption is often made that L_{Te} is zero, and that the form of the refractive index spectrum can be deduced from that of temperature and humidity. Thus, if the temperature and humidity spectra are propor-

⁵ The constants in this equation are derived from those of N' above, using (14) of the Appendix.

tional to $k^{-5/3}$ it would follow that the refractive index spectrum is also proportional to $k^{-5/3}$. Since turbulence theories predict the forms of the temperature and humidity spectra, it would follow that the refractive index spectrum could be deduced theoretically. Actually, however, the cospectrum is not always negligible, as shown in Fig. 16. In fact, it may far outweigh the temperature spectrum. Note that on March 13 and March 28 (both unstable days) the curves with and without the cospectrum often differ by a factor of two or more. This is sufficient to cause the form of the refractive index spectrum to be substantially different from that of the temperature and humidity spectra if the cospectrum differs from them in a consistent manner. Only three cospectra have been computed. These preliminary results do not indicate that the cospectrum has a very consistent form. Therefore, it probably does not affect the average shape of the refractive index spectrum very much. Note that the cospectrum is much more important on March 28 and March 13 than on April 16, when the lower atmosphere was relatively stable.

Comparison of Eulerian Space and Time Spectra

In 1938, G. I. Taylor suggested that the frequency analysis of velocity variations measured at a point was approximately identical with the wave number analysis of the velocity variations along a line in the direction of the air stream.

On April 24 and April 25 an SNB-5 aircraft equipped with a microwave refractometer made several passes by the captive balloon. The purpose of these tests was to check the adequacy of aircraft for measuring small scale (a few feet) features in the atmosphere and to verify Taylor's hypothesis at high wave numbers. Gifford [18] has concluded from theoretical considerations based on work by Ogura [19] that Taylor's hypothesis should apply in the atmosphere for small values of u^2/U^2 , where U is ambient wind speed and u is the turbulent perturbation. According to Panofsky [20], Bunker obtained experimental data in 1953 using an accelerometer in an aircraft which flew by a tower on which wind measuring instruments were located. These spectra seem to verify the Taylor hypothesis for scale sizes down to about the size of the aircraft. Using aircraft flights by the balloon, it was hoped that it would be possible to check this hypothesis for dynamically passive parameters (such as refractive index) at much higher wave numbers than had been previously examined. This was made possible by the extremely fast response of the microwave refractometer and recorder used in the aircraft. Scale sizes down to approximately 2 feet were easily measurable. On April 24 the aircraft made four passes by the balloon while it was at 1400 feet. Fig. 17 shows the average of the four aircraft spectra and the corresponding point spectrum measured by the captive balloon. The agreement is excellent. In fact the individual aircraft spectra differed from each other considerably more than

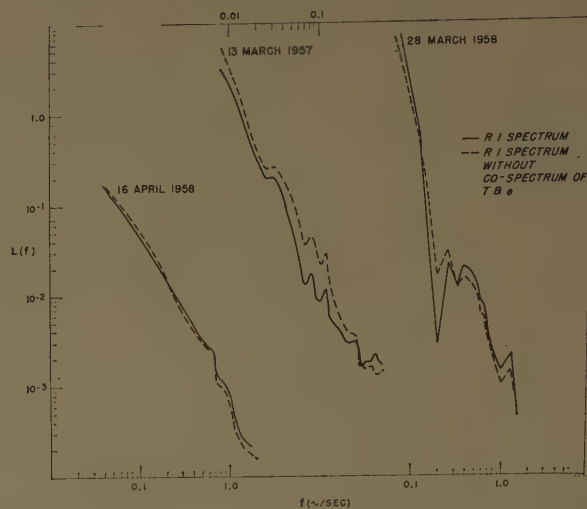


Fig. 16—Refractive index spectra computed from temperature and vapor pressure spectra with (solid line) and without (dashed line) cospectrum of temperature and humidity. L is proportional to $E(k)$ and is defined in the Appendix.

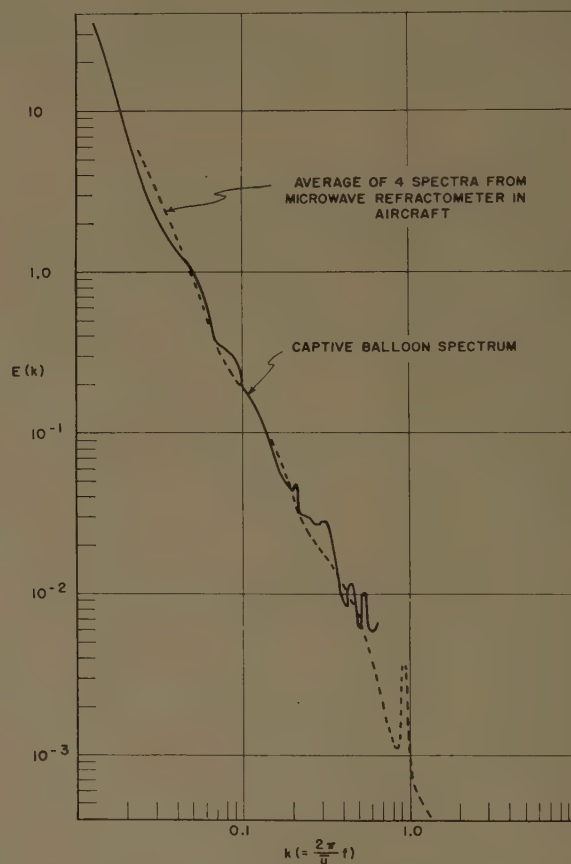


Fig. 17—Airplane vs balloon spectra from data recorded at 1400 feet on April 24, 1958.

the balloon spectrum differs from the aircraft average spectrum. A line appears in the aircraft spectra at a wave number of 0.95. This corresponds to the engine rpm of the aircraft and is probably propeller noise. On April 25, balloon spectra were measured at 1500 feet MSL at 1008 PST, and at 2000 feet MSL at 1052 and 1100 PST. The aircraft made fly-bys at 2000 feet MSL

at 1044 and 1048 PST. The results again show satisfactory agreement, though it is not as impressive as that on April 24. The runs were made in the neighborhood of the sharp peak in intensity shown on Fig. 4 and large variations in both space and time have probably affected the results. Altogether the fly-bys appear to support Taylor's hypothesis in the atmosphere at very high wave numbers. It also appears that aircraft measurements can be used to measure reliably scale sizes much smaller than the aircraft itself.

CONCLUSIONS

The following conclusions appear to be justified from the data obtained in this study:

1) Intensity and scale size *increase* with height under convectively unstable conditions. This increase may extend to at least half the depth of the mixed layer, as shown by data collected on March 28, 1958.

Scale size and intensity *decrease* sharply with height through a stable layer as shown by the April 25 data.

2) Power spectra obtained under unstable conditions differ significantly in the lower frequencies from those obtained within a stable layer, although both seem to approach the $-5/3$ law at high wave numbers. Under *unstable* conditions there is slightly *more* energy in the lower frequencies than would be predicted by the $-5/3$ law, and log-log plots of the spectra tend to have positive curvature. A region of energy input somewhat lower than the wave numbers examined in this report is suggested by the March 28 data.

Under *stable* conditions the spectra showed a large *deficit* of energy in the lower wave numbers. This deficit becomes more pronounced with elevation within the stable layer. The energy at high frequencies is surprisingly conservative.

3) Methods of computing microwave scattered fields from intensity and scale size of refractive index perturbations obtained from measured auto covariance are unreliable. The intensity $(\bar{N}')^2$ is controlled by the energy in the lower frequencies, while microwave scattered fields are effected by the high frequencies, and the form of the spectrum often varies considerably through its total range.

4) The experimental auto covariances can best be represented by an exponential function or by a modified Bessel function of the second kind and $\frac{1}{3}$ order for the range of scale sizes here considered.

5) There was no evidence that the pressure spectrum recorded on March 13, 1958 differed significantly in form from the temperature and humidity spectra recorded at the same time.

6) The cospectrum of temperature and humidity was sometimes found to be important. If deductions about the form of the refractive index spectrum are to be made from the form of the temperature and humidity spectra, the cospectrum should be taken into account, especially under conditions of convective instability.

7) Taylor's hypothesis is verified at frequencies and wave numbers which were not examined heretofore.

APPENDIX

DIGITAL METHOD FOR COMPUTING POWER SPECTRUM

Tukey [21], Panofsky and McCormick [22], Potter [23] and Munk *et al.* [24] have discussed digital techniques for computing spectra with high-speed digital computers. The transform relationship was made use of between the covariance function and the power spectrum:

$$R(\tau) = \int_0^\infty E(\omega) \cos \omega \tau d\omega \quad (14)$$

$$E(\omega) = \frac{2}{T \rightarrow \infty} \frac{1}{\pi} \int_0^T R(\tau) \cos \omega \tau d\tau \quad (15)$$

where τ is the lag time in the covariance analysis and $\omega = 2\pi f$ where f is frequency in cycles per second. If the record is periodically sampled such that successive samples are separated by a time interval Δt , the highest usable frequency in the record is $(2\Delta t)^{-1}$. Therefore $f = (2\Delta t)^{-1}h/m$ where $h=0, 1, 2, 3, \dots, m$, and $\tau = p\Delta t$ where $p=0, 1, 2, 3, \dots, m$. m is the number of lags of length Δt used in the covariance analysis.

Numerical integration of (15) gives

$$E(\omega) \cong \frac{2}{\pi} \Delta t \sum_{p=0}^{p=m} \delta R(p) \cos \frac{\pi h p}{m} \cdot$$

$$\delta = \frac{1}{2} \quad \text{for } p=0 \quad \text{or } p=m.$$

If we assume

$$L(h) = \frac{2}{m} \sum_{p=0}^{p=m} \delta R(p) \cos \frac{\pi h p}{m},$$

we have:

$$E(\omega) = \frac{T}{\pi} L(h),$$

where T is the total time interval over which the lag, τ , extends.

The various $R(p)$ and $L(h)$ corresponding to auto- and cross-covariances and co- and quadrature-spectra are obtained as follows. The covariance functions are first computed. Let one data sample be represented by $x_1, x_2, x_3 \dots x_i \dots x_N$ and another by $y_1, y_2, y_3 \dots y_i \dots y_N$. The auto- and cross-covariances are given by

$$R_{11}(p) = \frac{1}{N-p} \sum_{i=0}^{i=N-p} x_i x_{i+p}$$

$$R_{22}(p) = \frac{1}{N-p} \sum_{i=0}^{i=N-p} y_i y_{i+p}$$

$$R_{12}(p) = \frac{1}{N-p} \sum_{i=0}^{i=N-p} x_i y_{i+p}$$

$$R_{21}(p) = \frac{1}{N-p} \sum_{i=0}^{i=N-p} y_i x_{i+p} \quad (16)$$

The ordinates of the spectra are given by:

Power spectra

$$L(h) = \frac{1}{m} \left[R_{11}(0) + \sum_{p=1}^{p=m-1} R_{11}(p) \left(1 + \cos \frac{\pi p}{m} \right) \cos \frac{\pi p h}{m} \right]$$

$$L(h) = \frac{1}{m} \left[R_{22}(0) + \sum_{p=1}^{p=m-1} R_{22}(p) \left(1 + \cos \frac{\pi p}{m} \right) \cos \frac{\pi p h}{m} \right].$$

Cospectrum

$$L(h) = \frac{1}{m} \left[R_{12}(0) + \sum_{p=1}^{p=m-1} \frac{R_{12}(p) + R_{21}(p)}{2} \cdot \left(1 + \cos \frac{\pi p}{m} \right) \cos \frac{\pi p h}{m} \right].$$

Quadrature-Spectrum

$$L(h) = \frac{1}{m} \left[\sum_{p=1}^{p=m-1} \frac{R_{12}(p) - R_{21}(p)}{2} \cdot \left(1 + \cos \frac{\pi p}{m} \right) \sin \frac{\pi p h}{m} \right].$$

The "smoothing function" $[1 + \cos (\pi p/m)]$ was suggested by Press and Tukey [15]. It has the effect of reducing the "sidelobes" produced by the digital nature of the filtering process at the expense of somewhat broadening the main band pass.

Tukey has discussed the dependence of ordinate accuracy on sample size and number of ordinates. If the data are actually normally distributed, a X^2 distribution for the variances implies that

$$\beta = 2.5 \frac{N - m}{m}$$

where β is "degree of freedom." Actually, Tukey recommends

$$\beta = 2 \frac{N - m}{m},$$

since actual data are not likely to be exactly normally distributed. The behavior of Chi squared for varying degrees of freedom indicates the ordinate reliability. Tukey [21] and Potter [23] have published curves showing the limits within which the actual ordinates will lie 90 per cent of the time. Table IV shows some typical values. The degrees of freedom, and therefore the ordinate confidence for the spectra in this report, are shown in Tables I and II.

TABLE IV

Degrees of Freedom	Ordinate Range		
	Ordinate Range (observed/average)		
100	1.25	—	0.80
75	1.28	—	0.76
50	1.33	—	0.70
25	1.48	—	0.59
10	1.80	—	0.40

ACKNOWLEDGMENT

The author wishes to express his appreciation to R. U. F. Hopkins, W. F. Moler, and N. R. Ortwein for many helpful discussions, and to Profs. R. Bolgiano of Cornell University's School of Electrical Engineering and J. Gerhardt of the University of Texas EERL for critically reading the manuscript prior to publication.

Ensign G. B. Hayes was primarily responsible for the success of the data-collecting operations, and the exhaustive computer programming and data analysis were carried out by F. A. Sabransky.

The cooperation of the personnel of the Fleet Weather Facility, NASNI, under Commander Davies, and of the operations and maintenance personnel of NASNI, was especially important to the successful completion of the measurement program.

BIBLIOGRAPHY

- [1] H. G. Booker and W. E. Gordon, "A theory of radio scattering in the troposphere," *Proc. IRE*, vol. 38, pp. 401-412; April, 1950.
- [2] R. Bolgiano, "The role of turbulent mixing in scatter propagation," *IRE TRANS. ON ANTENNAS AND PROPAGATION*, vol. AP-6, pp. 161-168; April, 1958.
- [3] R. A. Silverman, "Turbulent mixing theory applied to radio scattering," *J. Appl. Phys.*, vol. 27, pp. 699-705; July, 1956.
- [4] G. K. Batchelor, "The Scattering of Radio Waves in the Atmosphere by Turbulent Fluctuations in Refractive Index," *School of Elect. Engrg., Cornell University, Ithaca, N. Y., Res. Rept. EE 262*; September 15, 1955.
- [5] S. Corrsin, "On the spectrum of isotropic temperature fluctuations in an isotropic turbulence," *J. Appl. Phys.* vol. 22, pp. 469-473; April, 1951.
- [6] A. M. Obukhov, "Struktura temperaturnogo polia v turbulentnom potoke (Structure of the temperature field in a turbulent current)," *Akad. Nauk, SSSR*, vol. 13, pp. 58-69; January, 1949.
- [7] E. Inoue, "On the temperature fluctuations in a heated turbulent fluid," *Geophysical Notes, Tokyo University, Tokyo, Japan*, vol. 3, pp. 1-5; 1950.
- [8] F. Villars and V. F. Weisskopf, "On the scattering of radio waves by turbulent fluctuations of the atmosphere," *Proc. IRE*, vol. 43, pp. 1232-1239; October, 1955.
- [9] C. L. Pekeris, "Note on the scattering of radiation in an inhomogeneous medium," *Phys. Rev.*, vol. 71, pp. 268-269; February 15, 1947.
- [10] L. S. G. Kovasznay, M. S. Uberoi, and S. Corrsin, "The transformation between one and three-dimensional power spectra for an isotropic scalar fluctuation field," *Phys. Rev.*, vol. 176, pp. 1263-1264; October 15, 1949.
- [11] G. K. Batchelor, "The theory of homogeneous turbulence," Cambridge University Press, Cambridge, Eng.; 1953.
- [12] Y. Ogura, "Temperature fluctuations in an isotropic fluid," *J. Meteor.*, vol. 15, pp. 539-546; December, 1958.
- [13] A. L. Crozier, "Captive balloon refractovariometer," *Rev. Sci. Instr.*, vol. 29, pp. 276-279; April, 1958.

- [14] C. T. Johnson and J. R. Chiles, "The NEL T21 Microbarographic Recording System," U. S. Navy Electronics Lab., San Diego, Calif., USNEL Rept. No. 773; April 16, 1957.
- [15] H. Press and J. W. Tukey, "Power spectral methods of analysis and their applications to problems in airplane dynamics," Bell Telephone Lab. Agard Flight Test Manual, vol. 4, pp. 1-39.
- [16] E. E. Gossard and W. H. Munk, "On gravity waves in the atmosphere," *J. Meteorol.*, vol. 11, pp. 259-269; August, 1954.
- [17] F. N. Edmonds, F. X. Bostick and J. R. Gerhardt, "Power Spectra Evaluations for Selected Airborne Microwave Refractometer Recordings," Univ. of Texas, Austin, Elect. Eng. Research Lab. Rept. 6-24; August 15, 1958.
- [18] F. Gifford, Jr., "The relation between space and time correlations in the atmosphere," *J. Meteorol.*, vol. 13, pp. 289-294; June, 1956.
- [19] Y. Ogura, "The relation between the space- and time-correlation functions in a turbulent flow," *J. Meteorol., Soc. Japan*, 2nd Series 31, pp. 355-369; December, 1953.
- [20] H. A. Panofsky and I. Van der Hoven, "Structure of Small Scale and Middle Scale Turbulence at Brookhaven," Mineral Industries Experiment Station Scientific Rept. 1, Pennsylvania State Univ., State College, Contract AF 19(604)-1027; March, 1956.
- [21] J. W. Tukey, "The Sampling Theory of Power Spectrum Estimates," Symp. on Applications of Autocorrelation Analysis to Physical Problems, Woods Hole, Mass., pp. 47-67; June 13-14, 1949.
- [22] H. A. Panofsky and R. A. McCormick, "Properties of spectra of atmospheric turbulence at 100 metres," *Quart. J. Roy. Meteorol. Soc.*, vol. 80, pp. 546-564; October, 1954.
- [23] C. A. Potter, "Information Recovery from Finite-Sample Fluctuation Data," U. S. Navy Electronics Lab., San Diego, Calif., NEL Rept. 831; February 26, 1958.
- [24] W. H. Munk, F. Snodgrass and M. J. Tucker, "Spectra of low frequency ocean waves," *Bull. Scripps Inst. Oceanog.*, Univ. Calif., La Jolla, vol. 7, pp. 283-362; October, 1959.

Aircraft Scintillation Spectra*

ROBERT B. MUCHMORE†

Summary—Using the model of aircraft reflection developed by DeLano, the spectra of the reflection signals are found. Spectra for the amplitude of the rectified return, for the angular fluctuation signal associated with a fixed radar line-of-sight (effective radar center fluctuation), and for the angular fluctuation signal associated with a zero time constant servo (apparent radar center fluctuation) are derived. Several types of target motion are considered: uniform rotation, random rotation, and rectilinear velocity toward the radar itself. Each of these motions produces a characteristic spectrum and the properties of these spectra are pointed out and their significance in radar system design emphasized. In particular, the importance of the spectral density at zero frequency of the apparent radar center is shown in relation to systems using very rapid automatic gain control (AGC). It is shown that such use of very fast AGC may increase this noise density by a factor of approximately three, and thus increase the system noise.

I. INTRODUCTION

THE rectified amplitude of the wave returned from an aircraft target, as observed in the video circuits of a radar, is known to fluctuate. Further, the point seemingly indicated by a tracking radar as the center of the target varies in position with time. These two phenomena together are lumped under the title of aircraft scintillation because of the similarity to effects observed on the stars. The scintillation of the stars, however, is basically a different phenomenon; it is produced by propagation perturbations in the space between the source and the observer, while aircraft scin-

tillation is produced by interference between various reflection points on a complex target.

DeLano,¹ by introducing a simple model, has computed the probability distributions of the return signal and its envelope after rectification, and of two sorts of angular variations or scintillations. As a means of introducing the notation to be used in this paper, DeLano's results will be reviewed very briefly.

The target is represented as a collection of a large number of individual scatterers which reflect waves of statistically independent amplitude and phase. It is further assumed that conditions are met for application of the central limit theorem in probability theory. Thus the return RF signal is asymptotically normal and the envelope has (asymptotically) a Rayleigh distribution.

DeLano assumes a conically-scanning radar tracker and shows that one can add together the error signals produced by individual scatterers and obtain a sum U , which is the net error acting to perturb the tracking function. The point on the target towards which the antenna must point for this perturbing signal to have a zero mean ($\bar{U}=0$) is called the effective radar center. An antenna servo of very long time constant would tend to seek this point. The quantity U is asymptotically normal and, in one coordinate on the target,¹

$$\overline{U^2} = \frac{b_0^2}{2} \frac{\overline{x_n^2}}{r^2}, \quad (1)$$

* Manuscript received by the PGAP, April 30, 1959; revised manuscript received, October 5, 1959. Much of the material in this paper appeared originally in "Theoretical Scintillation Spectra," Hughes Aircraft Co., Los Angeles, Calif., Tech. Memo. no. 271; March 1, 1952.

† Space Technology Labs., Inc., Los Angeles, Calif.

¹ R. H. DeLano, "A theory of target glint or angular scintillation in radar tracking," *PROC. IRE*, vol. 41, pp. 1778-1784; December, 1953.

where b_0 is the antenna sensitivity in per unit modulation per radian, E is the amplitude of the return, r is range to the target, and x_n is lateral position on the target of the n th reflecting element. One has also that E and U are independent. (A bar over a quantity represents the stochastic mean or expectation.)

The apparent radar center ϵ is defined as that point where the instantaneous error signal is zero. This is the point toward which a zero time constant antenna servo would always point. This point may be shown to have,¹ in one dimension on the target, a probability density function which is Student's t distribution with 2 degrees of freedom.

$$p(\epsilon) = b_0 \left[\frac{\overline{E^2}}{8\overline{U^2}} \right]^{1/2} \left[1 + \frac{b_0^2 \overline{E^2}}{2\overline{U^2}} \epsilon^2 \right]^{-3/2}. \quad (2)$$

For a target symmetrical about two axes x and y one can show by a slight extension of DeLano's methods that

$$p(\epsilon_x, \epsilon_y) = b_0 \left[\frac{\overline{E^2}}{2\pi \overline{U_x^2} \overline{U_y^2}} \right]^{1/2} \cdot \left[1 + \frac{b_0^2 \overline{E^2} \epsilon_x^2}{2\overline{U_x^2}} + \frac{b_0^2 \overline{E^2} \epsilon_y^2}{2\overline{U_y^2}} \right]^{-2}. \quad (3)$$

The quantity ϵ is defined as

$$\epsilon = \frac{U}{b_0 E}, \quad (4)$$

and it can be shown that the use of very fast (essentially instantaneous) gain control in a tracking radar converts the target noise U , seen by a slow servo, into ϵ . The instantaneous center ϵ does not possess finite mean square as is obvious from (2). Thus, one expects the noise to increase, although not to infinity in a practical system of course, when a fast gain control is used.

This paper is concerned with results on spectra of the amplitude E , the fluctuation U observed by a slow servo with slow gain control, and the apparent or instantaneous radar center ϵ . Spectra are calculated in Section II for angular motion of the target about its center for both uniform and random rotation. The effects of range closure are calculated in Section III and the effect of an instantaneous AGC on the spectrum is discussed in Section IV.

Although the results are largely unavailable for publication at this time, experimental tests have shown the general validity of the models used here. Actual aircraft targets are, of course, far more complicated than these very simple models. General features of the results have, however, been verified; this leads one to believe that the methods may be applied to other examples where data are lacking.

II. SPECTRA PRODUCED BY TARGET ROTATION

A. Uniform Target Rotation

To illustrate the methods this first example will be worked through in some detail. Consider a simple target model as pictured in Fig. 1. Scatterers are consid-

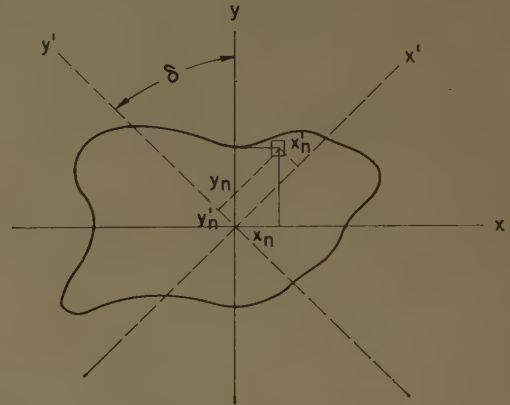


Fig. 1—Target model.

ered to be spread in some manner over an irregular area. The axes x, y are target axes and x', y' are the rectangular axes of error resolution for a tracking antenna. The n th scatterer at point x_n, y_n is shown. The scattered field is picked up by the receiving antenna and appears in the receiver circuits as a voltage

$$V(t) = \sum_p a_p e^{i(\omega_0 t + \theta_p + \phi_p)} \quad (5)$$

where a_p is the amplitude due to the p th element, ω_0 is the angular carrier frequency, ϕ_p is a random phase angle uniformly distributed from 0 to 2π , θ_p is given by

$$\theta_p = 2kd_p, \quad (6)$$

and the sum is over all scatterers. In (6) $k = 2\pi/\lambda_0 = \omega_0/c$ and d_p is the distance in the range direction from the p th element to some arbitrary plane placed normal to the line of sight connecting the radar and the target center. The factor 2 accounts for two-way transmission. One assumes a_p and ϕ_p are independent and that a_p, a_q and ϕ_p, ϕ_q are independent for $p \neq q$.

In the following, it will be assumed that the scattering lobe patterns of the individual scatterers are wide compared to the lobes produced by an array of length L . Since one can assume that the elements are smaller in size than L , this will almost certainly be true. This assumption allows one to consider only phase changes for the individual scattered waves and to ignore any amplitude changes.

Suppose the line of sight is normal to the page in Fig. 1, and let the target rotate at rate $\Omega(t)$ about the y axis.

Then

$$\theta_p = z \frac{\omega_0}{c} x_n \int_0^t \Omega(t) dt \quad (7)$$

with the assumption that the total angle turned $\int_0^t \Omega(t) dt$ is small. Using (5),

$$V(t) = \sum_p a_p \cdot \exp \left[i \left(\omega_0 t + \phi_p + \frac{2\omega_0}{c} x_n \int_0^t \Omega(t) dt \right) \right]. \quad (8)$$

It is convenient to approximate the sum over p by a stochastic integral over the x, y plane.

$$V(t) \cong \iint_A \exp \left[i \left(\omega_0 t + \frac{2\omega_0 x}{c} \int_0^t \Omega(t) dt \right) \right] \cdot h(x, y) d^2 H(x, y). \quad (9)$$

$H(x, y)$ is a complex additive process with

$$\overline{d^2 H(x_1, y_1) d^2 H(x_2, y_2)} = 0 \text{ for either or both } x_1 \neq x_2, \\ y_1 \neq y_2 \text{ true,} \quad (10)$$

$$\overline{|d^2 H(x, y)|^2} = dx dy$$

and $h^2(x, y)$ is the power reflection density over the area A .

The y integral in (9) is over all scatterers with the same Doppler shift and the x integral is (effectively) over all Doppler shifts. Thus the average total power returned is

$$\overline{|V(t)|^2} = \int_A \int_A \int_A \int_A \exp \left[i \left(\omega_0 t + \frac{2\omega_0 x_1}{c} \int_0^t \Omega(t) dt \right) \right] \\ \cdot \exp \left[-i \left(\omega_0 t + \frac{2\omega_0 x_2}{c} \int_0^t \Omega(t) dt \right) \right] \\ \cdot h(x_1, y_1) h(x_2, y_2) \overline{d^2 H(x_1, y_1) d^2 H(x_2, y_2)} \quad (11)$$

$$= \int_A \int_A h^2(x, y) dx dy. \quad (12)$$

Eq. (10) was used in going from (11) to (12).

Consider first uniform target rotation of a simple line target about the y axis (see Fig. 2). Then $\Omega(t) = \Omega_0$, a constant, and (9) can be written

$$V(t) = \int_{-L/2}^{L/2} \exp \left[i \left(\omega_0 t + \frac{2\omega_0 x \Omega_0}{c} t \right) \right] g(x) dF(x) \quad (13)$$

where the (trivial) integration over y has been performed leaving functions of x only in the integral. By

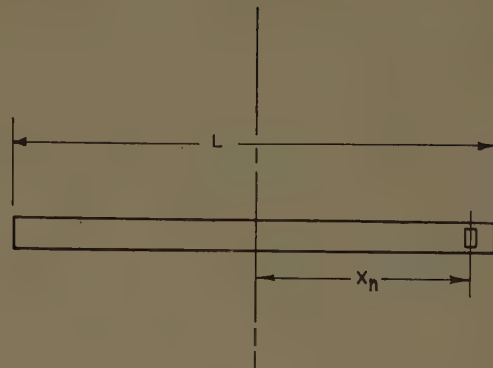


Fig. 2—Line target model.

a change of variable (13) becomes

$$V(t) = \int_{f_0-f_m}^{f_0+f_m} e^{i2\pi f t} g \left[\frac{c(f-f_0)}{2f_0\Omega_0} \right] dF \left[\frac{c(f-f_0)}{2f_0\Omega_0} \right]. \quad (14)$$

$$f_m = \frac{f_0 L \Omega_0}{c}. \quad (15)$$

This is simply an equation for a sum of incoherent waves of frequencies

$$f = f_0 \left(1 + \frac{2x\Omega_0}{c} \right). \quad (16)$$

Eq. (14) is in the form of a spectral representation for a random process and thus the spectral distribution function $Z(f)$ for V is given by²

$$dZ_V(f) = g^2 \left[\frac{c(f-f_0)}{2f_0\Omega_0} \right] \overline{\left| dF \left[\frac{c(f-f_0)}{2f_0\Omega_0} \right] \right|^2} \\ = g^2 \left[\frac{c(f-f_0)}{2f_0\Omega_0} \right] \frac{c}{2f_0\Omega_0} df \quad (17)$$

and the power spectral density is

$$W_V(f) = \frac{dZ_V(f)}{df} = \frac{c}{2f_0\Omega_0} g^2 \left[\frac{c(f-f_0)}{2f_0\Omega_0} \right]. \quad (18)$$

If one assumes a uniform density of scatterers along L ,

$$g^2(x) = g_0^2 \quad (19)$$

and

$$W_v(f) = \frac{c g_0^2}{2f_0\Omega_0}; \quad f_0 - f_m \leq f \leq f_0 + f_m \\ = 0 \text{ elsewhere,} \quad (20)$$

and the power spectral density of V is constant over a band centered about the carrier.

² J. L. Doob, "Stochastic Processes," J. Wiley and Sons, Inc., New York, N. Y., p. 527; 1953.

The usual radar has an approximately linear detector but it can be shown³ that the spectrum of a square law detector is a good approximation to that of a linear detector. The spectrum of the envelope of a square law detector with $W_v(f)$ as the spectrum of the applied noise is the convolution of $W_v(f)$ with itself and this yields for the normalized spectrum

$$w_E(f) = \frac{W_E(f)}{\int W_E(f) df} = \frac{1}{f_m} \left(1 - \frac{f}{2f_m}\right); f \leq f_m$$

$$= 0; \quad f > f_m. \quad (21)$$

This is plotted in Fig. 3.

To find the spectrum of U , the fluctuations about the effective (or long time average) radar center, a monopulse type tracking system will be assumed.⁴ The basic direction sensing element in this system is the phase detector of Fig. 4. The RF outputs of two closely spaced antennas (or two closely spaced feeds for one reflector or lens) are both added and subtracted. The sum $V_s(t)$ and difference $V_d(t)$ are fed to the circuit of Fig. 4 as shown. One has (see Appendix I) for U

$$U(t) = |V_s + V_d| - |V_s - V_d|. \quad (22)$$

The antennas whose outputs are differenced have patterns as shown in Fig. 5 with

$$V_d = V_1 - V_2. \quad (23)$$

Operation in the center, linear part of the crossover is assumed and the crossover is assumed to be aligned with the target center. Taking account of the positions of the various individual scatterers at the target, the difference voltage in one tracking antenna coordinate x' is

$$V_{dx'}(t) = 2b_0 \iint_A \exp \left[i \left(\omega_0 t + \frac{2\omega_0 x}{c} \int_0^t \Omega(t) dt \right) \right] \cdot \frac{x'}{r} h(x, y) d^2 H(x, y) \quad (24)$$

where b_0 is the slope of the antenna pattern near crossover in volts per radian, and r is range to the target. Eq. (24) can be written for the target of Fig. 2 and for constant angular rate Ω_0 about the y' axis which is now as-

³ J. L. Lawson and G. E. Uhlenbeck, "Threshold Signals," McGraw-Hill Book Co., Inc., New York, N. Y., pp. 62-63; 1950. (The approximation is considerably better than is indicated by the inexact Figure on p. 63.)

⁴ R. H. DeLano, "Angular Scintillation of Radar Targets with Monopulse and Interferometer Target Seekers," Hughes Aircraft Co., Los Angeles, Calif., Tech. Memo. no. 257; November 1, 1950. This paper shows that all common types of radar trackers produce, at long range, similar results for scintillation. In a simple way, one can see this readily by noting that any direction finder, such as a radar tracker, operates by finding the direction of the normal to the surfaces of constant phase of the incident wave. Thus all systems will measure the same fluctuations in this direction (assuming far-field conditions).

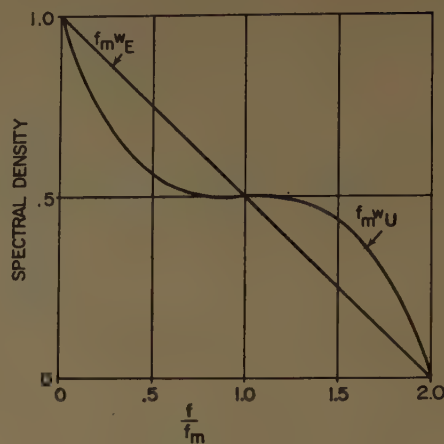


Fig. 3—Spectra for uniform target rotation.

$$f_m = \frac{L\Omega_0}{\lambda_0}$$

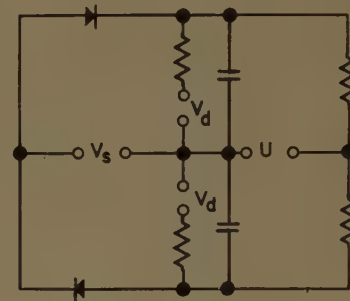


Fig. 4—Phase detector.

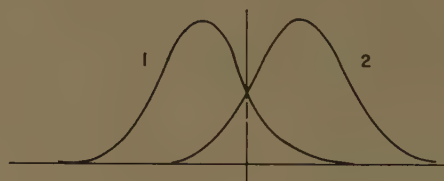


Fig. 5—Difference antenna patterns.

sumed to coincide with the y axis.

$$V_{dx'}(t) = \frac{2b_0}{r} \int_{f_0-f_m}^{f_0+f_m} e^{i2\pi f t} \frac{c(f-f_0)}{2f_0\Omega_0} \cdot g \left[\frac{c(f-f_0)}{2f_0\Omega_0} \right] dF \left[\frac{c(f-f_0)}{2f_0\Omega_0} \right]. \quad (25)$$

The power spectral density of $V_{dx'}$ is thus

$$W_{V_{dx'}}(f) = \frac{b_0^2 c^2 g_0^2}{r^2 f_0^2 \Omega_0^2} (f-f_0)^2; \quad f_0 - f_m \leq f \leq f_0 + f_m$$

$$= 0; \quad \text{elsewhere.} \quad (26)$$

As indicated in Appendix I, one obtains the spectrum of U from the convolution of (20) and (26). The normalized spectrum is

$$w_U(f) = \frac{W_U(f)}{\int_0^\infty W_U(f) df} = \frac{1}{2f_m} \left(2 - 3 \frac{f}{f_m} + 3 \frac{f^2}{f_m^2} - \frac{f^3}{f_m^3} \right), \quad (27)$$

and this is also plotted in Fig. 3.

One of the significant features of the spectra of Fig. 3 is their lack of frequency components higher than $2f_m$ and the sudden rise in power content below $2f_m$. An airplane traveling at 600 feet per second in a 2g turn has an Ω_0 of approximately 0.107 rad/second. If $L = 100$ feet and $f_0 = 10^{10}$ cps, this yields $f_m = 107$ cps, which is rather higher than is measured in straight and level flight. Two deductions are important: 1) the usual antenna pointing servo with a bandwidth of a few cycles can do a very good smoothing job on U , and 2) a conical scan system with scan frequency less than $2f_m$ will encounter extra noise because of components in E getting through the scan frequency circuits. These components appear when $2f_m > f_{scan}$ and thus may appear during target maneuvers and not be present otherwise.

It should be emphasized here that no accounting has been made of possible independent target motions such as propeller spinning, general vibration, bending movements, etc. All of these contribute Doppler shifts of their own and may produce components spread rather widely over the spectrum. The important point is that measurements made in straight and level flight will show *only* these latter components. In violent maneuvers there may be large increases in spectrum energy content near the scan frequency and these would be unsuspected from a simple evaluation of conditions in unperturbed flight.

The spectrum $w_U(f)$ given in (27) applies to the angular variations about the effective (or mean) radar center. The fluctuations that a zero time constant pointing servo would follow have been shown to have different characteristics. In particular, the point ϵ which such a system would track is given by (4). To compute its spectrum one finds first the autocorrelation

$$R_\epsilon(\tau) = \overline{\epsilon(t)\epsilon(t+\tau)} = \frac{1}{b_0^2} \overline{U(t)U(t+\tau)} \overline{E^{-1}(t)E^{-1}(t+\tau)} \quad (28)$$

and then, from the transform of this, the spectrum. The two averages in (28) have been separated because U and E are asymptotically independent (see Appendix I).

The autocorrelation of U is

$$R_U(\tau) = \int_0^\infty W_U(f) \cos 2\pi f \tau df = \overline{U^2} \rho_U(\tau) \quad (29)$$

with $\rho_U(\tau)$ defined as the normalized autocorrelation function. From (27) and (29) one obtains, for uniform target rotation,

$$\rho_U(\tau) = \frac{3 \sin^2 y}{y^2} + \frac{3 \sin 2y}{y^3} - \frac{6 \sin^2 y}{y^4} \quad (30)$$

with

$$y = 2\pi f_m \tau. \quad (31)$$

It remains to find the autocorrelation of E^{-1} .

Set $E(t) = E_1$ and $E(t+\tau) = E_2$. Using the joint density function of E_1 and E_2 and given by Rice,⁵

$$\overline{E_1^{-1}E_2^{-1}} = \frac{1}{s^4(1-t^2)} \int_0^\infty dE_1 \int_0^\infty dE_2 I_0 \left[\frac{tE_1E_2}{s^2(1-t^2)} \right] \cdot \exp \left[-\frac{E_1^2 + E_2^2}{2s^2(1-t^2)} \right] \quad (32)$$

where $I_0[x]$ is the modified Bessel function of the first kind, and

$$s^2 = 2 \int W_V(f - f_0) df, \quad (33)$$

$$t(\tau) = \frac{2}{s^2} \int W_V(f - f_0) \cos 2\pi f \tau df \quad (34)$$

and W_V is taken to be an even function about f_0 .

Evaluating the integral in (32) one has

$$R_\epsilon(\tau) = \frac{\overline{U^2}}{b_0^2 s^2} \rho_U(\tau) K[t(\tau)] \quad (35)$$

where $K[x]$ is the complete elliptic integral of the first kind. A plot of $R_\epsilon(\tau)$ for uniform rotation is given in Fig. 6. Note the logarithmic singularity at the origin which is indicative of the infinite mean square value of ϵ .

$W_\epsilon(f)$ is the cosine transforms of (34). For uniform target rotation, one has

$$t(\tau) = \frac{\sin 2\pi f_m \tau}{2\pi f_m \tau} \quad (36)$$

and this, plus (30) for $\rho_U(\tau)$ substituted into (35), makes a difficult expression to transform. One can, however, examine some of the properties of $W_\epsilon(f)$ without finding the complete solution. Using expansions of ρ_U and t about $\tau = 0$,

⁵ S. O. Rice, "Mathematical analysis of random noise," *Bell. Sys. Tech. J.*, vol. 24, pp. 46-108; January, 1945.

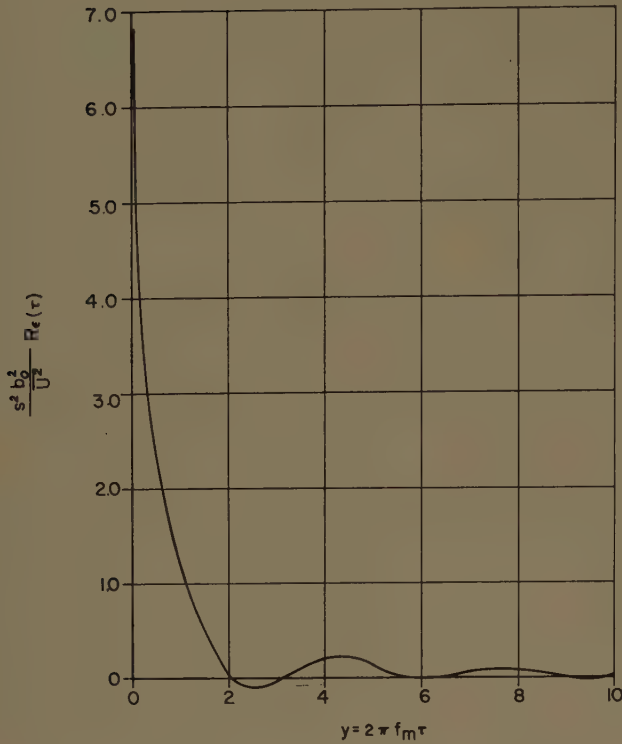


Fig. 6—Autocorrelation of instantaneous (apparent) radar center for uniform rotation of a long, thin target.

$$\begin{aligned}
 W_e(f) &= 4 \int_0^\infty R_e(\tau) \cos 2\pi f \tau d\tau \\
 &= \frac{4\bar{U}^2}{b_0^2 s^2} \int_0^\infty \left[1 - \frac{7}{15} (2\pi f_m \tau)^2 + \dots \right] \\
 &\quad \cdot K \left[1 - \frac{1}{6} (2\pi f_m \tau)^2 + \dots \right] \cos 2\pi f \tau d\tau \\
 &\cong \frac{2\bar{U}^2}{b_0^2 s^2} \int_0^\infty \log \left(1 + \frac{12}{\pi^2 f_m^2 \tau^2} \right) \cos 2\pi f \tau d\tau \quad (37)
 \end{aligned}$$

for $f \rightarrow \infty$. The result of integrating and letting f become large is

$$W_e(f) \rightarrow \frac{\bar{U}^2}{b_0^2 s^2 f}; \quad f \rightarrow \infty. \quad (38)$$

Thus

$$\int_0^\infty W_e(f) df \rightarrow \infty$$

and it must since $\epsilon \rightarrow \infty$.

To find the value of $W_e(f)$ for small f , expand the elliptic integral in series. This yields

$$\begin{aligned}
 W_e(f) &= \frac{\pi \bar{U}^2}{2s^2} \int_0^\infty \rho_U(\tau) \left[1 + \frac{1}{4} t^2(\tau) + \frac{9}{64} t^4(\tau) + \dots \right] \\
 &\quad \cdot \cos 2\pi f \tau d\tau. \quad (39)
 \end{aligned}$$

The spectrum of ϵ is

$$\begin{aligned}
 W_e(f) &\cong \frac{\pi \bar{U}^2}{2s^2} \left[w_U(f) + \frac{1}{4} \int w_U(f_1) \right. \\
 &\quad \left. \int w_t(f_2) w_t(f - f_1 - f_2) df_1 df_2 + \dots \right] \quad (40)
 \end{aligned}$$

with

$$w_t(f) = \frac{W_v(f - f_0)}{V^2}. \quad (41)$$

Evidently $(\pi \bar{U}^2 / 2s^2) w_U(f)$ is the first approximation to $W_e(f)$. It must be remembered, though, that this is increasingly worse as $f \rightarrow \infty$ because $W_e(f) \sim 1/f$ for large f , while $W_U(f)$ goes to zero much faster (for uniform rotation it is exactly zero for $f > 2f_m$).

The spectral density at zero frequency is of especial interest in system design because system bandwidths are often small compared to the bandwidth of W_U . One has

$$\begin{aligned}
 W_e(0) &= \frac{\pi \bar{U}^2}{2s^2} \int_0^\infty \rho_U(\tau) \left[1 + \frac{1}{4} t^2(\tau) + \frac{9}{64} t^4(\tau) + \dots \right] \\
 &\quad \cdot \cos 2\pi f \tau d\tau. \quad (42)
 \end{aligned}$$

See Section IV for a further discussion of this point.

B. Nonuniform Rotation

Uniform rotation of the target is a simple assumption but at times other than violent maneuvers the assumption may not be justified. During more normal flight, the aircraft's motion is affected more by winds and turbulence in the atmosphere so that the target's angular motions are small, random, and average to zero. Again, propeller noise and vibration are neglected; the principal result below is that under rough flight conditions the spectrum is broadened much as it is for nonrandom maneuvers.

Using the general methods above a good approximation to $W_E(f)$ is found in Appendix II. Normalizing it, one has

$$\begin{aligned}
 w_E(f) &= \frac{4a}{\sqrt{\pi}} [e^{-a^2 f^2} - \sqrt{\pi} a f \operatorname{erfc}(af)] \\
 a &= \lambda_0 / 2\pi L f_b \sqrt{\Theta^2} \quad (43)
 \end{aligned}$$

where $\bar{\Theta}^2$ is mean square target angle variation and f_b is a measure of the bandwidth of Θ (see Appendix II). This function is plotted in Fig. 7. If one picks $\sqrt{\bar{\Theta}^2} = 1^\circ$, $L = 100$ ft, $f_b = \frac{1}{6}$ cps, and $\lambda = 0.1$ square foot, one obtains a one-half power bandwidth of approximately 7 cps, which is about the right order of magnitude based on measurements in straight and level flight at low altitudes where turbulence is often encountered.⁶

⁶ Unpublished data.

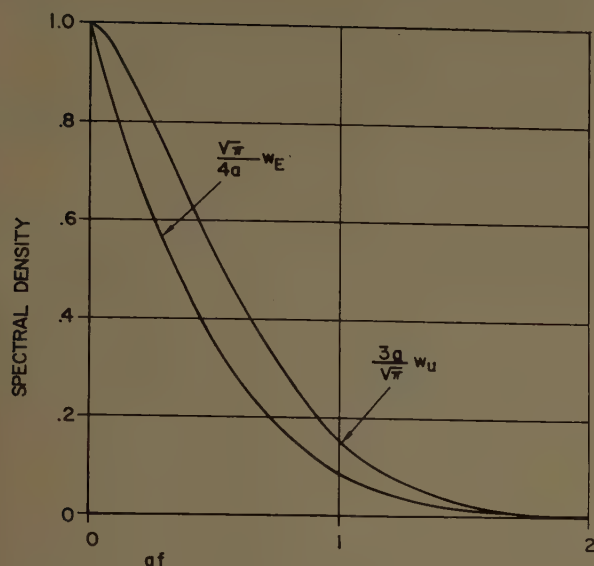


Fig. 7—Spectrum for random rigid body rotation.

$$a = \frac{\lambda_0}{2\pi L f_b} \sqrt{\theta^2}.$$

The spectrum of U follows from straightforward application of the same principles as before. With the same approximation as in Appendix II,

$$w_U(f) \cong \frac{3a}{\sqrt{\pi}} [e^{-a^2 f^2} + a^2 f^2 Ei(-a^2 f^2)]. \quad (44)$$

This function also is plotted in Fig. 7.

The spectrum of ϵ , the instantaneous center, is derivable as before from the spectra of E and U .

III. SPECTRA PRODUCED BY RANGE CLOSURE

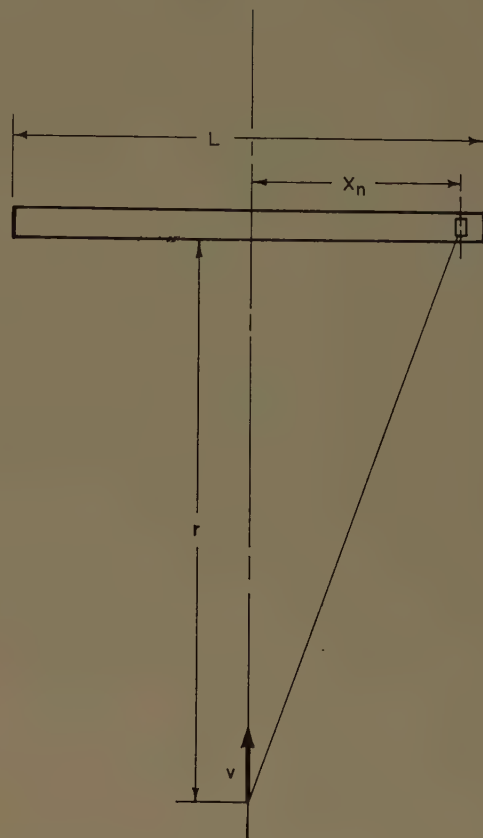
Thus far it has been tacitly assumed that target and radar were at constant distance from one another. Suppose one has the situation pictured in Fig. 8. The same target as before is assumed, but now the radar is approaching the target center at velocity v_0 . This produces a Doppler shift in the returned wave in general. More specifically, the return from each scattering element has a different Doppler shift, and thus a band of frequencies is returned.

Letting the velocity of the radar with respect to some point x be $v(x)$, one has for the received signal

$$V(t) = \int_{-L/2}^{L/2} \exp \left[i \left(\omega_0 t + \frac{2\omega_0 v(x)t}{c} \right) \right] g(x) dF(x). \quad (45)$$

From the geometry of Fig. 8,

$$v(x) = \frac{V_0}{\sqrt{1 + \frac{x^2}{r^2}}} \quad (46)$$

Fig. 8—Target model showing range closure at velocity v .

and, if $L \ll r$ as will generally be the case where the following analysis is valid (far field of the radar antenna),

$$v(x) \cong v_0 \left(1 - \frac{x^2}{2r^2} \right). \quad (47)$$

Setting

$$\Delta v = v_0 - v(x), \quad (48)$$

and putting

$$f_1 = f_0 + \frac{2f_0 v_0}{c}, \quad (49)$$

(45) can be written

$$V(t) = \int_{-L/2}^{L/2} \exp \left[i \left(\omega_1 t - \frac{2\omega_0 \Delta v(x)t}{c} \right) \right] g(x) dF(x). \quad (50)$$

The frequency f_1 is the Doppler-shifted frequency returned from the target center while the term in Δv gives the spread due to the finite extent of the target. The phenomenon is a consequence of the finite angular extent of the target as viewed by the radar.

For $L \ll r$,

$$\Delta v(x) \cong \frac{v_0 x^2}{2r^2} \quad (51)$$

and, as in the development preceding (18), one can obtain the power spectral density of V from (50). It is

$$W_V(f) = g_0 r \sqrt{\lambda_0 / v(f_1 - f)}; \quad f_1 - f_c \leq f \leq f_1 \\ = 0 \quad \text{elsewhere} \quad (52)$$

with

$$f_c = \frac{v_0 L^2}{4\lambda_0 r^2} \quad (53)$$

Note that points equidistant from the center return equal frequencies here in contrast to the rotation case where the returned frequencies were equally, but oppositely, deviated from the carrier. Thus $W_V(f)$ in (52) is not symmetric about a midpoint.

Spectral densities for E and U can be obtained by the methods used in Section II. One obtains as normalized spectral densities

$$w_E = \frac{-1}{f_c} \log \left[\sqrt{\frac{f_c}{f}} - \sqrt{\frac{f_c}{f} - 1} \right]; \quad 0 \leq f \leq f_c \\ = 0; \quad \text{elsewhere} \quad (54)$$

$$w_U = \frac{3}{2f_c} \sqrt{1 - \frac{f}{f_c}}; \quad 0 \leq f \leq f_c \\ = 0; \quad \text{elsewhere.} \quad (55)$$

The spectra above are actually time-dependent since f_c is proportional to r^{-2} and $r = r_0 - v_0 t$ where r_0 is some initial range at time $t=0$. Also, although it does not show in the normalized form in (55), the amplitude of W_U varies since, by (1), $\overline{U^2}$ is proportional to r^{-2} .

If the system time constants are such that r changes by only a small amount during a period equal in length to one time constant, one may use a quasi-stationary approximation and treat the spectra as constant but with parameters appropriate to the time era in question. It is also interesting to note that the spectral density at zero frequency, a quantity often of interest to the system designer, is independent of both range and target size. From (1) and (55)

$$W_U(0) = \frac{\lambda_0 b_0^2 \overline{E^2}}{2v_0} \quad (56)$$

Although the mean square value of U becomes very large at short range, it is all produced through widening of the spectrum; the density at zero frequency remains constant.

IV. EFFECT OF AUTOMATIC GAIN CONTROL ON SCINTILLATION NOISE

The random amplitude E of the scattered signal affects the tracking function of an automatic tracking radar. With no AGC the signal used to null the antenna pointing servo has two terms,¹ one is U and the other is a term proportional to E and to the difference ζ between the angle of the antenna axis and the angle to the mean

target center. Thus the error signal is

$$e \sim U - b_0 \zeta E + b_0 E m(t) \quad (57)$$

where $m(t)$ represents the (time-dependent) motion of the mean target.

A simple servo might make the rate of train of the antenna axis proportional to the error. If the reference direction is taken through the mean radar center, the servo equation could be

$$F(p) p \zeta = -e = -U + b_0 \zeta E - b_0 E m(t) \quad (58)$$

or

$$\left[\frac{F(p)p}{b_0} - E \right] \zeta = -\frac{U}{b_0} - E m(t) \quad (59)$$

where $F(p)$ is some operator characteristic of the individual servo and $p = d/dt$. Many systems are of this type.

When the system bandwidth is much less than the spectral width of E , one has approximately¹

$$\left[\frac{F(p)p}{b_0 \overline{E}} - 1 \right] \zeta = -\frac{U}{b_0 \overline{E}} - \frac{E}{\overline{E}} m(t). \quad (60)$$

This is a simple, constant coefficient differential equation with a random forcing function $-U/b_0 \overline{E}$. Knowing $m(t)$, $\overline{U^2}$, and the spectra derived above, one can solve for the mean square system error, optimize $F(p)$, etc.

The extreme opposite from no AGC at all is to use an essentially instantaneous AGC. This has the effect of multiplying the error signal by \overline{E}/E so that (57) becomes^{1,7}

$$e' = \frac{U \overline{E}}{E} - b_0 \zeta \overline{E} + b_0 \overline{E} m(t). \quad (61)$$

The variable gain has been corrected and (60) becomes

$$\left[\frac{F(p)p}{b_0 \overline{E}} - 1 \right] \zeta = -\frac{U}{b_0 \overline{E}} - m(t), \quad (62)$$

but the scintillation portion of the forcing function is $-U/b_0 \overline{E}$ instead of $-U/b_0 E$ and is now the quantity defined in (4) as the instantaneous radar center.

Thus correcting one fault has introduced another. Whether or not any advantage has been gained depends upon the relative importance of gross target motion (movement of the target mean) and scintillation noise. This question cannot be answered in general but must be considered individually for each system in combination with its particular mission.

The quantity $m(t)$ will not be considered further here but some additional remarks may be made about the scintillation term. If the servo bandwidth is narrow, only the spectral density at zero frequency of the forcing function is of importance. To compare (60) and (62), the ratio

⁷ R. H. DeLano and I. Pfeffer, "The effect of AGC on radar tracking noise," PROC. IRE, vol. 44, pp. 801-810; June, 1956.

$$q = W_{\epsilon}(0) / \frac{W_U(0)}{b_0^2 \bar{E}^2} \quad (63)$$

is of direct interest. From equations developed in Section II

$$q = \frac{\pi^2}{4} \frac{\int_0^\infty d\tau \rho_U(\tau) \left[1 + \frac{1}{4} t^2(\tau) + \frac{9}{64} t^4(\tau) + \dots \right]}{\int_0^\infty d\tau \rho_U(\tau)} \quad (64)$$

which, to a first approximation, is

$$q \cong \frac{\pi^2}{4} +. \quad (65)$$

In (64), q will always be greater than $\pi^2/4$ because, as seen from (40) where the spectral density convolutions are all non-negative, the additional terms will all be greater than, or equal to, zero. It can be shown⁷ that the increase of $\pi^2/4$ is due to an increase in mean gain of the AGC, while further increases in q are produced by intermodulation products. Eq. (40) shows this very plainly; the first term gives the $\pi^2/4$ in (64) while additional terms are clearly cross-modulation terms. The zero-frequency scintillation noise power density is thus greater than $\pi^2/4 \cong 2.5$ times as much when a very fast AGC is used—the AGC has effectively increased this portion of the system noise.

As an example, the spectra of rigid body target rotation [(21) and (27)] have been used in computing q . The value obtained by numerical integration is $q \cong 2.75$. Other calculations using spectra for U and E not easily related to target motion have shown values of q ranging from 2.8 to 3.14. Experimental results^{7,8} have borne out the above conclusions and have shown, in addition, how closely one can approach an instantaneous AGC without serious detrimental effects on the scintillation portion of the total noise.

V. CONCLUSION

Although the models used are admittedly rough and simple, calculations of spectra based on them have shown a number of features which are readily seen to be more or less independent of the detailed models themselves. First, a target in rapid rotation about its own center of gravity shows a spread in spectral width with constant rms value. A servo passing only low frequencies shows improvement, but a system based on lobing in the high-frequency range may show definite deterioration in performance. Second, range closure produces a very similar effect with the interesting difference that total rms goes up inversely as range but leaving the spectral density at zero frequency unchanged.

⁸ J. H. Dunn and D. D. Howard, "The effect of automatic gain control performance on the tracking accuracy of monopulse radar systems," *PROC. IRE*, vol. 47, pp. 430-435; March, 1959.

Finally, an analysis of the effects of rapid AGC shows it to have not unmixed blessings. Certain terms do decrease, but another, the angular scintillation term, rises in both rms value and zero frequency spectral density.

APPENDIX I

ANGULAR ERROR SIGNAL DERIVATION

From the circuit of Fig. 4, the angular error signal $U(t)$ is given by

$$U(t) = |V_s(t) + V_d(t)| - |V_s(t) - V_d(t)| \quad (66)$$

where the absolute magnitude signs mean "envelope of." The quantity $V_s(t)$ is just twice (9) for $V(t)$. Note that $V(t)$ is an expression for a "narrow-band" noise function and, according to Rice,⁵ one can write

$$V_s(t) = \alpha_1(t) \cos \omega t + \alpha_2(t) \sin \omega t \quad (67)$$

where α_1 and α_2 are, as shown by DeLano,¹ asymptotically normal and independent. The envelope function itself can be written in the usual way as

$$|V_s(t)| = |E_s(t) e^{i\theta_s(t)}| \quad (68)$$

with

$$E(t) = E_s(t) = \sqrt{\alpha_1^2 + \alpha_2^2}$$

$$\theta_s(t) = \tan^{-1} \frac{\alpha_2}{\alpha_1} \quad (69)$$

Similarly, from (24) for $V_{dx'}(t)$,

$$V_{dx'}(t) = \beta_1(t) \cos \omega t + \beta_2(t) \sin \omega t \quad (70)$$

and

$$E_{dx'}(t) = \sqrt{\beta_1^2 + \beta_2^2}$$

$$\theta_{dx'}(t) = \tan^{-1} \frac{\beta_2}{\beta_1} \quad (71)$$

DeLano has shown¹ that α_1 , α_2 , β_1 , β_2 , are all (asymptotically) normal and mutually independent. One has also that E_s , $E_{dx'}$, θ_s , $\theta_{dx'}$, are mutually independent.

If the range to the target is much greater than the target lateral extent, one will have $\beta \ll \alpha$. One can then expand (66) for U , dropping higher-order terms in β , to obtain

$$U = \frac{2(\alpha_1\beta_1 + \alpha_2\beta_2)}{E_s} = 2(\beta_1 \cos \theta_s + \beta_2 \sin \theta_s). \quad (72)$$

Because θ_s , β_1 , and β_2 are all asymptotically independent of E , one has that E and U are asymptotically independent. The above argument, which follows DeLano, shows that $E(t)$ and $U(t)$ approach independence for the same time t .

One can show further that $E(t_1)$ and $U(t_2)$ become independent for all t_1 and t_2 . One has E independent of β_1 and β_2 always, since their independence is basically contingent on the independence of the relative angle δ of the coordinate systems in Fig. 1 and the amplitudes and

phases of the scattered signals and this assumption seems quite reasonable.

From Rice⁵ the joint density of the envelopes and phases of a narrow band noise is

$$p(E_1, E_2, \theta_1, \theta_2) = \frac{E_1 E_2}{4\pi^2 A} \exp \left[-\frac{R_0}{2A} (E_1^2 + E_2^2) + \frac{\lambda_{13}}{A} E_1 E_2 \cos(\theta_2 - \theta_1) + \frac{\lambda_{14}}{A} E_1 E_2 \sin(\theta_2 - \theta_1) \right] \quad (73)$$

where

$$E_1 = E(t_1)$$

$$E_2 = E(t_2)$$

$$\theta_1 = \theta(t_1)$$

$$\theta_2 = \theta(t_2)$$

$$W(f) = \text{Power spectral density}$$

$$A = \sigma^4 - \lambda_{13}^2 - \lambda_{14}^2$$

$$\sigma^2 = \text{mean square of narrow-band noise} = \int_0^\infty W(f) df$$

$$\lambda_{13} = \int_0^\infty W(f) \cos 2\pi(f - f_0)\tau df, \quad \text{and}$$

$$\lambda_{14} = \int_0^\infty W(f) \sin 2\pi(f - f_0)\tau df.$$

By integrating the density function over E_2 and θ_1 , one obtains

$$p(E_1, \theta_2) = \frac{1}{2\pi} \frac{R}{\sigma^2} e^{-R^2/2\sigma^4} \quad (74)$$

which shows that E_1 and θ_2 are independent for all t_1 and t_2 . Therefore, $E_s(t_1)$ is independent of $\theta_s(t_2)$ and thus U and E are independent at all times.

From (72) one can deduce an approximate spectrum for U as follows. The correlation function of U is

$$\begin{aligned} \overline{U(t)U(t+\tau)} &= 4[\overline{\beta_1(t)\beta_1(t+\tau)} \overline{\cos \theta_s(t) \cos \theta_s(t+\tau)} \\ &+ \overline{\beta_2(t)\beta_2(t+\tau)} \overline{\sin \theta_s(t) \sin \theta_s(t+\tau)} \\ &+ \overline{\beta_1(t)\beta_2(t+\tau)} \overline{\cos \theta_s(t) \sin \theta_s(t+\tau)} \\ &+ \overline{\beta_1(t+\tau)\beta_2(t)} \overline{\cos \theta_s(t+\tau) \sin \theta_s(t)}]. \quad (75) \end{aligned}$$

As already mentioned, the β terms and θ_s terms are independent and therefore the averages can be broken into products of averages as above.

One has⁵

$$\begin{aligned} \overline{\beta_1(t)\beta_1(t+\tau)} &= \overline{\beta_2(t)\beta_2(t+\tau)} = \lambda_{\beta 13}(\tau); \\ \overline{\beta_1(t)\beta_2(t+\tau)} &= -\overline{\beta_2(t)\beta_1(t+\tau)} = \lambda_{\beta 14}(\tau). \quad (76) \end{aligned}$$

The cosine correlation in (75) can be readily obtained using the work of Bunimovich⁹ as

$$\begin{aligned} \overline{\cos \theta_s(t) \cos \theta_s(t+\tau)} &= \frac{\lambda_{\alpha 13}}{2\sigma_\alpha^2 p_\alpha^2} [E(p_\alpha) - p_\alpha'^2 K(p_\alpha)] \\ &\cong \frac{\lambda_{\alpha 13}}{8\sigma_\alpha^2} \left[1 + \frac{p_\alpha^2}{8} + \frac{3p_\alpha^4}{64} + \dots \right] \\ &\cong \frac{\lambda_{\alpha 13}}{8\sigma_\alpha^2} \quad (77) \end{aligned}$$

and it is easily shown that this same result holds for $\overline{\sin \theta_s(t) \sin \theta_s(t+\tau)}$. In (77) $K(x)$ and $E(x)$ are respectively the complete elliptic integrals of the first and second kinds. Also

$$p_\alpha^2 = \frac{1}{\sigma^4} (\lambda_{\alpha 13}^2 + \lambda_{\alpha 14}^2)$$

$$p_\alpha'^2 = 1 - p_\alpha^2.$$

Using the same methods employed by Bunimovich, one can obtain

$$\begin{aligned} \overline{\cos \theta_s(t) \sin \theta_s(t+\tau)} &= -\overline{\sin \theta_s(t) \cos \theta_s(t+\tau)} \\ &= \frac{\lambda_{\alpha 14}}{2\sigma_\alpha^2 p_\alpha^2} [E(p_\alpha) - p_\alpha' K(p_\alpha)] \\ &\cong \frac{\lambda_{\alpha 14}}{8\sigma_\alpha^2}. \quad (78) \end{aligned}$$

Thus

$$\overline{U(t)U(t+\tau)} = \frac{\lambda_{\beta 13}(\tau)\lambda_{\alpha 13}(\tau)}{\sigma_\alpha^2} + \frac{\lambda_{\beta 14}(\tau)\lambda_{\alpha 14}(\tau)}{\sigma_\alpha^2} \quad (79)$$

Taking the cosine transform of this expression and making use of the relations following (73), one obtains

$$W_U(f) = \frac{1}{\sigma_\alpha^2} \int_0^\infty df_1 W_\alpha'(f_1 - f) W_\beta'(f) \quad (80)$$

where

$$W'(f) = W(f + f_0).$$

APPENDIX II

SPECTRUM OF E FOR RANDOM ROTATION

To treat this case, put

$$\Theta(t) = \int_0^t \Omega(t) dt; \quad (81)$$

then $V(t)$ can be written

$$V(t) = \iint_A \exp i \left[\omega_0 t + \frac{2\omega_0 x}{c} \Theta(t) \right] h(x, y) d^2 H(x, y). \quad (82)$$

⁹ V. I. Bunimovich, "Fluctuating processes as oscillations with random amplitudes and phases," *Zhur. Tekh. Fiz.*, vol. 19, pp. 1231-1259, 1949.

One recognizes with

$$\exp i \left[\omega_0 t + \frac{2\omega_0 x}{c} \Theta(t) \right] \tag{83}$$

$$\Phi^{(m)}(z) = \frac{d^m}{dz^m} \frac{\exp(-z^2/2)}{2\pi} \tag{89}$$

as the equation of a unit amplitude, phase modulated wave with modulating function $\Theta(t)$.

To compute the spectrum of V find first its auto-correlation function.¹⁰

$$z = \frac{\sqrt{2}(f_0 - f)}{f_b D} . \tag{90}$$

$$R_V(\tau) = \overline{V(t)V(t+\tau)} = \int_A \int_A \int_A \int_A \exp i \left\{ \omega_0 t + \frac{2\omega_0 x_1 \Theta(t)}{c} \right\} \exp i \left\{ \omega_0(t+\tau) + \frac{2\omega_0 x_2 \Theta(t+\tau)}{c} \right\} \\ \cdot h(x_1, y_1) h(x_2, y_2) d^2 H(x_1, y_1) d^2 H(x_2, y_2)$$

which becomes

$$R_V(\tau) = \cos \omega_0 \tau \int_{-L/2}^{L/2} \exp \{ -D^2 [1 - \rho_\Theta(\tau)] \} g^2(x) dx \tag{84}$$

for the long, thin target. In (84)

$$D^2 = \frac{4\omega_0^2 \overline{\Theta^2} x^2}{c^2} ; \tag{85}$$

$$\rho_\Theta(\tau) = \frac{\overline{\Theta(t)\Theta(t+\tau)}}{\overline{\Theta^2}} . \tag{86}$$

If $L \gg \lambda_0 = c/f_0$, it is reasonable to assume $D \gg 1$, and, if this assumption can be made, the analysis is much simplified. The above assumptions seem reasonable for aircraft targets and wavelengths in the microwave range. With these assumptions, the spectrum of V depends on the probability density of Θ , which can very reasonably be taken as normal and not on the spectrum of Θ , which is in general unknown. The argument here is roughly as follows: Rate of change of phase is frequency, and if phase variations are normal, so are frequency variations. For very large frequency variations, the spectrum of V is determined primarily by the probability of a given frequency deviation from the carrier, and hence the spectrum is determined by the probability density. If this has a Gaussian form the spectrum will also.¹¹

The bandwidth of the spectrum of Θ must be known, and, to be specific take

$$W_\Theta(f) \sim \exp(-f^2/f_b^2) \tag{87}$$

with f_b a measure of bandwidth. The cosine transform of R_V is W_V and this can be expanded¹⁰ in a series of inverse powers of D which is valid for $D \gg 1$.

$$W_w(f) = \frac{2^{1/2}}{f_b} \int_{-L/2}^{L/2} \frac{g^2(x)}{D} \cdot [\Phi^{(0)}(z) + \Phi^{(4)}(z)/8D^2 + \dots] dx \tag{88}$$

If $D \gg 1$, only the first term need be used, and the spectrum of each element of W_V is Gaussian (a consequence, not of (87), but of the assumed normalcy of Θ).

A useful criterion for determining from empirical data when D is large can be derived from another expansion of $W_V(f)$ which applies when D is small.¹⁰

$$W_V(f) = \int_{-L/2}^{L/2} g^2(x) e^{-D^2} \left\{ \delta(f - f_0) + \frac{D^2}{\sqrt{\pi} f_b} \cdot \exp[-(f - f_0)^2/f_b^2] + \frac{D^4}{2^{3/2} \pi^{1/2} f_b} \cdot \exp[-(f - f_0)^2/2f_b^2] + \dots \right\} dx. \tag{91}$$

In this representation there is a carrier [represented by the delta function $\delta(f - f_0)$] of amplitude proportional to e^{-D^2} . If the ratio of carrier to continuous noise spectrum is too large, it can be expected that a Rayleigh distribution of E will not be obtained. Fig. 9 shows some curves taken from Rice⁵ giving the probability density of the envelope of a carrier plus noise as a function of α , the ratio of peak carrier to rms noise. From these curves it may be estimated that any α of the order of unity will

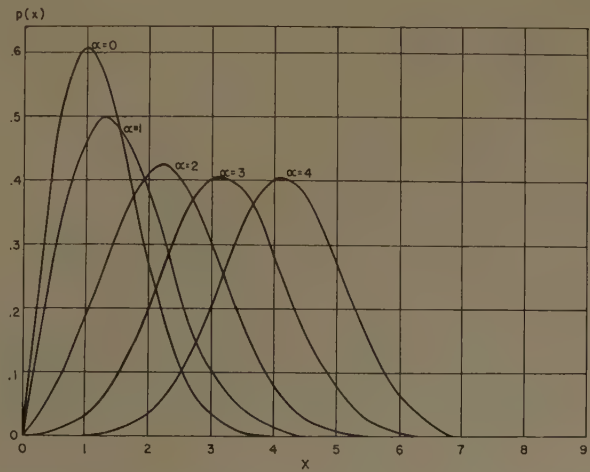


Fig. 9—Distribution of envelope of noise plus sine wave (after Rice). α =ratio of peak sine wave to rms noise. X =amplitude of noise plus sine wave.

¹⁰ D. Middleton, "The distribution of energy in randomly modulated waves," *Phil. Mag.*, vol. 42, pp. 689-707; July, 1951.
¹¹ For a detailed justification, see *ibid*.

give a density function which might be mistaken for a Rayleigh type when the fluctuations of sampling are considered.

A trial calculation in (91) shows that the carrier will about equal the total noise when D is equal to or a little less than 1. The first term of (88) is a good approximation when $D=1$. The conclusion, therefore, is that whenever the amplitude density function can be fairly represented as being of the Rayleigh type, the first term of (88) may be used to give the spectrum of V .

The spectrum of V will be taken, then, as

$$W_V(f) = \frac{1}{\sqrt{\pi} f_b} \int_{-L/2}^{L/2} \frac{g^2(x)}{D} \exp [-(f-f_0)^2/f_b^2 D^2] dx \quad (92)$$

and, using (19) for $g(x)$ and (85) for D ,

$$W_V(f) = -\frac{g_0^2 \lambda_0}{4\pi^{3/2} f_b \sqrt{\Theta^2}} Ei \left[-\frac{(f-f_0)^2 \lambda_0^2}{4\pi^2 f_b^2 L^2 \Theta^2} \right]. \quad (93)$$

The exponential integral is defined

$$-Ei(-x) = \int_x^\infty \frac{du}{u} e^{-u}. \quad (94)$$

The spectrum is obtained by convolution of $W_v(f+f_0)$ [see (92)] with itself, using (19) and (85) for $g(x)$ and D respectively. Ignoring multiplicative factors

$$W_E \sim \int_{-L/2}^{L/2} dx_1 \int_{-L/2}^{L/2} dx_2 \int_0^\infty dy \frac{e^{-c^2 y^2/x_1^2}}{x_1} \cdot \frac{e^{-c^2 (y-f)^2/x_2^2}}{x_2} \quad (95)$$

with

$$c = \frac{\lambda_0}{4\pi f_b \sqrt{\Theta^2}}. \quad (96)$$

Integrate over y first to obtain (again dropping constant factors)

$$W_E \sim \int_0^{L/2} dx_1 \int_0^{L/2} dx_2 \frac{e^{-c^2 f^2/x_1^2 + x_2^2}}{\sqrt{x_1^2 + x_2^2}}. \quad (97)$$

Upon changing to polar coordinates in the x_1, x_2 plane one has

$$W_E \sim \int_0^{\pi/2} d\theta \int_0^{L/2} dr e^{-c^2 f^2/r^2} + 2 \int_{L/2}^{L/\sqrt{2}} dr e^{-c^2 f^2/r^2} \int_{\cos^{-1} L/2r}^{\pi/4} d\theta. \quad (98)$$

The first term on the right may be integrated to obtain

$$\frac{\pi L}{4} \left[e^{4c^2 f^2/L^2} - \frac{2\sqrt{\pi} cf}{L} \operatorname{erfc} \left(\frac{2cf}{L} \right) \right] \quad (99)$$

while, for the second term, one obtains after integrating over θ ,

$$2 \int_{L/2}^{L/\sqrt{2}} dr e^{-c^2 f^2/r^2} \left(\frac{\pi}{4} - \cos^{-1} \frac{L}{2r} \right). \quad (100)$$

By a change of variable this becomes

$$L \int_{1/\sqrt{2}}^{\sqrt{2}} dz \frac{\left(\frac{\pi}{4} - \cos^{-1} z \right)}{z^2} e^{-4c^2 f^2 z^2/L^2}. \quad (101)$$

It is easily shown that

$$\begin{aligned} \frac{\pi}{4} \frac{\sqrt{2}}{\sqrt{2}-1} \left(z - \frac{1}{\sqrt{2}} \right) &\geq \left(\frac{\pi}{4} - \cos^{-1} z \right) \\ &\geq \sqrt{2} \left(z - \frac{1}{\sqrt{2}} \right) \end{aligned} \quad (102)$$

and using these one obtains bounds on the integral (101) as follows:

$$\begin{aligned} \frac{\sqrt{2} \pi L}{8(\sqrt{2}-1)} M &> \int_{1/\sqrt{2}}^{\sqrt{2}} dz \frac{\left(\frac{\pi}{4} - \cos^{-1} z \right)}{z^2} e^{-4c^2 f^2 z^2/L^2} > \frac{L}{\sqrt{2}} M \end{aligned} \quad (103)$$

$$\begin{aligned} M &= \frac{1}{2} \left[Ei \left(-\frac{4c^2 f^2}{L^2} \right) - Ei \left(-\frac{2c^2 f^2}{L^2} \right) \right] \\ &= e^{-2c^2 f^2/L^2} + \frac{1}{\sqrt{2}} e^{-4c^2 f^2/L^2} \\ &= \frac{\sqrt{2} \pi cf}{L} \left[\operatorname{erf} \frac{\sqrt{2} cf}{L} - \operatorname{erf} \frac{2cf}{L} \right]. \end{aligned} \quad (104)$$

One now has an upper and lower bound for W_E . These have been plotted in Fig. 10 along with the expression of (99). This last is evidently a good approximation even though slightly outside the bounds. The normalized form of this approximation is used in the text.

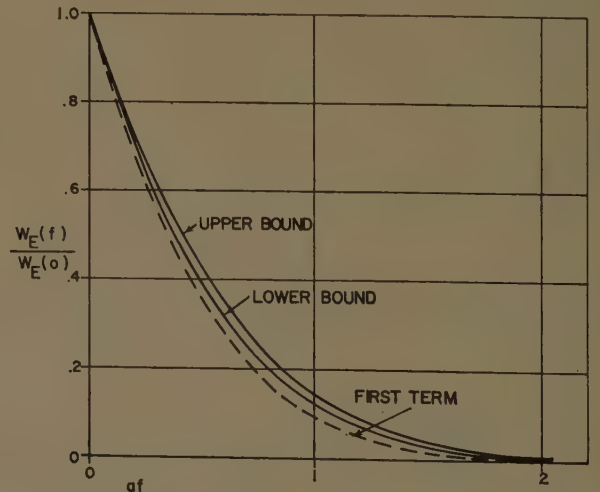


Fig. 10—First approximation and upper and lower bounds to spectrum of E for random rigid body rotation.

Apparent Thermal Noise Temperatures in the Microwave Region*

ERIC WEGER†

Summary—The necessary equations are presented for obtaining the noise temperature due to thermal radiation which would be sensed by a receiver with an antenna located at some altitude above the earth. Emission and absorption of radiation by the atmosphere is considered. Calculated over-all absorptivities and apparent atmospheric temperatures are given as a function of antenna observation angle for beam paths through the atmosphere. Six wavelengths in the microwave band and three types of weather conditions were chosen for the calculations. Some typical antenna temperatures are presented as examples of the magnitudes of the effects to be expected as a function of the type of surface being viewed, the weather, and polarization.

INTRODUCTION

THE effective range of radar systems used for surveillance or mapping is determined by the operating receiver noise level. For the new low-noise-level microwave amplifiers, this level is established not by the internal system noise but by the thermal radiation picked up by the antenna. It is therefore important to consider the sources and the magnitude of this radiation. The most important source of this noise is thermal radiation by the surface of the earth. The attenuation of this radiation by the atmosphere which intervenes between the earth and the antenna affects the thermal radiation sensed by the receiver, as does radiation by the atmosphere itself.

This paper presents the general formulas which are used to determine the resulting radiation fluxes at the antenna. Some calculated results, based on known emissivities and absorption factors, are presented for six wavelengths in the microwave region and three types of weather conditions. These can be used to establish the operating noise level of a receiver. The present treatment is restricted to a unidirectional antenna with a beamwidth defined as the angle between half-power points of the main lobe. Sidelobe effects are not considered. The receiving system is assumed to be viewing the earth at some angle from an altitude of 10 km or higher.

The evaluation of the equations to obtain quantitative data requires a knowledge of surface emissivities and atmospheric attenuation data. There is an abundance of material in the literature on the absorption of radiation by the constituents of the atmosphere. A con-

siderable amount of data has also been collected^{1,2} on the emissivities of typical terrestrial surfaces. These measurements have been made with a radiometer first proposed by Dicke.³ It is impossible here to delve into these subjects. But use is made of some of the available data in the calculations which are presented.

The energy leaving the earth's surface will include radiation which is reflected from the sky. In a previous paper,⁴ the author has dealt with the question of the atmospheric radiation reflected by a terrestrial surface. The results obtained there are used in the present discussion.

To conform with the standard usage in noise level calculations, the various radiation fluxes are expressed in terms of apparent temperatures.

DEFINITION OF APPARENT TEMPERATURE

The spatial geometry of the problem under discussion is shown in Fig. 1. As a simplification, the earth is considered as a flat surface. This will not cause any significant error as long as the altitude of the receiver is not very great. The antenna is located at R , a distance H above the surface. The look angle is ϕ degrees from vertical and an area dA is being viewed on the surface. The length of the beam is N , where $N = H \sec \phi$. The co-ordinate in the direction of the beam is n , while the co-ordinate in the vertical direction (from the antenna towards the earth) is z . The antenna beam encompasses $d\omega = dA/N^2 \cos \phi$ steradians. For the purposes of the following arguments the antenna will be considered a sphere with a diameter dR .

In order to express the radiant fluxes in terms of apparent temperatures it is necessary to compare them to the flux from a black surface. Therefore we will first consider dA as such a surface with temperature T_b . The space between dA and R is assumed to be vacuum. According to the Rayleigh-Jeans expression for the radiant flux of a black body, the amount of power impinging on dR from dA is

¹ E. A. Lewis, J. P. Casey, and A. J. Vaccaro, "Polarized Radiation from Certain Thermal Emitters," Air Force Cambridge Res. Center, Bedford, Mass., Tech. Rept. 54-6; February, 1954.

² C. W. Tolbert, C. O. Britt, and A. W. Straiton, "Apparent Temperatures of Some Terrestrial Materials and the Sun at 4.3 Millimeter Wavelengths," Elec. Engrg. Res. Lab., The University of Texas, Austin, Rept. No. 93; July, 1957.

³ R. H. Dicke, "The measurement of thermal radiation at microwave frequencies," *Rev. Sci. Instr.*, vol. 17, pp. 168-275; July, 1946.

⁴ E. Weger, "Apparent sky temperatures in the microwave region," to be published in *J. Meteorology*.

* Manuscript received by the PGAP, August 5, 1959. The work reported in this paper was done for the Air Arm Div. of Westinghouse Electric Corp. under Contract AF 39(602)-1826 sponsored by Rome Air Dev. Center of the USAF Air Research and Development Command.

† The Johns Hopkins University, Baltimore, Md.

$$\begin{aligned} (d^2Q_{A,R})_b &= \frac{2ckT_b}{\lambda_m^4} \Delta\lambda \frac{dR}{N^2} dA \cos\phi \\ &= \frac{2ckT_b}{\lambda_m^4} \Delta\lambda d\omega dR, \end{aligned} \quad (1)$$

where $\Delta\lambda$ is the bandwidth of the receiver and λ_m is the mean wavelength in the band. (c and k are the velocity of light in vacuum and Boltzmann's constant, respectively.)

Now, considering dA to be a real surface, and a layer of atmospheric gases to exist between dA and R , the radiative flux would be written

$$d^2Q_{A,R} = \frac{2ckT_A'}{\lambda_m^4} \Delta\lambda \exp\left(-\int_0^N a dn\right) d\omega dR. \quad (2)$$

T_A' is the apparent surface temperature which can be written

$$T_A' = \epsilon_\phi T_A + \rho_\phi T_S. \quad (3)$$

In (3), T_A is the actual thermodynamic surface temperature and T_S is the sky temperature seen at dA . The quantities ϵ_ϕ and ρ_ϕ are the emissivity and reflectivity, respectively, of the surface at dA . The exponential expression in (2) represents the effect of atmospheric attenuation and a is the absorption factor. It is related to the usual attenuation coefficient in db/km by

$$a \cong 0, 23 \text{ db}_{\text{att}}. \quad (4)$$

The absorption factor is a function of the composition and temperature of the atmosphere as well as a function of wavelength. It can be calculated theoretically for gases but must usually be determined experimentally for clouds, rain, etc. The absorption factor is, of course, a variable for an atmospheric path whose properties

vary with distance. The matter present in the atmosphere not only serves to attenuate the surface-originated radiation but contributes its own radiation. The radiant flux intensity emitted by a differential volume of gas dV into a differential solid angle $d\Omega$ is

$$d^3Q_V = \frac{2ackT_g}{\lambda_m^4} \Delta\lambda dV d\Omega, \quad (5)$$

where T_g is the gas temperature in the system being used and

$$dV = n^2 d\omega dn. \quad (6)$$

The differential solid angle $d\Omega$ subtended by the antenna at some element in its beam path is

$$d\Omega = \frac{dR}{n^2}. \quad (7)$$

Thus, (5) becomes

$$d^3Q_V = \frac{2ackT_g}{\lambda_m^4} \Delta\lambda d\omega dR dn. \quad (8)$$

The radiation emanating from an atmospheric volume element situated a distance n from R is attenuated in the same exponential fashion as surface radiation before it reaches the sensing device. The total radiant flux which falls on the antenna from the section of the atmosphere encompassed by the beam $d\omega$ is obtained by integrating along n , taking into account the attenuation factor.

$$d^2Q_{V,R} = \frac{2ck}{\lambda_m^4} \Delta\lambda \left[\int_0^N a T_g \exp\left(-\int_0^n a dn\right) dn \right] d\omega dR. \quad (9)$$

The total radiant flux reaching the antenna is obtained by combining (2) and (9):

$$\begin{aligned} d^2Q_{(AV),R} &= \frac{2ck}{\lambda_m^4} \Delta\lambda \left[T_A' \exp\left(-\int_0^N a dn\right) \right. \\ &\quad \left. + \int_0^N a T_g \exp\left(-\int_0^n a dn\right) dn \right] d\omega dR, \end{aligned} \quad (10)$$

or

$$d^2Q_{(AV),R} = \frac{2ck}{\lambda_m^4} \Delta\lambda [T_R' + T_R''] d\omega dR, \quad (11)$$

where T_R' and T_R'' represent the first and second parts of the expression in brackets in (10). Substituting

$$T_R = T_R' + T_R'' \quad (12)$$

into (11), the expression

$$d^2Q_{(AV),R} = \frac{2ckT_R}{\lambda_m^4} \Delta\lambda d\omega dR \quad (13)$$

is obtained. It will be noted that T_R corresponds to T_b in (1). T_R is defined as the apparent antenna temperature, *i.e.*, the external noise temperature.

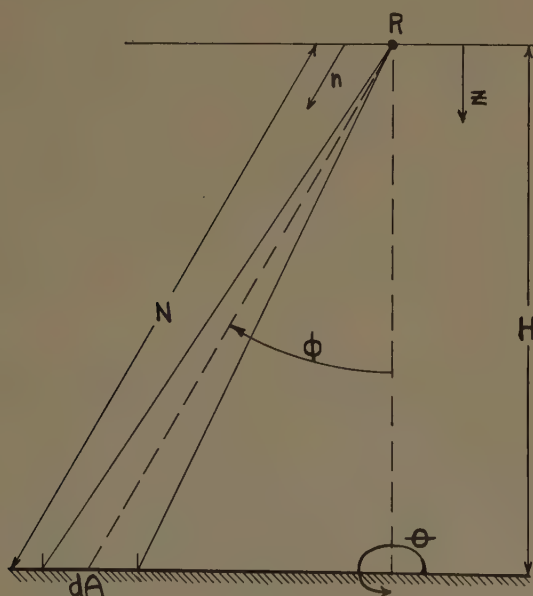


Fig. 1—Coordinate system.

Polarization effects have not been discussed. While the total flux measured by a polarized antenna will be less than that given above, the apparent temperature definitions remain unchanged. The appropriate emissivities and reflectivities must, of course, be used for any given polarization.

CALCULATED RESULTS

Some typical values of T_R'/T_A' (which is really an over-all absorption factor) and T_R'' were computed for six wavelengths and three types of weather conditions. An IBM 704 Computer was used for the calculations. An upper effective limit of 10 km was assumed for the atmosphere, since the concentrations of oxygen and water vapor (the main absorbers in the microwave region) above that altitude do not contribute appreciably to radiation or attenuation. An antenna height of 10 km or greater was assumed. For purposes of simplification, nonvariance of weather conditions with θ (see Fig. 1) was assumed. The absorption factors data which were used in the calculation have been discussed elsewhere.⁴ The computed points are shown in Figs. 2-7 for a range of ϕ from 0° to 70° .

The data presented in Figs. 2-7, plus the sky temperatures presented in Figs. 3-5 of Weger,⁴ were used to calculate some typical apparent temperatures of

surfaces as they would be "seen" by a receiver situated about 10 km above the earth's surface. Some available surface emissivity data at 0.86 cm and $\phi = 30^\circ$ for four types of surfaces were used.

Gas radiation is essentially unpolarized. When we discuss solid surface radiation, however, polarization effects must be taken into account. Therefore the calculations presented in Tables I and II are made for both horizontally and vertically polarized radiation. For the present calculations, only grass was regarded as a diffuse reflector, while the water, concrete, and asphalt were treated as Fresnel reflecting surfaces. The reflective character of a surface depends on the ratio of its relative roughness to the wavelength of the impinging radiation. Unless the surface roughness of the concrete or asphalt surfaces is of the order of 0.3 to 3 cm in the present instance (a highly unlikely condition) the assumption of specular reflection is justifiable. Smooth water is, of course, a Fresnel reflector. As the roughness of the water surface increases, the approximation becomes less valid. Again the criterion will be the ratio of roughness to wavelength.

Weather conditions corresponding to Cases I and III, as detailed in Figs. 2, 4, 5, and 7, were used in the calculations.

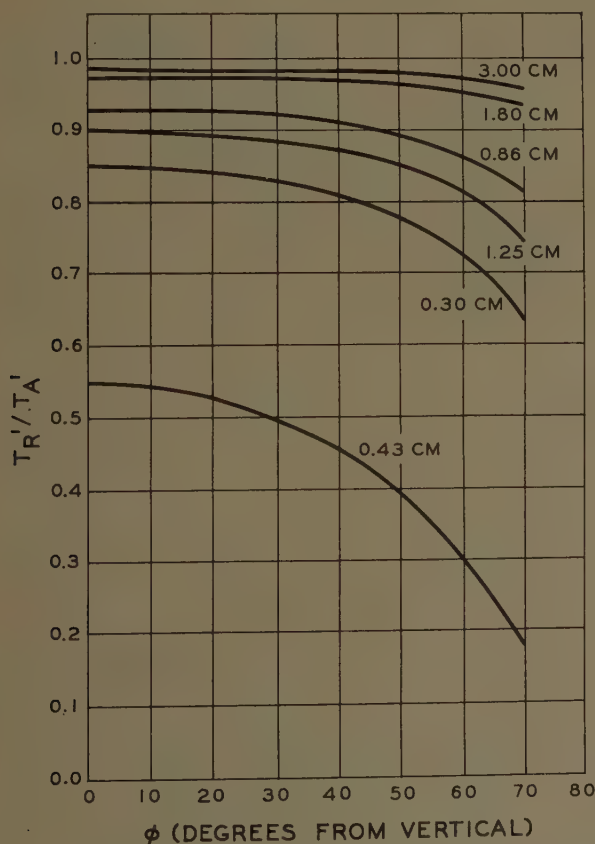


Fig. 2—Over-all atmospheric attenuation factor (T_R'/T_A') as a function of ϕ and wavelength, Case I. Conditions: clear sky; 1 per cent absolute humidity at sea level; sea-level temperature 290°K .

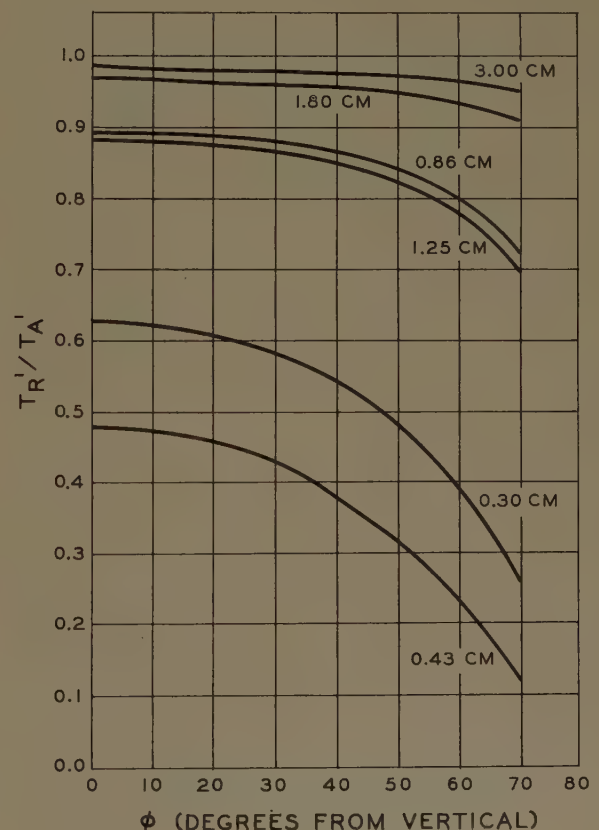


Fig. 3—Over-all atmospheric attenuation factor (T_R'/T_A') as a function of ϕ and wavelength, Case II. Conditions: moderate cloud cover (0.3 g water/m^3) between 3000 and 6000 feet; 1 per cent absolute humidity at sea level; sea-level temperature 290°K .

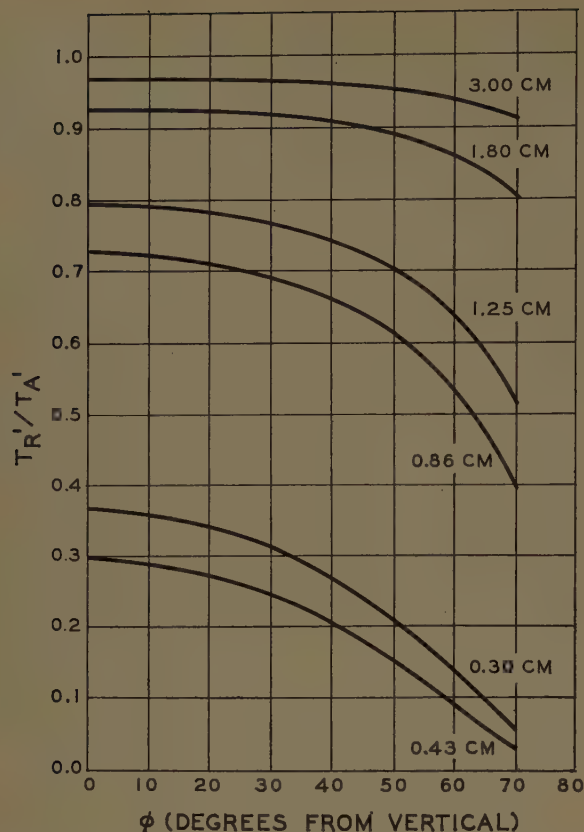


Fig. 4—Over-all atmospheric attenuation factor (T_R'/T_A') as a function of ϕ and wavelength, Case III. Conditions: moderate rain (4 mm/hour) between 0 and 3000 feet; moderate cloud cover (0.3 g water/m³) between 3000 and 6000 feet; sea-level temperature 290°K.

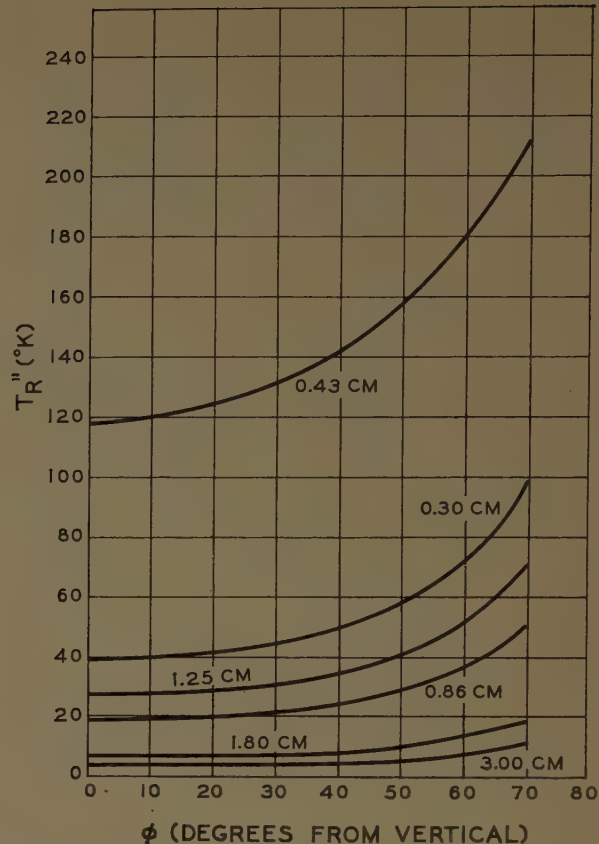


Fig. 5—Temperature contribution (T_R'') of the intervening atmosphere between sea level and 32,000 feet as a function of ϕ and wavelength, Case I. Conditions: clear sky; 1 per cent absolute humidity at sea level; sea-level temperature 290°K.

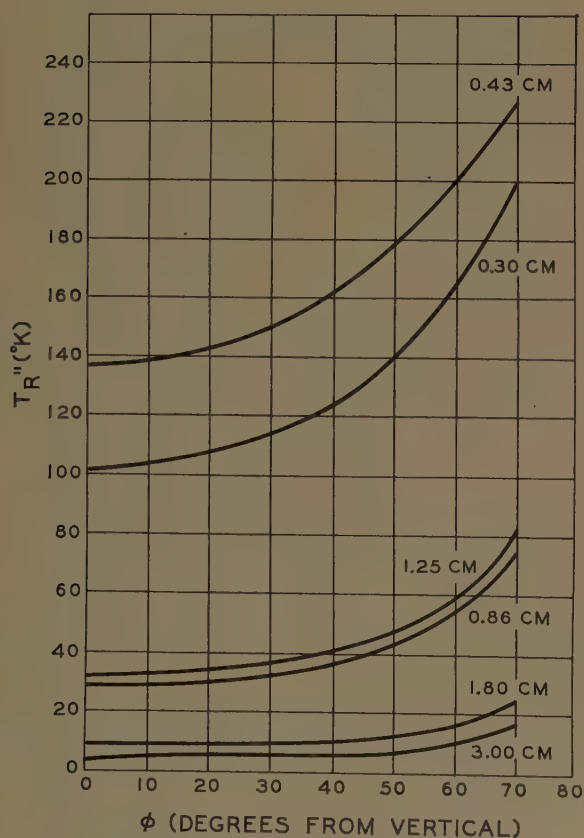


Fig. 6—Temperature contribution (T_R'') of the intervening atmosphere between sea level and 32,000 feet as a function of ϕ and wavelength, Case II. Conditions: moderate cloud cover (0.3 g water/m³) between 3000 and 6000 feet; 1 per cent absolute humidity at sea level; sea-level temperature 290°K.

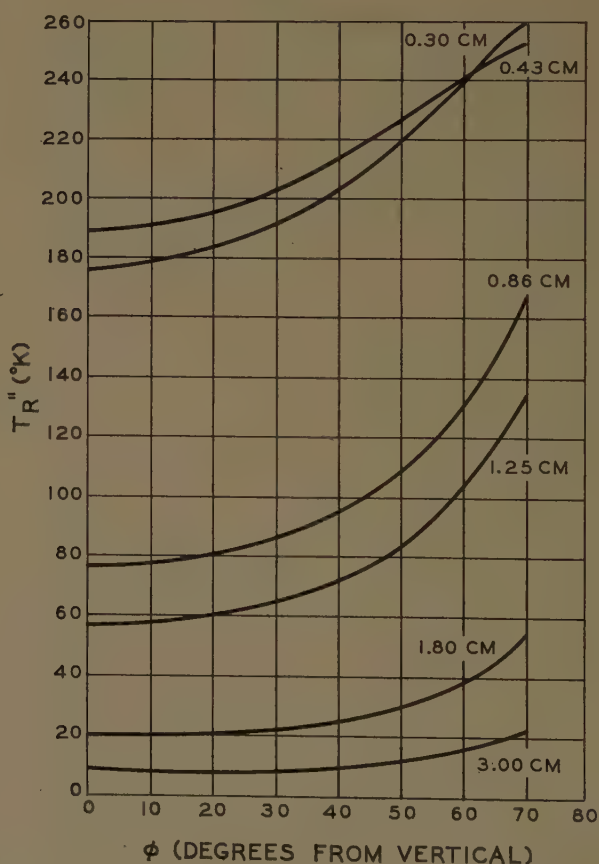


Fig. 7—Temperature contribution (T_R'') of the intervening atmosphere between sea level and 32,000 feet as a function of ϕ and wavelength, Case III. Conditions: Moderate rain (4 mm/hour) between 0 and 3000 feet; moderate cloud cover (0.3 g water/m³) between 3000 and 6000 feet; sea-level temperature 290°K.

TABLE I
APPARENT TEMPERATURES FOR A CLEAR SKY

Surface	Horizontal Polarization		Vertical Polarization	
	Emissivity (ϵ_ϕ)	Apparent Temperature T_R ($^{\circ}\text{K}$)	Emissivity (ϵ_ϕ)	Apparent Temperature T_R ($^{\circ}\text{K}$)
Water	0.41	142	0.50	169
Grass	0.98	283	0.99	284
Concrete	0.88	257	0.94	272
Asphalt	0.89	261	0.95	275

DISCUSSION

It will be noted that T_R'/T_A' and T_R'' are very dependent on wavelength. This is to be expected because of a similar dependence of the absorption factors. For example, there is a maximum in the absorption curve of oxygen near 0.43 cm. This contributes to the fact that, for any one angle, the temperatures at this wavelength are higher than for any of the other wavelengths for which results were obtained. However, the difference between the temperatures at 0.3 and 0.43 cm decreases as the weather conditions become progressively worse. This is due to the fact that attenuation of microwave radiation by condensed water in the atmosphere increases monotonically as wavelength decreases.⁴ The temperature factors at 0.3 cm will therefore increase more rapidly as the amount of condensed water vapor in the atmosphere increases than will the temperature factors at 0.43 cm.

For similar reasons, the 1.25-cm and 0.86-cm curves interchange position in the increasing order of temperature as the weather conditions change from clear to cloudy. There is a water vapor absorption maximum at 1.25 cm. As atmospheric condensed water content increases, however, the higher attenuation at 0.86 cm of this additional constituent causes the 0.86-cm factors to be higher than the 1.25-cm factors for rainy sky con-

TABLE II
APPARENT TEMPERATURES FOR UNIFORM MODERATE RAIN

Surface	Horizontal Polarization		Vertical Polarization	
	Emissivity (ϵ_ϕ)	Apparent Temperature T_R ($^{\circ}\text{K}$)	Emissivity (ϵ_ϕ)	Apparent Temperature T_R ($^{\circ}\text{K}$)
Water	0.41	205	0.50	228
Grass	0.98	286	0.99	286
Concrete	0.88	271	0.94	280
Asphalt	0.89	272	0.95	282

ditions. As expected, attenuation and atmospheric radiation factors for all wavelengths increase with increasing condensed water content in the atmosphere.

It is noted in Fig. 7 that the 0.30-cm and the 0.43-cm curves cross at about 62° . This is due to the increasing (with ϕ) pathlength which traverses condensed water regions, where the absorption factor for 0.30 cm is higher than that at 0.43 cm.

The calculated temperature data presented in Tables I and II demonstrate that atmospheric conditions will significantly influence measured apparent temperatures. Radiation from surfaces of low emissivity, such as smooth water or bright metals, will be affected to the greatest extent. It will be noted that inclement weather conditions have the effect of raising the apparent temperatures, the effect being greatest for low-emissivity materials. This is to be expected because of the increased atmospheric radiation occurring under these conditions.

The temperatures for vertical polarization are consistently higher than those for horizontal polarization. The theory for Fresnel surfaces predicts that the vertically-polarized emissivity of a smooth surface is higher than the horizontally-polarized emissivity at all incidences other than 0° and 90° . The same relationship is valid qualitatively for rough surfaces.

communications

Patterns of a Radial Dipole on an Infinite Circular Cylinder: Numerical Values*

CURT A. LEVIS†

FORMULAS for the far-field patterns of simple antennas near circular cylinders were calculated by Carter over 15 years ago.^{1,2} The title of one of his papers, "Antennas and Cylindrical Fuselage," immediately suggests aircraft and missile antennas as an important area of application, but little use has been made of this theory because of the difficulty of the numerical calculations. To remedy this difficulty, a table³ has now been calculated for short radial dipoles mounted at the surface of an infinite cylinder one wavelength or less in diameter. Although the table is too long to be published here, its existence should be of interest to antenna designers.

The table may be used to obtain three closely related functions. Listed directly is the radial electric field com-

ponent when an incident plane wave is diffracted by the cylinder as in Fig. 1, but with the stub not present. From this, the transmitting patterns of a short stub or dipole situated as shown may be obtained by a simple arithmetic manipulation. The same is true of the receiving patterns of the stub or dipole for arbitrary incident polarization. Values of θ vary in steps of 5° from 5° to 175° , and those of ϕ in steps of 5° from 0° to 90° . Because of symmetry, these values suffice for complete spherical

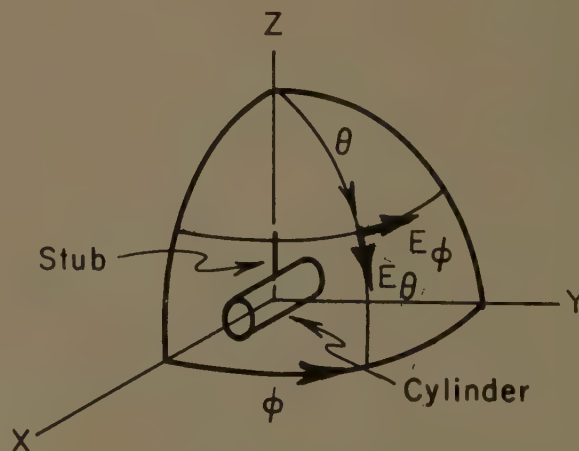


Fig. 1—Coordinate system for use with table.

* Manuscript received by the PGAP, September 12, 1959. Work in this paper sponsored by the Air Res. and Dev. Command, Wright Air Development Center, Dayton, Ohio.

† Antenna Lab., Dept. of Elec. Engrg., The Ohio State University, Columbus, Ohio.

¹ P. S. Carter, "Antenna arrays around cylinders," *Proc. IRE*, vol. 31, pp. 671-693; December, 1943.

² P. S. Carter, "Antennas and Cylindrical Fuselage," RCA, Rocky Point, N. Y., Rept. 895-11; December, 1943.

³ C. A. Levis, "Patterns of a Radial Dipole on an Infinite Circular Cylinder: Numerical Values," Antenna Lab., The Ohio State University Res. Foundation, Columbus, Ohio, Rept. 667-51, prepared under Contract AF 33(616)-3353, Wright Air Dev. Center, Wright-Patterson Air Force Base, Dayton, Ohio; February 27, 1959.

coverage. The cylinder radius varies from 0.05λ to 0.50λ in steps of 0.05λ , where λ is the free-space wavelength. The table is available on punched cards for further calculations (e.g., patterns of arrays of radial stubs, interpolation, or transformation to other coordinate systems). The coordinate system of Fig. 1 was chosen because of its direct applicability to aircraft problems.

In practical applications, finite cylinders and fuselages

are used, for which the infinite cylinder model is a zero-order approximation. To obtain an estimate of the accuracy, the patterns were measured for a brass tube 4 feet long, closed at the ends, with a radial stub 0.6 cm long fitted at the midpoint. The patterns measured at $\lambda = 12.7$ cm ($a/\lambda = 0.2$) and $\lambda = 6.35$ cm ($a/\lambda = 0.4$) are compared to the computed values in Fig. 2. In parts (a) to (j) of Fig. 2 the patterns were measured at the

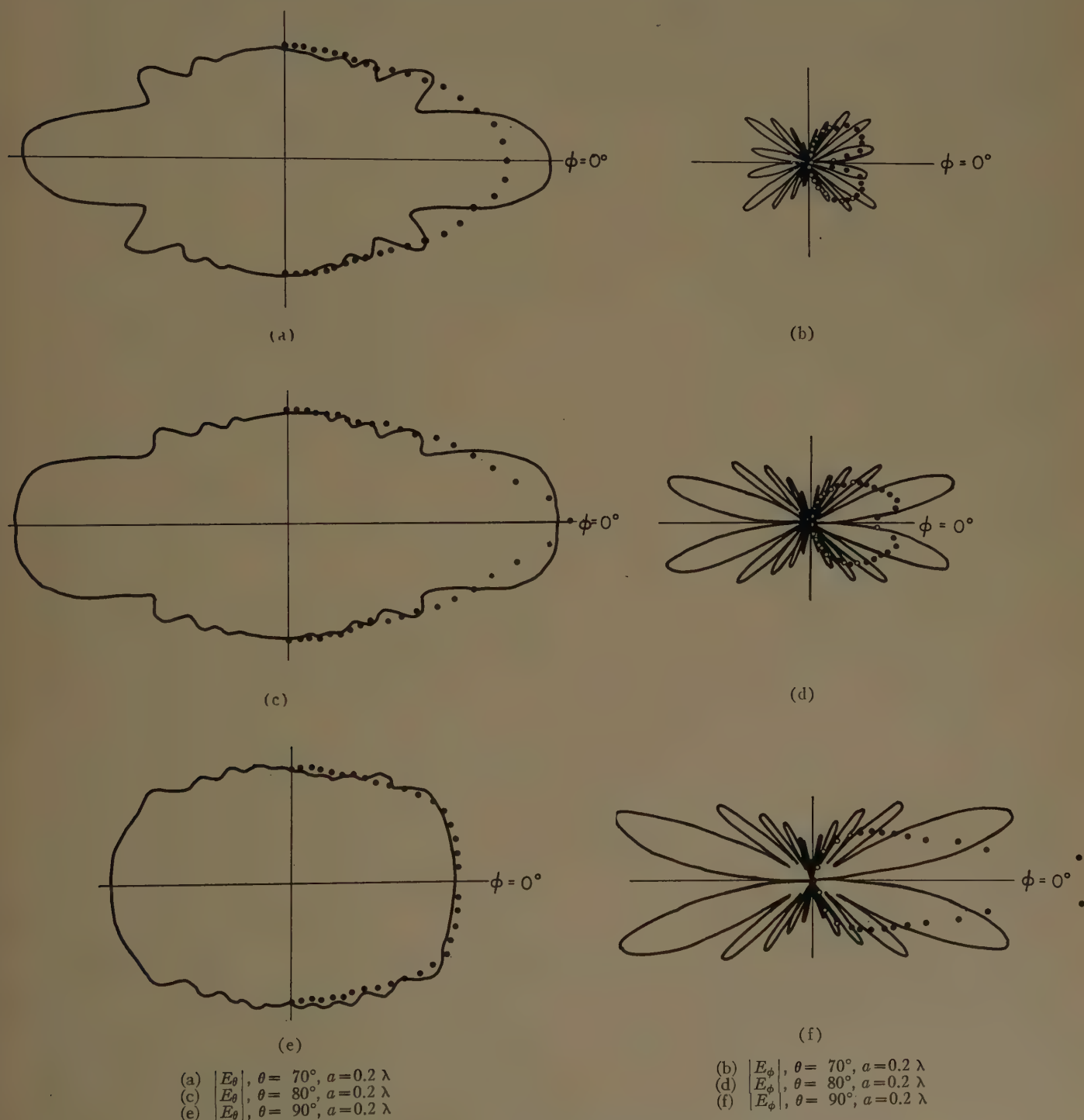
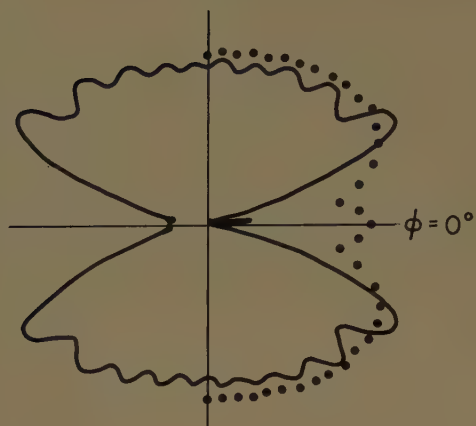


Fig. 2—Comparison of measured patterns (solid line) and calculated values (dots and circles).

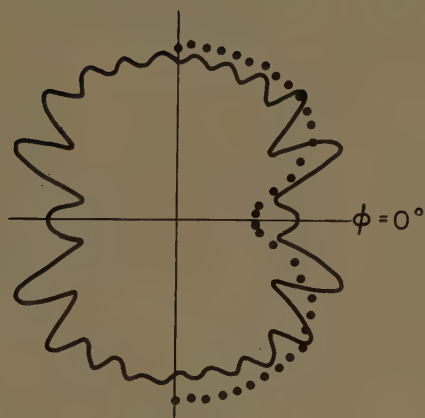
(Fig. 2 cont'd next page)



(g)



(h)



(i)



(j)



(k)



(l)

(g) $|E_\theta|$, $\theta = 100^\circ$, $a = 0.2 \lambda$
 (i) $|E_\theta|$, $\theta = 110^\circ$, $a = 0.2 \lambda$
 (k) $|E_\theta|$, $\theta = 90^\circ$, $a = 0.4 \lambda$

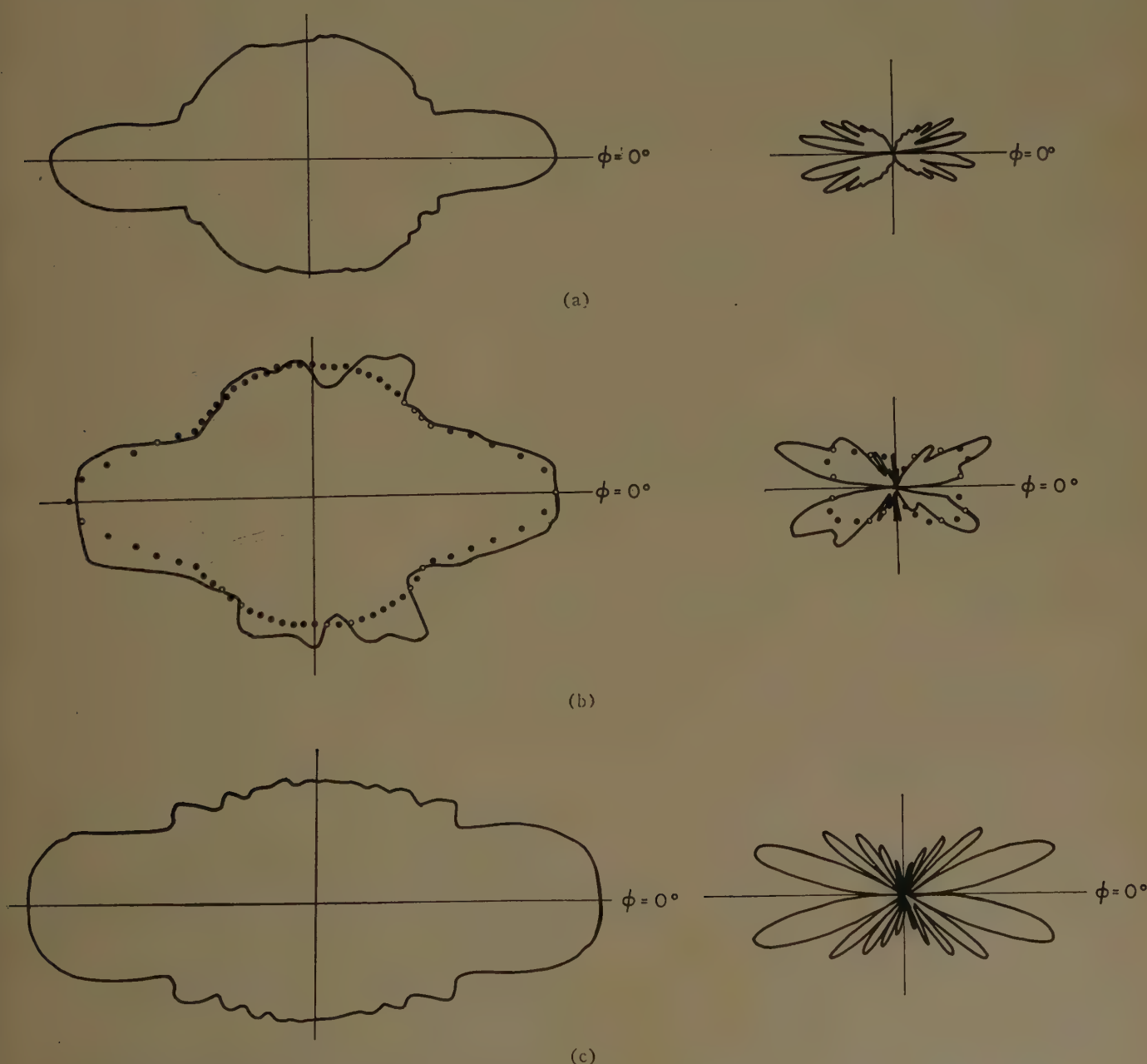
(h) $|E_\phi|$, $\theta = 100^\circ$, $a = 0.2 \lambda$
 (j) $|E_\phi|$, $\theta = 110^\circ$, $a = 0.2 \lambda$
 (l) $|E_\phi|$, $\theta = 100^\circ$, $a = 0.4 \lambda$

Fig. 2—(Cont'd)

same gain setting and the computed points are plotted to a single scale; thus these patterns serve to confirm the variation with θ as well as with ϕ . From the measurements it appears that the calculations give excellent results in the directions where the finite cylinder length produces no serious diffraction effects. The calculated values predict an approximate average in those directions, and for those components, for which the finite cylinder length does produce a diffracted fine lobe structure. The fine lobes themselves are not predicted by the table. Agreement is poorest for the fine lobe structure near the cylinder axis ($\theta = 90^\circ$, $\phi = 0^\circ$ or 180°).

The validity of using this simplified model for aircraft

antennas is investigated briefly in Fig. 3. The center panels show the patterns measured 10° below the horizon for a simulated 2-inch (diameter) stub, 15.6 inches long, located 65 feet back from the nose on the bottom center-line of the fuselage of a B-47 aircraft. The measurements were made on a 1/40 scale model at $\lambda = 11.03$ cm. The superimposed dots show values as given by the calculated table for $a/\lambda = 0.35$, which is the approximate value for this location. Also shown are the patterns for the 4-foot cylinder described above at the frequencies for which $a/\lambda = 0.4$ (top) and $a/\lambda = 0.2$ (bottom). In this case, that of a stub well removed from wings and control surfaces, it is found that the cylindrical fuselage is



(a) Four-foot cylinder, $a/\lambda = 0.4$. (b) B-47 aircraft and calculated points, $a/\lambda = 0.35$. (c) Four-foot cylinder, $a/\lambda = 0.2$.

Fig. 3—Comparison of calculated patterns with measurements of a stub antenna mounted on a B-47 aircraft and on a finite cylinder. At left: $|E_\theta|$; at right: $|E_\phi|$.

the primary factor in determining the patterns, and that fair predictions can be made by use of the calculated results.

Plans for this table originated during an investigation of the directional errors of airborne Adcock antennas by R. E. Webster and the author in 1953. In order to estimate the effect of the fuselage, some rough and laborious calculations were made with a desk calculator and interpolation graphs constructed from existing tables. Although these calculations did show the gross effects, they were too inexact to warrant publication. The subsequent establishment of a computation laboratory at The Ohio State University and installation of an IBM 650 computer made a more exact and extended table possible.

Before proceeding with the calculation it was necessary to check Carter's original results, which had been

quoted at variance in a later publication. The formulas were rederived by Webster and the author, working separately and independently, and Carter's results were obtained in each case. These results were specialized to the case of a stub directly on the cylinder surface.

ACKNOWLEDGMENT

The author is indebted to D. Stickler for a further check on the derivations. The experimental results were obtained at the inception of the program in 1953, and the assistance of B. Murphy is gratefully acknowledged. This table would have been impossible without the excellent cooperation of The Ohio State University Numerical Computation Laboratory and especially of Dr. R. Reeves, who wrote the machine program for the computation.

Linear Arrays with Arbitrarily Distributed Elements*

H. UNZ†

Summary—A linear array with general *arbitrarily* distributed elements is discussed. A matrix relationship is found between the elements of the array and its far-zone pattern. The lower bound of the stored energy and the Q factor of the array are found. A figure of merit for the array is defined.

THE far-zone pattern of a linear array with arbitrarily distributed similar elements is given by:

$$F(\phi) = \sum_{l=0}^L A_l e^{ikx_l \sin \phi}. \quad (1)$$

Using the Jacobi expansion¹

$$e^{iz \sin \phi} = \sum_{n=-\infty}^{+\infty} e^{in\phi} J_n(z), \quad (2)$$

we get

$$F(\phi) = \sum_{n=-\infty}^{+\infty} e^{in\phi} \sum_{l=0}^L A_l J_n(kx_l). \quad (3)$$

* Manuscript received by the PGAP, March 24, 1959. This work was supported by the U. S. Navy at the University of California, Berkeley, under contract No. N7onr-29529. The material was included in a thesis submitted in partial satisfaction of the requirements for the Ph.D. degree at the University of California, Berkeley, November, 1956.

† Elec. Engrg. Dept., University of Kansas, Lawrence, Kans.

¹ G. N. Watson, "A Treatise on the Theory of Bessel Functions," Cambridge University Press, Cambridge, Eng.; 1952.

Since $F(\phi)$ is a periodic function with respect to ϕ , it can be expanded in a complex Fourier series with the coefficients:

$$f_n = \sum_{l=0}^L A_l J_n(kx_l). \quad (4)$$

Eq. (4) gives a direct relationship between the currents in the elements of the array, their distribution along the axis of the array, and the coefficients of the complex Fourier expansion of the radiation pattern.

Since (4) must hold for every n , it may be written in a matrix form:

$$f_n = [J_{nl}] A_l. \quad (5)$$

In case we want to get a prescribed radiation pattern from $L+1$ arbitrarily distributed radiators, we have to find the inverse matrix $[J_{nl}]^{-1}$; but then we can use only the first $L+1$ coefficients f_n of the Fourier series.

Expansion (2) is not the only possible one. Other expansions in terms of Legendre polynomials and Gegenbauer polynomials might be found and similar identities might be derived.²

² H. Unz, "Linear Arrays with Arbitrarily Distributed Elements," Electronics Res. Lab., Univ. of California, Berkeley, Rept. Ser. No. 60, Issue No. 168; November 2, 1956. (Navy Contract N7onr-29529)

The total radiated power of the linear array with arbitrarily distributed similar elements is given by:²

$$P = \frac{\omega^2 \mu^2}{4\pi\eta} \sum_{l=0}^L \sum_{m=0}^L A_l A_m^* I(|x_l - x_m|), \quad (6)$$

where $I(|x_l - x_m|)$ is the interaction coefficient, and may be found for basic array (isotropic radiators) and for dipole elements array in Fig. 1. In case of a basic array with multiples of half wavelength distribution of the radiators we get from (6) and Fig. 1:

$$P = \frac{\omega^2 \mu^2}{4\pi\eta} \sum_{l=0}^L |A_l|^2; \quad (7)$$

however, this is not a physically realizable array.

The gain of the array may be shown² to be

$$G = \frac{\sum_{l=0}^L \sum_{m=0}^L A_l A_m^*}{\sum_{l=0}^L \sum_{m=0}^L A_l A_m^* I(|x_l - x_m|)}. \quad (8)$$

Taking the stored energy U in the immediate neighborhood of the radiators only, we can define the Q factor of the array

$$Q = \omega \frac{U}{P}. \quad (9)$$

It may be shown² that we get:

$$Q = \frac{Q^I}{G^I} \frac{\sum_{l=0}^L |A_l|^2}{\sum_{l=0}^L \sum_{m=0}^L A_l A_m^* I(|x_l - x_m|)} \quad (10)$$

where Q^I and G^I are the Q factor and the gain of each element of the array by itself.

The "figure of merit" ξ of the array may be defined from (8) and (10) to be

$$\xi = (L + 1) \frac{Q/Q^I}{G/G^I} = (L + 1) \frac{\sum_{l=0}^L |A_l|^2}{\left| \sum_{l=0}^L A_l \right|^2}. \quad (11)$$

In general we are interested in making ξ small. It may be shown that in case of $A_l = \text{Const}$, we get the minimum value of ξ , and always $\xi \geq 1$. In case of super-gain array, ξ will be very large and the array will not be effective (the gain per unit of stored energy will be very small.)

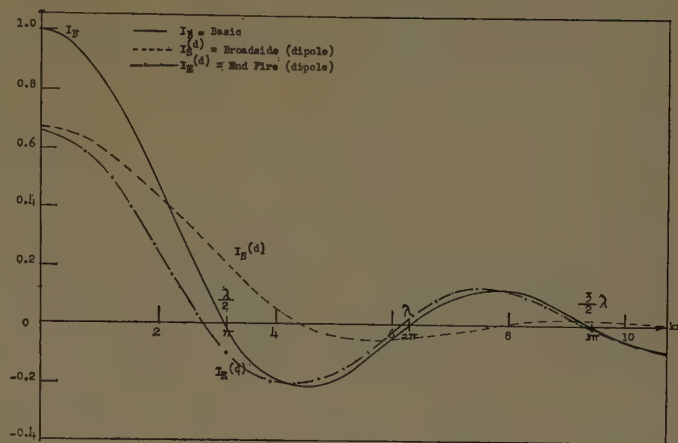


Fig. 1—Interaction coefficients.

The suggestion is made for the use of arbitrarily distributed elements in linear arrays. A general theory has been given² in order to analyze the performance of such arrays, as well as to compare them.

In the arrays with equally-spaced elements, we say that each element has one degree of freedom, *i.e.*, its complex amplitude. A linear array with L equally-spaced elements has L degrees of freedom, since we can match L coefficients of the Fourier series. By taking the general case of arrays with arbitrarily distributed elements, we add to each element another degree of freedom, *i.e.*, its position along the axis of the array. Although there are certain restrictions on the position of the element along the axis of the array,² the array with arbitrarily distributed elements has more degrees of freedom than a similar array with equally-spaced elements. Therefore the array with arbitrarily distributed elements needs, in general, fewer elements in order to achieve the same performance as an array with equally-spaced elements. In case we want to take the same number of elements, the performance of the array with arbitrarily distributed elements can be made better. Using the above suggestions, the designer of arrays will have more latitude in his work in order to achieve the required pattern and performance of the array. Examples of design may be found in the original paper.²

The above approach may be extended to two and three dimensional arrays.³

³ H. Unz, "Multi-Dimensional Lattice Arrays with Arbitrarily Distributed Elements," Electronics Res. Lab., Univ. of California, Berkeley, Rept. Ser. No. 60, Issue No. 172; December 19, 1956. (Navy Contract No. N7onr-29529.)

Synthesis of Nonseparable Two-Dimensional Patterns by Means of Planar Arrays*

A. KSIENSKI†

IN many applications of two-dimensional arrays, the pattern is specified in the two principal planes, and usually involves directive patterns in either one or both planes. In such applications the synthesis may be carried out by using a product of two arrays, synthesizing the pattern in one plane by means of one array, and then considering that array as an element of an array at right angles to it. Such a representation assumes that the desired pattern is separable into two independent patterns for the two principal planes. In recent applications the pattern requirements are specified not only in the principal planes but throughout the (θ, ϕ) space (where θ and ϕ are the observation angles). Moreover some applications may involve nonseparable patterns, as for example multiple, independent beams, or the illumination of certain ranges of (θ, ϕ) by specific patterns (cosecant²). Another example of a nonseparable pattern in θ and ϕ is the "element factor" which is usually ignored, but in the case of stringent accuracy requirements has to be considered.

We shall presently consider a two-dimensional array of apertures and show that one can synthesize by means of such an array any desired pattern, whether separable or not, and specified throughout the (θ, ϕ) space. Specifically, we will show that the array can be made to represent a Fourier series in two dimensions. The apertures are similarly excited except for an arbitrary complex constant representing magnitude and phase. For convenience of computation we will assume a rectangular aperture but this does not limit the results to such apertures. The far field of a rectangular aperture is given by:¹

$$g_{00}(\theta, \phi) = \int_{-a_1/2}^{a_1/2} \int_{-b_1/2}^{b_1/2} F(\xi, \eta) \cdot \exp [jk \sin \theta (\xi \cos \phi + \eta \sin \phi)] d\xi d\eta \quad (1)$$

where ξ, η are the source variables and $F(\xi, \eta)$ is the aperture excitation, and the aperture dimensions are $a_1 \times b_1$ (see Fig. 1).

The far field expression for an aperture whose center is displaced from the origin (na) along the ξ axis and (mb) along the η axis (where $a \geq a_1; b \geq b_1$) may be shown to be:²

$$g_{mn}(\theta, \phi) = A_{mn} \exp [jna k \sin \theta \cos \phi + jmb k \sin \theta \sin \phi] g_{00}(\theta, \phi) \quad (2)$$

where A_{mn} is a complex constant representing the amplitude and phase ratios of the m, n th aperture as compared to the one at the origin. Combining the contributions of all the elements in the array we obtain the total radiation expression:

$$g(\theta, \phi) = g_{00}(\theta, \phi) \sum_m \sum_n A_{mn} \cdot \exp [jna k \sin \theta \cos \phi + jmb k \sin \theta \sin \phi]. \quad (3)$$

Factoring out the expression $g_{00}(\theta, \phi)$ and fixing the values of $a = \lambda/2 = b$ we obtain

$$G(\theta, \phi) = \frac{g(\theta, \phi)}{g_{00}(\theta, \phi)} = \sum_m \sum_n A_{mn} \cdot \exp [jn\pi \sin \theta \cos \phi + jm\pi \sin \theta \sin \phi]. \quad (4)$$

Given a desired far field pattern specified in (θ, ϕ) space— $H(\theta, \phi)$ —it can be mapped uniquely on a unit sphere centered at the origin. One can now project this spherical surface on a square whose sides are two units long and whose center is at the origin (see Fig. 2). This is equivalent to transforming the spherical coordinates (θ, ϕ, r) where $r=1$ into rectangular coordinates and

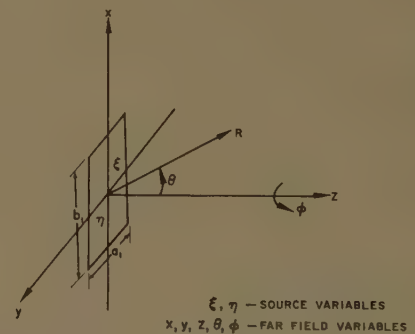


Fig. 1.

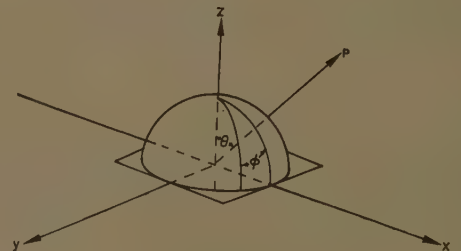


Fig. 2.

* Manuscript received by the PGAP, October 15, 1959.

† Microwave Lab., Hughes Aircraft Co., Culver City, Calif.

¹ S. Silver, "Microwave Antenna Theory and Design," McGraw-Hill Book Co., Inc., New York, N. Y., p. 180; 1949.

² For details see A. Ksienski, "Synthesis of Antenna Radiation Patterns from Discrete Sources," Ph.D. dissertation, University of Southern California, Los Angeles, Calif., pp. 54 ff.; 1958.

then letting $z=0$. This transformation preserves the uniqueness of the mapping for a half sphere corresponding to the half space of interest ($z \geq 0$), but does distort the pattern. The same distortion however is also applied to the array pattern which is similarly transformed, so that the correct pattern will be obtained. The approximate characteristics, however, of the Fourier series representation may be affected somewhat. Carrying out the above mentioned transformation on $G(\theta, \phi)$ we obtain,

$$G(x, y) = \sum_m \sum_n A_{mn} \exp[jn\pi x + jm\pi y] \quad (5)$$

where

$$\begin{aligned} x &= \sin \theta \cos \phi; & y &= \sin \theta \sin \phi; & -1 \leq x \leq +1; \\ -1 \leq y \leq +1; & 0 \leq \theta \leq \pi/2; & 0 \leq \phi \leq 2\pi; \end{aligned}$$

which for $m, n \rightarrow \infty$ forms a complete orthogonal system of functions in two dimensions permitting the approximation of an arbitrary $H(x, y)$ subject only to Dirichlet conditions, namely a two-dimensional Fourier series. Thus if an optimum approximation in the mean square sense to $H(x, y)$ is desired, the excitation coefficients are given by

$$A_{mn} = \frac{1}{4} \int_{-1}^1 \int_{-1}^1 \frac{H(x, y)}{g_{00}(x, y)} \exp[-jn\pi x - jm\pi y] dx dy. \quad (6)$$

For other fitting criteria the A_{mn} coefficients may be subsequently modified as in the one-dimensional case.³ The important point is, however, that one can synthesize patterns which are nonseparable in either (θ, ϕ) or (x, y) or in neither. To show a simple example of a nonseparable pattern consider a pattern that is to be of

constant amplitude (unity) for $0 \leq \phi \leq 90^\circ$, $0 \leq \theta \leq 90^\circ$ and $180^\circ \leq \phi \leq 270^\circ$, $0 \leq \theta \leq 90^\circ$, and zero elsewhere. Translating into x, y coordinates

$$f(x, y) = 1 \quad \begin{cases} 0 \leq x, y \leq 1 \\ -1 \leq x, y \leq 0 \end{cases} \quad (7)$$

and

$$f(x, y) = 0 \quad \text{elsewhere.}$$

The excitation coefficients are given by (assuming an array of point sources)

$$A_{mn} = \frac{C}{mn} \quad \text{for } m \text{ and } n \text{ odd,}$$

where C is a constant;

$$= 0 \quad \text{otherwise} \quad (8)$$

which may be obtained almost by inspection. However it is easy to show that it is impossible to satisfy the conditions of (7) by means of a product function of the form $f(x, y) = f_1(x)f_2(y)$. A pattern of some importance is one requiring a cosecant shaped beam for only one section of (θ, ϕ) space, e.g., $0 \leq \phi \leq 90^\circ$ and $\theta_1 \leq \theta \leq 70^\circ$. In terms of x, y the cosecant pattern is given by $1/\sqrt{x^2 + y^2}$. Thus the excitation coefficients would be given by

$$\begin{aligned} A_{mn} &= \int_{\theta_1}^{\sin \theta_1} \int_{\sqrt{\sin^2 \theta_1 - x^2}}^{\sqrt{\sin^2 \theta_2 - x^2}} \\ &+ \frac{1}{4} \int_{\sin \theta_1}^{\sin \theta_2} \int_0^{\sqrt{\sin^2 \theta_2 - x^2}} \frac{\exp[-jn\pi x - jm\pi y]}{\sqrt{x^2 + y^2}} dx dy. \quad (9) \end{aligned}$$

In addition to the synthesis of non separable patterns the results are useful in the cases where the pattern behavior is of importance outside the principal planes where ϕ is neither zero nor 90° .

A Method to Reduce Antenna Ground Reflections*

DAVID SABIH†

IN many cases of antenna measurements such as antenna positioning or antenna pattern measurements, it becomes desirable to reduce or eliminate antenna ground reflections, because they lead to erroneous results and yield a distorted pattern. The following is a brief description of a method to reduce ground reflections. The method is based upon frequency-modulating the signal radiated from the antenna to be posi-

tioned, or whose radiation pattern is to be measured.

Fig. 1 shows the physical relationship between the transmitting antenna and the receiving antenna in the usual setup for antenna pattern measurement. L is the distance between the transmitting antenna and the receiving antenna, and h is the height of the transmitting antenna above ground level (h is also the height of the receiving antenna).

As shown in Fig. 1, the ground reflection is considered as being produced by an image antenna. The signal

³ J. C. Simon, "Applications of periodic functions approximation to antenna pattern synthesis and circuit theory," IRE TRANS. ON ANTENNAS AND PROPAGATION, vol. AP-4, pp. 429-440; July, 1956.

* Manuscript received by the PGAP, September 11, 1959.

† Systems Res. Lab., Motorola, Inc., Riverside, Calif.

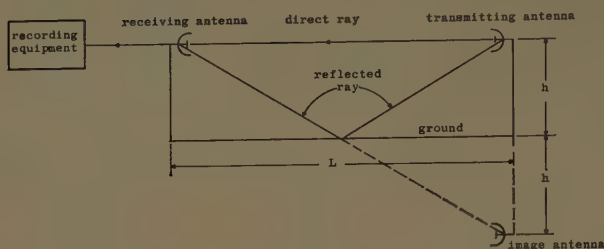


Fig. 1.

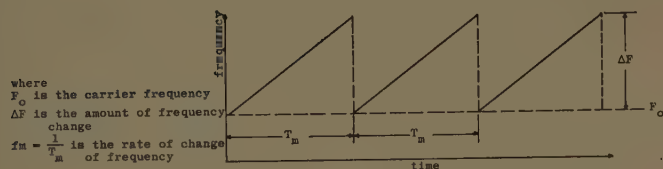


Fig. 2.

transmitted by the antenna is frequency-modulated; its characteristics are shown in Fig. 2. The time required for the direct ray to reach the receiving antenna is given by

$$T_d = \frac{L}{C}$$

where C is the velocity of propagation in free space, while the time required for the reflected ray to reach the receiving antenna is

$$T_R = \frac{\sqrt{L^2 + 4h^2}}{C}$$

A comparison between T_d and T_R will yield the fact that $T_R > T_d$. A portion of the transmitted signal is also fed to the receiving antenna through a waveguide whose total length is denoted by W . The time required for the signal through the waveguide to reach the receiving antenna is given by

$$T_w = \frac{W}{V_g}$$

where V_g is the velocity of propagation of energy along the waveguide. Since V_g is less or equal to the velocity of light, and W is larger than the reflected ray path of

$$\sqrt{L^2 + 4h^2},$$

then

$$T_d < T_R < T_w.$$

Fig. 3 is a plot of frequency vs time for the signals reaching the receiving antenna through the various paths. The signals received by the antenna through the direct and reflected paths are mixed in a mixer with the signal from the waveguide as shown in Fig. 4.

As shown in Fig. 3, f_{bd} is the beat frequency between the direct ray signal and the waveguide signal while f_{bR} is the beat frequency between the reflected ray signal and the waveguide signal. By inspecting Fig. 3, it can

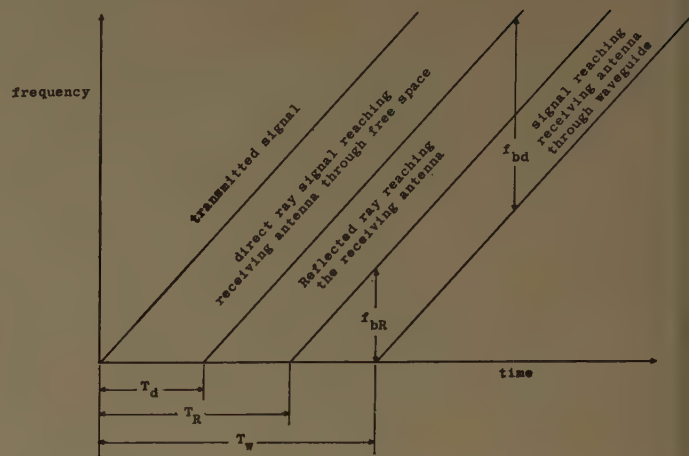


Fig. 3.

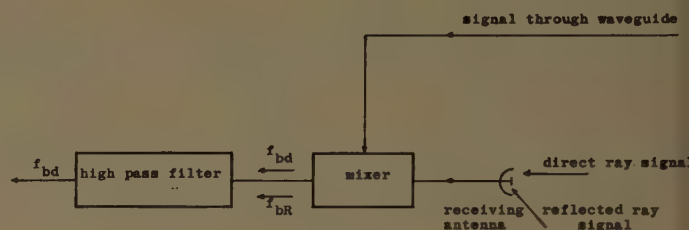


Fig. 4.

be shown that f_{bd} is greater than f_{bR} . This physical fact can also be shown mathematically

$$f_{bd} = \dot{F}(T_w - T_d)$$

$$f_{bR} = \dot{F}(T_w - T_R)$$

where \dot{F} is the rate of change of frequency.

$$\frac{f_{bd}}{f_{bR}} = \frac{T_w - T_d}{T_w - T_R}$$

since $T_R > T_d$; then

$$T_w - T_d > T_w - T_R.$$

Therefore, f_{bd} is greater than f_{bR} .

Thus, feeding the output of the mixer to a high-pass filter designed to pass f_{bd} , but to reject f_{bR} , will result in rejection of the reflected energy. The degree of reducing or eliminating the reflected signal will depend mainly on the design of the high-pass filter.

The following numerical example illustrates the method of reducing antenna ground reflections.

$$F_0 = 10,000 \text{ mc}$$

$$\Delta f = 100 \text{ mc}$$

$$f_m = 1 \text{ kc}$$

$$L = 100 \text{ meters}$$

$$h = 10 \text{ meters}$$

$$w = 120 \text{ meters}$$

$$T_d = \frac{100}{3 \times 10^8} = 0.333 \times 10^{-6} \text{ seconds}$$

$$T_R = \frac{\sqrt{(100)^2 + (20)^2}}{3 \times 10^8} = 0.340 \times 10^{-6} \text{ seconds}$$

$$F = \frac{\Delta F}{T_m} = \Delta F f_m = 10^{11}.$$

A waveguide whose dimensions are 2×1 cm is used to guide the energy from transmitting antenna to receiving antenna, hence

$$\lambda_c = 4 \text{ cm for the TE}_{10} \text{ mode}$$

$$V_g = C \sqrt{1 - \left(\frac{\lambda}{\lambda_c}\right)^2} = 3 \times 10^{10} \sqrt{1 - \left(\frac{3}{4}\right)^2} \\ = 1.98 \times 10^8 \text{ meters per second}$$

$$T_w = \frac{120}{1.98 \times 10^8} = 0.605 \times 10^{-6} \text{ seconds}$$

$$f_{bd} = F(T_w - T_d) = 27.2 \text{ kc}$$

$$f_{bR} = F(T_w - T_R) = 26.5 \text{ kc}$$

Thus a high-pass filter passing 27.2 kc and rejecting 26.5 kc will reduce appreciably the antenna ground reflections.

ACKNOWLEDGMENT

The author gratefully acknowledges the help rendered by B. Kopeloff in developing the ideas presented in this paper.

Impulse Excitation of a Conducting Medium*

J. GALEJS†

Summary—The depth of penetration into a conducting medium, where sinusoidal surface excitations generate peak magnetic fields or derivatives equal to those of an impulse-type surface excitation, are calculated. Finite pulses generate fields similar to those of a surface impulse provided they are sufficiently short. The maximum permissible pulse duration is proportional to the square of the specified penetration depth. In order to exhibit minimum attenuation, the excitation fields must be unipolar over a time period comparable with the transient duration. Such fields may be generated within the induction field of the source.

EXCITATION of a conducting medium by transient dipole sources and also by transient surface waves has been investigated by several authors.¹⁻⁸ The transient fields that are attenuated propor-

tionally to an inverse power of the distance may be expected to be stronger than the exponentially attenuated sinusoidally varying fields. Still, such a comparison has not been made. Also problems associated with the generation of appropriate transient pulses require a brief discussion.

Particularly simple relations are obtained by a surface wave excitation of a semi-infinite conducting medium. The subsurface field caused by a sinusoidal surface excitation $H_0 \exp(j\omega t)$ (ignoring the field variation along the surface) is⁹

$$H(z, t) = H(z, \omega) e^{j\omega t} = H_0 \exp[\pm \sqrt{2j\omega} \sqrt{0.5\mu\sigma} z] e^{j\omega t}, \quad (1)$$

where the plus and minus signs refer to negative and positive frequencies ω respectively. The response to an impulse

$$H_0(t) = \delta(t) H_0 T \quad (2)$$

is obtained by integrating (1) as

$$H(z, t) = \frac{1}{2\pi} \int_{-\infty}^{\infty} H(z, \omega) e^{j\omega t} d\omega = \frac{4DH_0T}{\sqrt{\pi} z^2} u^{3/2} e^{-u}, \quad (3)$$

where

$$D = 1/(\mu\sigma) \\ u = z^2/(4Dt) = z^2\mu\sigma/(4t). \quad (4)$$

⁹ This equation applies strictly to a plane wave excitation of an infinite medium with neglected displacement currents.

* Manuscript received by the PGAP, April 13, 1959.

† Applied Res. Lab., Sylvania Electronic Systems, Waltham, Mass.

¹ J. R. Wait, "Transient electromagnetic propagation in a conducting medium," *Geophysics*, vol. 16, pp. 213-221; April, 1951.

² J. R. Wait, "A transient magnetic dipole source in a dissipative medium," *J. Appl. Phys.*, vol. 24, pp. 341-343; March, 1953.

³ W. J. Yost, "The interpretation of electromagnetic reflection data in geophysical exploration," *Geophysics*, vol. 17, pp. 89-105; January, 1952.

⁴ B. K. Bhattacharyya, "Propagation of transient electromagnetic waves in a conducting medium," *Geophysics*, vol. 20, pp. 959-961; October, 1955.

⁵ B. K. Bhattacharyya, "Propagation of transient electromagnetic waves in a medium of finite conductivity," *Geophysics*, vol. 22, pp. 75-88; January, 1957.

⁶ B. K. Bhattacharyya, "Electromagnetic fields of a transient magnetic dipole on the earth's surface," *Geophysics*, vol. 24, pp. 89-109; February, 1959.

⁷ P. I. Richards, "Transients in conducting media," *IRE TRANS ON ANTENNAS AND PROPAGATION*, vol. AP-6, pp. 178-182; April, 1958.

⁸ J. Keilson and R. V. Row, "Transfer of transient electromagnetic surface waves into a lossy medium," *J. Appl. Phys.*, vol. 30, pp. 1595-1598; October, 1959.

The voltage induced in a pickup loop located in the dissipative medium is proportional to the time derivative of $H(z, t)$ in (1) or (3). By equating either the fields of (1) and (3) or their derivatives, one obtains the curves plotted in Fig. 1. Considering an excitation frequency $\omega = 10,000$ radians per second, an impulse excitation of $T = 10^{-4}$ second produces weaker H fields in sea water within the range of $z = 7.5$ to 18.9 meters and weaker derivatives within the range of $z = 15.7$ to 36.5 meters.

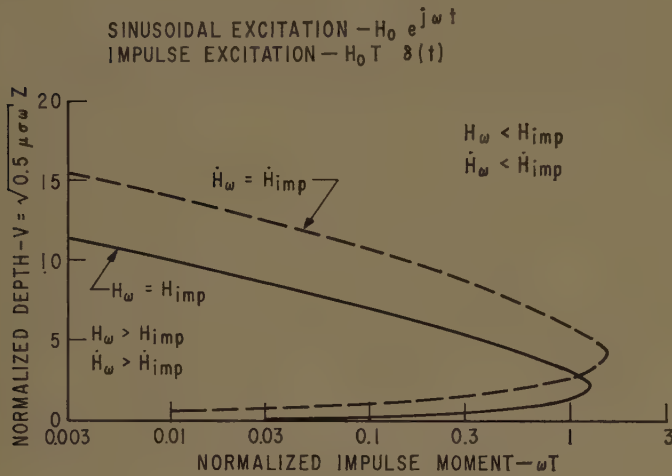


Fig. 1—Comparison of sinusoidal and impulse excitation.

The response to a finite pulse is obtained by convolving the impulse response (3) with the specified pulse shape. This response has been calculated for a surface excitation H_0 which is inversely proportional to the pulse duration T . Computation shows that the peak field caused by a finite pulse excitation is larger than 96 per cent of the peak field caused by the impulse excitation, if the pulse duration is less than

$$T_c = \frac{z^2}{8D} = 6.28 \times 10^{-7} z^2 \quad (5)$$

with $\sigma = 4$ mho/meter (sea water). The peak value of $H(z, t)$ is larger than 96 per cent of the peak derivative of the impulse response if the pulse duration is less than $T_c/4$. The earlier example considered an impulse excita-

tion $H_0(t) = H_0 T \delta(t)$ with $T = 10^{-4}$ seconds. The peak fields or field derivatives generated by a finite H_0 surface pulse of duration T will be at least 96 per cent of the peak fields or field derivatives generated with the above impulse excitation at depths below 12.7 and 25.4 meters respectively.

The noted difference in attenuation characteristics between sinusoidal and unipolar excitation may be explained qualitatively by considering the effects of transients caused by the sinusoidally varying fields during successive half cycles of the signal. The short positive half cycle is followed by a short negative half cycle, both of which generate long transients which are almost equal in amplitude but opposite in polarity and hence essentially cancel. Only unipolar pulses with non-subtracting transients exhibit the low attenuation.

The subsurface transient fields may be generated by sources located in the lossless medium consisting of a superposition of electric and magnetic dipoles. The surface excitation may be estimated from the free space fields of the sources and their images. Thus

$$H_e = \sum_i \frac{l_i}{4\pi} \left(\frac{I_i}{R_i^2} + \frac{\dot{I}_i}{cR_i} \right), \quad (6)$$

$$H_m = \sum_i \frac{a_i^2}{4} \left(\frac{I_i}{R_i^3} + \frac{\dot{I}_i}{cR_i^2} + \frac{\ddot{I}_i}{c^2 R_i} \right), \quad (7)$$

where l is the length of the current element and a is the radius of the current loop. Unipolar induction or static fields are obtained from unipolar current pulses in electric and magnetic dipoles respectively. The corresponding radiation and induction fields will be bipolar. The fields are positive during the rise time of the current pulse and negative during the decay time, but they will appear as quasi-unipolar if the successive bipolar transients do not overlap at the specified penetration depth. Steady, long duration currents produce the desired fields only during their rise and decay times. Such currents may be feasible with magnetic dipoles, but they are improbable with electric dipoles. Essentially unipolar surface pulses that exhibit low attenuation with increasing penetration depth into the lossy medium are thus feasible only within the induction field of the sources.

Electromagnetic Transients in Conducting Media*

S. H. ZISK†

Summary—In a recent paper, Richards derives expressions for the electric and magnetic fields of a short pulse of electric or magnetic dipole moment in a conducting medium. An alternative analysis is given which explains certain unusual results of the original work as arising from dispersion in the conducting medium and from the frequency dependence of the attenuation factor of the fields. The conclusion drawn is that communication by pulses is expected to be inferior to that by low-frequency continuous waves.

IN a recent paper by Richards¹ there appears an analysis of the propagation of a short, unidirectional pulse of electromagnetic radiation in a conducting medium. He obtains interesting solutions for Maxwell's equations in the median plane for arbitrary time-varying electric and magnetic dipoles. The solutions contain inverse Laplace transforms of relatively involved expressions, which can then be simplified by a proper choice of the time variation of the radiating dipole. In an example given in the paper, it is shown that a dipole pulse at the origin propagates in a rather peculiar fashion. The most striking prediction is that the amplitude decays as $1/r^3$ or $1/r^4$, rather than exponentially as is expected for a continuous wave in a conducting medium. In addition, the pulse is expected to lengthen with distance traveled, and the average propagation velocity to decrease.

One's initial reaction is that of excitement at a possibly new effect to be applied, for example, to underwater communication. In an effort to improve our understanding of the physical principles back of these results, we applied the technique of Fourier analysis and resynthesis to the short pulse. If the variation of attenuation and propagation velocity with frequency is considered for the case of a conducting medium, one begins to suspect that the higher-frequency components of the pulse are attenuated more rapidly than their lower-frequency companions. Qualitatively, this dispersion alone could account for at least the alteration of the pulse shape and the slower decay which were reported in the paper.

Let a plane-wave pulse of shape $f(t)$ and width δ be generated in the y - z plane ($E_y = E_z = 0$, $H_y = H_z = 0$, for $x = 0$ and $|t| > \delta/2$; $E_x = H_x = 0$ everywhere). Then the Fourier transform of $f(t)$ is

$$G_0(\omega) = \frac{1}{\sqrt{2\pi}} \int_{-\delta/2}^{\delta/2} f_0(t) e^{-j\omega t} dt.$$

This spectrum of frequencies passes through a filter consisting of x meters of the medium whose electrical characteristics are given by σ , ϵ , and μ . The transmission characteristic of the "filter" is

$$E/E_0 = e^{kx}, \quad (1)$$

where k can be derived from two of Maxwell's equations [just as (1) is so derived]:²

$$\begin{aligned} \nabla \times E &= -\mu \frac{\partial H}{\partial t} \\ \nabla \times H &= \epsilon \frac{\partial E}{\partial t} + \sigma E. \end{aligned}$$

From the condition of plane-wave propagation, each component whose time dependence is $e^{j\omega t}$ is found to have a propagation constant

$$k = -\left(\omega/u \sqrt{\frac{j\sigma}{\omega\epsilon} - 1}\right) \quad (2)$$

where $u = 1/\sqrt{\mu\epsilon}$ and k is chosen negative to agree with the physical fact of the attenuation of the wave with distance. For normal conductors, including sea water at frequencies up to at least 100 mc, $\sigma/\omega\epsilon \gg 1$, and

$$k \simeq -\left(1/u \sqrt{\frac{\sigma}{2\epsilon}}\right) \sqrt{\omega} - j\left(\sqrt{\frac{\sigma}{2\epsilon\omega}} \cdot 1/u\right) \omega. \quad (2a)$$

Here the real term expresses the attenuation constant of the wave and the imaginary term contains the velocity of propagation. Note that the propagation velocity $[\sqrt{2\epsilon\omega/\sigma} \cdot u]$ is much smaller than c at all frequencies where the medium can be treated as continuous. Assume, for simplicity, that $G_0(\omega) = -G(\text{constant})$; the original $f(t)$ is then a Dirac impulse. After x meters of propagation, the spectrum function becomes

$$G(\omega) = G \exp\left(-\frac{\omega}{u} \sqrt{\frac{j\sigma}{\omega\epsilon} - 1} x\right) \quad (3)$$

from (1) and (2). Taking the inverse transform, we obtain

$$f(t, x) = \int_{-\infty}^{\infty} \exp\left[-\frac{\omega}{u} \sqrt{\frac{j\sigma}{\omega\epsilon} - 1} x + j\omega t\right] d\omega, \quad (4)$$

* Manuscript received by the PGAP, October 6, 1959.
† Dept. of Elec. Engrg., Stanford University, Stanford, Calif.
Formerly at Research Labs., Hughes Aircraft Co., Culver City, Calif.

¹ P. I. Richards, "Transients in conducting media," IRE TRANS. ON ANTENNAS AND PROPAGATION, vol. AP-6, pp. 178-182; April, 1958.

² See, for example, J. A. Stratton, "Electromagnetic Theory," McGraw-Hill Book Co., Inc., New York, N. Y., pp. 270-276; 1941.

where G has been normalized to unity. Eq. (4) can be rewritten as

$$f(t, x) = \int_{-\infty}^{\infty} \exp \left\{ t \left(-\frac{\omega x}{ut} \sqrt{\frac{j\sigma}{\omega\epsilon}} - 1 + j\omega \right) \right\} d\omega, \quad (4a)$$

which is in a form suitable for integration by the saddle-point method.³

The derivative of the term in parentheses is set equal to zero, and two saddles are found. After making the approximation $(x/t)^2 \ll u^2$, which was justified above, the saddles are located at

$$\omega_0 = \left(\frac{j\sigma}{\epsilon} \right)^+ \quad \text{and} \quad \left(-\frac{j\sigma x^2}{4\epsilon u^2 t^2} \right).$$

Both are on the imaginary axis, but the contribution from the first is found to be negligible. After the same approximation is applied the result is

$$f(t, x) = \frac{E(t, x)}{E_0} \simeq \sqrt{\frac{\pi}{\epsilon u^2 t^3}} \exp \left(-\frac{\sigma x^2}{4\epsilon u^2 t} \right) \quad (5)$$

which has been plotted in Fig. 1 for $x = 100$ meters in sea water.

Let us find the time at which \bar{E} reaches a maximum at the distance x by differentiating f with respect to t .

$$t_{\max} = \frac{1}{3} \left(\frac{\sigma x^2}{4\epsilon u^2} \right).$$

³ P. M. Morse and H. Feshbach, "Methods of Theoretical Physics," McGraw-Hill Book Co., Inc., New York, N. Y., pp. 434 ff.; 1953. In 4(a), for practical reasons, the exponent is considered to decay to zero in the limit as ω approaches infinity rather than oscillating. This is equivalent to substituting a finite-width pulse for the impulse $f(t)$.

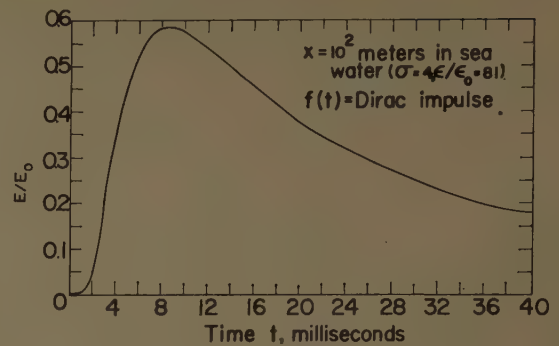


Fig. 1.

At this value of t ,

$$f_{\max} = \frac{E_{\max}}{E_0} = \left(\sqrt{\frac{\pi u^4}{\epsilon^4 (\pi/12)^3}} \right) \left(\frac{1}{x^3} \right). \quad (6)$$

So far we have shown that both the pulse shape and the inverse-cube attenuation follow from the increase in the relative importance of the lower frequencies (2), as the pulse propagates. The low average velocity of the pulse also follows from this fact and from the $\sqrt{\omega}$ dependence of the phase velocity.

One fact is evident from the type of approach used here. There does not appear to be any new phenomenon which might be exploited for a practical purpose. It has been shown that the higher-frequency components of a single-pulse source take no part in the propagation of energy over any great distance in a conducting medium. Propagation problems involving more complex wave shapes can be treated by neglecting their higher-frequency components, which will be attenuated in any case, although a better technique might be to use low-frequency wave shapes wherever possible for more efficient utilization of the available energy.

Contributors

William S. Ament (SM'55) was born in Pomona, Calif., on September 13, 1918. He received the A.B. degree with honors from Pomona College in 1939, and was a graduate assistant in physics there until 1940. After two years as a graduate student at Brown University, Providence, R. I., he was employed by the Naval Research Laboratory, Washington, D. C., in 1942. His work there was in the field of radio-wave



W. S. AMENT

propagation and radar, and he served as Assistant Head of the Wave Propagation Branch of the Electronics Division. He received the Ph.D. degree in applied mathematics from Brown University in 1959, and is presently a scientific liaison officer at the London, Eng., branch office of the Office of Naval Research.

Dr. Ament is a member of RESA.



Herman V. Cottony (M'45-SM'51) was born in Nizhni-Novgorod, Russia, on March 27, 1909. He received the B.S. degree in 1932 from Cooper Union Institute of Technology, New York, N. Y., the M.S.E.E. degree in 1933 from Columbia University, New York, N. Y., and the E.E. degree in 1946 from Cooper Union.



H. V. COTTONY

From 1935 to 1937, he was a research engineer with Sonotone Corporation,

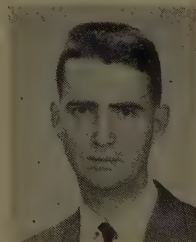
Elmsford, N. Y. In 1937, he joined the staff of the National Bureau of Standards, Washington, D. C. During World War II, on military leave from the NBS, he was at Signal Corps laboratories in various capacities, and served as Chief of the Thermionics Branch. He is presently Chief of the Antenna Research Section, Boulder Laboratories, National Bureau of Standards.

Mr. Cottony is a member of Tau Beta Pi, RESA, Commission VI of URSI, and U. S. Preparatory Committee III of CCIR.



James M. Flaherty (A'54-M'55) was born on July 3, 1925, in Pittsburgh, Pa. He received the B.S.E.E. degree from the Carnegie Institute of Technology, Pittsburgh, Pa., in 1948 and the M.S.E.E. degree from the University of Pittsburgh in 1956. During World War II, he served as an infantry communica-

tions technician in the U. S. Army and in 1949 he was commissioned as a Second Lieutenant in the Signal Corps Reserves. Since



J. M. FLAHERTY

1948, he has been employed as a research engineer on the technical staff of the Westinghouse Research Laboratories near East Pittsburgh, Pa., where his work has been concerned with antennas, electromagnetic wave propagation, radar systems, and microwave components.



Earl E. Gossard was born in Eureka, Calif., on January 8, 1923. He received the B.A. degree in meteorology in 1948 and the M.S. and Ph.D. degrees in physical oceanography in 1951 and 1956, respectively, from the University of California at Los Angeles.



E. E. GOSSARD

In 1948 he joined the U. S. Navy Electronics Laboratory, San Diego, Calif., as a meteorologist and has since been engaged in research in micrometeorology and the atmospheric physics and its effect on microwave propagation for the purpose of achieving more accurate operational predictions of radio and radar performance.

Mr. Gossard is a member of the American Meteorological Society and the American Geophysical Union.



Charles W. Harrison, Jr. (SM'57), for a photograph and biography, please see page 124 of the January, 1960, issue of these TRANSACTIONS.



Eugene Kadak (A'43-M'56) was born on March 4, 1919, in Scranton, Pa. He received the A.A. degree in 1939 from Scranton Keystone College, Scranton, and the B.S.E.E. degree in 1942 from Case Institute of Technology, Cleveland, Ohio.

From 1942 to 1947, he was employed as a radar and communications design engineer at the Westinghouse Electronics Division in Baltimore, Md., where most of his experience was with receiving systems. At present, he is on the staff of the Westinghouse Research Laboratories in Pittsburgh, Pa.,

which he joined in 1947 as a research engineer. During much of this time he has been a group leader in charge of a number of en-



E. KADAK

gineers and technicians employed in the development of an X-band airborne FM gunlaying radar. He has done a great deal of theoretical systems analysis work, particularly on radar, involving such considerations as clutter, noise, and jamming. More recently, he has concentrated on

a search for solutions to the problem of providing low-inertia high-gain antennas for early warning radar and has co-authored a number of papers in this field. This effort has resulted in the invention of several novel, very promising low-inertia types of antennas. He now has the engineering responsibility for the moving strip-map display development work being done at the Laboratories.

Mr. Kadak is a member of Eta Kappa Nu.



Joseph B. Keller, for a photograph and biography, please see page 205 of the April, 1959, issue of these TRANSACTIONS.



Ronold W. P. King (A'30-SM'43-F'53), for a photograph and biography, please see page 125 of the January, 1960, issue of these TRANSACTIONS.



George W. Leopard (S'42-A'48-SM'55) was born on January 17, 1910 in Shreveport, La. He received the B.S. degree in physics from Centenary College of Louisiana, Shreveport, in 1932.



G. W. LEOPARD

In 1942, he completed the wartime accelerated electronics courses for officers in the graduate schools of Harvard University and the Massachusetts Institute of Technology, both in Cambridge, Mass. He received

the M.S.E.E. degree from the University of Maryland, College Park, in 1959.

During World War II, he was an electronics officer in the U. S. Navy. Since 1947, he has been employed by the Electronics Test Division of the Naval Air Test

Center, Patuxent River, Md., and has been successively in charge of the evaluation of airborne search radar, electronic countermeasures equipment, and aircraft antennas. He is presently the Head of the Communication and Navigation Branch.



R. B. Muchmore (S'39-A'40-SM'49) was born on July 8, 1917, in Augusta, Kans. He received the B.S.E.E. degree in 1939 from the University of California, Berkeley, and the E.E. degree in communications engineering from Stanford University, Stanford, Calif., in 1942.

From 1942 to 1946 he was employed by the Sperry Gyroscope Co., Garden City, N. Y., as a project engineer working in the fields of antennas and

microwave test equipment. In 1946, he joined the staff of the Guided Missile Laboratory at the Hughes Aircraft Co., Los Angeles, Calif., where he did systems and noise analysis. From 1954 to 1958, he was with the Ramo-Wooldridge Corp., Los Angeles, Calif., as a senior member of the technical staff doing systems analysis and work in the field of radio propagation. He is now Director of the Guidance Research Laboratory, Space Technology Labs., Inc., Los Angeles, Calif.

Mr. Muchmore is a member of Sigma Xi, RESA, the Acoustical Society of America, and U. S. Commission II of URSI.



R. B. MUCHMORE

G. H. Owyang was born in Tientzin, China, on July 7, 1925. He received the B.S.E.E. degree from La Universitato Utopia, Shanghai China, in 1944, and the M.S. and Ph.D. degrees from Harvard University, Cambridge, Mass., in 1950 and 1959, respectively.



G. H. OWYANG

From 1944 to 1949, he worked with the Shanghai Power Company, China, as an engineer. He has also been on the engineering staff of Devanco Inc. and Frank L. Capps and Co., both in New York, N. Y. He was a research assistant at Gordon McKay Laboratory, Harvard University, and is now at the Radiation Laboratory, The University of Michigan, Ann Arbor.

Dr. Owyang is a member of Sigma Xi.



Eric Weger was born in Frankfurt, Germany on January 14, 1930. He received the B.E. degree in chemical engineering from The Johns Hopkins University, Baltimore, Md., in 1951. In 1955, he received the D.Eng. degree, also from The Johns Hopkins University. Since 1955 he has been assistant professor of chemical engineering at Johns Hopkins.



ERIC WEGER

In 1957 he became

associated with the Westinghouse Air Arm Division in Baltimore on a part-time basis. He has been concerned with problems in the areas of microwave and infrared thermal radiation.

Dr. Weger is a member of Sigma Xi and Tau Beta Pi.



Alvin C. Wilson (M'57) was born in Casper, Wyo., on September 24, 1925. From 1943 to 1945, he was a radio operator and technician in the U. S. Army, with service in Europe. He received the B.S.E.E. degree in 1948 from the University of Colorado, Boulder.



A. C. WILSON

From June, 1948 to June, 1949, he did seismograph work with the Stanolind Oil and Gas Company, Fort Worth, Tex. From June, 1949 through January, 1951, he was employed as an electrical engineer with the Standard Engineering and Manufacturing Company, Denver, Colo. From February, 1951 to October, 1955, he was a member of the civilian instructor staff in radar bombing systems at Lowry Air Force Base, Denver, Colo. Since October, 1955, he has been an electronic engineer in the Radio Propagation Physics Division of the National Bureau of Standards, Boulder, Colo.

Mr. Wilson is a member of RESA.

FOR INFORMATION CONCERNING ADVERTISING RATES

Contact

MR. DELMAR C. PORTS
Jansky and Bailey, Inc.
1339 Wisconsin Avenue N.W.
Washington 7, D.C.
Telephone: Federal 3-4800

INSTITUTIONAL LISTINGS

The IRE Professional Group on Antennas and Propagation is grateful for the assistance given by the firms listed below, and invites application for Institutional Listing from other firms interested in the field of Antennas and Propagation.

AERO GEO ASTRO CORP., 1200 Duke St., Alexandria, Va.

Research and Development; Antennas; Transponders; Command Receivers; Augmenters; Telemetry-Radar

ANDREW CORPORATION, 363 E. 75th St., Chicago 19, Ill.

Antennas, Antenna Systems, Transmission Lines, Development and Production.

ANTLAB, INC., 6330 Proprietors Rd., Worthington, Ohio

Antenna Pattern Range Systems—Recorders & Mounts.

BLAINE ELECTRONETICS, INC., 14757 Keswick St., Van Nuys, Calif.

Antennas, Paraboloids, Scale Models, Antenna Radiation Pattern Measurement Towers.

DEVELOPMENTAL ENGINEERING CORP., 1001 Conn. Ave. N.W., Washington, D. C. and Leesburg, Va.

Research, Development, Installation of Antennas and Antenna Equipment for Super Power Stations.

THE GABRIEL LABORATORIES, Div. of the Gabriel Co., 135 Crescent Road, Needham Heights 94, Mass.

Research and Development of Antenna Equipment for Government and Industry.

HUGHES AIRCRAFT COMPANY, Culver City, Calif.

Research, Development, Mfr.: Radar, Missiles, Antennas, Radomes, Tubes, Solid State Physics, Computers.

I-T-E CIRCUIT BREAKER CO., Special Products Div., 601 E. Erie Ave., Philadelphia 34, Pa.

Design, Development and Manufacture of Antennas, and Related Equipment.

JANSKY & BAILEY, INC., 1339 Wisconsin Ave. N.W., Washington 7, D. C.

Radio & Electronic Engineering; Antenna Research & Propagation Measurements; Systems Design & Evaluation

MARK PRODUCTS CO., 6412 W. Lincoln Ave., Morton Grove, Ill.

Multi Element Grid Parabolas, Antennas for Two-Way Communications, R & D.

THE W. L. MAXSON CORP., 475 Tenth Ave., New York 18, N.Y.

Research, Development, & Manufacture of Airborne, Missile & Ordnance Systems & Equipment.

TRANSCO PRODUCTS, INC., 12210 Nebraska Ave., Los Angeles 25, Calif.

Res., Design, Dev., & Mfr. of Antenna Systems & Components for Missile, Aircraft & Ground Installations

WEINSCHEL ENGINEERING COMPANY, INC., Kensington, Md.

Antenna Pattern Receivers; Bolometer Amplifiers; Modulated Microwave Sources;
Insertion Loss Measuring Systems

WHEELER LABORATORIES, INC., Great Neck, N. Y.; Antenna Lab., Smithtown, N. Y.

Consulting Services, Research and Development, Microwave Antennas and Waveguide Components.

WIND TURBINE COMPANY, West Chester, Pa.

Complete Antenna Systems and Towers

The charge for Institutional Listing is \$25 for one issue or \$100 for six consecutive issues (one year). Application may be made to the Technical Secretary, The Institute of Radio Engineers, 1 East 79th Street, New York 21, N. Y.